Development of Supramolecular Resists for Advanced Lithography

A thesis submitted to the University of Manchester

for the degree of Doctor of Philosophy

in the Faculty of Science and Engineering

2021

Hayden R. Alty

Department of Chemistry

School of Natural Sciences

TABLE OF CONTENTS

Word Count: 41111

LIST OF COMMON ABBREVIATIONS

EBL – Electron Beam Lithography

IBL – Ion Beam Lithography

HIBL – Helium Ion Beam Lithography

EUV(L) – Extreme Ultra Violet (Lithography)

SEM – Scanning Electron Microscope

HIM – Helium Ion Microscope

PE(s) – Primary Electrons(s)

SE(s) – Secondary Electron(s)

AE(s) – Auger Electron(s)

PI(s) – Primary Ion(s)

LER – Line Edge Roughness

HVM – High Volume Manufacture

UoM – University of Manchester

XPS – X-ray Photoelectron Spectroscopy

II

LIST OF FIGURES

LIST OF TABLES

IV ABSTRACT

With the death of Moore's Law approaching due to 193 immersion lithography reaching its ultimate resolution limit, new advanced lithographic techniques are required to reach beyond the 5 nm node. The current successor to 193 immersion lithography is EUV lithography the success of which relies on the manufacture and reliability of photomasks. The demand on mask manufacture is to produce smaller on wafer features without increase lead times. To successfully meet this target, new resist materials must be developed for electron and ion beam lithography. Thus, a series of modular supramolecular resists were designed and investigated. To expedite the design process an ion and electron simulation, named EXCALIBUR, was developed to simulate new resists before synthesis to identify viable candidates for characterization. EXCALIBUR employs Monte Carlo methods to simulate full secondary and auger electron cascades generated in electron and ion beam exposures. Using this design process an indium ring based electron beam resist ($[NH_2(allyl)_2][In_7NiF_8(O_2C^tBu)_{16}]$) was developed which was capable of producing 50 nm pitch lines with a dose of 1400 pC/cm using 30 kV electrons and a chromium ring ion beam resist ($[NH_2(allyl)_2][Cr_7NiF_8(O_2C^tBu)_{16}]$) which yielded 16 nm pitch lines with a dose of 22pC/cm using 35 kV Helium ions. The supramolecular resists also can be deposited through sublimation which provides the basis for a novel 3D resist lithography technique.

DECLARATION

No portion of the work referred to in the thesis has been submitted in support of an application for another degree or qualification of this or any other university or other institute of learning.

COPYRIGHT STATEMENT

i. The author of this thesis (including any appendices and/or schedules to this thesis) owns certain copyright or related rights in it (the "Copyright") and s/he has given The University of Manchester certain rights to use such Copyright, including for administrative purposes.

ii. Copies of this thesis, either in full or in extracts and whether in hard or electronic copy, may be made only in accordance with the Copyright, Designs and Patents Act 1988 (as amended) and regulations issued under it or, where appropriate, in accordance with licensing agreements which the University has from time to time. This page must form part of any such copies made. Presentation of Theses Policy You are required to submit your thesis electronically Page 11 of 25

iii. The ownership of certain Copyright, patents, designs, trademarks, and other intellectual property (the "Intellectual Property") and any reproductions of copyright works in the thesis, for example graphs and tables ("Reproductions"), which may be described in this thesis, may not be owned by the author, and may be owned by third parties. Such Intellectual Property and Reproductions cannot and must not be made available for use without the prior written permission of the owner(s) of the relevant Intellectual Property and/or Reproductions.

iv. Further information on the conditions under which disclosure, publication and commercialisation of this thesis, the Copyright and any Intellectual Property and/or Reproductions described in it may take place is available in the University IP Policy (see http://documents.manchester.ac.uk/DocuInfo.aspx?DocID=24420), in any relevant Thesis restriction declarations deposited in the University Library, The University Library's regulations (see http://www.library.manchester.ac.uk/about/regulations/) and in The University's policy on Presentation of Theses

ACKNOWLEDGEMENTS

I would like to express my gratitude to my supervisors Dr. Scott Lewis, Prof. Richard Winpenny and Prof. Stephen Yeates, who put their faith in me and gave me their patience, guidance, and the opportunity to travel abroad and work with a variety of people over the course of my PhD.

I would also like to personally thank Eric Whittaker for his wisdom and counsel; Guy DeRose for his enthusiasm in my research; Chris Muryn for his knowledge and support; Grigore Timco, Antonio Fernandez, Richard Grindell and everyone in the Molecular Magnets Group for their endeavours to synthesise the resist materials this work is based on; Ahmad Chaker for his ceaseless work ethic and willingness to help; Alex Walton for his help collecting XPS data; Ranjan Ramchandra who didn't ignore my emails and was willing to dig through his old research to help me when I reached out; and many more staff and students in the Department of Chemistry and the Photon Science Institute who have helped and inspired me.

Finally, I would like to thank my family and friends, for their continued support over the last 3 and a half years, without whom I would certainly not have been in the position to complete a PhD.

PREFACE

This thesis is based on work that has been ongoing since 2015 which is when I started my master's degree project as part of my undergraduate studies (Physics MPhys) at the University of Manchester. It was during this time I learned the art Electron Beam Lithography and began simulating electron scattering in resists. At this point I had no intention of doing a PhD, but Scott and Richard allowed me to explore and carve my own niche in their research which created the seed that became, and gave me the confidence to pursue, the work in this thesis.

1

INTRODUCTION

Contents

The improvement in the performance and reduction in the size of microprocessors has led to huge increases in processing power of all consumer technology. These microprocessors are an integrated circuit (IC) which was first developed in 1958 [1]. An IC is a group of electronic components and transistors imbedded in the surface of a silicon wafer or "chip". The constant scaling of these transistors drives the semiconductor industry and as

the demand for more powerful computers increases, constant progress in manufacturing processes must be made. The benchmark for this progress is based upon an observational law first noted by Gordon Moore founder of Intel. In 1965 he noted that the number of transistors per unit area would double every 18 months [2]. This prediction, which became known as 'Moore's Law', held true for the following decade until 1975 when Moore saw a downturn in the speed of development and so adjusted his prediction to doubling every two years [3]. This revised law became the benchmark for the industry defining targets and forecasts for the subsequent decades as the semiconductor industry continued to achieve this target over this period. This progress is displayed in Figure **1.1** which shows the number of transistors per microprocessor increasing between 1970 and 2018.
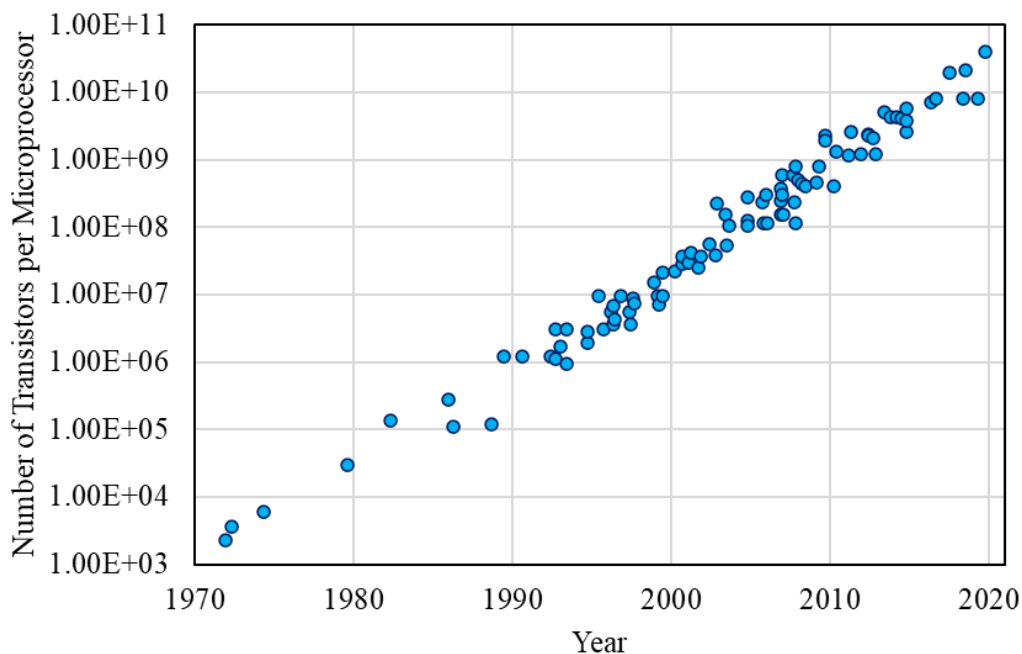
Figure 1.1 *A plot of the increase in the number of transistors per microprocessor between 1970 and 2018 showing the history and progression of the semiconductor industry driven by Moore's law (reproduced using data from* [4]*)*

However, the last decade has seen a slow decay in the rate of growth leading some commentators including Moore himself to declare the 'death' of Moore's law [5], predicting this decline to increase over the coming years [6]. This means that new manufacturing techniques and technologies are needed now more than ever [7].

To keep pace with Moore's law and the demand from the consumer market a series of targets have been set for manufacturing which mark a reduction in feature size whilst still maintaining or more often improving throughput. These benchmarks are known as nodes and have a dimension in nanometres related to them, however they can be misleading as the size associated with them does not relate directly to a resolution in the IC fabrication. For example, Intel is manufacturing at the 10 nm node and this is just a name for their current manufacturing process and not a description of the critical dimension (CD) of the IC which are expected to have a feature pitch of 34 nm [8]. Pitch is a form of measure of the resolution of lithographic features which considers the periodicity of the structures, i.e. how closely features can be patterned next to each other, as opposed to measuring the dimensions of a single feature. It is commonly interchangeably with half pitch which is when the features and spaces between features are the same size, which is a pattern density of 50%. So, the names of the nodes have been set to follow the trend of Moore's law, as the industry must show significant improvement to sell products and make profits and attract investors, but the minimum feature size on a chip does not match this. The next node will be the 5 nm node which is expected to have a feature pitch of 24 nm [9], beyond which quantum tunnelling in 2D devices becomes problematic [10].

1.1 <u>Lithography</u>

Lithography is a pattern transfer technique where a resist material is used to protect an underlying substrate into which a pattern is to be transferred. Areas of the resist are exposed changing its solubility to a developing solvent. The resist is then developed exposing parts of the substrate corresponding to the pattern of exposure. When this matrix is subsequently etched, the resist material resists the etchant, hence its name, protecting the underlying substrate and allowing the uncovered areas to be etched, thus transferring

the pattern from the resist layer into the substrate. The resist can then be removed leaving the final substrate structures which can then be metalized.

Since its invention in the 1700s Lithography has been one of the most prevalent and successful methods of pattern transfer [11], However, it was only in the 1960s that lithography, as we know it today, started to be used in the manufacture of devices [12]. Coinciding with the arrival of ICs, manufacturers needed a way to create circuits which are imbedded into the surface of a semiconductor and turned to using photographic exposure and etching techniques to pattern transistors onto a germanium substrate. In doing so Lathrop and Nall created a process of manufacturing calling it Photolithography [13]. Although similar techniques existed prior to Lathrop and Nall coining the term, they were the first to use Photolithography in the creation of semiconductor circuits. Photolithography uses photons to expose a pattern into a resist material. However, this is not the only method of exposure. In Electron Beam Lithography (EBL) and Ion Beam Lithography (IBL), a beam of electrons or ions, as opposed to photons, is used to expose the resist [14 - 16]. Less commonly used are Nano Imprint Lithography, [17, 18] which uses mechanical force to change the solubility of the resist, and Scanning Probe Lithography, which uses the field effect at the tip of a probe to oxidize a material which can then be selectively etched [19].

Lithography is the main method of fabrication used in semiconductor industry and has been the only manufacturing technique that has been able to maintain the pace set by Moore's law and the subsequent demands by industry. However, this has become increasingly difficult because, as well as the higher resolutions and smaller CDs that are required, low exposure doses are a necessity to increase manufacturing through-put. The dose of a resist is a measure of the level of exposure needed for the expected structures to be resolved after development. For photolithography, the dose is given by,

$$D_{PL} = \frac{\Phi.t}{A}$$

where D is the dose delivered to the sample usually measured in mJ/cm^2, Φ is the photon flux at the sample and t is the dwell time, which is how long the area, A, is being exposed. For electron beam lithography the dose is given by [20],

$$D_{EBL} = \frac{I.t}{A}$$

As before D is the dose delivered to the sample usually measured in μC/cm^2 for an area or pC/cm for a single pixel line, '*I*' is the beam current or flux of the electron beam and t is the dwell time which is how long the beam stays on the area that is being exposed.

When manufacturing ICs the flux of the source is fixed and is limited by the system, the area is set by the size of the structures being created, therefore the only factor that can be varied to change the dose is the time of the exposure. The time of the exposure is important as the more time it takes to expose a wafer the lower the throughput will be. The time for an exposure can be reduced by using a more sensitive resist, ergo the resist is more susceptible to exposure. This is where resist development is essential to the progress of lithography because as the processes to create smaller and smaller features become more complex and time consuming, then a more sensitive resist that does not compromise the resolution is needed.

1.2 <u>Exposure Types and Mechanisms</u>

When a resist material is exposed, it undergoes a localised chemical change altering its solubility. If the resist becomes more soluble then this is known as a positive tone resist which means that the exposed area will be washed away when the resist is developed. The opposite case, where the resist becomes less soluble when exposed, is a negative tone resist [21]. This is displayed in Figure **1.2**. The difference between the two tones of resist is due to the exposure mechanics responsible for changing the solubility.

Positive tone resists are usually large molecule polymer resists. These resists may have other smaller molecule additives and activators but for the most part they are made up of large polymer chains with molecular weight on the order of tens or hundreds of

thousands. The main process for the exposure of positive tone resists is chain scissioning [22]. This is a process where an incoming photon or electron breaks the bonds between monomers breaking the polymer chain into smaller molecules. These smaller molecules will have an increased solubility than the longer chains and hence be more soluble in the developing solvent. The speed of this process can be amplified by including photoacid generators (PAG) in the resist which when ionized during exposure become free radical molecules which will react with the polymer causing more chain scissioning events [23]. This technique is employed to form a group of resists known as Chemically Amplified Resists (CAR's).
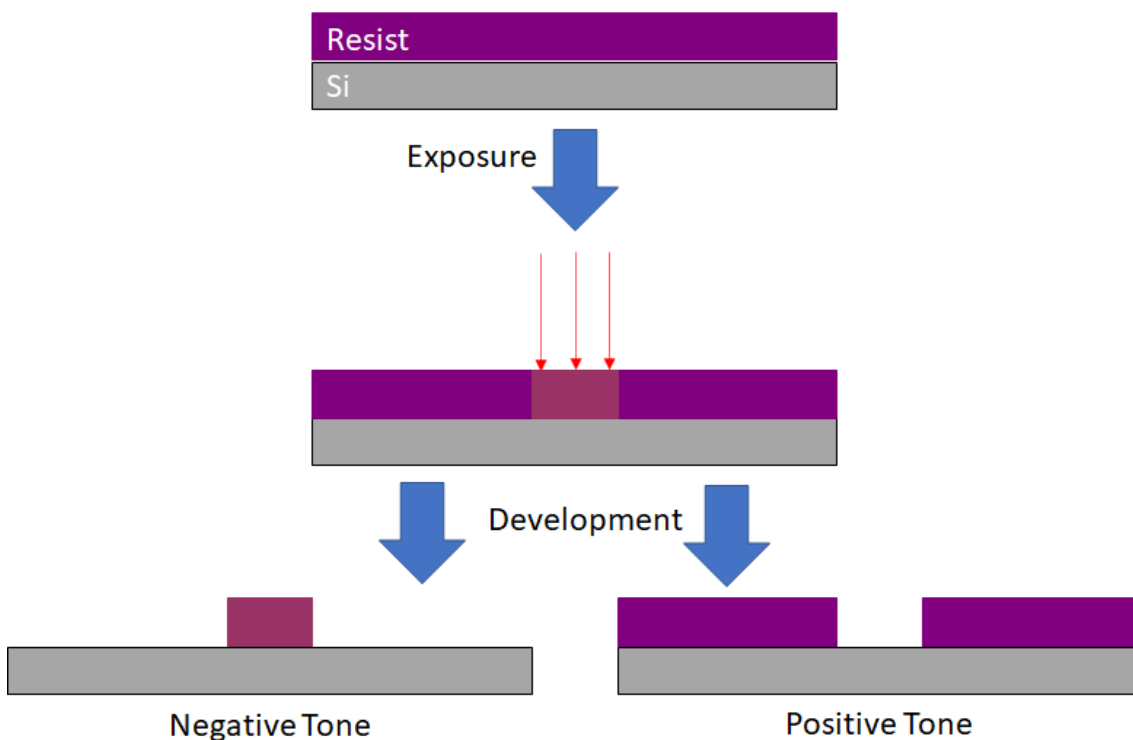
Figure 1.2 *The difference between positive and negative tone resists after exposure and development.*

For negative tone resists one common mechanic of exposure is cross linking. This is the opposite process to chain scissioning where bonds in the smaller molecules are broken leading them to react with each other creating larger molecules [24]. This also occurs with polymers where large chains become interconnected or cross linked however this process usually requires significantly higher doses than positive tone exposure so by virtue is less

common. The outcome of cross linking is that the larger molecules become less soluble meaning they are left behind after development. In metal organic resists, if cross linking does not occur then the organic component of the resist which allows the metal compound to be dissolved in common solvents, may be split from the metal component. The organic component is then either diffused out of the material as a gas or removed during development hence leaving the remaining insoluble metal compound to form the required structures.

1.2.1 Photolithography

Currently, Photolithography is the main method of manufacture for integrated circuits [25]. The industry standard technique is 193 nm immersion lithography where a 193nm wavelength light source is used as the exposure source. This process uses immersion resolution enhancement where a fluid replaces the gap between the lens (see Figure **1.3**) and the photoresist increasing the numerical aperture, so it is greater than 1 and greatly increasing resolution down to a feature size of 80 nm [26].
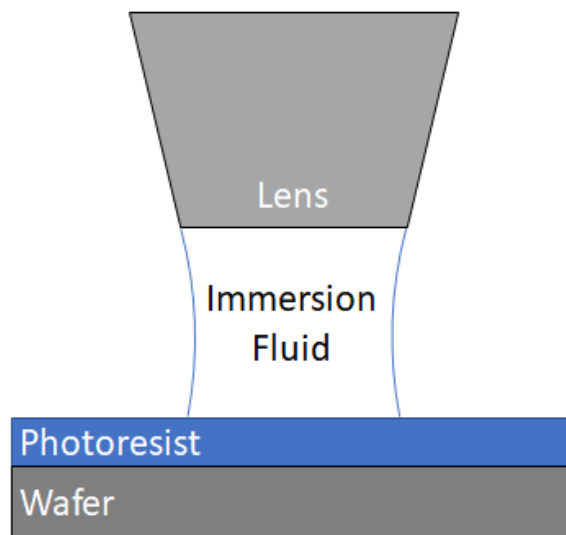
Figure 1.3 *A basic schematic of 193i lithography showing the immersion fluid between the lens and the resist which is used to reduce the numerical aperture of the and hence achieve sub-wavelength lithography.*

For this to work the immersion fluid must have a refractive index greater than 1 meaning that the wavelength of the 193 nm light will be reduced in the fluid increasing resolution. The current tool developed by ASML, the TWINSCAN NXT, has a throughput of 275, 300 mm wafers per hour with a sub 38 nm resolution [27]. Today, in order to pattern below this feature size quad patterning is used, where the same wafer is exposed multiple times in order to increase resolution and feature density solution (see Figure **1.4**) [28]. However, with 193 immersion lithography reaching its resolution limit even octuple patterning is being discussed as a possible next step for the industry [29].

However, every time a repatterning process is added, the time taken to completely pattern a wafer greatly increases. In turn this reduces through put which calls into question the benefit of such processes. It also greatly increases the overall cost of each wafer, and this cost will only increase as each new node is reached.
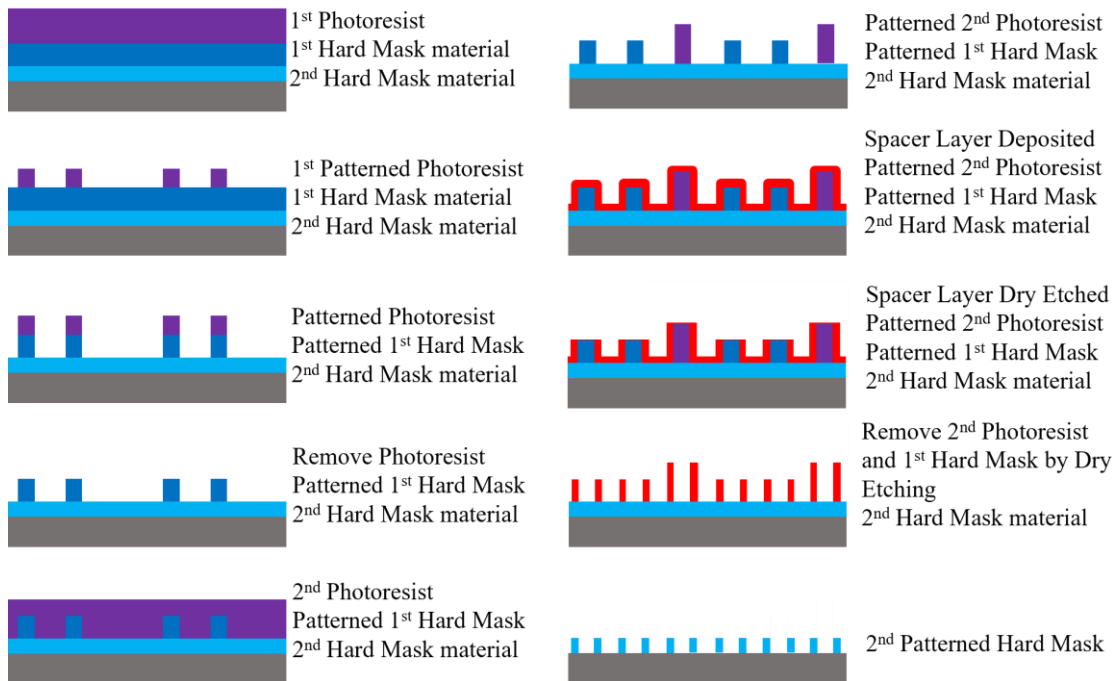
Figure 1.4 *A process flow of a double patterning lithographic process which is used to increase feature density beyond the limits of the lithographic processing.*

Immersion lithography has been optimized over its lifespan to reach current manufacturing specifications. For example, an anti-reflective top coating reduces the exposure time by reducing the number of photons reflected off the surface of the resist

21

increasing the efficiency of the exposure. In addition, top coatings can be used to increase adhesion of the immersion fluid to the surface helping prevent the chances of air gaps which cause aberrations in the exposure patterns reducing manufacturing yield [30]. The top coating also provides protection to the underlying resist from the immersion fluid preventing leaching of the photoacid generators and quenchers from the resist and diffusion of the immersion fluid into the resist which can cause swelling [31].

To project the exposure pattern onto the resist a photomask is used. Photomasks are usually quartz blanks which have a chromium stencil patterned on them. Chromium is used due to its opacity to the wavelength used in photolithography [32]. The non-patterned areas of the photomask allow transmission of deep UV light, so the photoresist can be exposed. The manufacture of photomasks is a costly and time-consuming process. This is because they must have virtually zero errors as any mask defects will be transferred to every wafer that is exposed with this mask. Also, these masks degrade overtime as they become contaminated during use, requiring cleaning and repair, limiting their lifetime. Photomasks are produced in sets for which, depending on the number of process layers i.e. the number of masks in the set, the price can reach upwards of $5 million [33].

193 immersion lithography has reached the end of its life span as the resolution limit for this technique means that it cannot maintain the progress required by industry.

1.2.2 Electron Beam Lithography

The potential of Electron Beam Lithography as a method of manufacturing became apparent with the development of gaussian beam scanning electron microscopes in the 1960's which provided the ability to direct write patterns pixel by pixel. The ability to expose a pattern pixel by pixel instead of through a mask meant that the limit of resolution was reliant on the pixel size or spot size of the electron beam [34]. In practice, the resolution is limited by the electron optics because as the spot size of the beam gets

smaller the current of the beam, which is the flux of the electrons in the beam, must also be reduced [34]. This leads to increased exposure time which makes the use of such resolution impractical. An alternate method of increasing the resolution is to increase the acceleration voltage of the beam. This, however, forms a trade-off, as higher energy electrons will interact much less with the target material. This is evident in the choice of acceleration voltages for different electron beam applications. For imaging, low acceleration voltages (~1 kV) are used as this will generate the most secondary electrons which are vital for generating an image. Conversely for high resolution lithography 100 kV tools are commonly used but the numbers of secondary electrons generated at these energies are greatly reduced. Another problem with this method of direct write exposure is the time taken to complete patterns pixel by pixel is impractically large when compared to the relatively quick exposures offered by optical lithography. The advent of the variable shaped beam (VSB) helped with this as it allowed the exposure of a number of pixels together to build patterns [12]. These tools employ 50 kV beam acceleration voltages because at this voltage the balance between resolution and secondary electron generation is found to be the most practical. As a commercial manufacturing process IBM had a lot of success using this method in combination with optical lithography throughout the 1970s and 1980s. In order again to reduce the electron optics problem and increase the number of pixels that can be exposed in one 'shot', development by Nikon began on an electron projection lithography system which could expose up to 10 million pixels at once [35]. This was achieved by separating the beam into smaller beamlets and the projecting them through a mask. This technology proved to be promising but unfortunately it was not ready to meet demand and was overtaken by the arrival of 193 immersion lithography. This led EBL technology to revert to scanning single beam systems reliant on sequential methods of exposure (pixel by pixel) and not a parallel exposure method like mask projection used in Photolithography. However, massively parallel EBL tools are again

being developed. IMS Nanofabrication in collaboration with JOEL have announced the IMS MBMW-101 which is a parallel mask writer using 262,144 beams with an energy of 50keV that can be individually rastered [36]. A similar system has also been developed by Mapper which uses 65,000 beamlets and boasts being able to write 300 mm wafers at 5 Kev with a resolution of 25 nm [37]. This shows that EBL is again become a viable high through put manufacturing process.

Even though it may no longer be used as prominently in the commercial production of ICs Electron beam lithography is still used in the production of photomasks and many other devices where ultra-high resolution beyond the limits of photolithography is needed. It is also being reintroduced in some areas of manufacture in a process dubbed 'complementary lithography' to make a few of the smallest structures on wafers patterned by 193 immersion lithography [38]. Many research applications use EBL for device manufacture as this is easier and less restrictive than having to produce a photomask for what may be a novel application. Additionally, in an environment where throughput is not a major concern then the longer write times of EBL can be ignored. Since the 1990's, many scanning electron microscopes (SEM) are able to focus a beam down to sub 10 nm spot sizes meaning that they can be converted into effective lithography tools for a relatively low cost in comparison to commercial EBL tools.

Conventional scanning electron microscopes consist of the following main components. Firstly, the source, which is where the electrons are generated, is usually a field emission gun [39]. This is a source that relies on the field emission effect where the emission of electrons from the tip is induced by the presence of a strong electro-static field as opposed to thermal emission sources which are dependent on thermionic emission from a hot filament. Once the electrons are emitted, they are accelerated down the column. The column of an SEM contains; the apertures, which provide a course cut off for the electrons and lenses; the condenser lenses, which collimate the beam turning the point

source of electrons into a parallel beam, the spot size of the beam is also controlled here; the stigmator, which controls the shape of the beam by stretching it in the x or y direction and the scan coils which control the raster of the beam. If the SEM is set up for lithographic applications, then the column will usually have an electrostatic beam blanker which is necessary to 'blank' the beam (deflect it away from the sample) as it scans over the surface in order to expose only specific areas of the write field [40]. Electrostatic fields are used due to their much faster switch times, compared to magnetic fields, due to magnetic hysteresis. Finally, the polepiece which acts as the objective lens is the last stage the electron beam passes through, this is where the beam is focused onto the sample below. All of this is shown in the schematic in Figure **1.5**. The layout of the components in the column of an SEM can vary from the schematic shown above. For example, in a Gemini column, which is the column design used for Zeiss and LEO microscopes, there is no cross over point which helps prevent aberrations in the beam. Also, the column contains an 8kV beam booster which maintains a high beam acceleration throughout the column [41]. In addition, the scan coils are located in the pole piece just before the objective lens.

An SEM which is to be used for lithography requires a few modifications. Firstly, a pattern generator is required which controls the scan coils of the SEM directing the beam to where it is required to expose a sample in a designated pattern. To properly determine the dose with which the resist is to be exposed, the current of the beam must be measured. This can be achieved by having a faraday cup on the sample holder which, when the beam is directed into will trap all the incoming electrons [43]. If the cup is then connected to a pico-ammeter, the beam current can be measured.
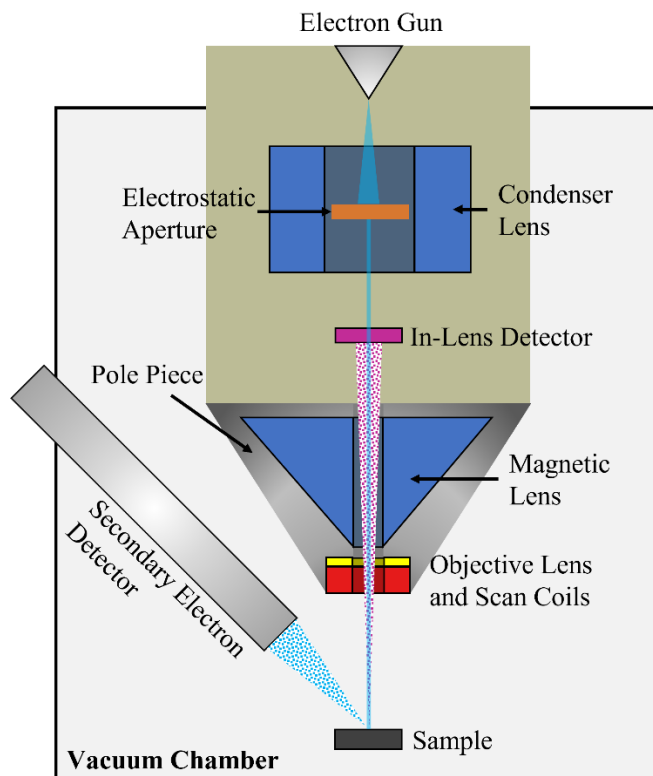
Figure 1.5 *Internal schematic of an SEM. Specifically this shows the architecture and*

beam path used in a Zeiss Gemini column [42].

1.2.3 <u>Helium Ion Beam Lithography</u>

Compared to Electron beam lithography (EBL), which has been used in manufacturing and analysis since the 1960s [12], Helium Ion Beam Lithography (HIBL), is a comparatively new technique which only became available with the development of the first helium ion microscope in 2007, the Zeiss Orion NanoFab [44]. Originally designated for high resolution imaging and less destructive ion milling for device manufacture, it soon became apparent that the microscope's inherent properties would be beneficial for lithography [45].

A Helium Ion Microscope uses a Gas Field Ion Source (GFIS) to generate a focused beam of He+ ions. In a GFIS a He gas is flowed over an atomically sharp tungsten tip. Due to this sharpness a large electric field is generated at the end of the tip which polarises the Helium ions drawing them toward the tip where they are then ionized

through electron tunnelling. These He ions are subsequently accelerated by a potential difference away from the tip and down the column [46] this is shown in Figure **1.6**.
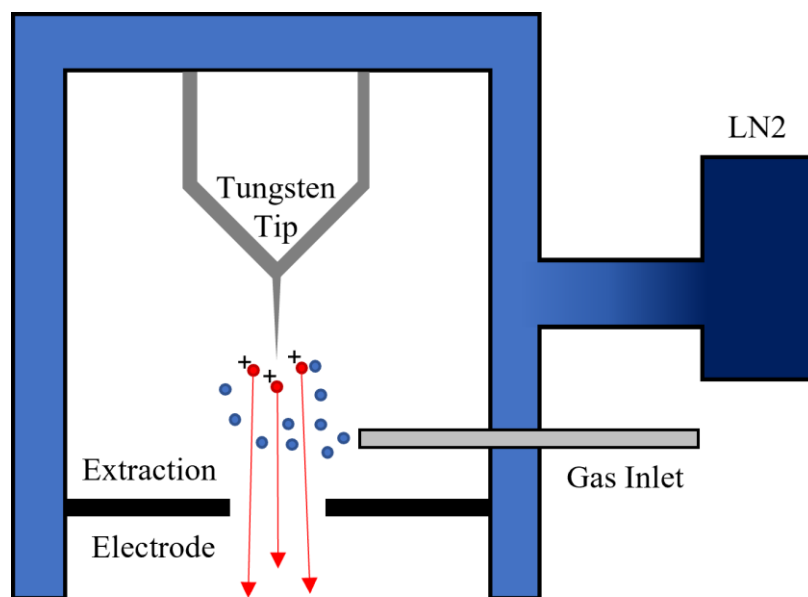
Figure 1.6 *Diagram of a Gas Field Ion Source (GFIS) used in a helium ion microscope*

Due to the shape of the tip, the beam can be generated from just a few points of emission. Depending on the applied fields the source can be reduced to just one point of emission however in practice this is unstable, so usually a self-stabilizing trio of atoms, a trimer, is used to generate the beamlets that form the beam. This small point of emission is what gives the ion beam its small spot size. While in operation the tip must be kept at a constant pressure (10-7 mbar) so that there are enough He atoms to form stable beamlets. The beam current scales with pressure, however when operating at higher pressures the risk of losing the trimer is increased leading to the need to reshape the tip through heating. The tip in the GFIS is also cryogenically cooled, this helps keep the tip stable in the presence of large electric fields and slows the He atoms around the tip making polarization and subsequent emission more probable [47]. With the beam only being emitted from three point sources this allows it to be focused to a spot size less than one nanometre.

1.2.4 <u>Advanced Lithography</u>

Currently still an area of development, EUV lithography is only recently starting to take over production from 193 lithography. This switch started in 2019 [48] coinciding with the first commercial EUV lithography scanner being developed by ASML [49]. EUV lithography uses 13.5 nm wavelength light to expose photo resists. An immediate benefit of EUV light is that the wavelength is much smaller than its predecessor, 193 nm, which provides an instant improvement in resolution without the need for immersion lithography and other resolution enhancing techniques. There are also some draw backs, one of the main ones being the problem of finding a suitable light source which is stable and reliable. Currently, the two most commonly used options are the afore-mentioned scanner, developed by ASML, or a synchrotron light source. The 13.5 nm light in a scanner is generated by firing a CO2 laser, with a wavelength of 10μm [50], at a tin plasma this excites the tin ions which then release photons of light at the required 13.5 nm wavelength. The light is then focused using a series of mirrors and lenses before finally being projected onto a mask and reflected towards the wafer. This is shown in Figure **1.7**.
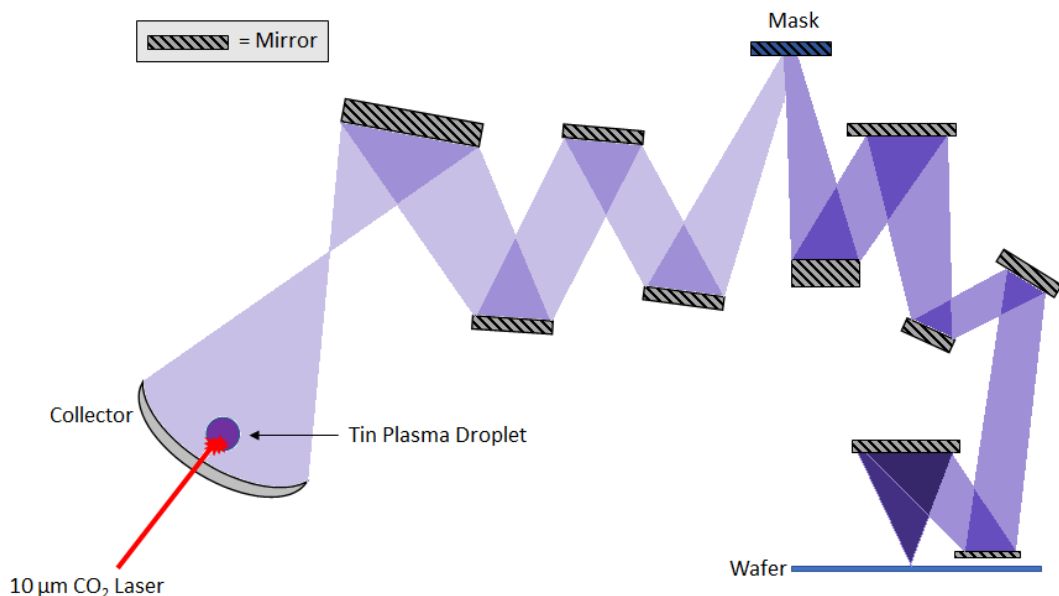
Figure 1.7 *Plasma light source and focusing path of EUV light in the ASML*

TWINSCAN NXE.

28

One of the main problems with this method is preventing the tin plasma from contaminating the mirrors which must then be regularly cleaned or replaced. This causes large periods of downtime for the tool reducing throughput and efficiency.

1.2.5 <u>Exposure Mechanics</u>

As explained previously the basic mechanisms of resist exposure such as chain scissioning and cross linking provide some understanding of resist exposure on a larger scale but to develop a resist more effectively the mechanics behind these processes must be understood. When a beam of photons, electrons or ions are incident on a resist material they will undergo scattering. As the incident object scatters it will change direction and may lose energy. This energy is transferred to the target material during scattering collisions. If the incident particle undergoes an elastic collision, then it changes direction and does not lose any energy, however if an inelastic collision occurs then energy will be transferred from the incident particle to the material. If this energy is sufficient then a secondary electron (SE) may be emitted. These electrons will go on the scatter themselves creating more collision events and further generations of SEs. It follows that the generation of the SEs is vital to increasing the sensitivity of a resist and hence reducing the exposure dose. However, when a particle scatters, the change in direction causes a divergence of the beam as it passes through the material. This potentially leads to a reduction in resolution as this effect will be greatly noticeable in thick films (>100nm) and can be avoided by using thinner films, but this comes at the cost of reduced etch performance. The divergence of the beam and SE generation means that it is not possible to generate structures that are the same size as the spot size of the beam, and increased sensitivity and hence increased SE generation usually leads to broader structures and therefore reduced resolution. The generation of SEs which expose the resist laterally, gives rise to the proximity effect which is where the exposure of adjacent areas accumulate. This increases the overall exposure of the area and can help reduce the

29

exposure doses needed to expose resists but will ultimately reduce the maximum resolution of the resist.

Photons used in lithography have much lower energy when compared to electrons by an order of 1000s, the most energetic photons used are those in EUV which have an energy of only 92eV in comparison to 100KeV electrons commonly used in lithography. This difference in energy means that SEs are generated by photon absorption, so typically a photon will be responsible for far fewer SEs and hence a much higher density of photons is needed to generate the same structure that much fewer electrons can produce. These SEs are also much lower energy meaning the number of subsequent generations of SEs will be reduced. Due to the absorptive nature of photon exposure the attenuation of the incident photons is greatly increased with a penetration depth of 10s of nanometres compared to the high energy electrons used in EBL which will travel through the resist layer and continue many microns into the substrate. This gives the benefit that much thicker films can be exposed using electrons.

Compared to electrons, helium ions can be focused to a much smaller spot size, and this combined with their higher momentum gives them a much lower beam divergence in resist materials compared to electron beams [51]. Also due to their much higher stopping powers and interaction cross sections, the SE yield from He ions is much higher, requiring a lower exposure dose suggesting reduced exposure times. The benefits of increased SE generation from ions as opposed to electrons make them a very attractive alternative for lithography compared to electrons. Another benefit of ions is that, for example, He atoms are ~7000 times more massive than electrons giving them a proportionally larger momentum, hence a much shorter de Broglie wavelength. This wavelength determines the ultimate resolution of the feature that can be imaged by a He beam. A downside of using ions for lithography is the much lower range of penetration compared to electrons. This reduced penetration depth means that thick films of resist

materials may not be fully exposed however, if resist materials are kept sufficiently thin then this problem can be negated.

1.3 <u>Pattern Transfer</u>

Once a resist has been exposed and developed, the pattern of structures that remain must be transferred into the substrate from which the actual devices and ICs will be made. This is a usually a crystalline semiconductor with the most common being silicon. To transfer the pattern into the substrate it must be etched. The resist will protect the substrate it covers from the etching process allowing the uncovered areas to be etched away. Resists are usually not completely impervious to the etching process and will be etched away with the substrate, however, they ideally have some increased resistance to the etchant and so will be etched more slowly. This gives rise to etch selectivity which is a ratio describing the amount of substrate etched compared to the amount of resist lost. For example, a resist with an etch selectivity of 2:1 means that for every 2 nm of substrate that is etched 1 nm of resist is lost. From this it is clear that if a resist material has a low etch selectivity, then its thickness must be increased. However, if the thickness is increased then this will usually mean lower resolution and larger structure pitch. Therefore, high etch selectivity is an essential feature for a resist.

In manufacturing there are two main types of etching which are wet and dry etching. Wet etching is where the substrate is submerged in an etching solution. Dry etching can be carried out using a plasma as shown in Figure **1.8**. This is also known as reactive ion etching (REI) which is a process where the substrate is bombarded with charged ions from the plasma [52]. These reactive ions sputter and react with the material pulling away portions of the surface, hence etching it.
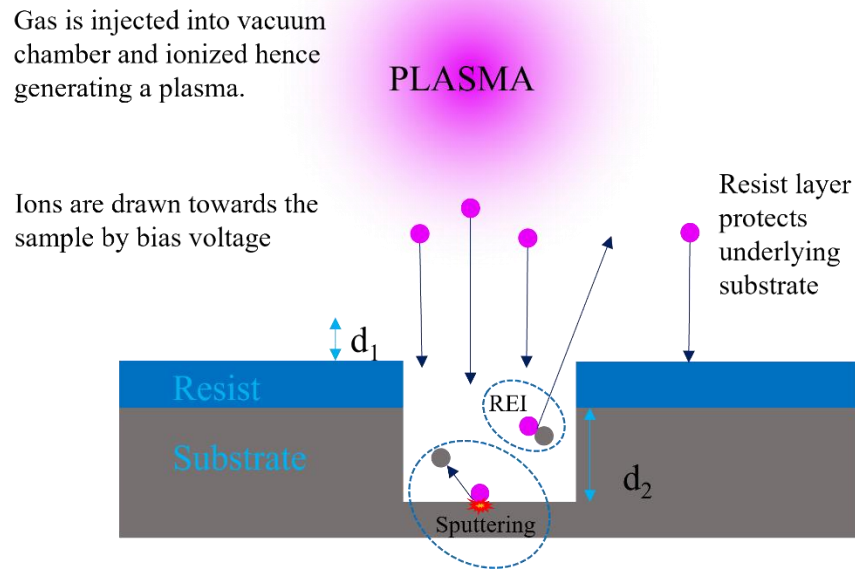
Figure 1.8 *Process schematic for plasma dry etching, showing etching through sputtering and reactive ion etching (REI). The ratio of d_2:d_1 is the etch selectivity of the resist.*

Wet etching is usually an isotropic process, which means that the substrate is etched in all directions at the same rate. This can lead to problems such as undercutting, where if the etch is much deeper that the pitch of the structures then their integrity will be compromised, or they may not have the straight side walls. Conversely, dry etching can be anisotropic or directional process where the etching process can be passivated using a second gas to protect the wall of the etched structures. This is known as the Bosch process and it reduces the lateral etching of the substrate meaning much deeper etches can be attained without losing the shape of the pattern [53].

1.4 **Photomask Fabrication**

All types of photolithography, excluding direct laser writing, depend on photomasks to project an exposure pattern onto the resist. These masks are themselves made using direct patterning lithography methods such as EBL or HIBL [54]. To create the pattern on a photomask which is to be projected, a material which can absorb the wavelength of light

being used must be patterned to cover areas of the mask. To pattern a mask a resist is applied to the top of an unpatterned mask blank which is then exposed and developed. The areas of the absorber layer, including an antireflective coating, which are no longer protected by the resist, are then etched away. The resist is subsequently removed leaving the completed pattern on the mask. This is not the end of the process however as any defect will be replicated in any future manufacturing therefore masks must have as few defects as possible. Consequently, the mask must be inspected, and any defects repaired. If there are too many defects, the mask cannot be used. This puts a high demand on the lithography and etching process to produce high fidelity, reproducible features. Also, any resist materials used must have the ability to withstand the dry etching process and allow for features as small as 44 nm to be transferred onto the mask [55]. These features are larger than the realised features on the wafer as the image projected by the mask is passed through lenses which reduce the feature size by up to 4 times. Figure **1.9** shows schematics of completed masks to show the difference in complexity between the 193 nm (DUV) and EUV masks. The DUV mask is relatively simple as it works in transmission where the light is transmitted through the quartz substrate with the absorber layer which is usually chromium blocking the light and projecting the pattern.

The EUV mask is fundamentally different as it works in reflection instead of transmission. This greatly increases the complexity of the mask as the reflector itself is 80 alternating layers of silicon and molybdenum. To prevent the reflector stack from becoming oxidised it is covered by a ruthenium capping layer. Ruthenium is chosen due to its transparency to the 13.5 nm wavelength [56].

To protect the capping layer during inspection and repair a buffer layer is used which must be etched afterwards, thus adding a further processing step. A variety of absorber materials can be used for EUV lithography with TaBN being amongst the most popular [57].
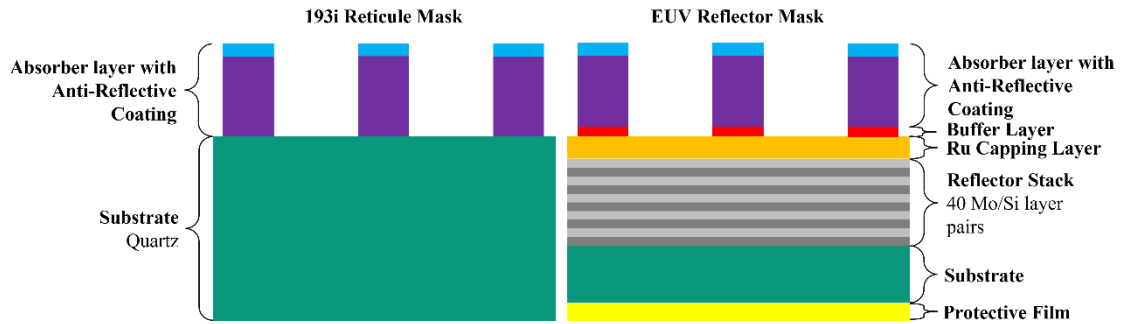
Figure 1.9 *Photomask schematics for 193 nm immersion lithography and EUV lithography.*

1.5 Resist Materials for Lithography

Before new resists can be developed the current state of the art must be assessed. This section will compare the many resists already published for different methods of lithography. It is essential that any new resists target properties where the currently available resists are lacking or offer improvements in resolution or sensitivity. The properties for all resists discussed in this section can be found in Table **1.1**. Current industry requirements for materials are determined by the next manufacturing node target. As discussed previously the 5 nm node is the next process target and this requires resists which can be patterned with structures with a pitch of 24 nm [9]. For EBL the dose is highly dependent on the beam energy and as it is not currently being used for high volume manufacturing there is no set target for dose. However, that is not to say the dose is not important, as EBL resists are used to pattern and repair photomasks, therefore any new resists developed should be targeting the 5 nm node with sensitivity similar to current commercial resists.

1.5.1 Positive Tone Resists

PMMA is one of the most widely available and commonly used electron beam resists due to its long shelf life and it stability during processing. It is usually used as a positive tone resist and has been patterned with structures as small as 4 nm [58 - 60]. Small features

can be created with relatively low-resolution lithography techniques, but this can only be achieved as isolated features, decreasing feature density which is undesirable for manufacture. With exposure doses ranging between 300-400 $\mu C/cm^2$ at 30 keV, PMMA has reasonable sensitivity to electron beam exposure which may also contribute to its popularity. With the potential for very high aspect ratios PMMA is useful in the fabrication of devices on the micro and nanoscale.

Like PMMA, ZEP-520A is a positive tone polymer-based resist for EBL. It has been shown to have an exposure dose of 245 $\mu C/cm^2$ at 30 keV [61] which is again similar to PMMA. However, compared to PMMA, ZEP-520A can achieve an increased feature density with 25 nm lines and spaces being reported at a dose of 250 $\mu C/cm^2$ at 100 kV [62] and 14 nm lines with a pitch of 40 nm with a dose of 180 pC/cm at 10 kV [63].

SML, developed by Scott Lewis (University of Manchester), is a resist that was designed for high aspect ratio fabrication [64]. It was designed to have similar processing properties to PMMA but with improvements in sensitivity and aspect ratio. The sensitivity was successfully increased with 14 nm lines with a pitch of 30 nm were produced with a dose of 107 $\mu C/cm^2$ at 30 kV [64]. SML has also been shown to produce structures with an aspect ratio of ~10:1 [65] whilst maintaining straight sidewalls. Although a 4 nm feature in a 140 nm thick resist was reported for PMMA giving an aspect ratio of 35:1 [60], this structure was anchored by a much larger structure and not free-standing lines like the 10:1 structures created in SML.

Chemical amplification of resist exposure has been proven to increase sensitivity of resist materials whilst still managing to achieve 36 nm pitch patterns [66]. Chemically amplified resists (CARs) are composite resists that rely on photo acid generators to expose the resist. These molecules are activated when exposed and are then encouraged to defuse through the resist in a post exposure bake. Molecules that slow this diffusion, known as quenchers, are also included in the resist to slow this diffusion and maintain

high resolution. Compared to PMMA and the other polymer-based resists, CARs offer great increases in sensitivity whilst still managing to achieve competitive resolutions. CSAR 62 is a commercial polymer resist, combined with CAR elements, that is widely used as both an electron beam and photo resist. CSAR 62 has a good sensitivity in electron beam with a dose of 140 $\mu C/cm^2$ at 100 kV [67]. However, compared to the other positive tone resists such as ZEP 520A and SML the resolution is not as good with only 40 nm lines with a pitch of 75 nm achieved even at 100 kV.

Despite not requiring development after exposure as it is a "self-developing" resist, the AlF_3 doped LiF is patterned as a positive tone material with the exposed material being removed during exposure by the electron beam. This novel method removes the need for post exposure development as the resist is desorbed from the substrate during exposure. Whilst 5 nm lines with a 30 nm pitch were way beyond the cutting edge for the time in 1995 the high dose of 100,000 pC/cm at 30 kV and problems with contamination and hence lithographic quality limited this resist [68].

1.5.2 <u>Negative Tone Resists</u>

As explained before PMMA is exposed by chain scissioning breaking its long polymer chains making it more soluble [69], however it can also be used as a negative tone resist [69, 70]. PMMA is activated as a negative tone resist by using a much higher exposure dose of more than 2000 pC/cm at 30 keV [70]. With this increase dose the polymer chains start cross linking making them insoluble in the developer solvent. The increase in dose makes PMMA less attractive as a negative tone resist.

As with PMMA there are a variety of polymers that can be cross linked, some of these can be crosslinked with a large enough dose whilst others require additives to promote crosslinking. ZEP 520A can be crosslinked and as with PMMA it requires a significantly larger dose, with 5250 pC/cm required to produce 23 nm lines with a pitch of 50 nm even though an acceleration voltage of 10 kV used [63]. An acceleration voltage

of 10 kV will give a much-reduced dose when compared to 30 kV or 100 kV. To combat the high doses needed for negative tone polymer resists more complex co-polymers have been developed such as the MAPDST-MMA co-polymer. This resist showed an improved sensitivity when compared to other negative tone polymer resists realising, 20 nm line space structures with a dose of 30 $\mu C/cm^2$ at 20 kV [71].

Molecular CAR resists have also proven to give better sensitivities for example, the fullerene-based IM-MFP$_{12-8}$ has achieved 20 nm structures with a 36 nm pitch with doses as low as 40 $\mu C/cm^2$ at an acceleration voltage of 20 keV [66]. Another example of a molecular CAR resist is a series calixarene composite resists comprised of TOMCA4 and a PAG. These resists have been shown to produce isolated 25 nm structures with a dose of 650 pC/cm at 30 kV [72].

Inorganic molecular resists also have proven to be successful negative tone resists. Perhaps the most well-known of these types of resists is HSQ which has been consistently shown to have excellent resolution and feature density for electron beam lithography [73, 74] and has achieved world record resolution for EUV [75]. This is a commercially available resist and is attractive due to the incredibly small resolutions of sub 10 pitch structures reported. However, the dose required to create structures at these feature sizes is large with a dose of 5000 $\mu C/cm^2$ with a beam voltage of 10 kV [73] for EBL. This limits its uses to research applications and hence it is not viable for high volume manufacture. An attempt to improve the shelf life and processing stability of HSQ led to the development of Medusa 82. This resist has been shown to have similar processing conditions as HSQ and has yielded 14 nm lines with a pitch of 40 nm and a dose of 1290 $\mu C/cm^2$ at 30 kV [76].

Small molecule metallic resists such a ZircSOx [77] and HafSOx [78] have greatly increased sensitivities producing some of the lowest dose resists whilst still producing high resolution structures. These resists have been shown to have doses as low as 50

$\mu C/cm^2$ [77] and can produce features as small as 9 nm [78], however these low doses come at a cost as the increased sensitivity lead to an increase in the shot noise of the exposure, reducing structure quality.

The resists discussed here clearly confirm the validity of the trade-off in the relationship between sensitivity and resolution for resist materials. This trade-off is the main obstacle that must be overcome when designing new resists that can achieve the resolution required by industry whilst also having a low enough sensitivity.

Table 1.1 *A table of properties of current state of the art resists. The information given includes the tone of the resist; the type of resist molecule; the maximum resolution of the molecule and the dose and exposure type this result was achieved with; The developer used; the aspect ratio i.e. the ratio of feature size and resist thickness. Dose for EBL is stated as either an area dose, μC/cm², a linear dose, pC/cm, or both. Abbreviations used: IPA is Isopropyl Alcohol; TMAH is Tetramethylammonium Hydroxide; MCB is Mono Chlorobenzene; PMMA is Poly(Methyl Methacrylate); HSQ is Hydrogen silsesquioxane; MAPDST-MMA is (4-(methacryloyloxy)phenyl)-dimethylsulfonium triflate; MAA is Methylacetoacetate; TOMCA4 is tetrakis(oxiran-2-ylmethoxy)-tetra-tert-butylcalix[4]arene.*

Name	Tone	Type	Resolution: Feature/Pitch	Area Dose	Line Dose	Exposure	Developer	Aspect Ratio	
Electron Beam Lithography			nm	μC/cm²	pC/cm	keV			
ZEP-520A	Positive	Polymer	55 / 72	245	-	30	Xylene	2.3:1	[61]
			25 / 50	250	-	100	Amyl Acetate	1.6:1	[62]
			13.4 / 40	-	180	10	Amyl Acetate	4.5:1	[63]
	Negative	Polymer	23.1 / 50	-	5250	10	7:3 IPA:H$_2$O	2.6:1	[63]
PMMA	Positive	Polymer	4 / -	100 - 400	440	30	3:1:1.5% IPA:MIBK:MEK	15:1	[58]
			4 / 80	325	-	80	7:3 IPA:H$_2$O	10:1	[59]
			4 / -	232	-	75	1:3 MIBK:IPA	35:1	[60]
	Negative	Polymer	15 / -	70,000	185,000	300	Acetone	2.7:1	[69]
			5 / 20	-	2000	30	MIBK	1:1	[70]
HSQ	Negative	Inorganic	4.5 / 9	-	5000	10	D.I. Water, 1% NaOH, 4% NaCl	1:2	[73]
			10 / 10	33444	8000	100	TMAH	1:1	[74]
SML	Positive	Polymer	32 / 70	-	550	30	7:3 IPA:H$_2$O	9:1	[65]
			14 / 30	107	-	30	7:3 IPA:H$_2$O	3.5:1	[64]
MAPDST-MMA co-polymer	Negative	n-CAR	20 / 40	35	-	20	TMAH	2.5:1	[71]
IM-MFP$_{12-8}$	Negative	CAR	20 / 36	40	240	20	1:1 MCB:IPA	1:1	[66]
CSAR 62	Positive	CAR	40 / 75	140	-	100	Amyl Acetate	1:1	[67]
HafSOx	Negative	Inorganic	9 / 21	800	-	30	3:1 H$_2$O:TMAH	1:1	[78]
ZircSOx	Negative	Inorganic	28 / 100	50	-	30	3:1 H$_2$O:TMAH	1.25:1	[77]
AlF3-doped LiF	Positive	Inorganic	5 / 30	-	100,000	30	Desorption	2:1	[68]
TOMCA4	Negative	Organic	25 / 200	-	650	30	MIBK	4:1	[72]
Medusa 82	Negative	Inorganic	14 / 40	1290	-	30	TMAH (AR 300-44)	10:1	[76]

1.6 <u>Simulation and Monte Carlo Modelling</u>

To develop new resist materials, it is necessary to understand the exposure mechanics and be able to simulate how a resist reacts during exposure. Using simulation in this way can reduce the time taken to develop new resists as it acts as a filter identifying suitable resists that can be investigated further through experimentation. Characterization of resists through experimentation is a time-consuming and expensive process and reducing this will increase the efficiency of the resist design process. To do this a Monte Carlo simulation for electron scattering in resist materials was developed.

Monte Carlo simulation is a modelling method which uses random numbers to determine solutions to numerical problems which have an outcome based on a probability distribution. The random numbers are used as inputs for the simulation, to compare probabilities of certain events occurring. Dating back as far as the 18th century, with Buffon's Needle experiment [79], Monte Carlo methods have been essential to solving many physical problems.

Due to the stochastic nature of electron scattering Monte Carlo modelling is widely used to simulate electron trajectories in resist material to determine how a resist will react when being exposed during EBL. There are already programs that can simulate electron scattering in materials, CASINO [80] and Penelope [81] are examples of free electron scattering Monte Carlo software. Tracer [82] is a proprietary software designed, by GenISys, to work with Beamer pattern generator software to optimise the doses used on patterns. These programs work well providing a decent understanding of electron interaction in a variety of materials, however, there are some limitations. None of these programs work with SEs beyond first generation. However, many of the subsequent generations of low energy electrons are an important source of exposure and they are themselves are also responsible for the generation of more SEs. Also, some more complex

electron interactions such as Auger electrons are not considered which are an important source of SEs.

1.7 <u>Aims and Motivations</u>

In summary, research into new resist materials that can produce the target feature size whilst maintaining or even reducing processing time is vital to the semiconductor industry and this is the motivation for this work. This project initially intended to develop and investigate new resists based on a family of supramolecular organo-metallic resists for both EBL and IBL. However, beyond this the intention was to develop a resist design process which can be used as a platform for streamlining the development of new resists. This process relies on Monte Carlo simulation to suggest candidates for experimentation. It is necessary to rule out resists through simulation as it too expensive and time consuming to test them all. To do this a new Monte Carlo simulation with the ability to simulate both ions and electrons in a range of materials with the aim of estimating the lithographic outcomes was developed. A simulation named "EXCALIBUR" has been developed to meet this goal.

Research has also been undertaken to investigate novel 3D lithographic techniques and the characteristics of the newly developed resists which allow this.

============================ NOTE ============================

The work contained in the following chapters are original and novel work developed for this thesis.

==

References

[1]   Saint, J.L., Saint, C., "Integrated circuit", Encyclopædia Britannica, Encyclopædia Britannica, inc. (2021)
(URL: https://www.britannica.com/technology/integrated-circuit
Accessed August 2021)

[2]   Moore, G.E., "Cramming more components onto integrated circuits", Electronics, Vol. 38 (1965)

[3]   Moore, G.E., "Progress in Digital Integrated Electronics", IEEE Text Speech (1975).

[4]   Rupp, K., "48 Years of Microprocessor Trend Data" (2020) (URL: https://github.com/karlrupp/microprocessor-trend-data Accessed September 2021)

[5]   Clark, D., "Moore's Law is showing its age", The Wall Street Journal, 16 July 2015 (2015)

[6]   Moore, G. E., "Gordon Moore: The Man Whose Name Means Progress, The visionary engineer reflects on 50 years of Moore's Law Interview with Rachel Courtland." Special Report: 50 Years of Moore's Law, IEEE Spectrum (2015)

[7]   Borodovsky, Y., "Marching to the beat of Moore's Law", Proc. SPIE 615301 (2006)

[8]   Intel's process size "Intel's 10 nm Technology: Delivering the Highest Logic Transistor Density in the Industry Through the Use of Hyper Scaling", Intel News Fact Sheet, Intel Newsroom (2017) (URL: https://newsroom.intel.com/newsroom/wp-content/uploads/sites/11/2017/09/10-nm-icf-fact-sheet.pdf Accessed September 2021)

[9]   International Roadmap for Devices and Systems, 2017 Edition, More Moore, IEEE (2017) (URL: https://irds.ieee.org/images/files/pdf/2017/2017IRDS_MM.pdf Accessed September 2021)

[10]   Sperling, E., "Quantum Effects At 7/5nm And Beyond", Semiconductor Engineering (2018) (URL: https://semiengineering.com/quantum-effects-at-7-5nm/ Accessed September 2021)

[11]   Meggs, P.B., "A History of Graphic Design", John Wiley & Sons, Inc. (1998)

[12]   Pfeiffer, H.C., "Direct write electron beam lithography: a historical overview", Proc. SPIE 7823 (2010)

[13]   Lathrop, J. W., "The Diamond Ordnance Fuze Laboratory's Photolithographic Approach to Microcircuits", IEEE Annals of the History of Computing, Vol. 35 (2013)

[14]   McCord, M.A., Rooks, M.J., "SPIE Handbook of Microlithography, Micromachining and Microfabrication", SPIE, Vol. PM39 (2000)

[15]   Tandon, U.S., "An overview of ion beam lithography for nanofabrication", Vacuum, Vol. 43 (1992)

[16]   Watt, F., Bettiol, A.A., Van Kan, J.A., Teo, E.J., Breese, M.B.H., "Ion Beam Lithography and Nanofabrication: A Review", International Journal of Nanoscience, Vol. 4 (2005),

[17] Traub, M. C., Longsine, W., Truskett, V. N., "Advances in Nanoimprint Lithography", Annual Review of Chemical and Biomolecular Engineering, Vol. 7:583-604 (2016)

[18] Chou, S.Y., Krauss, P.R., Renstrom, P.J., "Imprint Lithography with 25-Nanometer Resolution", Science, Vol. 272 (1996)

[19] Durrani, Z., et al., "Scanning probe lithography approach for beyond CMOS devices", Proc. SPIE 8680 (2013)

[20] Parker, N.W., Brodie, A.D., McCoy, J.H., "High-throughput NGL electron-beam direct-write lithography system", Proceedings Vol. 3997, Emerging Lithographic Technologies IV, Microlithography (2000)

[21] Levinson, H.J., "Principles of Lithography", Fourth Edition, SPIE (2019)

[22] Iwayanagi, T., Ueno, T., Nonogaki, S., Ito, H., Willson, C.G., "Materials and Processes for Deep-UV Lithography", *Electronic and Photonic Applications of Polymers*, Chapter 3, Advances in Chemistry, Vol. 218 (1988)

[23] Thackeray, J.W., "Chemically amplified resists and acid amplifiers", *Materials and Processes for Next Generation Lithography*, Edited by Lawson R.A., Robinson, A.P.G., 1st edition, Vol. 11, London, Elsevier Ltd (2016)

[24] Lawson, R.A., Chun, J.S., Neisser, M., Tolbert, L.M., Henderson, C.L., "Methods of controlling cross-linking in negative-tone resists", Proc. SPIE, 9051 (2014)

[25] Mack, C.A., "Field Guide to Optical Lithography", SPIE (2006)

[26] Mack, C.A., "Lecture 48, Lithography: Resolution and Immersion", lithoguru.com (2018) (URL: http://www.lithoguru.com/scientist/CHE323/ Lecture48.pdf Accessed August 2021)

[27] van Hoof, B., et al., "Layout independent leveling (LIL) on NXT:1980Di immersion scanners for enhanced productivity," Proc. SPIE 10147 (2017)

[28] Chao, W., Kim, J., Anderson, E.H., Fischer, P., Rekawa, S., and Attwood, D.T., "Double patterning HSQ processes of zone plates for 10 nm diffraction limited performance", Lawrence Berkeley National Laboratory (2009)

[29] Altamirano-Sánchez, E., et al., "Self-aligned quadruple patterning to meet requirements for fins with high density", SPIE Newsroom (2016)

[30] Wei, Y., Back, D., "Immersion lithography: topcoat and resist processes", SPIE Newsroom, (2007)

[31] Wei, Y., Back, D., "193nm immersion lithography: Status and challenges", SPIE Newsroom, (2007)

[32] Sturans, M., et al., "EL5: One Tool for Advanced X-Ray and Chrome on Glass Mask Making,", Journal of Vacuum Science & Technology B, Microelectronics and Nanometer Structures, Vol. 16 (1998)

[33] Lam, D., "Reducing IC Manufacturing Cost While Enhancing IoT Security", Global Semiconductor Alliance (2016) (URL: http://www.multibeamcorp.com/GSAIoTSecurity.pdf Accessed August 2021)

[34] Steenbrink, S. W. H. K., "High throughput maskless lithography: low voltage versus high voltage", Proc. SPIE 6921 (2008)

[35] Dhaliwal, R. S., "PREVAIL—Electron projection technology approach for next-generation lithography", IBM Journal of Research and Development, Vol. 45 (2001)

[36] Spengler, C., Platzgummer, E., Loeschner, H., "Multi-beam – enabling leading-edge mask writing (Conference Presentation)", Proc. SPIE 10810 (2018)

[37] Rio, D.J., Constancias, C., Martin, M., Icard, B., Van Nieuwstadt, J., Vijverberg, J., Pain, L., "5 kV multielectron beam lithography: MAPPER tool and resist process characterization", Journal of Vacuum Science & Technology B: Microelectronics and Nanometer Structures, Vol. 28 (2010)

[38] Lam, D., Liu, D., Prescop, T., "E-beam Direct Write (EBDW) as Complementary Lithography", Multibeam Corporation, (2010)

[39] Crewe, A.V., "Electron Gun Using a Field Emission Source", Review of Scientific Instruments, Vol. 39 (1968)

[40] Paik, H., Kirkland, E.J., Siegel, B.M., "Analytical calculation of electrostatic beam blanker performance", Journal of Physics E: Scientific Instruments, Vol. 20 (1987)

[41] Jaksch, H., Vermeulen, J-P., "New Developments in GEMINI® FESEM Technology", Zeiss (2005)

[42] Lenz, S., et al., "Novel Optical Design of Field Emission SEMs, Innovations in Gemini Column, Detection Technology and Variable Pressure Technology" (2015)

[43] Brown, K.L., Tautfest, G.W., "Faraday-Cup Monitors for High-Energy Electron Beams", Review of Scientific Instruments, Vol. 27 (1956)

[44] Elswick, D., Ananth, M., Stern, L., Marshman, J., Ferranti, D., Huynh, C., "Advanced Nanofabrication using Helium, Neon and Gallium Ion Beams in the Carl Zeiss Orion NanoFab Microscope.", Microscopy and Microanalysis, Vol. 19 (2013)

[45] van Veldhoven, E., Sidorkin, V., Chen, P., Alkemade, P., van der Drift, E., Salemink, H., Zanderbergen, H., Maas, D. "Nanofabrication with a High Resolution Helium Ion Beam.", Microscopy and Microanalysis, Vol. 16 (2010).

[46] Economou, N.P., Notte, J.A., Thompson, W.B., "The history and development of the helium ion microscope.", Scanning, Vol. 34 (2011)

[47] Hlawacek, G., Gölzhäuser, A., "Helium Ion Microscopy", NanoScience and Technology (2016)

[48] Turkot, B., Carson, S. L., Lio, A., Liang, T., Phillips, M., McCool, B., Stenehjem, E., Crimmins, T., Zhang, G., et. al. "EUV progress toward HVM readiness", Proc. SPIE 9776 (2016)

[49] Peeters, R., et al., "ASML's NXE platform performance and volume introduction" Proc. SPIE 8679 (2013)

[50] Endo, A., "CO2 Laser Produced Tin Plasma Light Source as the Solution for EUV Lithography", *Lithography*, InTech (2010)

[51] Hill, R., Notte, J.A., Ward, B.W., "The ALIS He ion source and its application to high resolution microscopy," Phys. Procedia 1 (2008)

[52] Jansen, H., et al., "A survey on the reactive ion etching of silicon in Microtechnology", J. Micromech. Microeng. Vol. 6 (1996)

[53] Blauw, M.A., Zijlstra, T., van der Drift E., "Balancing the etching and passivation in time-multiplexed deep dry etching of silicon", Journal of Vacuum Science & Technology B: Microelectronics and Nanometer Structures Processing, Measurement, and Phenomena, Vol. 19 (2001)

[54] Fujimura, A., Willis, J., "2020 Mask Maker Survey Conducted by the eBeam Initiative," Proc. SPIE 11518, Photomask Technology 2020, 115180E (2020)

[55] Morishita, K., et al., "Fabrication of Ta based absorber EUV mask with SRAF", Proc. SPIE 10807 (2018)

[56] Yan, P., Spiller, E., Mirkarimi, P., "Characterization of ruthenium thin films as capping layer for extreme ultraviolet lithography mask blanks", Journal of Vacuum Science & Technology B: Microelectronics and Nanometer Structures Processing, Measurement, and Phenomena, Vol. 25 (2007)

[57] Wu, M., et al., "Mask absorber for next generation EUV lithography", Proc. SPIE 11517 (2020)

[58] Hu, W., Sarveswaran, K., Lieberman, M., Bernstein, G.H., "Sub-10 nm electron beam lithography using cold development of poly(methylmethacrylate)", Journal of Vacuum Science & Technology B:

Microelectronics and Nanometer Structures Processing, Measurement, and Phenomena, Vol. 22 (2004)

[59] Yasin, S., Hasko, D.G., Ahmeda, H., "Fabrication of <5 nm width lines in poly(methylmethacrylate) resist using a water:isopropyl alcohol developer and ultrasonically-assisted development", Appl. Phys. Lett., Vol. 78 (2001)

[60] Liu, K., Avouris, P., Bucchignano, J., Martel, R., Sun, S., "Simple fabrication scheme for sub-10 nm electrode gaps using electronbeam lithography", Appl. Phys. Lett., Vol. 80 (2002)

[61] Tanenbaum, D.M., Lo, C.W., Isaacson, M., Craighead, H.G., Rooks, M.J., Lee, K.Y., Huang, W.S., Chang, T.H.P., "High resolution electron beam lithography using ZEP-520 and KRS resists at low voltage" Journal of Vacuum Science & Technology B: Microelectronics and Nanometer Structures Processing, Measurement, and Phenomena, Vol. 14 (1996)

[62] Fallicaa, R., Kazazis, D., "Lithographic performance of ZEP520A and mr-PosEBR resists exposed by electron beam and extreme ultraviolet lithography", Journal of Vacuum Science & Technology B, Vol. 35 (2017)

[63] Mohammad, M., Koshelev, K., Fito, T., Ai Zhi Zheng, D., Stepanova, M., Dew, S., "Study of Development Processes for ZEP-520 as a High-Resolution Positive and Negative Tone Electron Beam Lithography Resist.", Japanese Journal of Applied Physics. Vol. 51 (2012)

[64] Gangnaika, A., Georgieva, Y.M., McCarthy, B., Petkova, N., Djarab, V., Holmes, J.D., "Analysis of a novel electron beam lithography resist, SML and its comparison to PMMA and ZEP resists" Microelectronic Engineering, Vol. 123(2014)

[65] Mohammad M.A., Dew, S.K., Stepanova, M., "SML resist processing for high-aspect-ratio and high-sensitivity electron beam lithography", Nanoscale Research Letters, Vol. 139 (2013)

[66] Yang, D.X., Frommhold, A., Xue, X., Palmer, R.E., Robinson, A.P.G., "Chemically amplified phenolic fullerene electron beam resist", J. Mater. Chem. C, 2 (2014)

[67] Ito, H., Willson, C.G., "Chemical amplification in the design of dry developing resist materials", Polym Eng Sci, Vol. 23 (1983)

[68] Fujita, J., et al., "Sub-10 nm lithography and development properties of inorganic resist by scanning electron beams", Journal of Vacuum Science & Technology B: Microelectronics and Nanometer Structures Processing, Measurement, and Phenomena, Vol. 13 (1995)

[69] Hoole, A.C.F., Welland, M.E., Broers, A.N., "Negative PMMA as a high-resolution resist—the limits and possibilities", Semicond. Sci. Technol., Vol. 12 (1997)

[70] Duan, H., Winston, D., Yang, J.K.W., Cord, B.M., Manfrinato, V.R., Berggren, K.K., "Sub-10-nm half-pitch electron-beam lithography by using

polymethyl methacrylate as a negative resist", Journal of Vacuum Science & Technology B: Microelectronics and Nanometer Structures, Vol. 28 (2010)

[71] Singh, V., Satyanarayana, V.S.V., Sharma, S.K., Ghosh, S., Gonsalves, K.E., "Towards novel non-chemically amplified (n-CARS) negative resists for electron beam lithography applications", J. Mater. Chem. C, 2 (2014)

[72] Sailer, H., Ruderisch, A., Henschel, W., Schurig, V., Kern, D.P., "High resolution electron beam lithography using a chemically amplified calix[4]arene based resist", Journal of Vacuum Science & Technology B: Microelectronics and Nanometer Structures Processing, Measurement, and Phenomena, Vol. 22 (2004)

[73] Yang, J.K.W., et al., "Understanding of Hydrogen Silsesquioxane Electron Resist for Sub-5-nm-half-pitch Lithography", Journal of Vacuum Science & Technology B: Micro-electronics and Nanometer Structures, Vol. 27 (2009)

[74] Grigorescu, A.E., van der Krogt, M.C., Hagen, C.W., Kruit, P., "10 nm lines and spaces written in HSQ, using electron beam lithography", Microelectronic Engineering, Vol. 84 (2007)

[75] Fan, D., Ekinci, Y., "Photolithography reaches 6 nm half-pitch using extreme ultraviolet light", J. of Micro/Nanolithography, MEMS, and MOEMS, Vol. 15 (2016)

[76] Grube, M., Schille, B., Schirmer, M., Gerngroß, M., Hübner, U., Voigt, P., Brose, S., "Medusa 82—Hydrogen silsesquioxane based high sensitivity negative-tone resist with long shelf-life and grayscale lithography capability", J. Vac. Sci. Technol. B, Vol. 39 (2021)

[77] Stowers, J., Keszler, D.A., "High resolution, high sensitivity inorganic resists", Microelectronic Engineering, Vol. 86 (2009)

[78] Oleksak, R.P., "Chemical and Structural Investigation of High-Resolution Patterning with HafSOx", ACS Appl. Mater. Interfaces, Vol. 6 (2014)

[79] Buffon, G. "Essai d'arithmétique morale." Histoire naturelle, générale er particulière, Supplément, Vol. 4 (1777)

[80] Demers, H., Poirier-Demers, N., Real Couture, A., Joly, D., Guilmain, M., de Jonge, N., Drouin, D., "Three-dimensional electron microscopy simulation with the CASINO Monte Carlo software" Scanning, Vol. 33 (2011)

[81] Salvat, F., Fernandez-Varea, J.M., Acosta, E., Sempau, J., "PENELOPE, A Code System for Monte Carlo Simulation of Electron and Photon Transport", Proceedings of a Workshop/Training Course, OECD/NEA 5-7 November 2001 (2001)

[82] TRACER, GenISys GmbH, Munich, Germany

2

EXCALIBUR: A MONTE CARLO SIMULATION FOR DEVELOPING RESISTS FOR ELECTRON BEAM LITHOGRAPHY

Contents

To better understand electron beam lithography (EBL) it is important to be able to simulate and predict how electrons interact with the atoms and molecules of a material as they pass through it. As the incident electrons from the electron beam, also referred to as primary electrons (PEs), interact with a material they will undergo a variety of interactions which can generally be described as electron scattering. These scattering events may ionize atoms in the material generating secondary electrons (SEs) which will interact with the material in the same way as PEs albeit with lower energy. Understanding

how electrons scatter in materials is vital as it not only determines the trajectories of the electrons but also describes how the electrons lose their energy as they pass through the material. This transfer of energy is responsible for the ionization of atoms in the target material which leads to the breaking of bonds in molecules. This causes the chemical reactions and changes in solubility that contribute to the exposure of resists which is the underlying mechanic behind EBL. Therefore, the development of new materials and the refinement of exposure parameters that are essential to the advances of the semiconductor industry can be expedited with the use of EBL simulations.

2.1 Monte Carlo Simulations for Electron Beam Lithography

The use of Monte Carlo methods to simulate electron scattering is not new, with the first models and calculations being carried out in the 1960s [1]. Since the first simulations, and with the growth in access, availability, and power of computers, many electron scattering simulations have been developed for a wide range of applications. Whilst the number of simulations is numerous there are only a handful of established programs that are specifically designed with EBL in mind. These programs allow for the handling of multiple layers of resist and substrate materials and electron energy ranges suitable for EBL systems.

The purpose of simulation for designing and developing new resist materials is to remove some of the guess work involved in identifying suitable materials. Without simulation, resist development is based on knowledge of prior research and materials and drawing from adjacent lithography and fabrication techniques. This scatter gun approach is not only financially expensive but also time expensive. To fully characterise a resist's spin parameters, exposure parameters, lithographic performance and development regime can take many weeks and even months and days of equipment time. This does not include the time taken to synthesize the resist, which could involve complex and novel chemistry.

The benefit of using a simulation is that the sensitivity and resolution of a material can be predicted to identify candidates for synthesis and characterisation.

Two of the most widely used codes for lithographic applications are CASINO and TRACER [2, 3]. CASINO is a freely available program and TRACER is a proprietary software developed by GenISys. Both programs can successfully simulate electron beam exposures of materials, with TRACER going further with the ability to produce point spread functions that can be used in conjunction with BEAMER to predict exposure parameters with such features as proximity effect correction (PEC) [4]. This process uses simulated point spread functions of electrons in the resist to manipulate the exposure parameters and hence reduce process blur, maintaining the uniformity of the final structures. Whilst both pieces of software allow for the input of materials which are not already preprogramed, to develop new resists more control is needed over how the simulation handles new materials to understand how a change in resist chemistry could influence its lithographic performance. Both programs also produce electron trajectory plots, examples of which can be seen in Figure **2.1**. Both plots show the scattering of the PEs and 1st generation high energy SEs, but they do not show the complete picture. To fully simulate the SE cascade, multiple generations of SEs at all energy ranges must be simulated. It is through understanding these cascades that the effect of these low energy SEs on different resist materials and the consequent relationship between sensitivity and resolution can be predicted. Another source of low energy SEs that are not considered are those emitted through the Auger effect. Like SEs the AEs have an important role to play as Auger emission can lead to cascades of electrons being emitted again increasing the exposure of the resist. Without these SEs, the current simulations lack the detail to develop new resist materials.
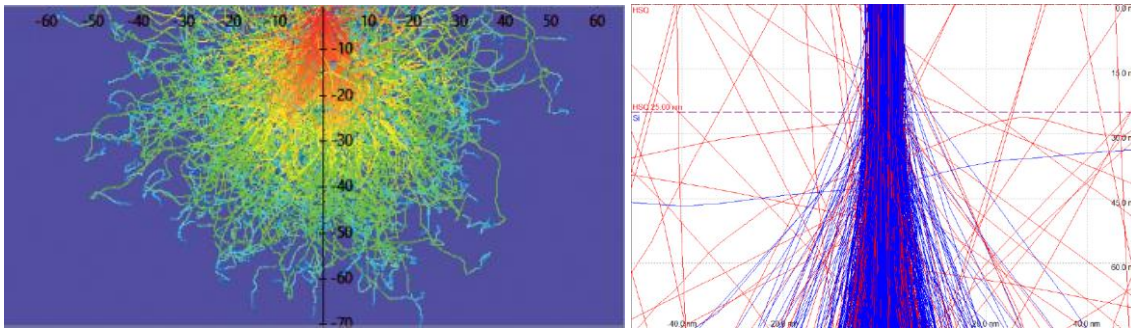
Figure 2.1 *TRACER [3] and CASINO plot examples showing electron trajectories from scattering in materials.*

2.2 <u>Electron Scattering Theory and Models</u>

There was a need for a new Monte Carlo simulation to be designed that could manipulate and combine, existing models to allow simulation of complex supramolecular structures and multicomponent resists. The aim when developing this code was to provide, as close as possible to, a complete picture of the trajectories of the PEs and the full SE cascade both spatially and energetically.

The main electron interactions that are considered in this model, shown in Figure **2.2**, are backscattered electrons, secondary electrons, and Auger electrons. No photon interactions are included in this model, the reasons, and considerations for this are discussed later.

Backscattered electrons (BSE) are PEs that undergo elastic collisions where the scattering angle is large enough such that the electrons are deflected back out of the resist. Alternatively, a PE may pass through the resist and substrate and undergo several interactions after which the electron is redirected out of the top of the resist.

Secondary electrons (SEs) are generated by inelastic collisions between an incident electron, either a PE or a SE with sufficient energy, and an orbital electron. If the energy transferred in the collision is not sufficient to ionize the atom and eject the SE, then the atom will be in an excited state where it has more energy than its ground state. This excess energy is released when the atom deexcites and a photon is released. The photons that are energetic enough to escape the resist and be detected, are usually x-rays.

51
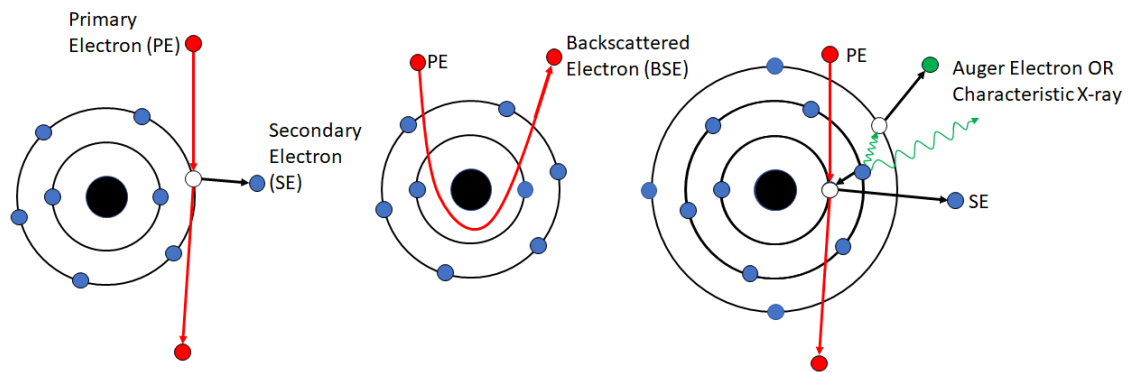
Figure 2.2 *The main electron interactions considered by the Monte Carlo model. This left image shows an inelastic scatter where a primary electron ionizes an atom ejecting a secondary electron. The middle shows the path of a primary electron that is backscattered due to the coulomb interaction between the nucleus of the atom and the primary electron. The right image shows two processes. Similarly, to the left image, a secondary electron is freed in a collision leaving a vacancy in an inner shell and in the following transition the excess energy is emitted as either a characteristic x-ray or an Auger Electron is emitted.*

These X-rays are characteristic to transitions between electron energy levels of specific atoms in the molecules of the resist [5]. They can be measured experimentally however they are not accounted for in this simulation.

The final interaction which is considered in the model is the emission of Auger Electrons (AEs). When an incident electron undergoes an inelastic collision, there is a chance that this collision is with an inner shell electron which is one with a higher binding energy and hence requires more energy to be ionized. If the interaction is of sufficient energy to cause an inner shell ionization, then this will leave an electron vacancy in a low energy electron shell which can be filled by an electron from a higher energy band. To do this the electron must lose energy by either transferring it to another orbital electron which is emitted from the atom as an AE or the energy is released as a characteristic X-ray. The shell from which an AE is emitted will now have a vacancy and if there any higher shell orbitals that can fill this vacancy then a similar transition will occur. This can mean the

ionization of an inner shell electron may lead to a cascade effect of AEs being emitted [6].

2.2.1 Fast Electron Scattering Model

The "fast" electron scattering model follows Joy's model for electron scattering [7]. For this model, the electrons are considered to be fast when their energies are E > 100 eV. The first equations that need to be considered are the elastic and inelastic scattering cross sections as they will determine how far an electron will travel in the resist before a collision i.e. the mean free path. Firstly, the elastic scattering cross section is given by,

$$\sigma_{elastic} = 5.21 \times 10^{-21} \frac{Z^2}{E^2} \frac{4\pi}{\alpha(1+\alpha)} \left(\frac{E+511}{E+1024}\right)^2 \qquad 2.1$$

where Z is the effective atomic number of the target molecule, E is the energy of the incident electron and α is the coulomb screening factor. The screening factor accounts for the screening of the charge of the atom's nucleus by the cloud of orbiting electrons. It is found using the following expression,

$$\alpha = 3.4 \times 10^{-3} \frac{Z^{0.67}}{E} \qquad 2.2$$

The scattering cross section determines the probability that an electron of energy, E, will undergo an elastic collision and scatter. The distance the electron will travel before such a collision is known as the mean free path, λ, which is given by,

$$\lambda_{elastic} = \frac{A}{N_A \rho \sigma_{elastic}} \qquad 2.3$$

where A is the molecular weight of the target molecule, N_A is the Avogadro's constant and ρ is the density.

The second scattering scenario are inelastic collisions. This is an event where energy is transferred from the incident electron to an orbital electron ionizing the atom and releasing an SE. The differential cross section for inelastic scattering collisions is given by,

$$\frac{d\sigma_{inelastic}}{d\Omega} = \frac{\pi e^4}{E^2}\left(\frac{1}{\Omega^2} + \frac{1}{(1-\Omega)^2}\right) \qquad 2.4$$

where E is the initial energy of the PE. After this interaction the PE and the SE will be indistinguishable so the one with the highest energy is taken to be the PE. Ω is the fraction of the incident energy that is transferred to the SE such that the SE will have an energy of ΩE and the PE will have an energy of *(1-Ω)E*. This restricts Ω to having values in the range $0 < \Omega < 0.5$, but as Equation 2.4 has asymptotic behaviour as Ω approaches zero then a nominally small cut-off limit is used for example $\Omega_C = 0.01$ which occludes this asymptotic behaviour without cutting out too much of the potential SE cascade. The inelastic cross section can then be found by integrating the differential cross section and therefore the mean free path is then given by,

$$\lambda_{inelastic} = \frac{A}{N_A Z \rho \sigma_{inelastic}} \qquad 2.5$$

The additional Z term used here when compared to Equation 2.3 is to account for the number of electrons present in the atom. The total mean free path for an electron moving in a material, which is the average distance an electron will move before colliding either elastically or inelastically can be found by,

$$\frac{1}{\lambda_{total}} = \frac{1}{\lambda_{el}} + \frac{1}{\lambda_{in}} \qquad 2.6$$

While the mean free path is the average distance that an electron will travel, an estimate of the actual distance travelled can be found using random sampling,

$$step = -\lambda \ln RND \qquad 2.7$$

where *step* is the distance the electron travels and RND is a randomly generated number between $0 \leq RND \leq 1$.

As an electron travels through the material, it will slowly lose energy. This model uses a constant energy loss model derived by Joy and Luo [8] which is based on the Bethe semi-empirical stopping power which defines the stopping power of the material,

$$\frac{dE}{dS} = -78500\frac{Z}{AE}\ln\left(1.166\frac{E + 0.85J}{J}\right)$$

2.8

where dE/dS is the stopping power; E is the energy of the electron; Z is the effective atomic number and A is the molecular weight of the material; J is the mean ionization potential. The mean ionization potential is given by,

$$J = \left[9.76Z + \frac{58.5}{Z^{0.19}}\right] \times 10^{-3} \quad \text{keV}$$

2.9

Once an electron has undergone a collision it will be deflected. The method of calculating these scattering angles is different for elastic and inelastic collisions. For elastic collisions the scattering angles are given by,

$$\phi = \cos^{-1}\left(1 - \frac{2\alpha\text{RND1}}{1 + \alpha - \text{RND1}}\right)$$

2.10

$$\psi = 2\pi\text{RND2}$$

2.11

where ϕ and ψ are the scattering angles that are shown in Figure **2.3**, and α is the screening factor (Equation 2.2), and RND1 and RND2 are randomly generated numbers. For inelastic scattering the PE is deflected by angle of α which is given by,

$$\sin^2\alpha = \frac{2\Omega}{2 + t - t\Omega}$$

2.12

where t is the kinetic energy to mass ratio (E_K/m_e) and, as before, Ω is the fraction of energy transferred from the PE to the SE. The SE is generated at an angle of γ which is given by,

$$\sin^2\gamma = \frac{2(1 - \Omega)}{2 + t\Omega}$$

2.13

An expression for Ω is given by,

$$\Omega = \frac{1}{1000 - 998\text{RND}}$$

2.14

Using this equation to calculate Ω, it can be seen ~90% of SEs generated have an energy fraction of $\Omega < 0.01$. This means that, due to such a small amount of energy being transferred to the SE, to conserve momentum the deflection angle for the PE will be small

on the order of 1-4°. Therefore, the much lower energy SEs are generated at an almost perpendicular angle (84-88°). This is important as it provides an insight into how SEs expose the resist. The perpendicular angle means that SEs provide a lateral exposure of the resist leading to proximity effects and broadening of structures. But their low energies also mean that they have a much higher chance of undergoing inelastic collisions exposing the resist. Therefore, SE generation is important for resist sensitivity but can lower resolution if the SEs are not controlled.
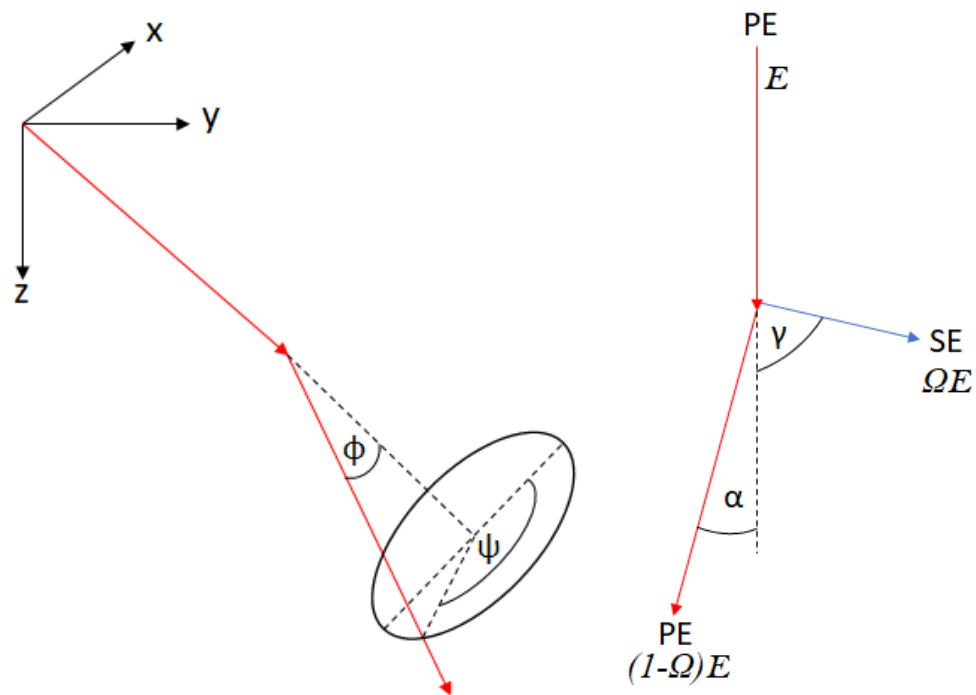
Figure 2.3 *Schematic for the scattering angles for elastic scattering on the left and inelastic scattering on the right. The elastic scattering diagram shows the full 3D scatter with azimuthal angels. The inelastic scattering diagram also shows the generation angle Secondary Electrons relative to the primary electron trajectory.*

2.2.2 Low Energy Quantum Model

The previous section has shown that while few PEs may drop below the 100 eV cut off for the 'fast' scattering model, within the resist layer, many of the SEs are generated at energies with an energy fraction of $\Omega < 0.01$ meaning that depending on the initial energy, they will be below the 100 eV threshold. This means that a low energy model is required

to simulate the full extent of these "slow" (low energy) SEs. The following model described here is based on a quantum scattering model derived by J. J. Sakurai [9]. This derivation uses the Born approximation for wave scattering, treating the incoming electron as a wave scattering off the atom which is treated as a hard sphere. Due to the low energy of the electrons considered by this model (<100 eV) the chance of an electron scattering elastically is greatly reduced in comparison to the higher energy model and can be ignored. Therefore, all collisions will be assumed to be inelastic collisions. This means that these low energy interactions will account for a large proportion of SE cascade. The inelastic scattering cross section is given by,

$$\sigma = \frac{4\pi}{k^2} \sum_{l=0}^{\infty} (2l + 1) \sin^2(ka)^{2l+1} \qquad 2.15$$

This is expanded for the first four dominant terms of l, the orbital angular momentum quantum number (l=0,1,2,3 or l=s,p,d,f), giving,

$$\sigma = \frac{4\pi}{k^2} \left(\sin^2(ka) + 3\sin^2(ka)^3 + 5\sin^2(ka)^5 + 7\sin^2(ka)^7 \right) \qquad 2.16$$

where k is the wavenumber which is given by,

$$k = \frac{\sqrt{2ME}}{\hbar} \qquad 2.17$$

and a was estimated to be ~0.025 nm (the atomic radius of Carbon) using the Thomas-Fermi atomic radius approximation,

$$a = 0.468Z^{-\frac{1}{3}} \text{ Å} \qquad 2.18$$

As with the fast scattering model the mean free path is calculated using Equation 2.5. The scattering angles for these collisions are calculated using the following equations. Ψ the azimuthal angle is calculated, as before, using Equation 2.11. In cases where s-wave scattering is dominant ϕ_s is given by,

$$\phi_s = 2\pi\text{RND} \qquad 2.19$$

However, when higher terms of l are included as in Equation 2.16, this formula, which assumes spherical symmetry, can no longer be used. Consequently, for these higher order waves the scattering angle is given by,

$$\phi_p = 2\sin^{-1}(\exp(-3\text{RND}))$$

2.20

The total scattering angle can then be calculated as a weighted average of the two angles giving,

$$\phi = \frac{1}{ka + (ka)^2}\left(ka\phi_s + (ka)^2\phi_p\right)$$

2.21

A method for determining energy transfer to SEs was suggested by Joy,

$$E' = E\sqrt{RND}$$

2.22

$$E'' = E\left(1 - \sqrt{RND}\right)$$

2.23

where E is the energy of the incident electron and E' is its energy after the collision. E'' is the energy given to the SE generated in the collision.

2.2.3 Auger Electron Generation

The generation of Auger electrons, as previously explained in section 2.2, is an important mechanic for the generation of SEs. The SEs generated from these events have low energy, compared to primary electrons, and therefore will be responsible for further chain reactions of inelastic scattering events generating more SEs. Thus, the addition of an Auger model will increase the ability of the model to simulate the full extent of SE generation. Auger electron emission requires an ionization of the inner shells of an atom. The cross section used for inner shell ionizations is the Casnati cross section [10] which is given by,

$$\sigma_c = \frac{a_0^2 F R^2 AB\ln U}{UE_U^2}$$

2.24

Where $a_0 = 5.292\text{x}10^{-11}$ m, which is the Bohr radius, R is the Rydberg unit of energy $R = 13.606$ eV and U is the overvoltage ratio given by $U=E/E_U$. E is the initial energy of the

incident electron and E_U is the electron binding energy of the inner shell electron. F is a relativistic correction given by the following equation [11],

$$F = \left(\frac{2+J}{2+T}\right)\left(\frac{1+T}{1+J}\right)^2 \times \left[\frac{(J+T)(2+T)(1+J)^2}{T(2+T)(1+J)^2 + J(2+J)}\right]^{\frac{3}{2}} \qquad 2.25$$

where,

$$J = \frac{E_U}{m_e c^2} \qquad 2.26$$

$$T = UJ \qquad 2.27$$

A and B are fitting parameters given by,

$$A = \left(\frac{E_U}{R}\right)^d \qquad 2.28$$

$$B = 10.57 \exp\left(-\frac{1.736}{U} + \frac{0.317}{U^2}\right) \qquad 2.29$$

$$d = -0.0318 + \frac{0.3160}{U} - \frac{0.1135}{U^2} \qquad 2.30$$

As discussed by Seah [12], whilst the Gryzinski cross section provides better accuracy for the range $4 \leq U \leq 15$ it is found to be too low by 10% for both $U < 4$ and $U > 15$ hence the preference for the Casnati cross section.

If the incoming electron successfully strikes out an inner shell electron, then an outer shell electron will fill this vacancy. In doing so it will need to lose energy which it will either pass to another orbital electron or an x-ray will be emitted. To determine the probability of an AE being emitted from a vacated shell the following equation may be used [13],

$$\gamma_{AX} = 1 - \frac{Z^4}{Z^4 + Z_0^4} \begin{cases} Z_0 = 32.4, \ X = K \\ Z_0 = 89.4, X = L \\ Z_0 = 155.9, X = M \\ Z_0 = 300, X = N \end{cases} \qquad 2.31$$

where Z is the atomic number of the atom in which the Auger transition is occurring. If the electron does not come through one of these transitions, then it can be assumed that an x-ray is emitted instead.

2.3 **Building a Simulation**

Using the theory laid out in section 2.2 it was possible to build a simulation. The simulation has been given the name *EXCALIBUR* which stands for **EX**posure **CAL**culations with **I**on **B**eams for **U**nderstanding **R**esists. The scripts that control the simulation were written in Python due to its simplicity and the availability of libraries. The scattering model described is not a perfect model of reality and some assumptions must be made to simplify the simulation and so it could be constructed in a way that is more applicable to the research environment and investigations for which it was designed. These assumptions are as follows,

❖ Material layers are infinite x-y planes with a thickness in z.

❖ Electrons that are backscattered out of the resist or transmitted out through the bottom of the substrate are considered to be terminated and no longer tracked.

❖ Electrons are tracked for the energy range $E_{beam} < Energy < E_{C-C}$, where E_{beam} is the beam energy of the simulation and E_{C-C} is the carbon-carbon bond energy, 3.6 eV.

❖ Above 100 eV electrons are treated classically using the fast electron model and below this limit electrons are treated using the slow electron model.

❖ Electrons are tracked by storing the coordinates of interactions, the energy after this interaction and the direction in which it will be travelling in the next step after scattering i.e. (x, y, z, Energy, x direction, y direction, z direction)

❖ The beam is considered to have a gaussian profile and hence PEs are distributed normally around the central point of exposure with a standard deviation that is determined by the spot size of the beam.

With these assumptions considered the overall architecture of the simulations is as follows:

1. Define layers and materials

2. Define patterns

3. Setup electron beam: energy, dose (or number of incident electrons), spot size.

4. Simulate PEs for each pattern point by point: record trajectories as coordinates and initial positions of any SEs and AEs generated.

5. Simulate SE Generations: record trajectories as coordinates and initial positions of any SEs and AEs for the next generation of the cascade.

6. Calculate energy deposit matrix: divide the resist up into cubes and sum all energy deposited in that box by any electrons passing through or any inelastic collisions occurring in the box.

7. Plot and output trajectory data

The process of tracking electrons is shown in more detail in Figure **2.4**. This loop is used for PEs, after all the PEs have been simulated then the SEs can be tracked using a truncated version of the loop that does not require the materials to be redefined. The loop is also simplified as it has no consideration for where the electron is in the layer matrix i.e. what material it is in or if it has left the matrix through either backscattering or transmission. This check is carried out at the start of a step and also at the end of a step to determine if the electron has crossed an interface between layers. If an electron crosses an interface, then the step is shortened to the point it crosses the boundary and a new step is calculated based on the parameters of the material into which it is transferring.

Also omitted from Figure **2.4** is the Auger model. As the propagation of the electron is not dependant on this process it was emitted, however, every time there is an inelastic collision a check occurs to determine if the ionization occurs in an inner shell

and then the possibility of AE being emitted from the shell and the energy that such an electron would be emitted with.
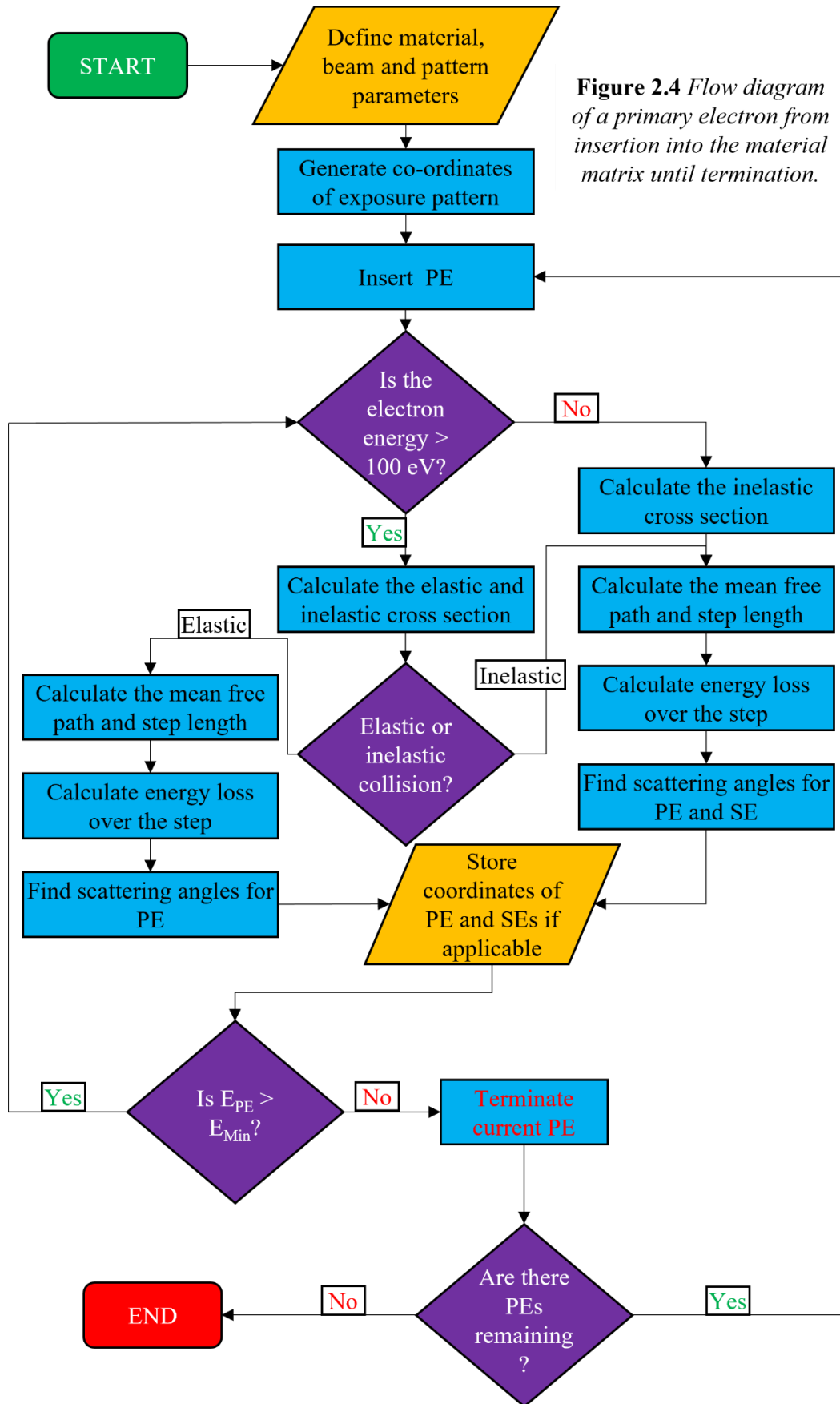
Figure 2.4 *Flow diagram of a primary electron from insertion into the material matrix until termination.*

2.4 <u>Modelling Resists</u>

Before running EXCALIBUR, the parameters of the materials, including any resists and substrates, are needed. The main material properties required are; *'Z'* which is the effective atomic number of the molecule; *'A'* which is the molecular weight of the molecule given in g/mol; *'ρ'* which is the density of the molecule or material given in g/cm^3; *'J'* which is the minimum ionization potential of the molecule given in keV (Equation 2.9) and the molecular formula for of the molecule. Some examples of conventional resist and substrate materials used for demonstration are given in the table below.

Table 2.1 *A table molecular formula and simulation parameters for some example resists used in lithography.*

Name	Formula	Effective Atomic Number, Z	Molecular Weight, A, (g/mol)	Density, ρ, (g/cm³)
PMMA	$(C_5O_2H_8)_n$	5.85	100.12(monomer)	1.18
HSQ	$H_8Si_8O_{12}$	10.85	424.74	1.325
UoM Resist	$Cr_8F_8(O_2C_5H_9)_{16}$	9.02	2185.88	1.21
Silicon	Si	14	28	1.44

The effective Z of a material is the weighted atomic number of a molecule and can be calculated simply from the chemical formula, for example, for a molecule with the formula $O_aC_bH_c$ the total atomic number is found by,

$$Z_{total} = Z_O a + Z_C b + Z_H c \qquad 2.32$$

The contribution of each atom of the molecule to the overall atomic number can then be found by,

$$Z_{eff} = Z_0 \frac{Z_O a}{Z_{total}} + Z_C \frac{Z_C b}{Z_{total}} + Z_H \frac{Z_H c}{Z_{total}} \qquad 2.33$$

The model allows for additive to be added to a resist material to allow for the simulation of composite resists and materials. These molecules can be added to the resist using the

same parameters as before and a ratio of the amount of additive compared to the main molecule. This method can also be used to break down a larger molecule into modular parts which can be changed for other molecules.

If a molecule has exposed double bonds in its structure such alkene (C=C) or carbonyl (C=O) then they can be counted for the molecule. These exposed double bonds are important because when they are struck by an electron, they have a chance to emit two SEs [14]. This means that a molecule with exposed double bonds has more potential to generate SEs compared to a molecule with the same properties which has no exposed double bonds.

2.5 <u>Results</u>

To demonstrate the data produced by *EXCALIBUR*, a comparison of the three resist materials described in Table **2.1** was carried out. These resists were the common resists PMMA and HSQ, chosen due to the extensive catalogue of available data which exists for these materials and a chromium ring resist ($[Cr_8F_8(O_2C^tBu)_{16}]$) developed at the University of Manchester and will be referred to as UoM Resist [15]. This is a generic example of the metal organic negative tone resists investigated and developed in this thesis (Chapter 3). For simplicity all the resists were simulated as 50 nm thick layers on a silicon substrate, with a PE beam energy of 30 keV and with an exposure of 10,000 PE's. The number of incident PEs was chosen as it corresponds to a line dose of 4000 pC/cm which is more than the dose needed to expose the resists and it also ensures that sufficient SEs are generated in all the resists that with 200 re-runs there will a statistical error $< 1\%$.

The first set of data that can be extracted from the model and perhaps the most important is the number of SEs that are generated in the resists. This data is shown in the Figure **2.5**. By comparing the number of SEs that are generated in the resists the relative sensitivities can be compared.
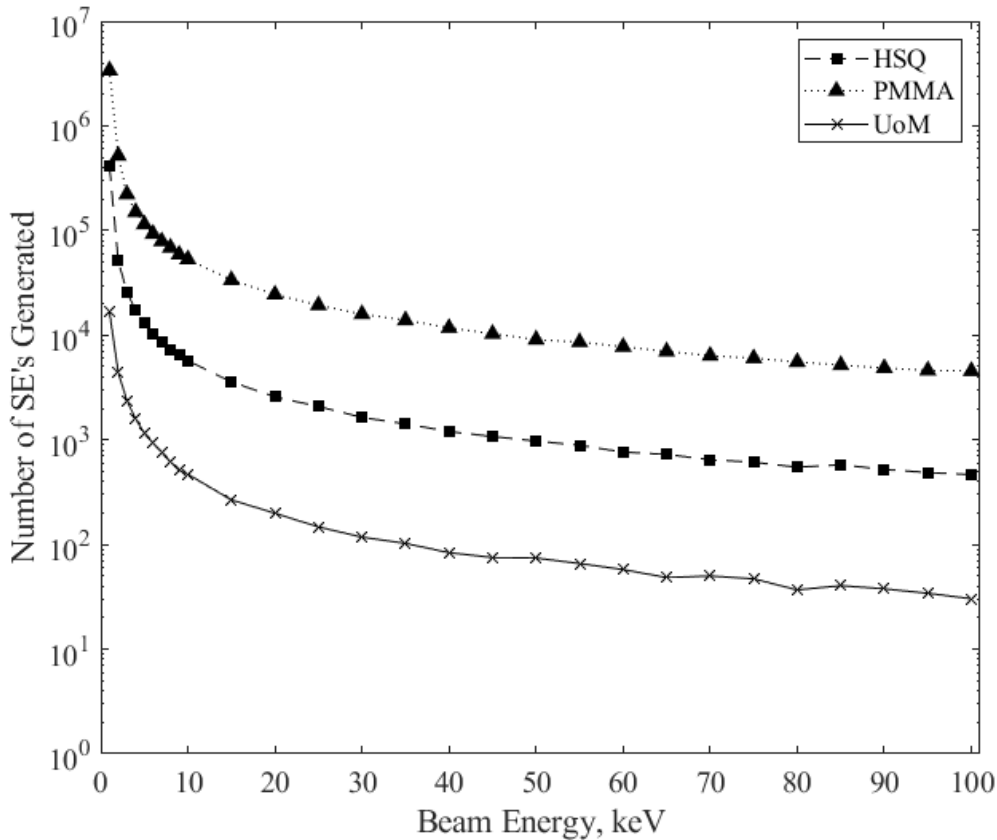
Figure 2.5 *A plot of the number SEs generated for HSQ, PMMA and the UoM resist over the range of 0 > E ≥ 100 keV. Each data point represents the average SEs generated from simulating 10,000 PEs repeated 200 times.*

Evidently PMMA is the most sensitive of the three resists producing more SEs than both HSQ and the UoM resist. This is not surprising as the dose required to expose PMMA in experimental conditions is the lowest of the three. At 30 kV the doses for the materials are 440 pC/cm for PMMA, 2000 pC/cm for HSQ and 28000 pC/cm for UoM Resist [16, 17, 15]. At 30 keV PMMA produces 9.5 times more electrons than HSQ and 130 times more electrons than the UoM resist. When compared with the doses of the materials these values show a trend and an ability to predict the relative sensitivities of materials when compared to each other. This method is limited in accuracy when comparing the expected doses of resist materials as the exposure dose of a material is a complex processing parameter relying on a number of factors, the most effectual of which is the developer regime which can lead to wildly varying doses depending on the developer used.

Alongside the total number of electrons generated it is also possible to record in which generation of the SE cascade these electrons were generated. The breakdown of the cascades for the three resists are shown in Figure **2.6**. It is evident that >95% of all SEs are generated by other SEs rather than the PEs. This is due to much lower energy of the SEs compared to the PEs which means that they enter the slow electron model much more promptly than the PEs most of which will pass out of the resist before they can lose enough energy to pass below the threshold.
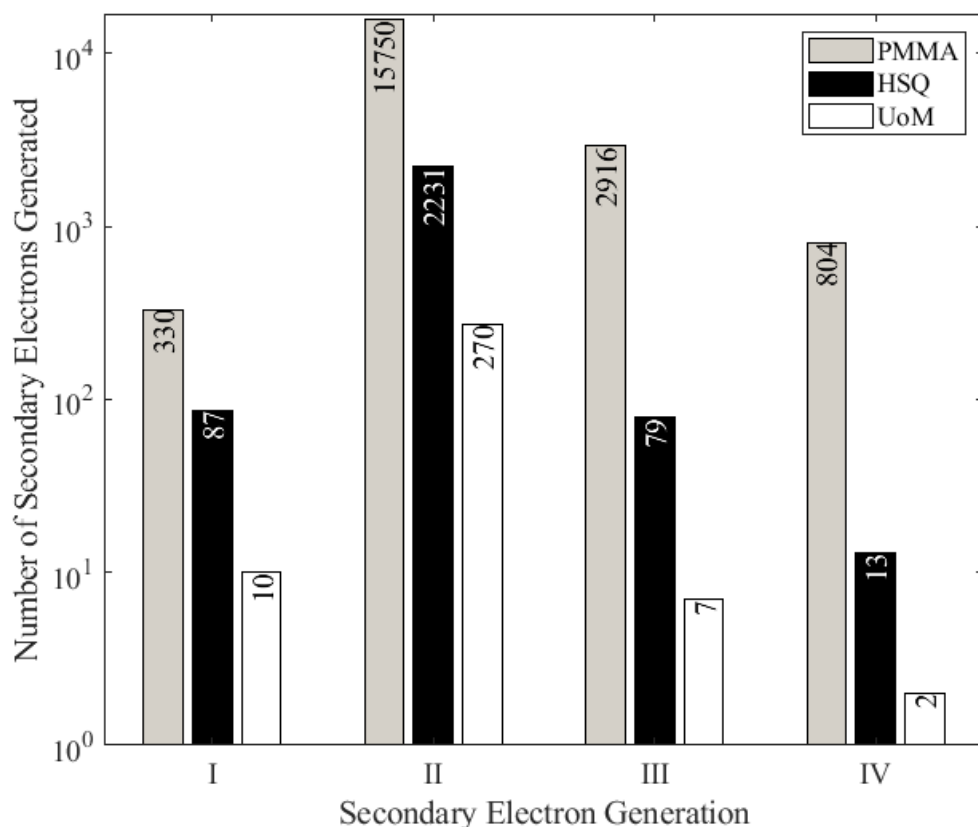
Figure 2.6 *A plot of the number of SEs generated for each generation of the SE cascade for PMMA, HSQ and the UoM resist.*

The coordinate data recorded by EXCALIBUR can be used to reproduce the trajectories of the electrons in the resist and substrate. These trajectory plots are plotted in real 3D space using MATLAB and the profile view of these plots are shown in Figure **2.7.a-c**. The profile views are useful for single spot exposures as they show the spread of the primary beam due to scattering as well as the proximity exposure caused by the lateral spread of the SEs in the resist. From these plots the effect of the resists' parameters on

the electrons can be observed, as per Equation 2.3 and 2.5 as the density of the material increases then it would be expected that the mean free path would decrease meaning more collisions and hence more SEs, however, this is countered by increasing the atomic weight of the material. Therefore, even though HSQ and the UoM resist have larger densities than PMMA, their larger atomic weights lead to the larger mean free paths overall.
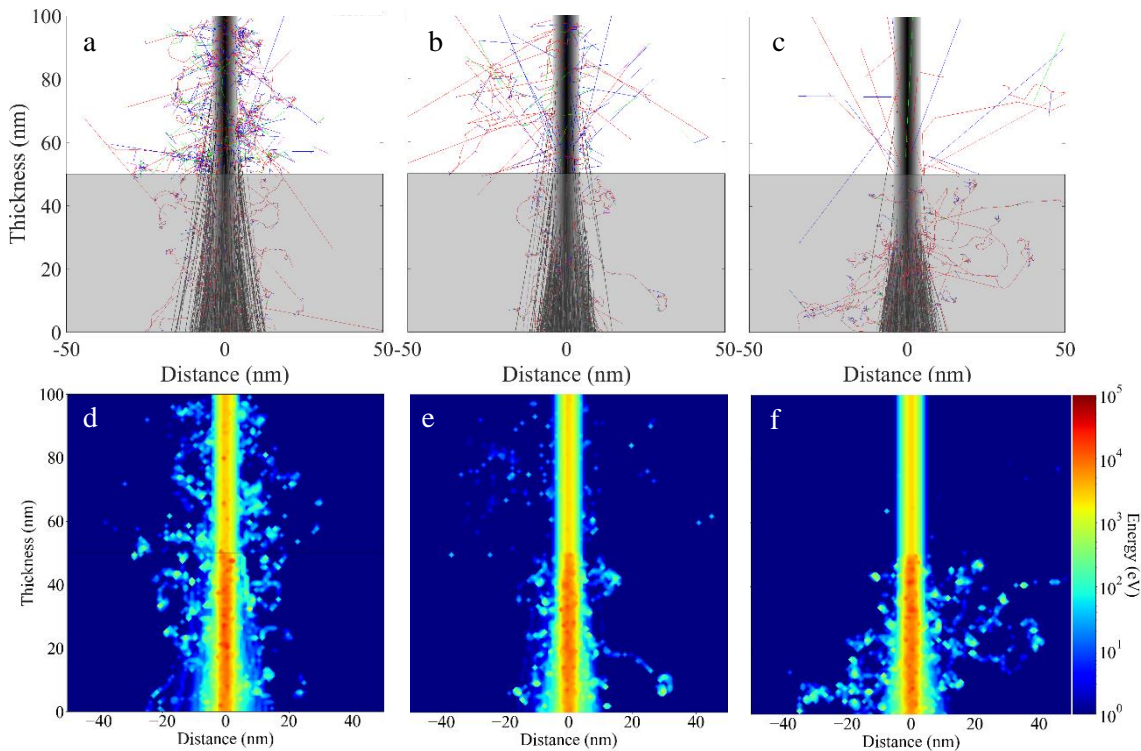
Figure 2.7 *(Top row) Electron trajectory plots generated using EXCALIBUR for 50 nm of (a) PMMA (b) HSQ and (c) UoM resist on 50 nm of silicon. Each simulation was run using an input of 10,000 PEs at an energy of 30 keV. (Bottom row) 2D X-Z energy deposit plots for (d) PMMA (e) HSQ and (f) UoM, generated from the same simulations used for (a-c).*

This also explains the lateral scattering that can be seen in the plots. In the HSQ and the UoM resist the SEs will travel much further than in the PMMA before scattering. A higher effective Z leads to a larger stopping power and a smaller inelastic mean free path. This again helps increase the sensitivity of the HSQ and the UoM resist. One feature that

the PMMA has that neither the HSQ nor the UoM resist have, is the exposed carbonyl group which again explains the increased sensitivity of the PMMA.

EXCALIBUR can also produce energy deposit plots to show where the energy from the electrons is being deposited in the resist through their constant energy loss due to the stopping power and inelastic collisions. For the three resists, the energy deposit heat maps are shown in Figure **2.7.d-f** in the same profile view as the trajectory plots.

The 2D X-Z heat maps shown here are a flattened 3D plots where all the energy deposits in the Y plane are stacked into one cell. It is useful to compare these plots with the trajectory plots as is shows that even though the mean free path for the lower sensitivity resists is increased compared to PMMA, and therefore the lateral spread of SEs is larger, the energy deposited in the resist by these electrons is much less. This is what gives the HSQ and the UoM resist a higher resolution, as it is the depositing of the energy in the resist that is exposing the resist.

Understanding the results of this model compared to an established model will always be difficult however as a qualitive comparison Figure **5.x** shows scattering trajectory plots produced using both CASINO and EXCALIBUR. The plots have been produced with primary beam energies of 30, 10 and 5 KeV and all were simulated using 10,000 electrons in Silicon. The plots show good agreement between the two models in terms of the spatial dispersion of the electron trajectories, however it is clear to see where the models differ. CASINO focuses on identifying backscattered electrons which are shown in red on the trajectory plots and EXCALIBUR shows the generations of SEs that are not tracked by CASINO.
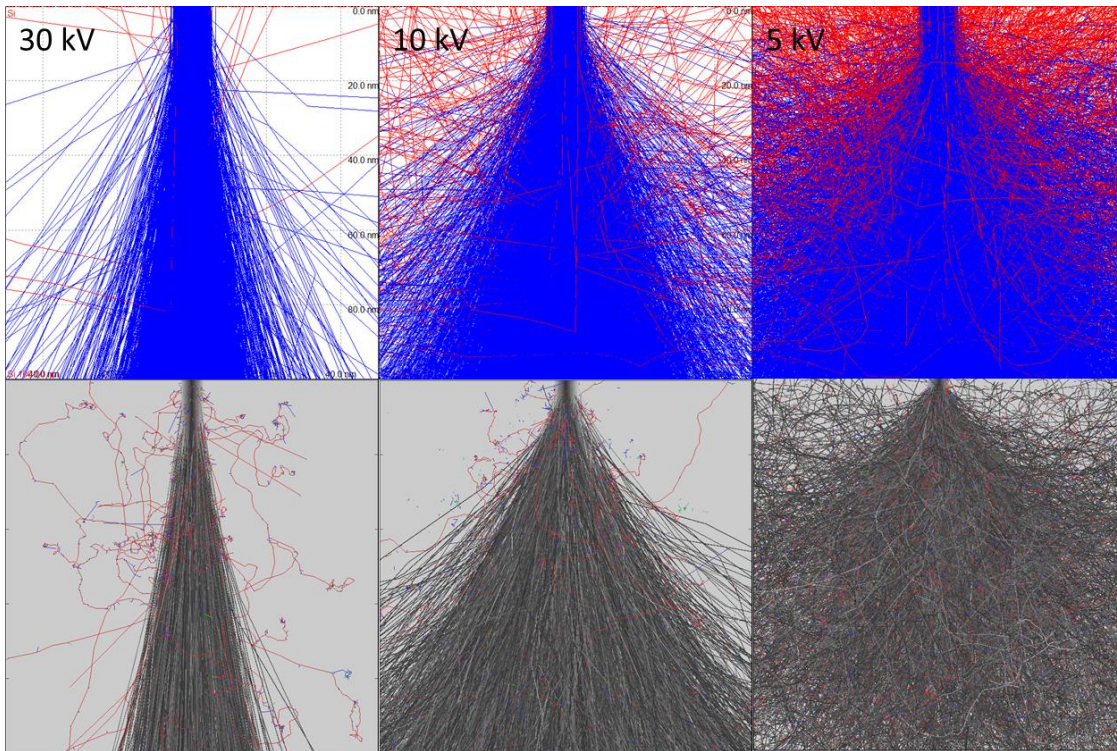
Figure 2.8 *(Top row) Electron trajectory plots generated using CASINO in 100 nm of Silicon at beam acceleration voltages of 30, 10 & 5 kV. (Bottom row) Electron trajectory plots generated using EXCALIBUR in 100 nm of Silicon at beam acceleration voltages of 30, 10 & 5 kV. Each simulation was run using an input of 10,000 PEs.*

2.6 <u>Summary</u>

The benefit of developing a simulation such as EXCALIBUR is that it provides an insight into the exposure of resist materials that helps streamline the resist development process. The time to simulate a new resist material is on the order of hours as opposed to the weeks needed to test a new material. Testing a new material involves finding a suitable casting solvent and determining spin parameters, then characterising the lithographic limits for dose and resolution and finally identifying a developing solvent and optimising the development process. This whole chain can take several weeks. If the new resist isn't already synthesised and the synthesis requires novel chemistry, then the whole time taken can be in the order of months. This shows the benefit that developing this simulation has on identifying new resists. Being able to predict the sensitivity of a proposed resist before

synthesis has even begun allows the development to be much more targeted, and the study can home in on the best candidate first.

There are, however, some drawbacks to this model. While certain lithographic parameters such as resolution can be simulated, the dose of a material is not solely reliant on the sensitivity of the material to exposure by electrons. Development after exposure will prove to problematic for the prediction of dose, as the intrinsic sensitivity of the resist to is not the same as dose after development. The amount of exposure that a resist needs will change depending on the developer used and therefore this cannot currently be accounted for.

References

[1] Green, M., "A Monte Carlo Calculation of the Spatial Distribution of Characteristic X-ray Production in a Solid Target", Proceedings of the Physical Society, Vol. 82 (1963)

[2] Demers, H., Poirier-Demers, N., Real Couture, A., Joly, D., Guilmain, M., de Jonge, N., Drouin, D., "Three-dimensional electron microscopy simulation with the CASINO Monte Carlo software" Scanning, Vol. 33 (2011)

[3] TRACER, GenISys GmbH, Munich, Germany

[4] Lopez, G.G., Azadi, M., Metzler, M.G., Belic, N., Hofmann, U., "Isofocal Dose Based Proximity Effect Correction Tolerance to the Effective Process Blur" Journal of Vacuum Science & Technology B, Vol. 35 (2017)

[5] Mathieu, Hans Jörg. "Auger electron spectroscopy." *Surface Analysis the Principal Techniques*, John Wiley & Sons, Ltd, pages 9-46 (2009):

[6] Matthew, J.A.D., "The Auger Process", *Scanning Auger Electron Microscopy*, John Wiley & Sons, Ltd, pages. 15-44 (2007)

[7] Joy, D. C., "Monte Carlo Modeling for Electron Microscopy and Microanalysis", New York: Oxford University Press (1995).

[8] Joy, D.C., Luo, S., "An Empirical Stopping Power Relationship for Low-Energy Electrons", Scanning, Vol. 11 (1989)

[9] Sakurai, J.J., Tuan, S.F., "Modern Quantum Mechanics.", Menlo Park, California; Wokingham: Benjamin-Cummings (1985).

[10] Casnati, E., Tartari, A., and Baraldi, C., "An empirical approach to K-shell ionisation cross section by electrons", J. Phys. B: At. Mol. Phys., Vol. 15 (1982).

[11] Quarles, C.A., "Semiempirical analysis of electron-induced K-shell ionization", Physical review. A, Vol. 13 (1976)

[12] Seah, M.P., Gilmore, I.S., "Quantitative AES VII. The ionization cross-section in AES", Surf. Interface Anal., Vol. 26 (1998)

[13] You, D. S., Li, H. M., and Ding, Z. J., "Monte Carlo simulation of Auger electron emission from thin film on substrate" J. Electron Spectrosc. Relat. Phenom., 222, pages156–161 (2018).

[14] Moreau, W.M., "State of the Art of Acrylate Resists: An Overview of Polymer Structure and Lithographic Performance", Proc. SPIE 0333 (1982)

[15] Lewis, S. M., DeRose, G. A., *__Alty, H. R.,__* Hunt, M. S., Li, J., Werthiem, A., Fowler, T., Lee, S. K., Muryn, C. A., Timco, G. A., Scherer, A., Yeates, S. G., Winpenny, R. E. P., "Design and implementation of the next generation electron beam resists for the production of EUVL photomasks", Proc. SPIE 10810 (2018)

[16] Hu, W., Sarveswaran, K., Lieberman, M., Bernstein, G.H., "Sub-10 nm electron beam lithography using cold development of poly(methylmethacrylate)", Journal of Vacuum Science & Technology B: Microelectronics and Nanometer Structures Processing, Measurement, and Phenomena, Vol. 22 (2004)

[17] Yang, J.K.W., et al., "Understanding of Hydrogen Silsesquioxane Electron Resist for Sub-5-nm-half-pitch Lithography", Journal of Vacuum Science & Technology B: Micro-electronics and Nanometer Structures, Vol. 27 (2009)

3

SUPRAMOLECULAR RESISTS FOR ELECTRON BEAM LITHOGRAPHY

Contents

The current generation of semiconductor manufacturing uses techniques and materials that have been developed side by side. Whilst the techniques may change more slowly, as with the current shift from 193 nm photolithography to EUVL, there is always a constant factor that drives scaling and that is the photomasks used to pattern the resists. As manufacturers are pushing to fully optimise this fabrication process the features demanded are becoming ever more complex and most importantly smaller. This reduction in size, is the first requirement needed from photomasks. Photomasks must be made using direct write lithography methods with electron beam lithography (EBL) being used for

27.6% of all masks and laser writing accounting for the rest [1]. However, as photomasks are needing higher resolutions the demand for EBL is also increasing. This also means that new resist materials are needed that can be patterned to structures on the order of 10 nm which is approximately the wavelength of EUV light as sub wavelength patterning is not currently being employed [2]. However current state of the art manufacturing targets for the latest EUV photomasks is 10 nm half pitch with the on-mask features being 4 times larger [3].

The second important relationship between photomasks and resists is time taken to manufacture photomasks. To maintain a high throughput of mask production resists must be sensitive enough to bring the exposure times low enough to meet this demand, where the current state of the art is 10 hours per mask at with a 20 nm feature size [4]. The sensitivity of a resist is determined by its dose, the more sensitive the lower the dose needed to expose it and the shorter exposure time needed.

Finally, the third relationship is reproducibility. The lithographic process needs to be consistent to maintain a high yield of mask production with as few defects as possible. The metric that is used to define a resist's ability to produce defect free structures is the line edge roughness (LER). This is a measure of how much the edge of structure deviates from the intended edge of the structure. It is these deviations that can cause defects if they become too large.

Together these three parameters; resolution, sensitivity and LER, form a trade-off, shown in Figure **3.1**, that must be considered when designing any new resist material. Resist materials tend to fall into two categories the first being the high resolution, high dose resists shown by Resist 1 and the second type are low dose, low resolution resists shown by Resist 2. The optimal, target resist is a combination of the high resolution of Resist 1 and the low dose of Resist 2. By using a sub optimal resist as a starting point the aim of resist development is to change the chemistry and the processing of a resist to

move toward the target resist. To do this a combination of simulation, to identify potential improvements to resist formulation, and experimentation, to confirm the improvement and optimise the lithographic processing, can be used.
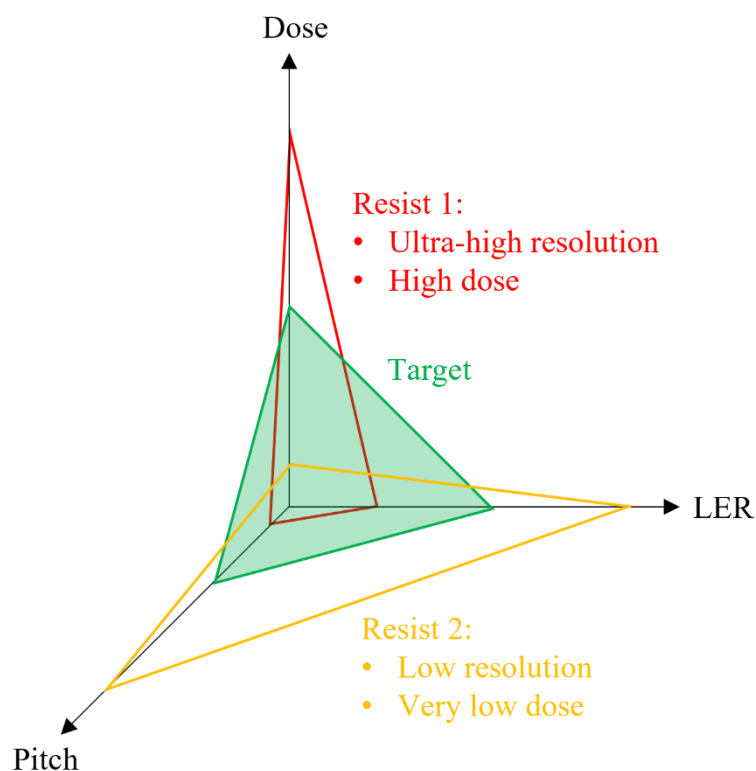
Figure 3.1. *The resist trade-off triangle showing the relationship between the dose, pitch and LER. Shown in green is the optimal target resist, shown in red is a high resolution, high dose resist and shown in yellow is a low-resolution low dose resist.*

3.1 <u>Supramolecular Resists: A Modular Resist Platform</u>

In this chapter a resist which fell into the ultra-high resolution, but high dose category was used as a starting point, with the aim being to use simulation and experimentation to improve the sensitivity of the resist. To this end a family of modular resists based on metal-organic molecules was developed, an example of which is shown in Figure **3.2**. A modular resist is a framework for resist design where a family of resists can be developed which have the same basic structure and chemistry but with changeable ligands. This can, in theory, control a resist's solubility and sensitivity without affecting the lithographic resolution and structure quality. The concept of modular resists was an essential focus

when developing these new resists as this allows a resist to be adapted to a range of situations without the need for a complete overhaul of synthesis which can take months of work.
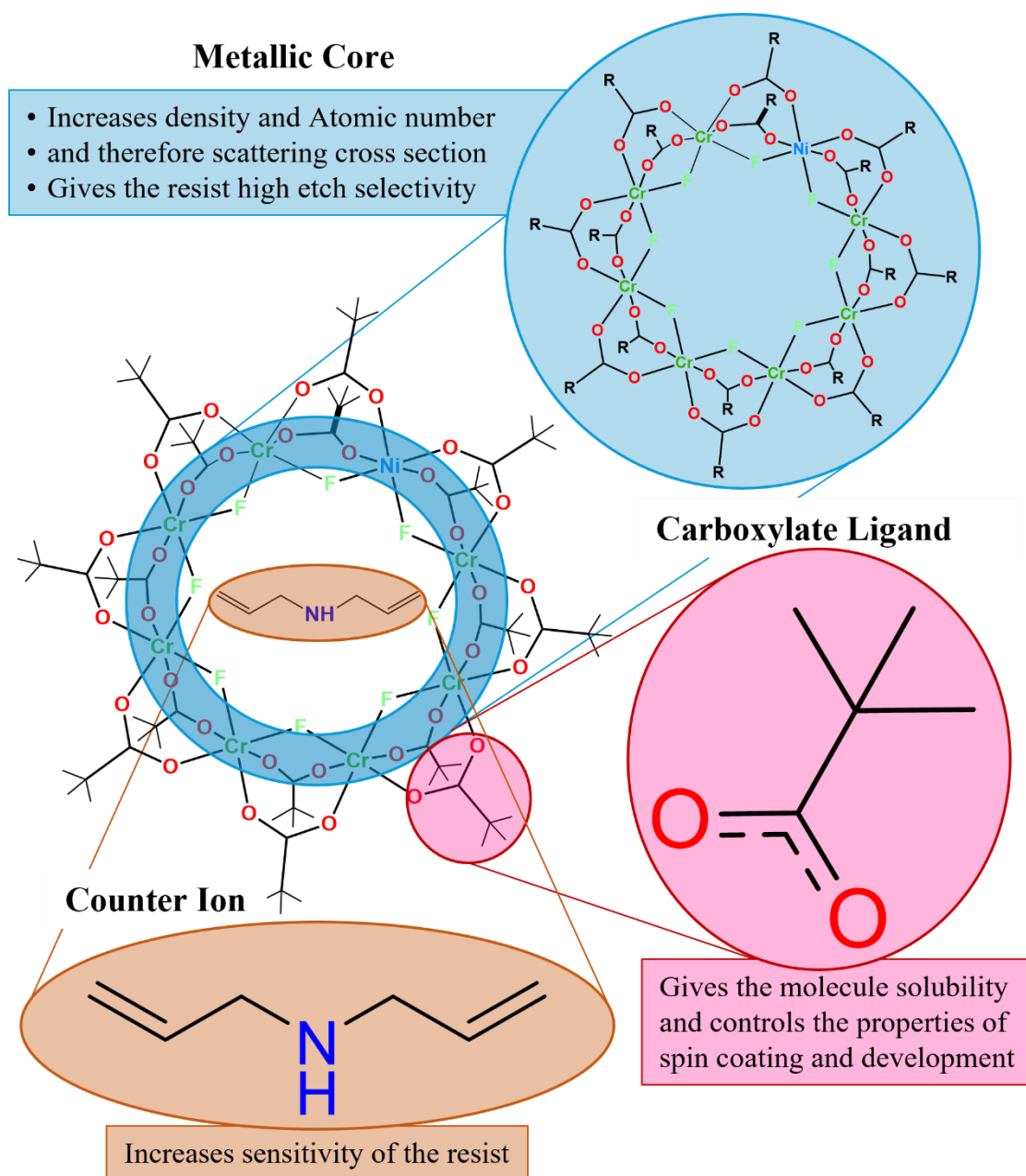
Figure 3.2. *An example of a modular resist with the main components highlighted.*

There are four main components that can make up the modular resists. First, is the metallic core which acts as the backbone of the resists to which all the other components are attached. Second, is the main ligand which is attached to the core of the ring and gives it solubility. Third, is the counter-ion which stabilizes heterometallic molecules but can also contain sensitivity increasing compounds. Finally, there are additional compounds that

can be added to the ring substituting for the main ligand. These additional substituents can increase sensitivity but often at the cost of solubility in the developing solvent which can decrease the final structure quality.

To simulate a resist in EXCALIBUR (Chapter 2) certain material parameters are needed. These material parameters are the effective atomic number, the density, the molecular weight, and the ionization potential of the material. Along with the energy of the electrons in the material determined by the initial beam acceleration voltage, these parameters control all the equations which govern the scattering of electrons in the material. The successful development of a new resist relies on understanding these parameters.

By increasing the effective atomic number there will be an increase in both the elastic and inelastic cross sections and therefore a reduction in the mean free path. The increase in the scattering cross sections means that a primary electron (PE) entering the resist material will undergo more collisions whilst it is in the resist. This means that there will be an increase in inelastic events and therefore more secondary electrons (SEs) will be generated. Similarly, a reduced mean free path leads to a PE travelling shorter distances between collisions and will therefore undergo more collisions whilst in the resist. There will also be an increase in the stopping power of the resist and hence a PE will lose energy faster which will again lead to an increase in scattering cross sections further increasing the number of secondary electrons generated. Similar effects are experienced by secondary electrons. Also considering that the generation angle of the secondary electrons is close to perpendicular to the direction of the PE beam then the secondary electrons will expose the resist laterally. The reduction of the mean free path is beneficial as they will not travel as far in the resist reducing this lateral exposure which is responsible for broadening of structures and hence a reduction in resolution. This shows that a high effective atomic number is a vital property to ensure a high sensitivity. The

effective atomic number of a resist can be increased by the addition of heavy metallic elements and by limiting the number of organic molecules.

An increase in density will also cause a reduction in the mean free path of all electrons in the resist. This will lead to more collisions in the resist and hence an increased number of SEs will be generated. This again shows the benefit of large metallic atoms as they will generally increase the density of the resist.

Increasing the molecular weight has the opposite effect as the previous two properties. This is due to the mean free path being directly proportional and the stopping power of the resist being inversely proportional to the molecular weight. Consequently, larger molecules cause a decrease in the sensitivity.

The ionization potential of a molecule is intrinsically linked to its effective atomic number and so it can be changed in the same way. Figure **3.3** simplifies how changing these parameters will affect the lithographic potential of a resist.
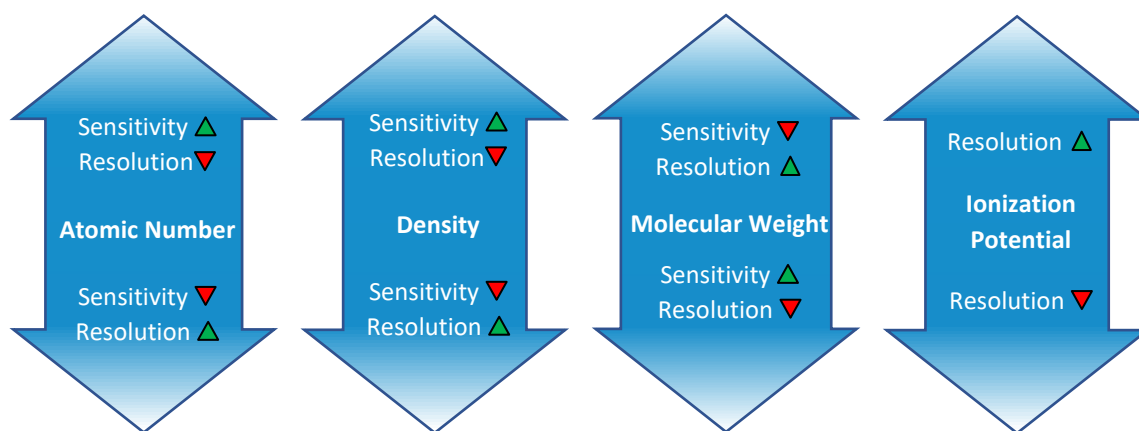
Figure 3.3 *Material input parameters for EXCALIBUR and their overall effect on the sensitivity and resolution of the resist material.*

For the case of these supramolecular resists a higher sensitivity is needed to reduce the exposure dose and time. As these resists have low density and high molecular weight, then the sensitivity can be increased by either increasing the density or reducing the molecular weight. In the case of the density, adding more heavy metal ions will be beneficial and to reduce the molecular weight the molecule could be reduced in size.

3.2 <u>Experimental Methodology</u>

3.2.1 <u>Resist Preparation</u>

A material that has been identified through simulation as a potential resist will then need to be synthesised. This work, which can take many months of development as it often involves novel chemistry and formulations, is carried out by members of the molecular magnets group at the University of Manchester and product development scientists from Sci-Tron a spin out company from the University of Manchester. Once the resist has been synthesised it can be characterised chemically using nuclear magnetic resonance spectroscopy (NMR), elemental analysis, mass spectrometry and X-ray single crystal diffraction (XRD).

These analysis techniques give information on the purity, content, and molecular structure of a resist to confirm that the expected molecule has been synthesised and there are no impurities. Impurities such as precursor materials or by products of the reactions in synthesis can be removed using column chromatography and filtration. Once the resist has been isolated in a crystalline or powder form it is then ready to be dissolved in the casting solvent. This is an important step as often the solvents used for synthesis are not appropriate for spin coating. The choice of this solvent is important as it will affect the quality of the film formed during spin coating. Most importantly the solubility of a resist in different solvents will vary greatly. This affects the concentration of the solution, i.e. the amount of resist dissolved in the casting solvent, and therefore the thickness of the film produced by spin coating. Also, if the boiling point is too low then some of the solvent will be lost during processing and filtering, changing the concentration of the resist solution.

Once the resist is fully dissolved in the casting solvent it must be filtered to remove any particles and undissolved material from the solution which would decrease the quality of the resist films. The filters used in this work are PTFE syringe filters with a pore size

of 200 nm for small batches or vacuum filtration using 25 nm pore size membranes for larger quantities. The filtration removes any particles remaining from synthesis, such as undissolved material, or picked up from a non-cleanroom environment. Depending on the material this process may need to be repeated multiple times.

3.2.2 <u>Spin Coating</u>

Spin coating is the method of deposition most used to apply resist films to a range of substrate materials. The substrate used for these resists are polished Si wafers with a native oxide. The wafers have a thickness of $525 \pm 20\,\mu\text{m}$ with a diameter of 100 mm. To make the wafers easier to manage and process they are cleaved, using a tungsten carbide scribe, into smaller samples usually 10 x 10 mm or 20 x 20 mm.

It is important to remove any dust or debris that would reduce film quality; hence the samples are cleaned using an ultrasonic bath. Firstly, they are cleaned twice in acetone for 3 mins to remove any organic contamination, then they are cleaned in isopropyl alcohol (IPA) for 3 minutes to remove any remaining inorganic material and to wash away the acetone which would otherwise stain the silicon when it dries. Next, the samples are blown dry using compressed nitrogen to stop staining of the silicon as the solvent dries. The samples can also be soft baked to remove any residual solvent.

To spin coat the resist a sample is placed on the vacuum chuck of the spin coater which uses a vacuum to hold the sample still while it is spun at high spin speeds. The spin coater is then programmed with the spin routine. The spin routine used for testing the resists has an acceleration time of 5 seconds and a deceleration time of 2 seconds and a spin duration of 30 seconds. The spin duration is long enough for the excess resist solution to be spun off the sample and produce a uniform film. The spin speed varies depending on the sample size and the resist used and can be between 1000 and 8000 rpm. Using a pipette, the resist solution is applied to the chip and to avoid the solvent from evaporating from the resist, the spin coater is started immediately. Alternatively, the resist can be

dropped onto the chip whilst it is spinning. Once the spin coater has finished any remaining solvent must be removed from the film. The usual method to do this is to soft bake the sample on a hot plate set at a temperature appropriate for the boiling point of the casting solvent. Some resists, however, are thermally sensitive and will decompose if exposed to heat. Instead, the solvent can be removed by placing the samples into a vacuum, where, due to the low vapour pressures of the solvents, they will out gas from the sample.

In the work described here the whole process was carried out in an ISO 5 clean room to keep the samples as clean as possible when being processed. A comparison of a resist film with no contaminants from processing and one with visible defects in the film is shown in Figure **3.4**.
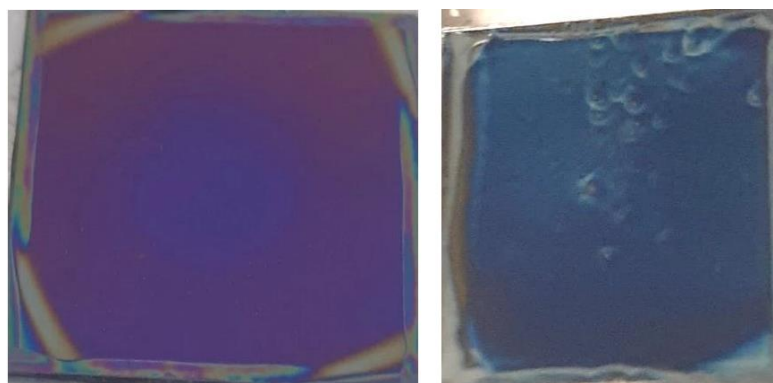
Figure 3.4 *Photographs showing a clean defect free film (left) and a film with large defects caused by contaminant molecules (right). These are resist **B** films prepared using the same method described in the this section. The samples are both 10 x 10 mm wafer chips.*

As shown, the two films for the same material can produce very different results. From the left sample it is evident that there is some variation in thickness (change in colour) from the centre compared to the edge. Also, the edge bead, which is the strip that can be seen around the edge of the film, is an effect caused by the forces from the sharp edge of the sample and the shrinking of the film as it dries. Lower viscosity resist solutions and higher boiling temperature solvents will generally reduce the edge bead. In the sample on

the right of Figure **3.4** defects in the film can be seen caused by particles trapped in the film. These cause 'comets' which produce streaks in the film where the resist is blocked from spreading uniformly across the sample during spin coating. These particles could be from synthesis that were not removed in filtering or silicon fragments and dust from cleaving the wafers which were not removed during cleaning.

3.2.3 <u>Exposure and Development</u>

For EBL, three different modified SEM systems were used: an FEI Sirion, a LEO 1550 and a Zeiss Sigma 300VP. All three systems are field emission SEMs (see Chapter 1.2.2) capable of producing sub 10 nm structures at a range of acceleration voltages from 1-30 kV. The sample is placed on a holder which is then mounted into the main chamber of the SEM. The chamber is then pumped down to pressures in the region of 2×10^{-5} mbar. The electron beam can then be turned on at the required beam acceleration voltage, 30 kV is used for writing as this is the highest acceleration voltage available and hence will have the lowest beam divergence. The beam is then focused and adjusted for astigmatism using a calibration standard (See Figure **3.5**).

Once the beam is focused the beam current is measured, which, when using a 10 µm aperture, is usually between 38-43 pA. It is necessary to measure the beam current so that the step size and the dwell time of the exposure pattern can be calculated to give the required dose. Control of the SEM is then switched over to the pattern generator. The pattern generator is an ELPHY Quantum system produced by RAITH [5]. Next the sample is exposed using a pattern designed to contain a range of doses and pitches. Once the writing is finished, the beam is switched off and the chamber can be vented, with dry nitrogen, to atmospheric pressure. The sample can then be developed using the developing solvent and dried using compressed air. Finally, the sample can be placed back into the SEM to be inspected and characterized.
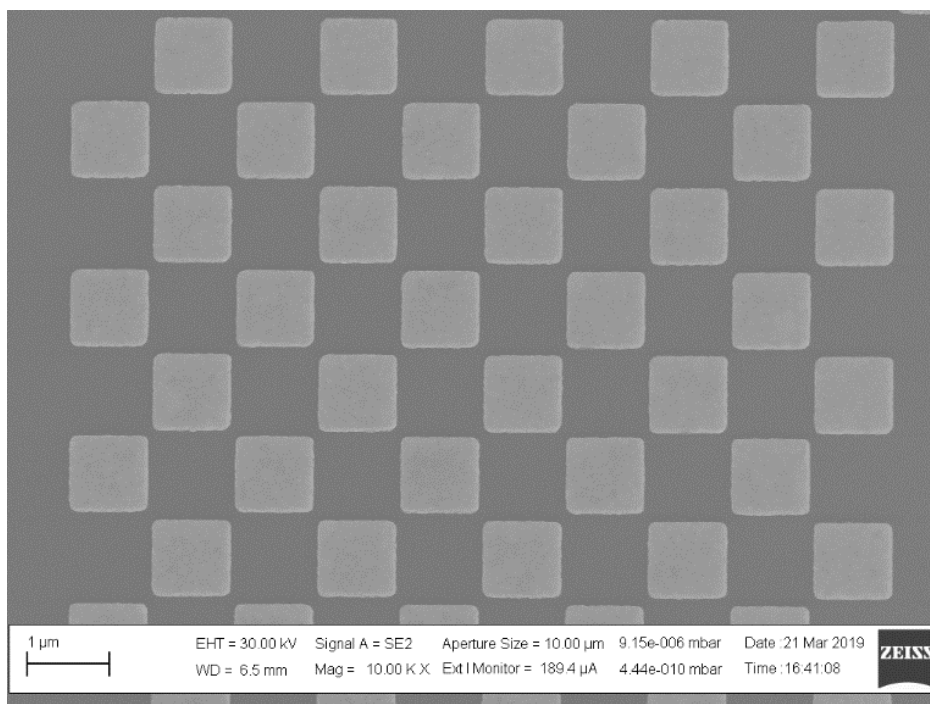
Figure 3.5. *An SEM image of the Chessy calibration standard, used to ensure the SEM is in focus before being used for exposure.*

3.3 <u>Results: Designing Modular Resists</u>

A series of resists based on the modular approach to designing resists were developed for electron beam lithography. The resists discussed in this section and their material parameters are shown in Table **3.1**. Also shown are the modular components of the resist and their percentage mass of the overall molecule to illustrate the changes between resists.

The family of resists that constitute the backbone of this work is the chromium ring family [6] which are organometallic rings made up of 8 metal atoms connected by fluorine atoms to form a ring. These rings are surrounded by carboxylate ligands which give the metallic rings solubility in common solvents. The first and most basic ring in this family is resist **A** which is a ring of 8 chromium atoms surrounded by 16 pivalates (ligand form of pivalic acid). This resist is the starting point for all the resists in this family and has been shown to have excellent resolution (when exposed at 100kV) and dry etch selectivity. 15 nm lines with a pitch of 40 nm were transferred into the silicon substrate showing an etch selectivity of 45:1 [7]. However, the dose for this resist was very large

requiring exposure doses of 61,000 $\mu C/cm^2$ which reduces its viability as a resist for fabrication of devices or photomasks. Another point of note is the reduction in thickness between the film before exposure and the height of the final structures by a factor of approximately 5, which would normally be of concern but due to the high etch selectivity the expected reduction in maximum etch depth is avoided. Despite these issues, it provides a good starting point for an evolutionary chain of resists where the aim is to increase the sensitivity and hence reduce the dose whilst maintaining its resolution. The parameters that give the resist good resolution are its low density and large molecular weight as these parameters limit the scattering cross sections of electrons in the resist and hence reduce lateral exposure.

The first step to improve the resist was to add a diallylammonium cation at the centre of the ring. This gave resist **B** which has the formula **[NH$_2$(allyl)$_2$][Cr$_7$NiF$_8$(O$_2$C^{t}Bu)$_{16}$]** [8]. To make this step the chromium ring had to be changed to a heterometallic ring [9] by substituting a chromium atom for a nickel. This allows the inclusion of a counter ion to balance the charge of the ring. This counter ion can simply be a singly charged ion e.g., caesium, however, more complex organic molecules such as amines can be used. In this case the amine used is diallylamine, which is protonated during the synthesis to become a diallylammonium cation; the inclusion of this molecule is based on the common accelerators and sensitivity promoters used in commercial positive tone resists. In this case as with PMMA (Chapter **1.5**), the hypothesis was that the alkene bonds on the diallylamine molecule would increase the sensitivity of the resist [10]. It would achieve this by acting as a source of secondary electrons and generating free radicals that would help destabilise the resist molecules and render them insoluble [11]. As the overall chemistry of resist **B** remains very similar compared to **A** it was predicted that the lithographic resolution would be unaffected whilst the sensitivity is increased.

To further increase the sensitivity, heavy metal salts can be hung on the outside of the ring. The heavy elements added in this way greatly increase the effective atomic number of the molecule in this region effectively acting as scattering point and hence a localised area of SE generation. Also, due to their weight, they dominate the molecule increasing the density and hence greatly increasing SE generation. To add these heavy elements to the ring, a pivalate ligand had to be substituted with an *iso*-nicotinate bridge which then allowed $HgCl_2$ (resist **C**: **$[NH_2(allyl)_2][Cr_7NiF_8(O_2C^tBu)_{15}(O_2CC_5H_4N\text{-}HgCl_2)]$**) and HgI_2 (resist **D**: **$[NH_2(allyl)_2][Cr_7NiF_8(O_2C^tBu)_{15}(O_2CC_5H_4N\text{-}HgI_2)]$**) to be attached to the ring.

Whilst the main purpose of this exploration of the modularity of the chromium ring family was to increase the sensitivity another approach that can be taken is to change the main ligand of the ring with the intention of changing the solubility of the resist to allow it to be processed in different solvents. To allow the solubility of the resist in anisole, the pivalate ligand was replaced with the benzoate ligand which would allow for the possibilities of the formulation of composites with PMMA. This led to the creation of resist **E**: **$[NH_2(allyl)_2][Cr_7NiF_8(C_6H_5COO)_{16}]$**. The reason a composite of this resist with PMMA is desirable, is that adding a resist such as this with its metal core could potentially increase the etch resistance. A foreseeable problem, however, with the inclusion of the benzoate, is that the phenyl rings that are being placed on the outside of the ring act as electron sinks, absorbing electrons and hence increasing the required exposure dose [12, 13]. The absorbing of the SEs by the phenyl rings also has the desirable effect of reducing the proximity exposure which will increase the resolution.

One of the main factors limiting the sensitivity of the chromium ring resist family is the large molecular weight and the relatively low density of the resist due to its geometry. Instead, an alternate direction, that was predicted to increase sensitivity, was to reduce the overall size of the molecule. A molecule that could fulfil this role whilst

maintaining the opportunity for potential modular chemistry, was a chromium triangle. Whilst a homometallic {Cr$_3$} triangle resist was synthetically possible; it was not possible to spin coat due to the presence of external counter ions (not contained within or attached to the molecule) in the solution. These counter ions greatly reduced film quality meaning the first resist had to be a heterometallic triangle. Resist **F** is a chromium triangle with a substituted nickel. Similarly, to resists **A** - **D** the main ligand for **F** is a pivalate. Unlike the chromium ring, the triangle has free sites that extra ligands can be attached to without the need for a substitution of the main ligand. Following the success of the addition of the diallylammonium to the chromium ring resists, a ligand with an exposed alkene bond was chosen to increase the sensitivity of the resist. This molecule was vinyl-pyridine (VinPyr) and therefore the full formula for **F** is **[Cr$_2$NiO(O$_2$C^{t}Bu)$_6$(VinPyr)$_3$]**.

Another direction that could be taken was to change the metal that makes up the core ring of the molecule. To this end an indium ring (resist **G**: **[NH$_2$(allyl)$_2$][In$_7$NiF$_8$(O$_2$C^{t}Bu)$_{16}$]**) was developed [14]. Indium was chosen due to its much higher atomic number compared to chromium and its sensitivity to other exposure sources such as EUV. Like the chromium ring resists (**B** - **D**) this indium ring has a pivalate as its main carboxylate ligand and a diallylammonium as the counter ion. The switch from chromium to indium will increase both the effective atomic number and the density of the molecule. This means as per section **3.1,** the probability of scattering and the stopping power of electrons in the resist will be increased which will lead to more SEs being generated and therefore an increase in sensitivity.

Table 3.1 *A table of resists **A – G** showing their molecular structures and simulation values: effective atomic number - Z_{eff}, molecular weight - A, density - ρ and mean ionization potential - J. Also shown are the modular components of the resist molecules and their simulation values. The percentage values in the component column are the weight percentage of each component as a fraction of the total molecule. *density values for the core components are not known as this cannot exists as its own compound, therefore overall values of the molecule were used.*
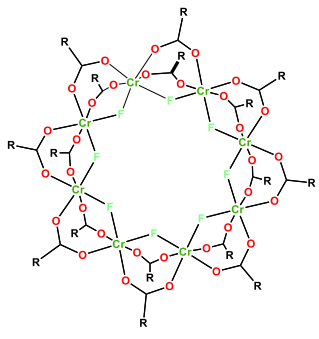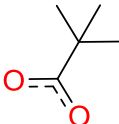
Resist	Component	Name/Formula	Z_{eff}	A (g/mol)	ρ (g/cm³)	J (keV)
A	/	**$Cr_8F_8(O_2C^tBu)_{16}$**	9.03	2186	1.21	0.127
	Core (25.98%)	Cr_8F_8	19.91	568.0	1.21*	0.227
	Ligand (R) (74.02%)	Pivalate ($O_2C_5H_9$)	5.76	101.1	0.90	0.098

Table 3.1 *Continued*
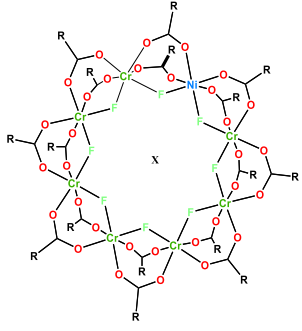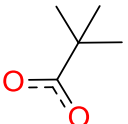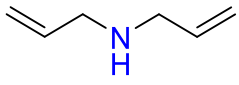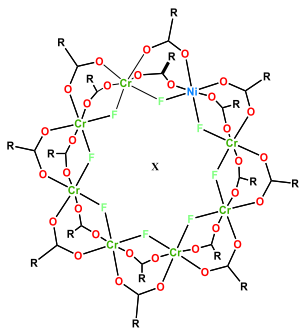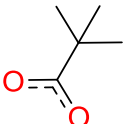
B	/	**[NH₂(allyl)₂]** **[Cr₇NiF₈(O₂CᵗBu)₁₆]**	8.99	2289	1.27	0.126
	Core (25.10%)	Cr₇NiF₈	20.39	574.7	1.27*	0.232
	Ligand (R) (70.66%)	pivalate (O₂C₅H₉)	5.76	101.1	0.90	0.098
	Counter-ion (X) (4.24%)	diallylammonium (NC₆H₁₁)	5.11	97.2	0.76	0.093
C	/	**[NH₂(allyl)₂]** **[Cr₇NiF₈(O₂CᵗBu)₁₅** **(O₂CC₅H₄N-HgCl₂)]**	13.50	2582	1.43	0.167
	Core (22.25%)	Cr₇NiF₈	20.39	574.7	1.43*	0.232
	Ligand (R) (58.74%)	pivalate (O₂C₅H₉)	5.76	101.1	0.90	0.098

Table 3.1 *Continued*
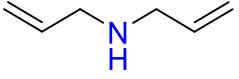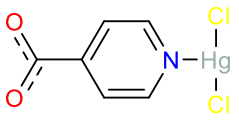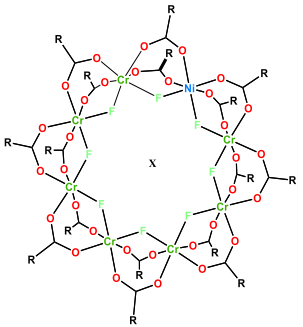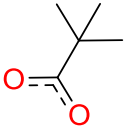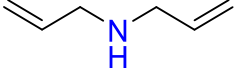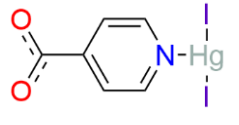
	Counter-Ion (X) (3.76%)	diallylammonium (NC₆H₁₁)	5.11	97.2	0.76	0.093
	Additional (R) (15.24%)	isonicotinate bridge + HgCl₂ (NC₆O₂H₄HgCl₂)	41.67	393.6	2.19	0.435
D	/	**[NH₂(allyl)₂] [Cr₇NiF₈(O₂CᵗBu)₁₅ (O₂CC₅H₄N-HgI₂)]**	16.41	2765	1.53	0.194
	Core (20.78%)	Cr₇NiF₈	20.39	574.7	1.53*	0.232
	Ligand (R) (54.86%)	pivalate (O₂C₅H₉)	5.76	101.1	0.90	0.098
	Counter-Ion (X) (3.51%)	diallylammonium (NC₆H₁₁)	5.11	97.2	0.76	0.093
	Additional (R) (20.85%)	isonicotinate bridge + HgI₂ (NC₆O₂H₄HgI₂)	49.86	576.5	2.57	0.514

Table 3.1 *Continued*
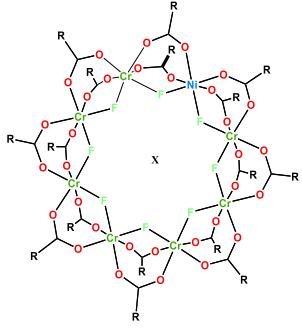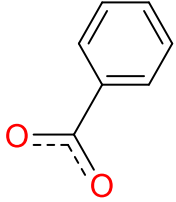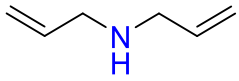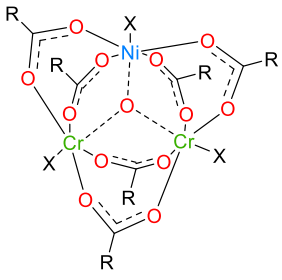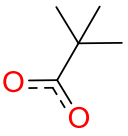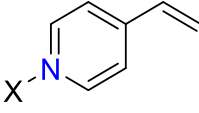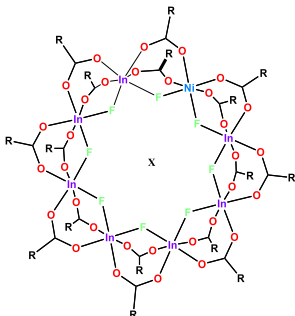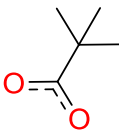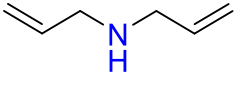
E	/	**[NH$_2$(allyl)$_2$]** **[Cr$_7$NiF$_8$(C$_6$H$_5$COO)$_{16}$]**	8.95	2610	1.10	0.126
	Core (22.02%)	Cr$_7$NiF$_8$	20.39	574.7	1.10	0.232
	Ligand (R) (74.26%)	benzoate (O$_2$C$_6$H$_5$)	6.12	121.1	1.08	0.101
	Counter-Ion (X) (3.72%)	diallylammonium (NC$_6$H$_{11}$)	5.11	97.2	0.763	0.093
F	/	**[Cr$_2$NiO(O$_2$C^{t}Bu)$_6$ (VinPyr)$_3$]**	8.29	1101	1.14	0.120
	Core (16.23%)	Cr$_2$NiO	23.81	178.7	1.14*	0.264
	Ligand (R) (55.12%)	pivalate (O$_2$C$_5$H$_9$)	5.76	101.1	0.903	0.098

Table 3.1 *Continued*

	Additional (X) (28.65%)	vinylpyridine ($C_7H_7N_1$)	5.50	105.1	0.975	0.096
G	/	**[NH₂(allyl)₂]** **[In₇NiF₈(O₂CᵗBu)₁₆]**	17.13	2730	1.51	0.201
	Core (37.16%)	In₇NiF₈	41.17	1014.4	1.51*	0.372
	Ligand (R) (59.28%)	pivalate ($O_2C_5H_9$)	5.76	101.1	0.903	0.098
	Counter-Ion (X) (3.56%)	diallylammonium (NC_6H_{11})	5.11	97.2	0.763	0.093

3.4 Results: Electron Scattering Simulations

Before any lithography or experimentation was carried out on any resist material they had to be simulated. The resists **A** – **G** were all developed using simulation before synthesis and all were chosen as they demonstrate chemical traits that raise their exposure to sensitivity compared to the starting resist **A**. To properly compare the materials using results from EXCALIBUR they had to be simulated in the same conditions and paramters in the simulation environment. Each resist was simulated as a 50 nm layer on a 50 nm Si layer. In real world conditions the silicon wafer substrate is 525 μm thick however in the simulation 50 nm of silicon is thick enough to simulate the resist-substrate interface and

any SE exposure from the Si back into the resist within a focus on the close proximity of the exposure area. At this point the doses required to expose the materials is an unknown quantity therefore to keep the exposure consisitent and comparable, an arbritary dose of 5000 pC/cm was used. This dose equates to an input of 12,500 PEs and the energy of these electrons was 30 keV which matches the 30 kV accelaration voltage of the equipment used for the lithography of these resists.

Using these parameters, the electron trajectory plots shown in Figure **3.6** were generated. Each pair of figures shows the trajectories of the PEs and SEs in each resist as well as the corresponding energy deposit plot. Viewing both of these plots side by side allows insight into not just the spatial distribution of the electrons in the simulation but also the energy that these electrons are transferring into the resist as they travel thorough and collide with the molecules in the resist.

Following the evolutionary sequence laid out in the previous section, comparing **A** (Figure **3.6.a&h**) with **B** (Figure **3.6.b&i**) shows the effect of adding the diallylammonium to the resist. It is clear in the trajectory plots that there is an increase in scattering and this is consistent with an increase in energy being deposited in the the resist outside of the PE beam. This shows that the alkene bonds from the diallylammonium and the slight increase in density have increased the number of SEs generated by **B** despite the reduction in Z_{eff} and the the increase in the molecular weight which as per Figure **3.3**. Similarly, **C** (Figure **3.6.c&j**) and **D** Figure (Figure **3.6.d&k**) show a further increase SE generation and energy deposits in the resists, this shows the effect, on the molecule, of the addition of the mecrury salts. The addition of the mercury has given an increase in the overall Z_{eff} of the molecule as well as the density, which prove to be significant enough to discount the increase in the molecular weight. The mercury salt effectively acts as a local scattering point generating SEs that will scatter with nearby constiutents of the molecule breaking apart the pivalate ligands exposing the resist. Resist **E** (Figure

3.6.e&l) shows the expected decrease in SE generation which, the reduction in Z_{eff} and the density and an increase in the molecular weight, would suggest. This decrease in SE generation is caused by changing the ligand from pivalate to benzote to allow solubility in anisole, which increases the amount of organic material and thus outweighs the metallic core in the ring leading to the decrease in the Z_{eff}. The first departure from the chromium ring is the chromium triangle resist **F** (Figure **3.6.f&m**) This resist again shows an increase in SE generation when compared to resist **A** which is consistent with the large reduction in the molecular weight of the resist and also the addition of the alkene bonds via the vinylpyridine. Finally, resist **G** (Figure **3.6.g&n**) once again shows the expected increase in SE generation caused by the change from chromium to indium which gave the metallic core more prominence in the ring increasing the Z_{eff} and the density. However, this effect is somewhat tempered by the large increase in the molecular weight.
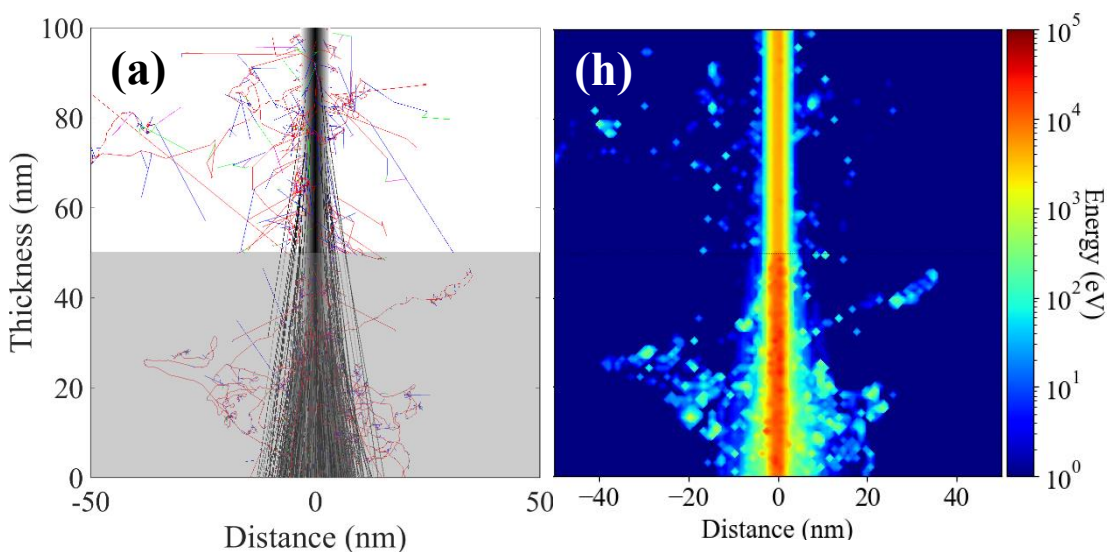
Figure 3.6 (*a-g*) *Electron trajectory plots for 50 nm of resists A-G on 50 nm of silicon exposed with a dose of 5000 pC/cm at 30 keV. This equates to 12,500 primary electrons input for the simulation. The colours of SEs are as follows gen I: red, gen II: blue, gen III: green & gen IV: magenta. Plotted using MATLAB (**h-n**). energy deposit plots of the electron trajectories. All simulations run using EXCALIBUR.*
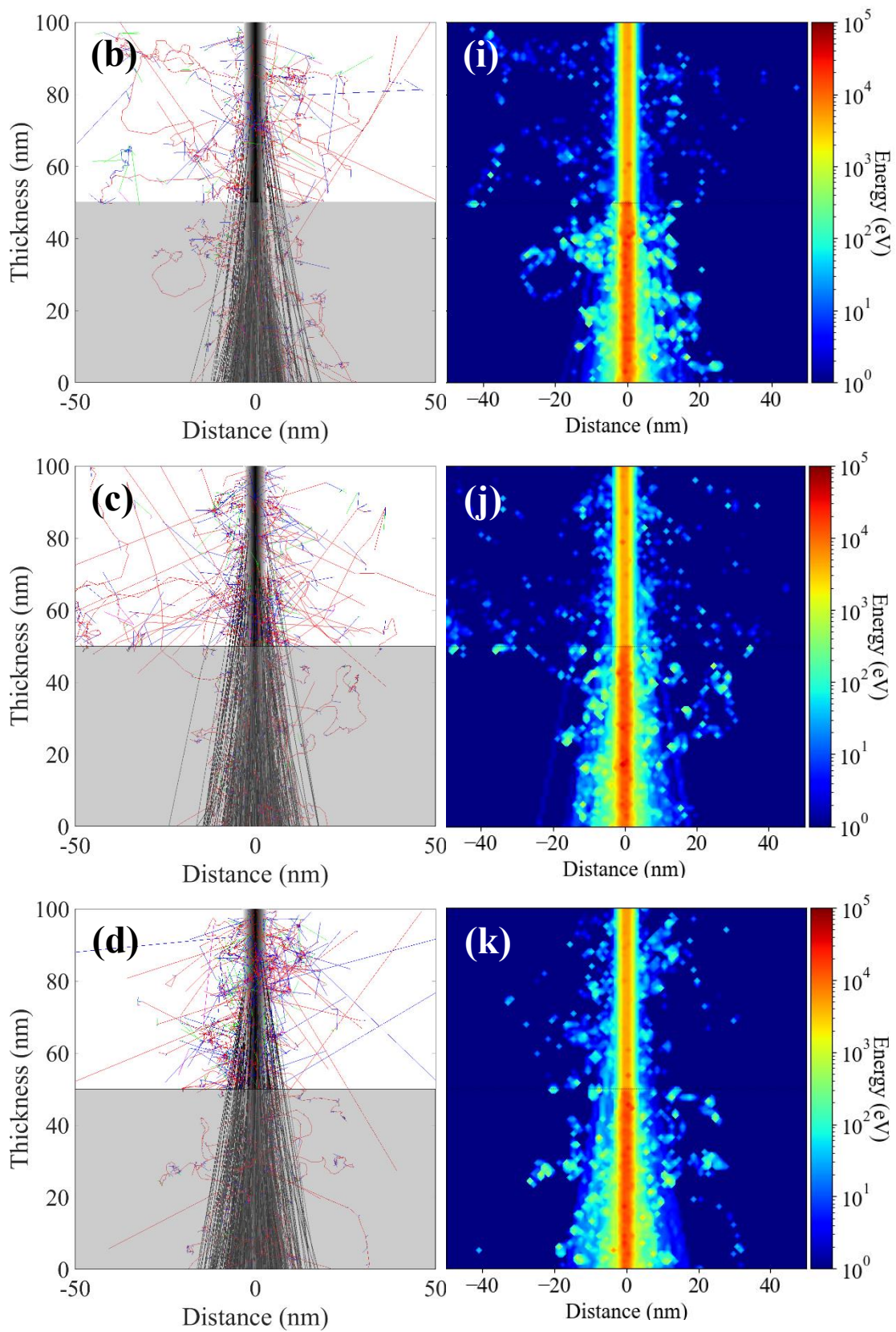
Figure 3.6 *continued*
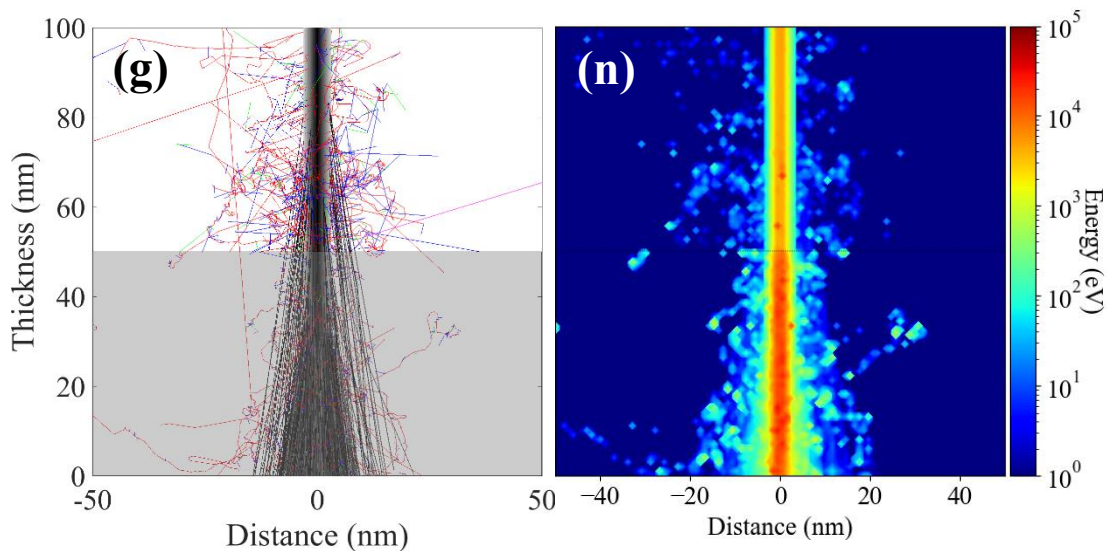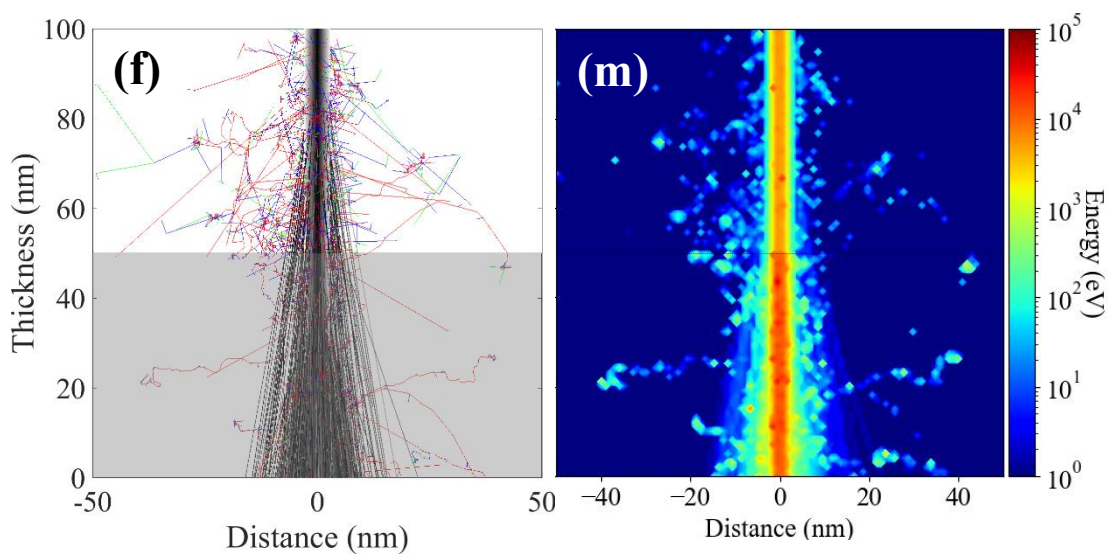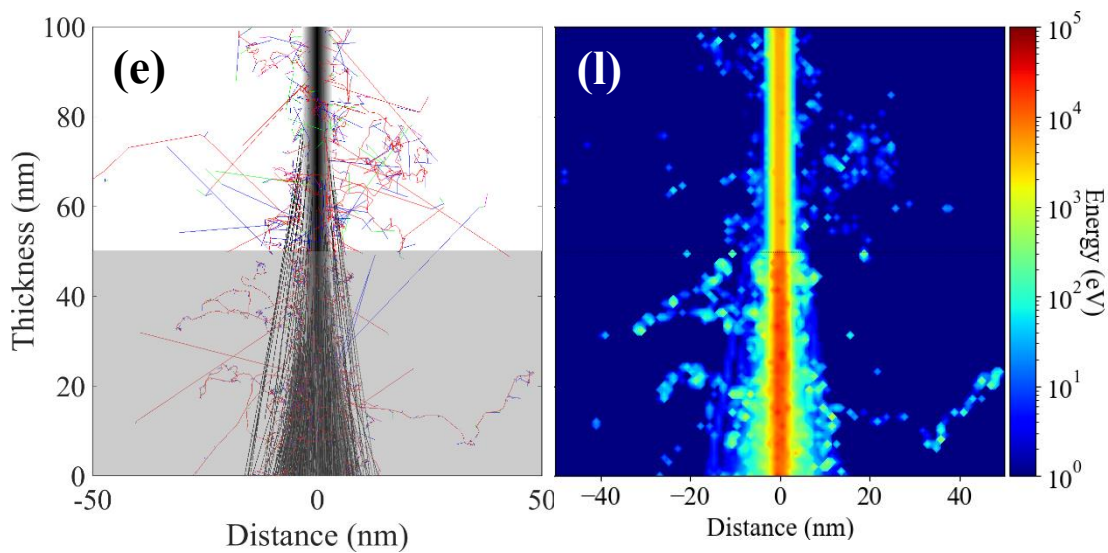
Figure 3.6 *continued*

Quantitatively, the effect of changes made for each resist are shown in Figure **3.7** where the number of SEs generated for a range of doses are compared for all the resists. This data is extracted directly from the model and consists of only the SEs generated in the resist ignoring those generated in the silicon substrate. To eliminate stochastic noise which is inherent when using Monte Carlo methods each simulation was run 200 times which reduced the statistical error to <1%. The dose here represents the number of incident PEs and considering these values and calculating the gradient of the line it is possible to calculate the number of SEs generated per PE or the SE yield. Here it is predicted that resist **D** will have the largest number of secondary electrons generated. If this corresponds directly to sensitivity, then **D** should have the lowest dose.
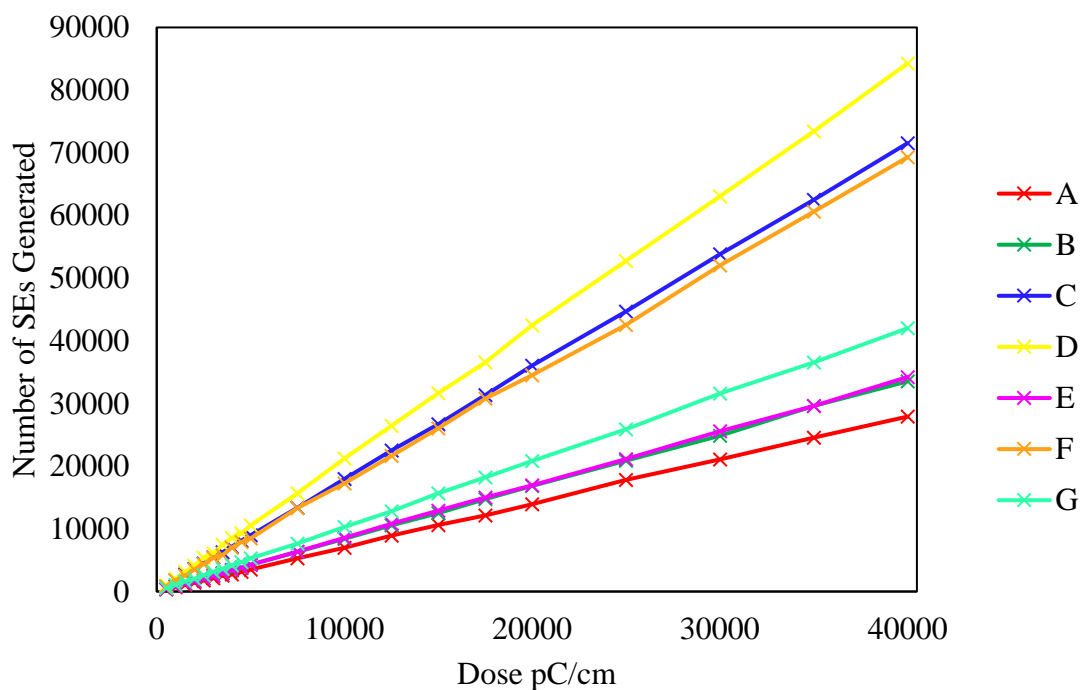
Figure 3.7 *Simulated number of SEs generated for a dose sweep for resists A – G. All resist were simulated as 50 nm thick layers with a 30 keV beam energy. The simulations were repeated 200 times to minimise error.*

The SE yields for the resists calculated from the gradients are given in Table **3.2**. Also shown in the table is the ratio of the yield for each resist compared to the yield for resist **B**. Despite **A** being the starting point upon which most of these resists are based, **B** is

chemically the most similar with only one change needed to get all other resists (apart from **F**).

Table 3.2 *A table of gradients of Figure **3.6** which represent the SE yield (γ) per PE. Also, the ratio of the SE yield compared to the SE yield of resist **B**.*

Resist	A	B	C	D	E	F	G
γ	0.28	0.33	0.72	0.84	0.34	0.69	0.42
γ/γ_B	0.83	1	2.14	2.51	1.02	2.06	1.25

============================= **NOTE** =============================

*As resists **C, D, E & G** all have similar structure and include the diallylammonium cation, they can all be considered as evolutions of resist **B** and for this reason it is used as the benchmark for comparison. This is the reason that the simulated SE yields in Table **3.2** are ratioed with **B**.*

==

3.5 <u>Results: Sensitivity and Resolution Characterisation</u>

Resists **A - G** were exposed using electron beam lithography. To keep the comparison between results sensible each resist was processed in the same manner using the same spin conditions and exposure parameters. To determine the dose of the resist a pattern was used that consisted of sets of 10 lines with each set increasing in dose factor. It can be assumed that if a pitch is not included in the results, then the lines weren't fully resolved, where either no individual lines can be identified or there was an overwhelming number of defects and bridging between the lines, which would not be viable for lithography.

The way the test pattern is designed means the best resolved lines exist on the threshold of exposure. Below this dose, the lines will be unresolved and above this dose, the lines will be properly exposed until they are overexposed. This means that often the imaged sets of lines may have lines missing, where underdosed lines have collapsed and

have not adhered to the substrate, subsequently being washed away in the developing solvent, thus showing the minimum exposure dose has been found. There will be some additional background exposure due to the proximity effect increasing the overall exposure of a set of lines. Therefore, the doses measured are the lowest doses achievable for the pitch.

The first molecule, **A**, has good solubility in a range of solvents including hexane and tert-butyl methyl ether (tBME) due to the pivalate ligands surrounding its metal core. For spin coating tBME was used as the casting solvent with a concentration of 15mg of **A** in 1 g of solvent giving 100 nm thick films at 8000 rpm. The resist was soft baked to remove the excess solvent at 100°C for 2 minutes. Due to the volatility of tBME, it has a very low boiling point of 55.2°C [15], most of the solvent will evaporate during spin coating. Figure **3.8** shows the SEM images of exposed single pixel lines in resist **A**. The lines show the minimum exposure doses for the resist at pitches of 60-100 nm. 60nm pitch was the lowest pitch resolved for this experiment using the Zeiss Sigma SEM. The structures show the resist has good resolution at a 30kV exposure voltage however the dose of 28,000 pC/cm at 60 nm pitch is very high compared to commercial negative tone EBL resists (Chapter 1.3). As expected, this puts this resist outside the target zone in the trade-off triangle (Figure **3.1**) but provides a starting point as a high-resolution, high dose, type resist.

100 nm Pitch
Dose: 22,000 pC/m

90 nm Pitch
Dose: 22,000 pC/m

80 nm Pitch
Dose: 24,000 pC/m

70 nm Pitch
Dose: 26,000 pC/m

60 nm Pitch
Dose: 28,000 pC/m

100 nm
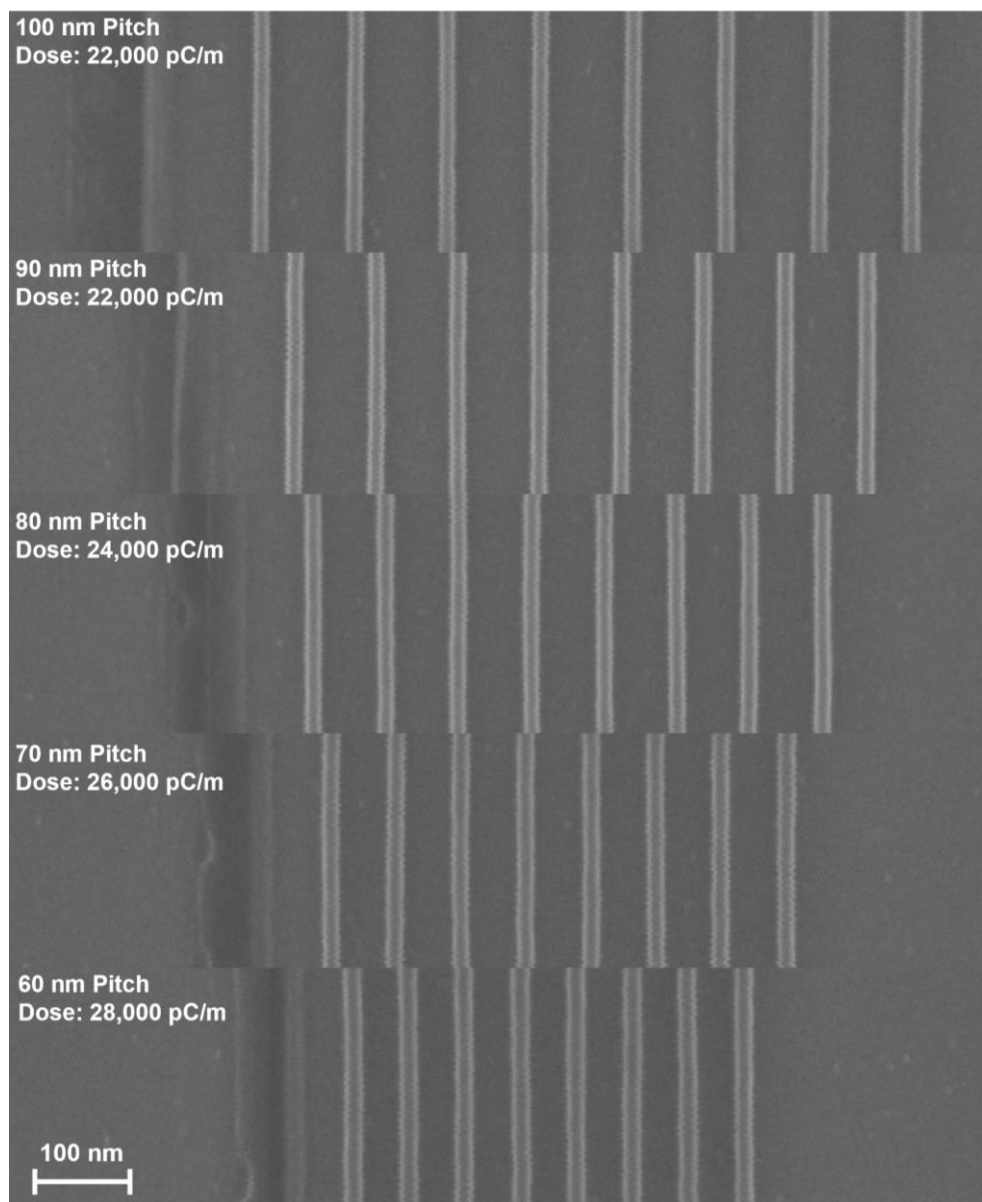
Figure 3.8 *An SEM micrograph lines patterns for pitches of 100 - 60 nm fabricated in resist **A**. All patterns were exposed with an acceleration voltage of 30 kV and a step size of 2 nm. The structures were developed in hexane for 10 seconds.*

As with resist **A**, resist **B** also has pivalate ligands and therefore it has similar processing properties. For spin coating the casting solvent was tBME and the films were spun to a thickness of 100nm at 8000 rpm from a solution of 15mg **B** in 1g tBME. A soft bake of 100°C for 2 minutes was used. The samples were written using an acceleration voltage of 30keV and a beam current of 40pA and then developed in hexane for 10 seconds before being blown dry with dry compressed air. Figure **3.9** shows the minimum exposure doses

for line structures in resist **B** at pitches of 50-100 nm. 50nm pitch was the lowest pitch
resolved for this experiment with a dose 10,000 pC/cm.

Figure 3.9 *An SEM micrograph lines patterns for pitches of 100 - 50 nm fabricated in*

resist B. All patterns were exposed with an acceleration voltage of 30 kV and a step size

of 2 nm. The structures were developed in hexane for 10 seconds.

It can be seen from the lithographic and simulation results which are compared in Figure **3.10**, that adding the diallylammonium had a large overall effect on the sensitivity of the resist decreasing the required exposure dose by an average of 3.1 for all pitches. The generation of secondary electrons can be assumed to be a direct indicator of resist exposure as it is the inelastic collisions that generate these SEs that are breaking the bonds in the resist and rendering it insoluble. The results of the simulation show a predicted increase in SE yield of only 1.2 for B compared to A. However, when the recorded experimental doses are used as input for simulation then there is a decrease in the total number of SEs generated by a factor of 2.6. Logically, this makes sense as a resist with a higher sensitivity should need a lower number of electrons to expose it. The effect of adding of the diallylammonium is that it has changed the density and the weight ratios of the ligand and the core when considered in the simulation (Table **3.1**). Additionally, increasing the density has increased the secondary electron generation in **B** leading to lower exposure doses. The alkenes on the diallylammonium also decreased the required exposure dose as when they are struck by an incident electron, they generate an additional secondary electron when the bond is broken. This increase in sensitivity compared to resist **A** (Figure **3.6**) has not resulted in a significant increase in the line width of the resolved structures. This is a success and an important step in understanding the essential function of the counter ion in the molecule and hence how it can influence further developments in modular resists.

Figure 3.10 *A plot of comparison of doses and simulated SE generation at these doses for resist* ***B*** *compared to* ***A***. *The simulation data is the average of 200 runs to minimise the error.*

Following on from the successful addition of the diallylammonium to the ring resists **C** and **D** were investigated. Once again, these molecules have similar chemistry to resist **A**, however, due to the substitution of the mercury salts, their solubility is considerably reduced. This enforced a practical limit on the number of ligands that could be substituted without impeding the solubility of the resist in the casting solvent. For spin coating, 15 mg of **C** was dissolved in 1 g tBME and produced 70 nm films at 8000 rpm. The decreased thickness is due to the increased molecular weight of the material, therefore decreasing the concentration of the resist solution. For the exposure, the resist was exposed using a 30 KeV beam energy and a current of 40pA. Once exposed, the sample was developed in hexane for 20 s to account for the reduced solubility and blown dry using dry compressed air. Resist **D** was cast in tBME with a concentration of 15 mg in 1g of solvent and spun at 8000 rpm to produce films with a thickness of 65 nm. The resist was then exposed in the Zeiss Sigma SEM using a 30KeV beam energy and a beam current of 40pA. After

exposure, the resist was then developed in hexane for 30 seconds to make sure all the remaining resist was removed and was then blown dry.

Figure **3.11** shows the exposure results for resist **C**. As previously explained, this is the minimum dose needed to produce uninterrupted structures and due to this some of the lines in the set may be collapsed. The micrographs show that 60 nm pitch was achieved with a dose of 3000 pC/cm.
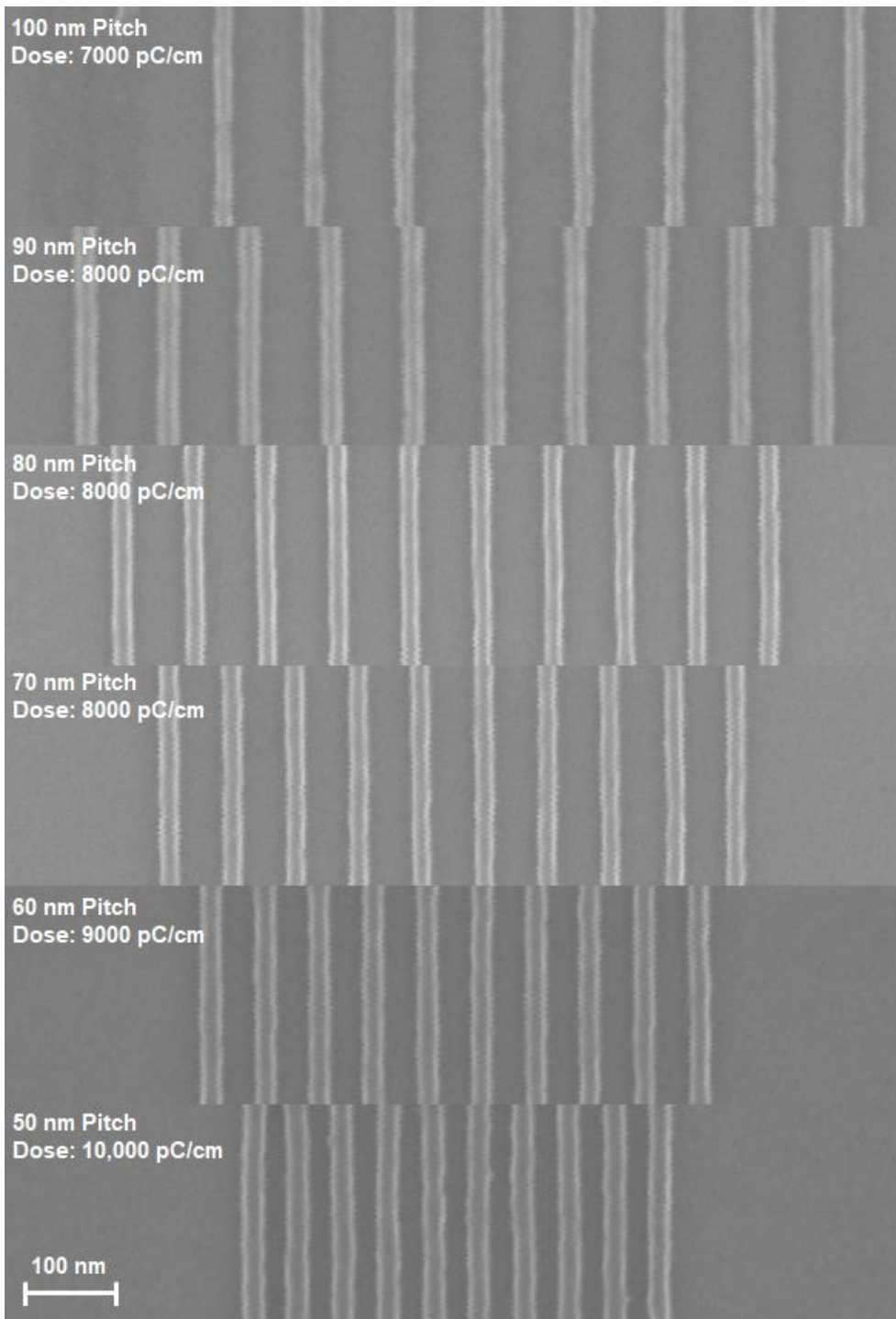

Figure 3.11 *An SEM micrograph lines patterns for pitches of 100 - 60 nm fabricated in resist **C**. All patterns were exposed with an acceleration voltage of 30 kV and a step size of 2 nm. The structures were developed in hexane for 30 seconds.*

Compared to resist **B** there has been a reduction of dose by a factor of 2.99 and once again the quality of lithography is consistent. Although 50 nm pitch was not resolved, these results are still of a good standard and the losses are offset by the greatly increased sensitivity and reduced dose.

Shown in Figure **3.12** are the SEM micrographs of the developed structure for resist **D**. As with **C**, the dose has been further reduced while still maintaining the quality of the lithography with 60 nm pitch being resolved at a dose of 2700 pC/cm. The reduction in dose for **D** compared to **C** is due to the additional mass provided by the iodines attached to the mercury. Additionally, the reduced solubility in the developing solvent means that the resist needs less exposure to become fully insoluble in the developer to the point where structures can be formed. The dose decrease from B to D was 3.17, which again shows the effect of the addition of the heavy mercury salt.

Figure 3.12 *An SEM micrograph lines patterns for pitches of 100 - 60 nm fabricated in resist **D**. All patterns were exposed with an acceleration voltage of 30 kV and a step size of 2 nm. The structures were developed in hexane for 30 seconds.*

In the interest of brevity and due to both **C** and **D** introducing similar mechanics the simulation results have been collated in Figure **3.13**. Here the doses from experimentation and the SE generation from simulation are compared to resist **B**. The results from experimentation show an increase in sensitivity from the addition of the $HgCl_2$ and HgI_2 being 2.99 and 3.17 respectively. This corresponds with the increase in SE yield of 2.14

and 2.51 with respect to **B**. However, as can be seen from Figure **3.13**, using the experimental doses as input for the simulation the number of SEs needed to expose the resist show that resist **D** requires more electrons to be fully exposed than resist **C**. However, these SEs are provided by the increase in secondary electron generators (the diallylammonium and the HgI_2) which shows some disconnect between the sensitivity of a resist to exposure and the SE yield.
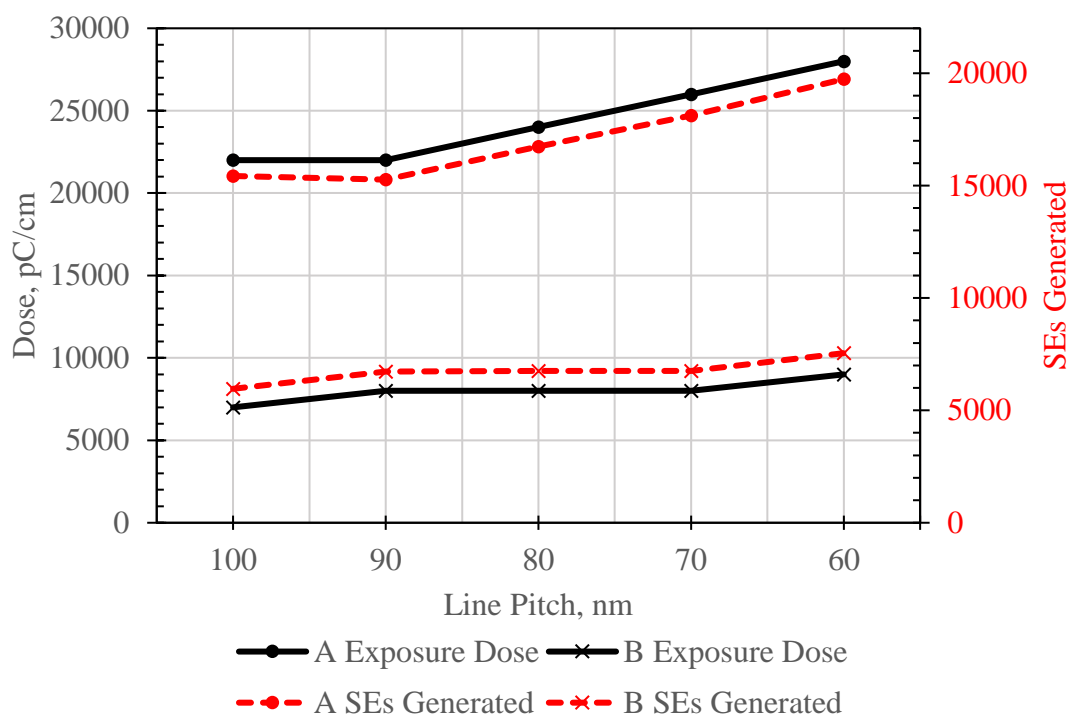

Figure 3.13 *A plot of comparison of doses and simulated SE generation at these doses for resist **C** and **D** compared to **B**. The simulation data is the average of 200 runs to minimise the error.*

As stated, the casting solvent for resist **E** was anisole and the concentration of the resist was 30 mg of **E** in 1 g of anisole. When spun at 4000 rpm this solution gave films with a thickness of 45 nm. As the boiling point of anisole was 153.8°C [16], the films were soft baked at 180°C for 2 mins to ensure all the casting solvent was fully evaporated. The resist was then exposed using the Zeiss Sigma at 30 KeV with a beam current of 42 pA. Anisole was used to develop the films post exposure with a development time of 30 seconds. Figure **3.14** shows the exposure results for **E**, which, as expected have greatly

increased doses compared to resist **B** with 40 nm pitch being resolved at a dose of 36,000 pC/cm. Due to the inclusion of the benzoate, the dose increased by a factor of 3.5 compared to when the pivalate ligand was used. This increase could be due to the change in developer due to the chemistry of the benzoate ligand, but the phenyl rings contained in this ligand will act as electron sinks blocking SEs from exposing the resist and reducing the dose [12, 13]. However, the results show excellent resolution and structure quality with the best resolution of the resists presented here.
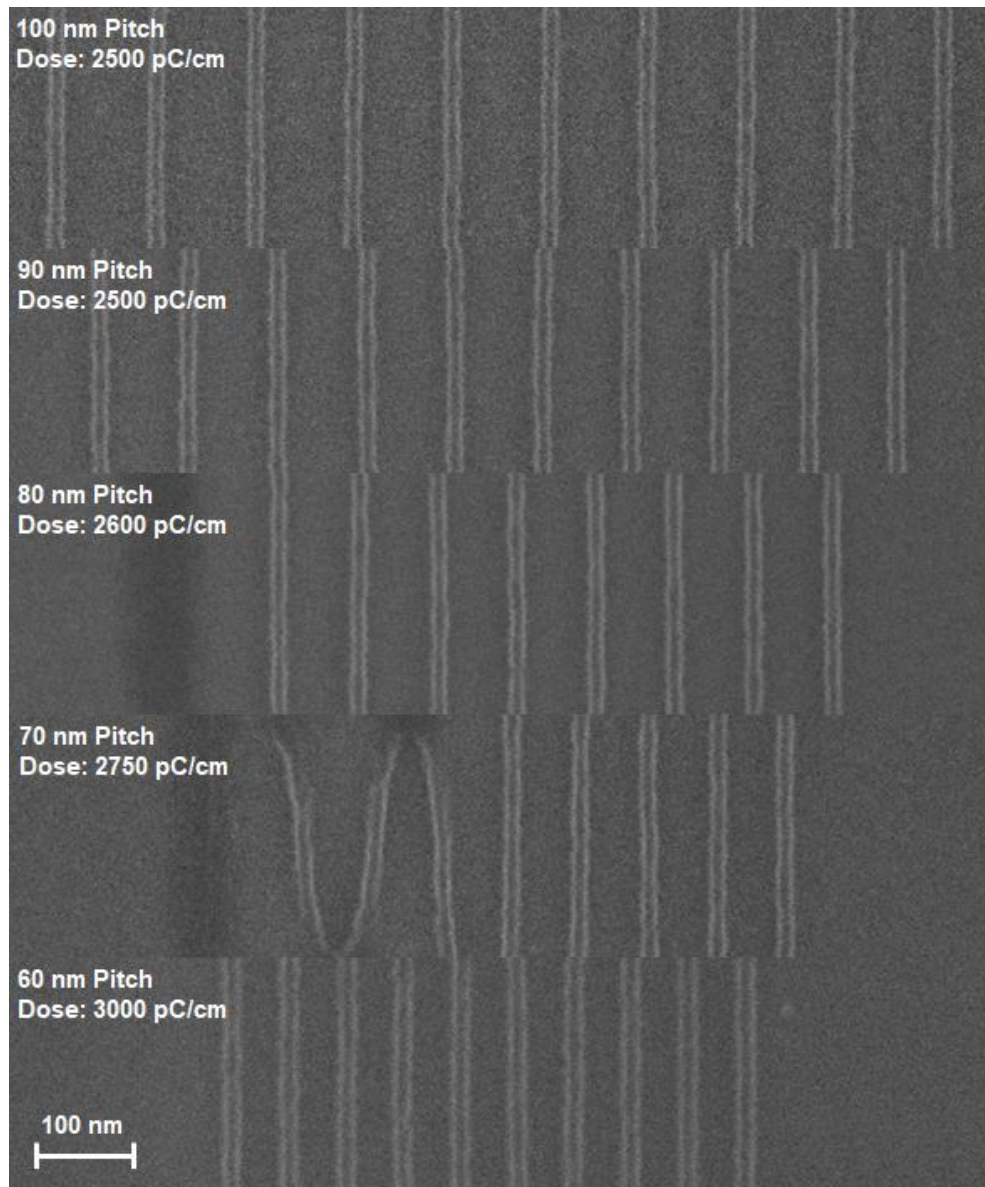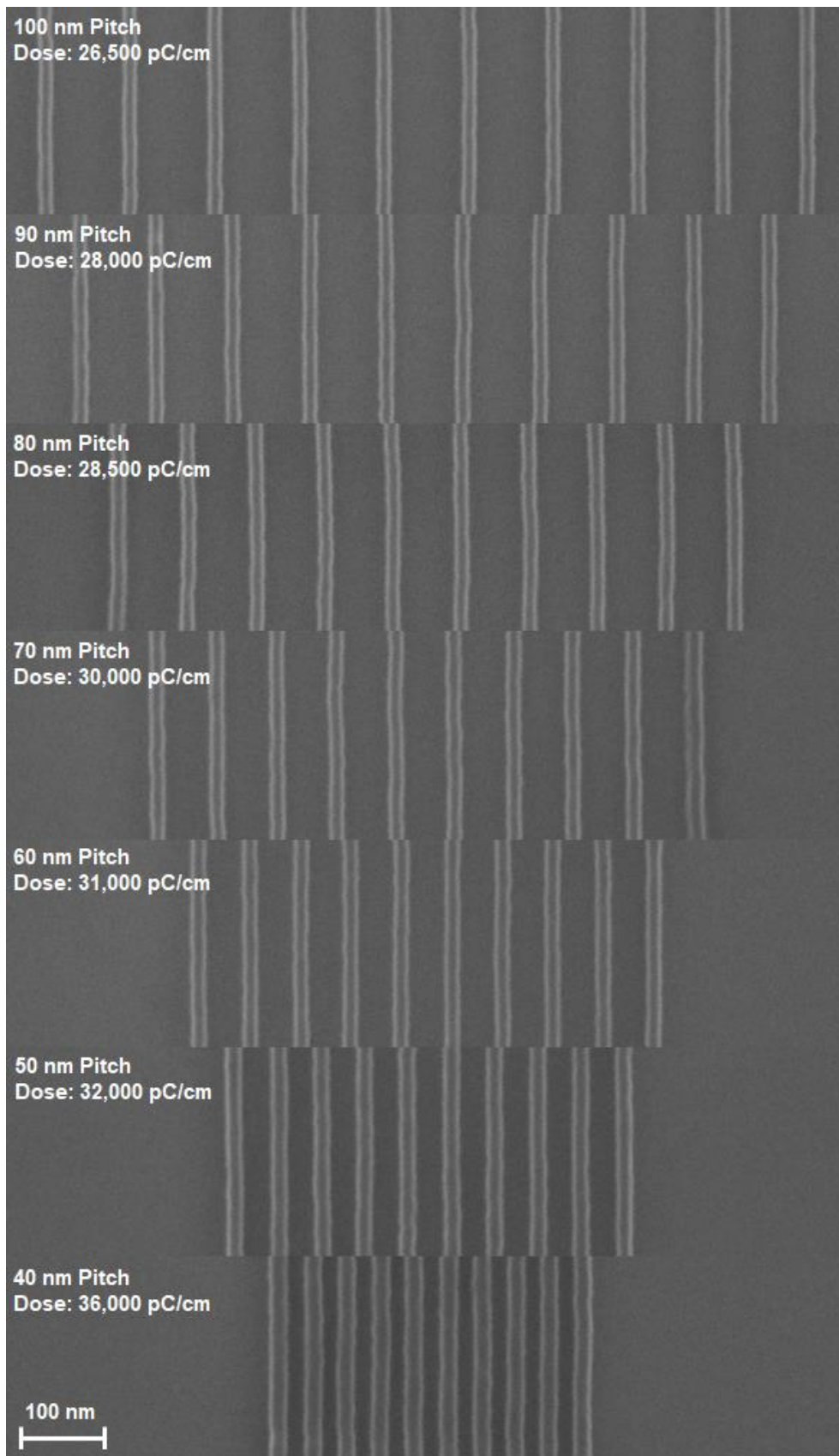
Figure 3.14 *An SEM micrograph lines patterns for pitches of 100 - 40 nm fabricated in resist **E**. All patterns were exposed with an acceleration voltage of 30 kV and a step size of 2 nm. The structures were developed in anisole for 30 seconds.*

The increase in dose predicted by the simulation compared to the experimental increase can be seen in Figure **3.15**. Here the model has underestimated the increase in dose as there was an increase in the SE yield in the model by a factor of 1.02 yet the dose does not reflect this. The reason for this discrepancy could be that the model does not account for the electron sink effect of the phenyl rings. Also, the simulation does not account for the change in developing solvents from hexane to anisole and therefore the effect of the resists solubility in the developer.
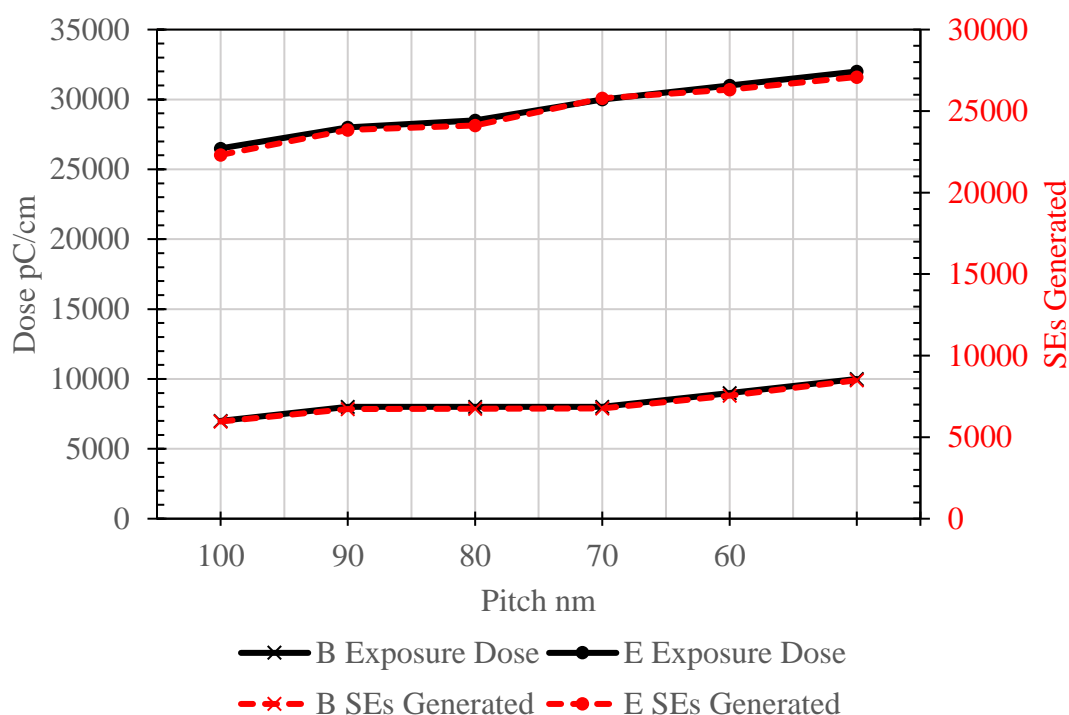
Figure 3.15 *A plot of comparison of doses and simulated SE generation at these doses for resist E compared to B. The simulation data is the average of 200 runs to minimise the error.*

For resist **F** the pivalate ligands that surround the triangle meant that this resist was soluble in tBME, however, its solubility was far lower than that of A - D with the concentration of 15 mg in 1g of solvent being near the saturation limit. As with the previous resists, F was exposed using a Zeiss Sigma with a beam energy of 30 KeV with a beam current of 40 pA. Figure **3.16** shows the results of exposing resist **F** and using hexane as the developer. As predicted, the reduction of the molecule size and the addition

of the vinyl pyridine caused an increase in sensitivity leading to the most sensitive chromium-based resist tested so far. A dose of 1450 pC/cm at 100 nm pitch meant a reduction in dose by a factor of 4.5 compared to resist **B** and a factor of 1.4 compared to resist **D** (the fastest chromium ring resist). Unfortunately, the quality of the lithography for this resist is poor with breaks in the structures. These breaks are undesirable as they will be transferred through into any device made using this resist. Also visible in the SEM micrographs is a scum layer which is not removed during developing.
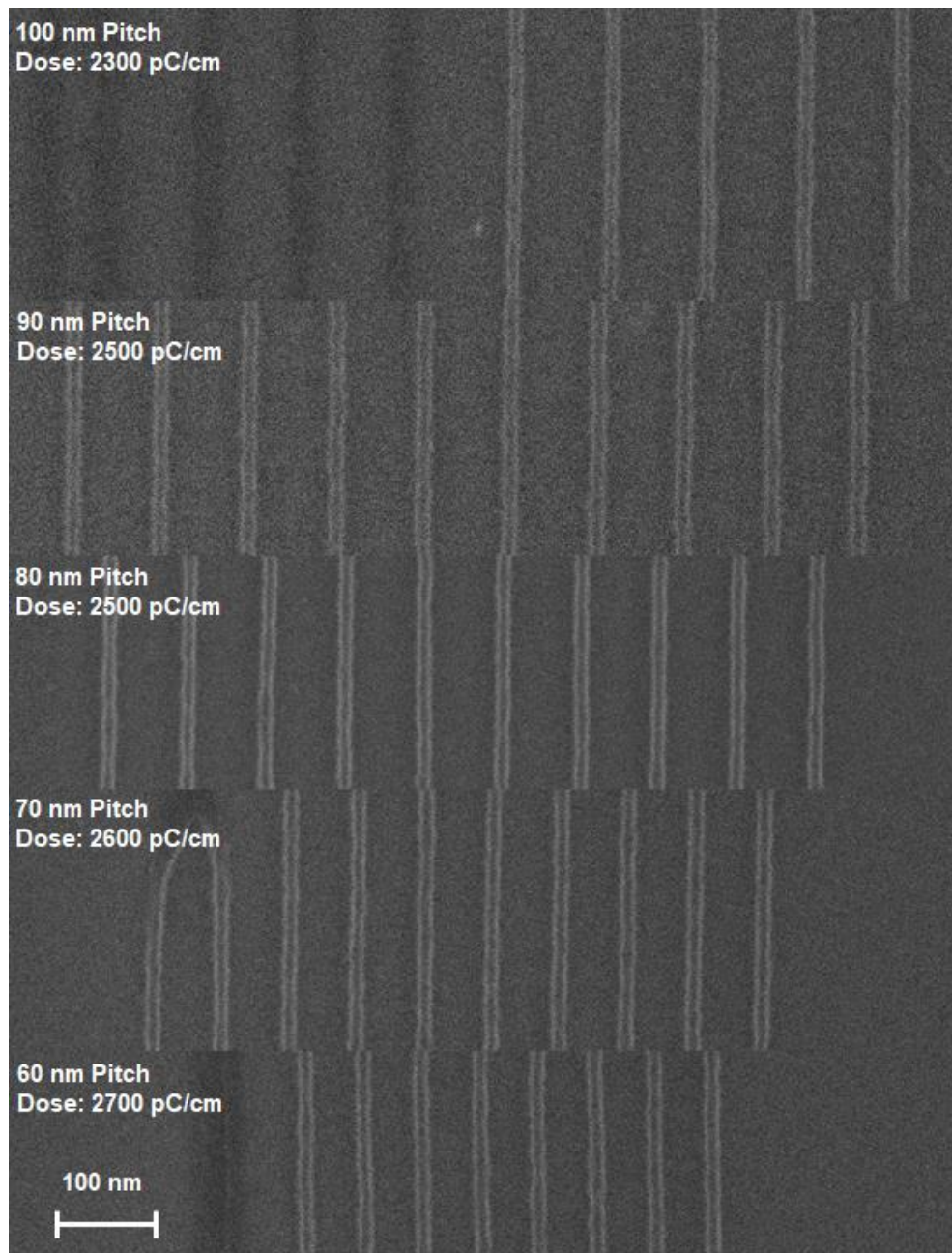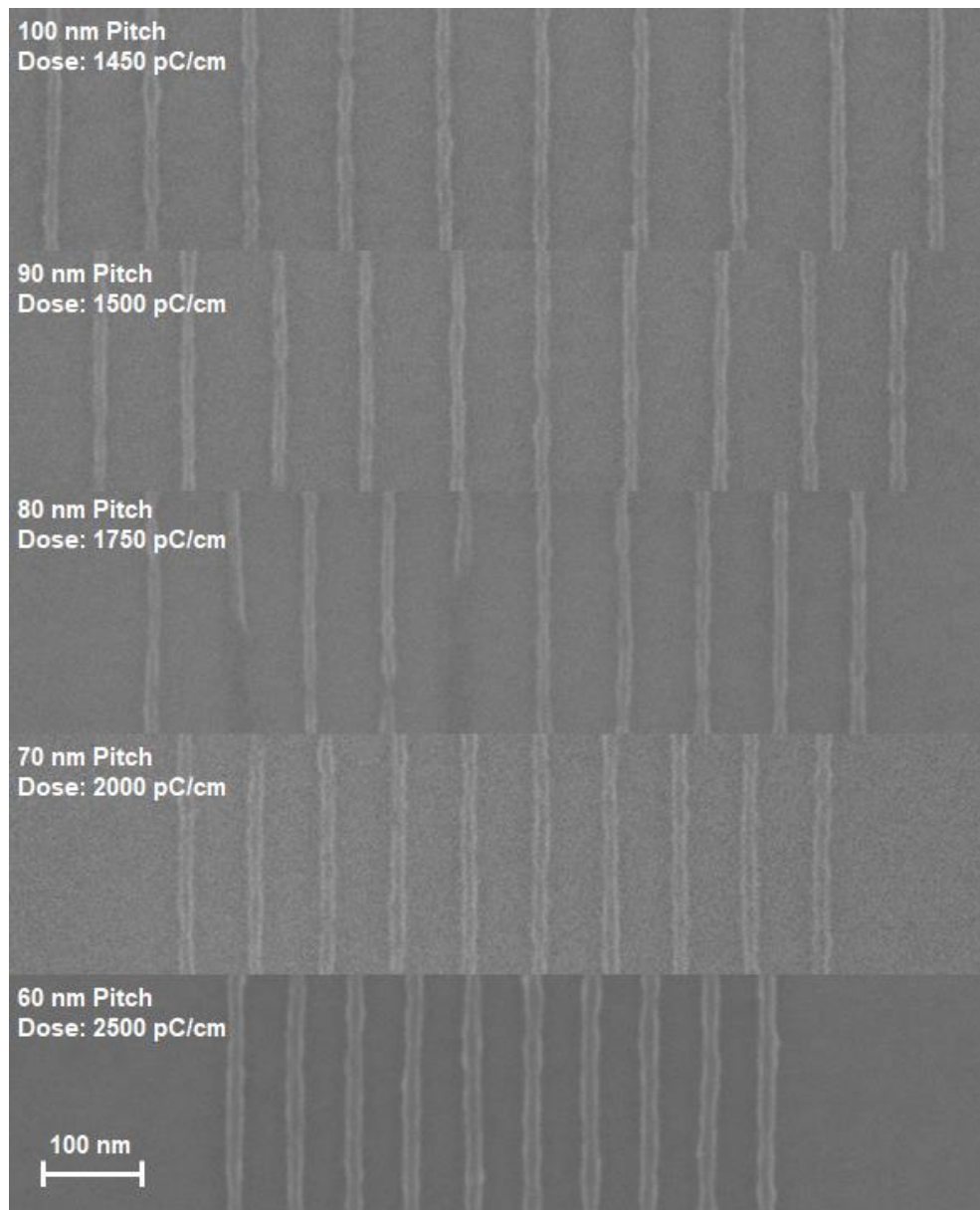
Figure 3.16 *An SEM micrograph lines patterns for pitches of 100 - 60 nm fabricated in resist **F**. All patterns were exposed with an acceleration voltage of 30 kV and a step size of 2 nm. The structures were developed in hexane for 30 seconds.*

To try and improve the quality of the structures another developer, propylene glycol methyl ether acetate (PGMEA) was used. Figure **3.17** shows the results when resist **F** was developed in PGMEA for 30 seconds.
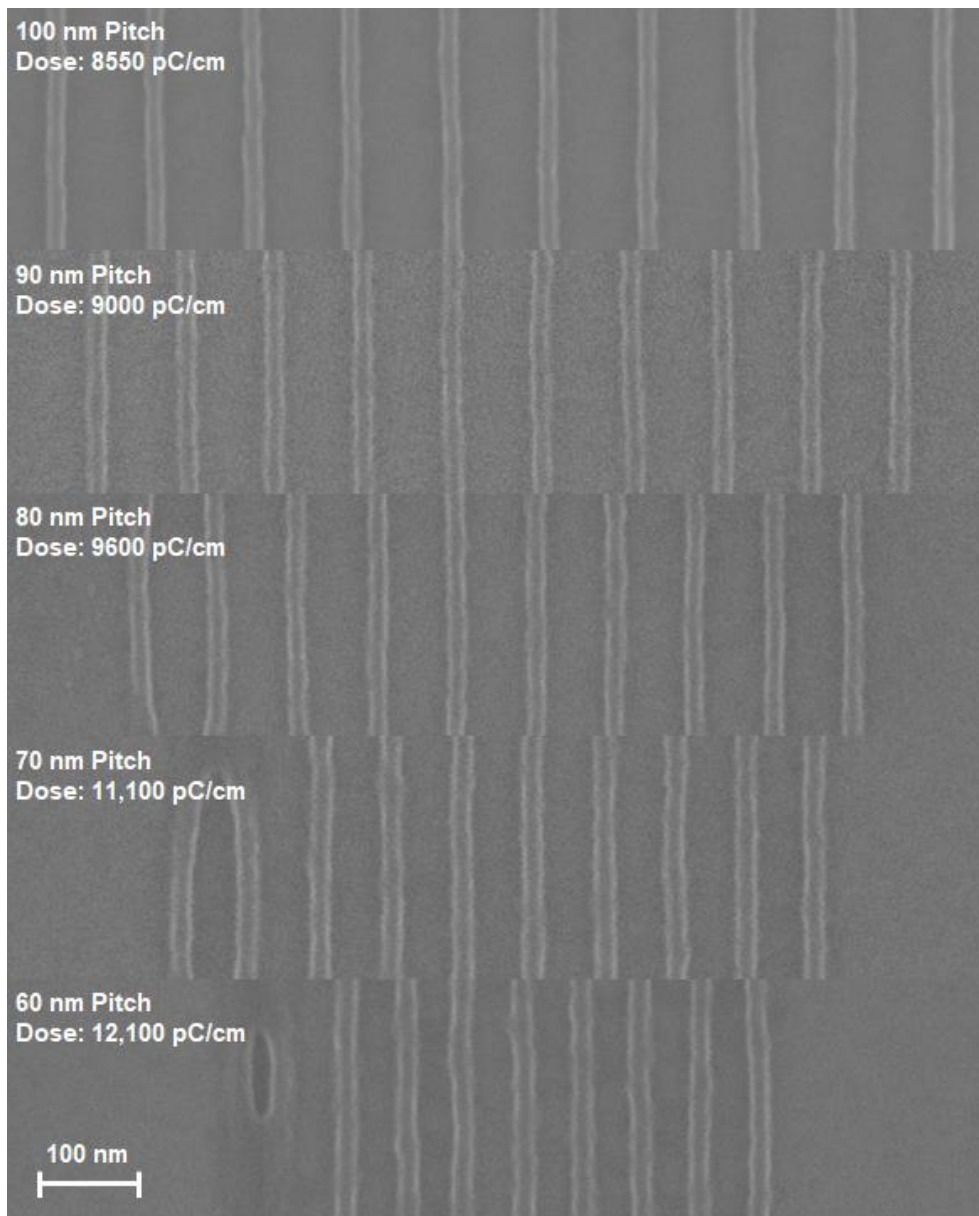
Figure 3.17 *A An SEM micrograph lines patterns for pitches of 100 - 60 nm fabricated in resist **F**. All patterns were exposed with an acceleration voltage of 30 kV and a step size of 2 nm. The structures were developed PGMEA for 30 seconds.*

Using this developer, instead of hexane, greatly increased the fidelity of the structures but increased the dose by 5.9 times to 8550 pC/cm at 100 nm pitch. The doses required with this developer are also 3.7 times slower than the fastest chromium ring resist which gave similar lithographic quality.

When the reduction in dose and the increase in SE yield are compared for this resist with respect to **B** in Figure **3.18**, it is found that despite a reduction in dose by a

factor of 4.5 the SE yield only increased by a factor of 2.06. The reduction in the SEs at the correct exposure dose shows a reduction by a factor of 2.12. This shows that the model has a weakness when comparing resists with large chemical differences and that whilst an increase in sensitivity can be predicted the accuracy is not reliable.
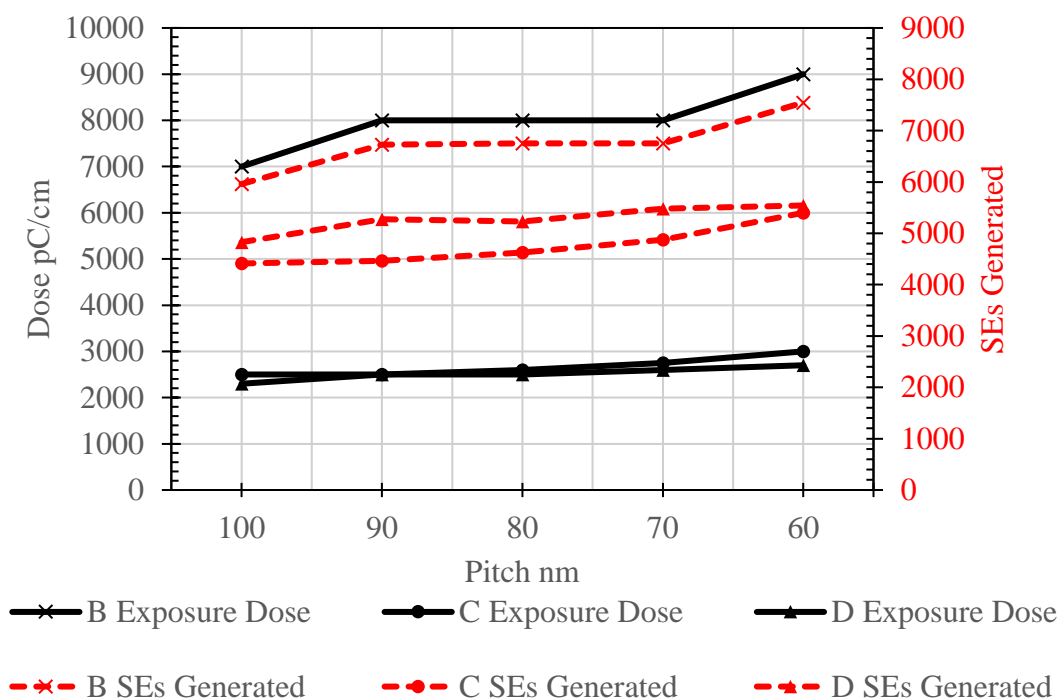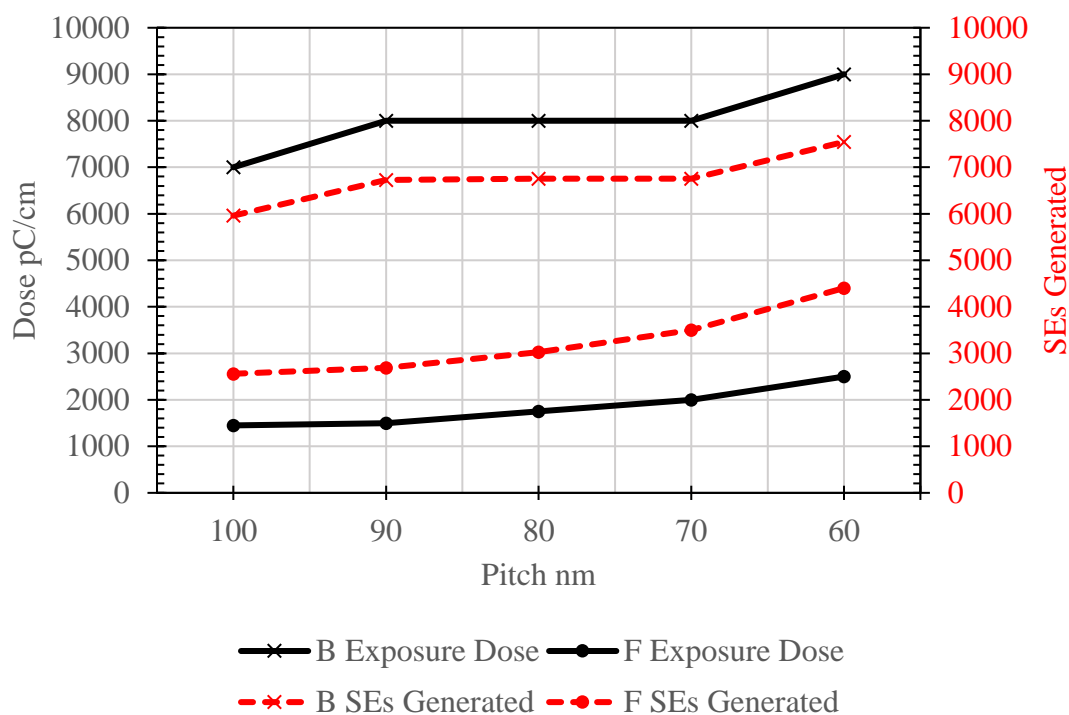

Figure 3.18 *A plot of comparison of doses and simulated SE generation at these doses for resist **F** compared to **B**. The simulation data is the average of 200 runs to minimise the error.*

Finally resist **G** was characterised. Due to it having the same pivalate ligand as **A** it exhibits very similar solubility in casting solvents and developers as well as similar spin properties. However, by replacing the chromium with indium the resist has become much more hydroscopic. To counter this, dry solvents were used as casting solvents to reduce the resists exposure to moisture in solution. Care had to be taken to reduce the exposure of this molecule to moisture and light which both caused decomposition of the resist in solution, leading to poor film quality and increased doses. For spin coating the resist was cast in dry hexane with a concentration of 15 mg of **G** in 1 g of dry hexane producing films with a thickness of 45 nm at a spin speed of 4000 rpm. Due to the thermal instability

of this resist, it cannot be baked after spin coating and so the casting solvent is removed in vacuum. The resist was exposed using 30 KeV beam energy and 39 pA using the LEO 1550 SEM. After exposure, the resist was developed using hexane for 10 seconds and then blown dry with dry compressed air. Figure **3.19** shows the developed indium ring structures. The doses for this resist are the best of any ring resist tested, having a dose of 1000 pC/cm which is 2.3 times lower than resist **D** at 100 nm. This resist was able to match the chromium ring for resolution achieving 50 nm pitch. The lines are very thin suggesting that with thinner films and using a 100 kV tool even lower pitches could be achieved. When compared to **B** the increase in sensitivity shows this resist is promising as the starting platform for a new resist family.
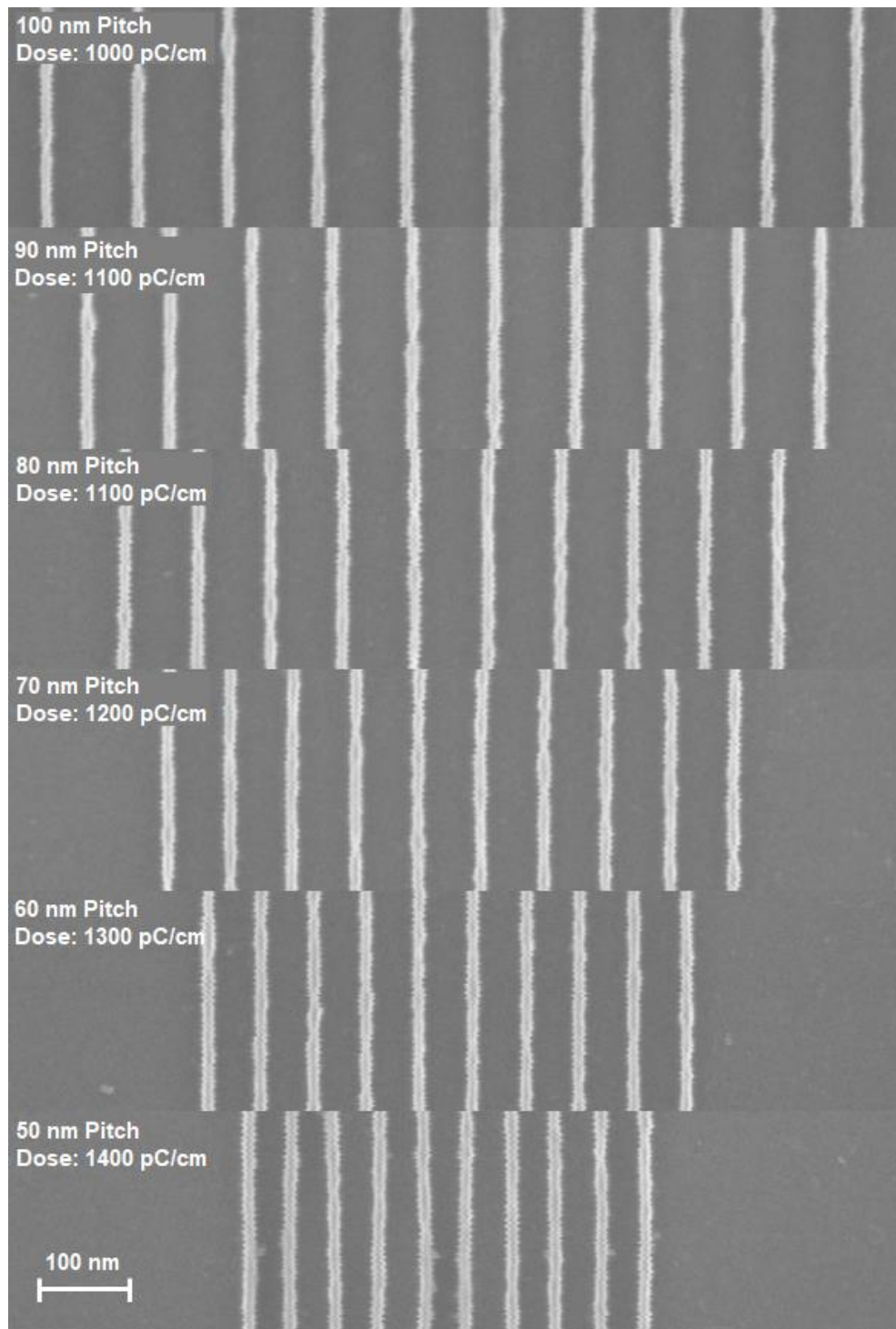
Figure 3.19 *An SEM micrograph lines patterns for pitches of 100 - 50 nm fabricated in resist **G**. All patterns were exposed with an acceleration voltage of 30 kV and a step size of 2 nm. The structures were developed in hexane for 10 seconds.*

When compared to resist **B** (Figure **3.20**) there was an average reduction in dose by a factor of 7.05 however there was only an increase in SE yield of 1.25 times. The average reduction in SEs at the correct exposure dose is 5.62. This shows that the sensitivity of

the resist does not only come from the effect of the change to indium on the Z_{eff} and the density but also the instability of the resist during processing to both moisture and temperature. This suggests that the sensitivity of a resist is not solely determined by the SE generation.
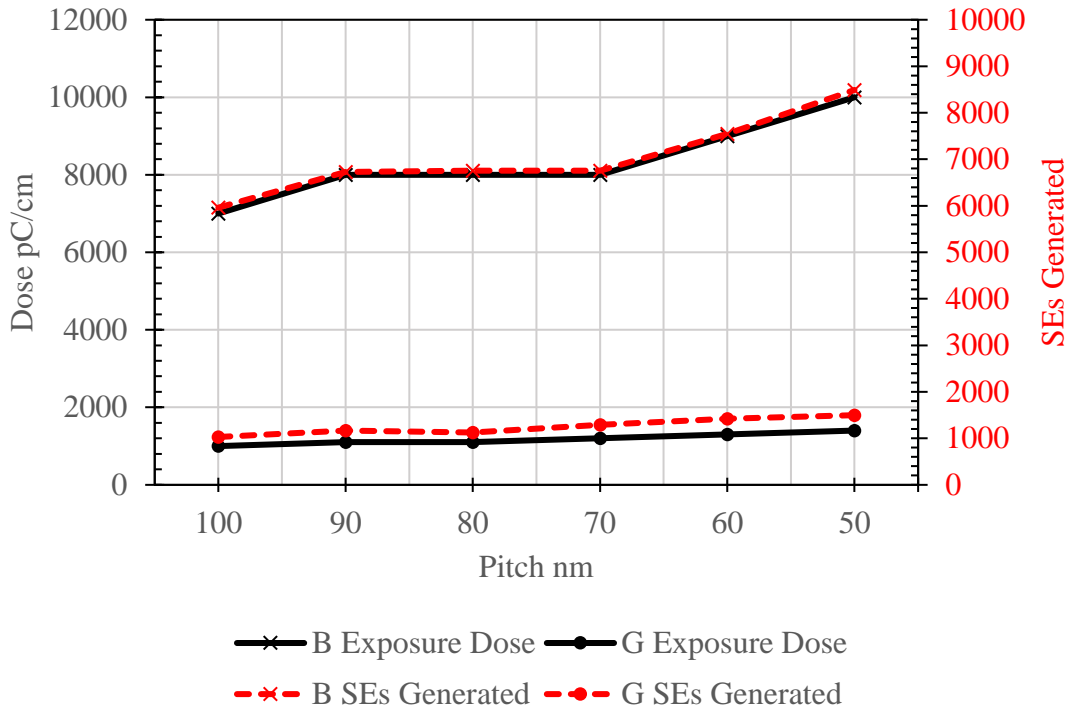
Figure 3.20 *A plot of comparison of doses and simulated SE generation at these doses for resist **G** compared to **B**. The simulation data is the average of 200 runs to minimise the error.*

Figure **3.21** shows a comparison of the doses for all the resists tested. It is clear to see that there is a near constant reduction in dose throughout the development of these new resists culminating with the development of the indium ring-based resist **G**.
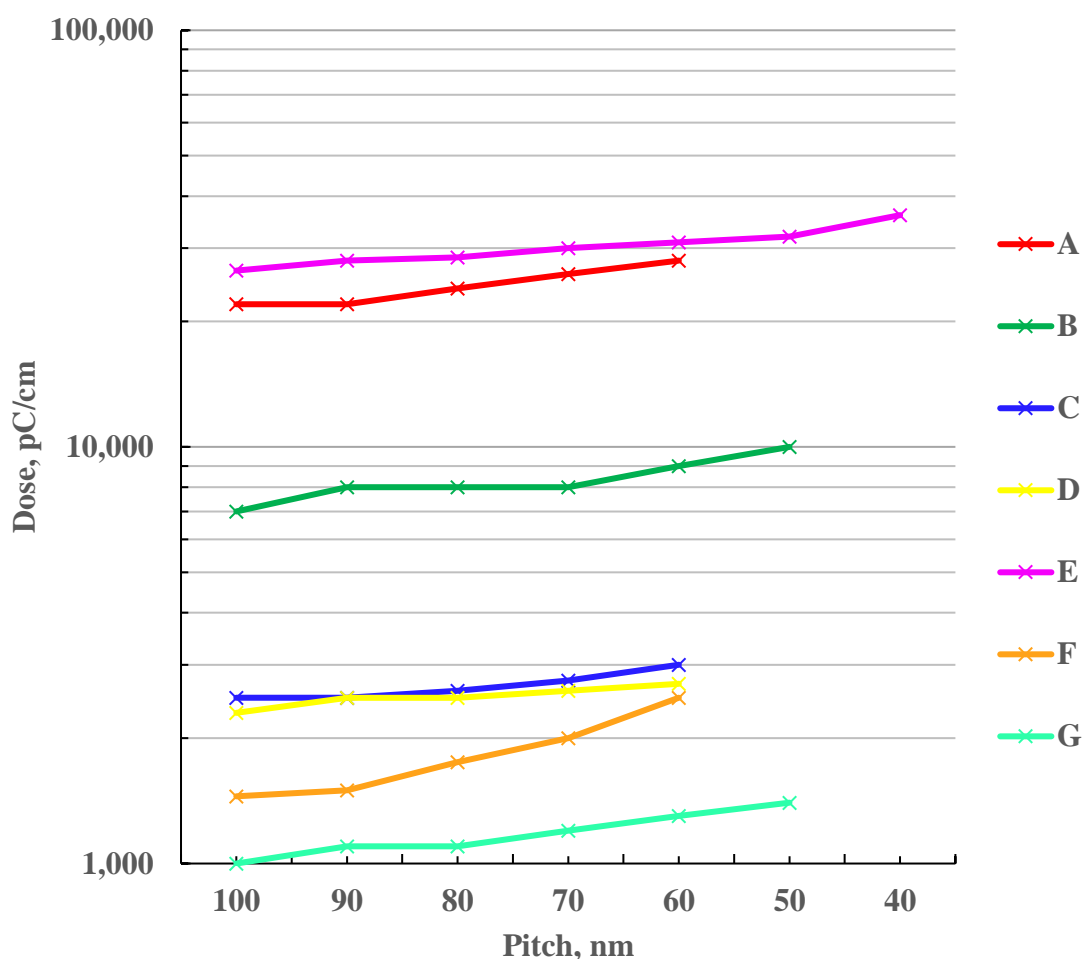
Figure 3.21 *A comparison plot of the doses for all modular resists **A** – **G** for all*

resolved pitches.

3.6 Results: What is Left Behind? - XPS Analysis

To better understand the exposure mechanics for the metal-organic supramolecular resists, X-ray photoelectron spectroscopy (XPS) was used to analyse the resist's chemical composition before and after exposure. By looking at the shifts in the peaks of the spectra, some approximations can be made about how the structures of the molecules are changing when being exposed. For the XPS analysis the near-ambient pressure X-ray photoelectron spectroscopy (NAP-XPS) system, at the Photon Science Institute at the University of Manchester, was used. Films of resist **D** were spun using the same parameters given in section **3.3.1**. As XPS would be able to probe the top 5 nm of the resist film, it was important that the films should be thick enough to ensure that the silicon substrate could

not be detected. As an analogue to exposure in an electron beam system, the resist was exposed using an electron gun used for Low-energy electron diffraction (LEED). The acceleration voltage for the LEED gun was only 750 V and the stage was biased to 250 V giving a total beam energy of 1 keV, but as the size or dose of exposure was not important to this experiment, this was not a concern.

Figure **3.22** shows the spectra for resist **D** with the black data showing unexposed resist and the red data showing exposed resist. For calibration, and so that they could be compared, the two data sets were normalised with respect to the carbon 1S peak. As can been seen in the enlarged subfigure of the carbon 1S peak, the main peak is relatively unchanged, however the side peak has been reduced. This side peak represents the O-C=O which is the carboxyl group responsible for connecting all ligands onto the metallic ring. Therefore, it can be inferred that, by breaking down these carboxylate bonds and removing ligands from the ring the solubility would be reduced. The breakdown of these ligands forms a CO and CO_2 gas mixture which diffuse out of the resist and is then removed from the vacuum via the pumps. This allows the formation of insoluble structures through exposure. This agrees with the hypothesised reduction in solubility of the rings with the removal of the ligands and matches observations where replacement of the pivalate ligand, with the isonicotinate + HgI_2 ligand, greatly reduced the solubility of the ring.

From the Cr 2p spectra it is evident that the peak has broadened and shifted to the right. This is indicative of a change of oxidation state of the chromium atoms in the ring which is again consistent with the removal of the carboxylate bonds from the ring. The chromium carboxylate bonds have been replaced with a mixture of CrO_x states which are insoluble in hexane, the developing solvent.

The main spectra also shows that the mercury which is present before exposure is no longer present after exposure. This suggests that the ligands which contain mercury

have been broken down and due to the low vapor pressure of the mercury, it diffused out of the film and sublimed in the vacuum.
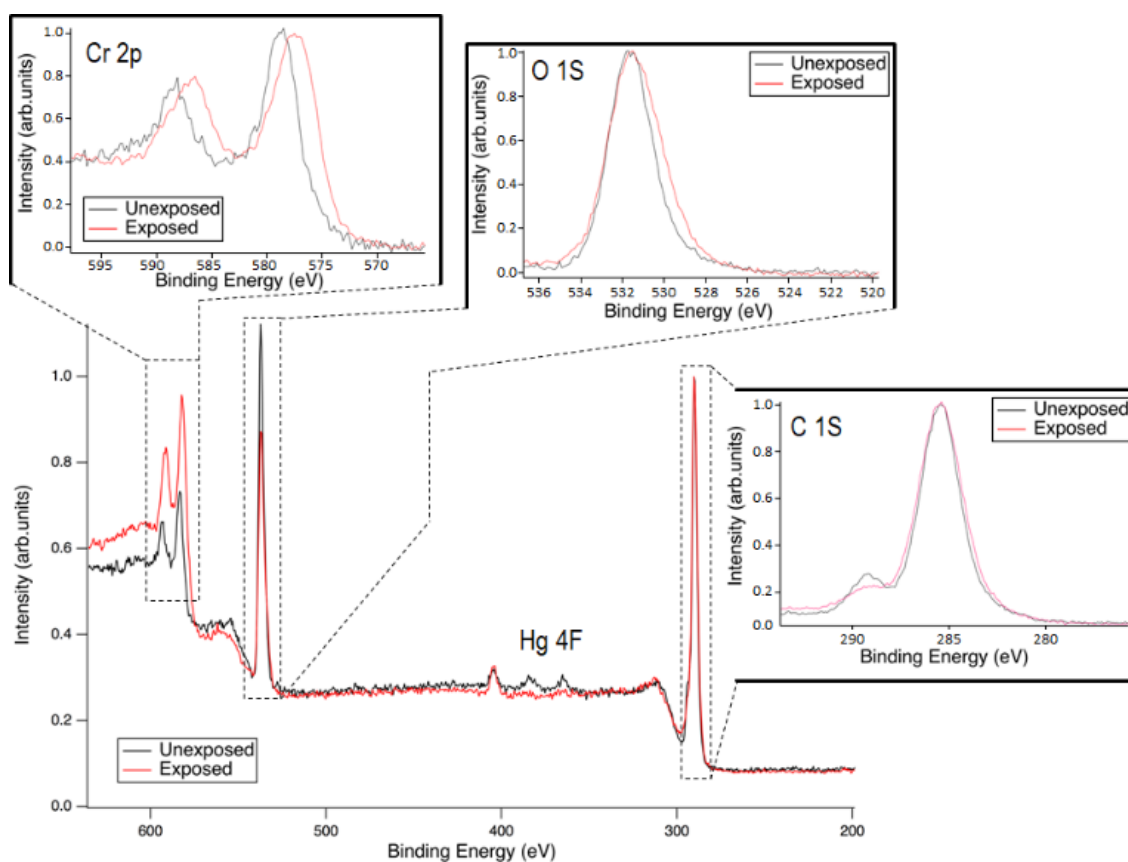
Figure 3.22 *A plot of the XPS spectra for resist **D**, before and after exposure. Inset are subfigures focusing on the Cr 2p, O 1s and C 1s spectra.*

3.7 <u>Summary</u>

In summary, a series of modular resists were developed which successfully improved on the initial resist, **A**. This resist had good lithographic performance but required a large exposure dose. A large dose makes using the resist for fabrication impractical due to the long exposure times needed. This reduces throughput for the manufacture of photomasks which is a critical metric in the semiconductor industry. The improvements for the main chromium ring family came from adding a diallylammonium counter ion in the centre of the ring and substituting an outer ligand with a carboxylate containing a HgI_2 molecule (resist **D**). This reduced the dose by a factor of 3.17 without compromising the lithographic performance. Just as important as this result was the confirmation of the

accuracy of the simulation and its viability as a method to identify a potential new resist material before synthesis. In practice, this process is not flawless because it cannot predict the solubility of a resist in a casting or developing solvent and hence its spin coating performance. It is also unknown if the synthesis is even possible but used in consultation with the synthesis team then it is a powerful tool.

According to the simulation model parameters reducing the molecule size whilst retaining similar chemistry was hypothesized to reduce the dose. This was confirmed by resist **F** which again showed a reduction in dose compared to resist **D**. However, the lithography was poor but could be improved by changing the developer from hexane to PGMEA, unfortunately, this increased the dose by a factor of 5.9.

The largest increase in sensitivity was found to be resist **G** which was attained by changing the chromium ring for an indium ring which gave a dose of 1500 pC/cm at 50 nm pitch. This resist gave an overall reduction in dose by a factor of 22 (at 100nm pitch) compared to the starting resist **A**. The next step in the development of these modular resists would be to add mercury ligands to the indium resist, which based on the impact on the chromium resists could potentially yield a resist with a dose of 390 pC/cm at 60 nm pitch.

References

[1] Fujimura, A., Willis, J., "2020 Mask Maker Survey Conducted by the eBeam Initiative," Proc. SPIE 11518, Photomask Technology 2020, 115180E (2020)

[2] Schuegraf, K., "Photomask challenges for data-centric computing in the 2020s", Proc. SPIE 11908 (2021)

[3] Shamoun, B., et al, "Multi-Beam Mask Writer in EUV era - Challenges and Opportunities", Proc. SPIE 11610, Novel Patterning Technologies 2021 (2021)

[4] Klein, C., Platzgummer, E., "MBMW-101: World's 1st High-throughput Multi-beam Mask Writer" Proc. SPIE 9985, Photomask Technology 2016 (2016)

[5]   ELPHY Quantum, Raith GmbH, Dortmund, Germany

[6]   McInnes, E. J. L., Piligkos, S., Timco, G. A., Winpenny, R. E. P., "Studies of chromium cages and wheels", Coordination Chemistry Reviews, Vol. 249 (2005)

[7]   Lewis, S. M., DeRose, G. A., ***Alty, H. R.,*** Hunt, M. S., Li, J., Werthiem, A., Fowler, T., Lee, S. K., Muryn, C. A., Timco, G. A., Scherer, A., Yeates, S. G., Winpenny, R. E. P., "Design and implementation of the next generation electron beam resists for the production of EUVL photomasks", Proc. SPIE 10810 (2018)

[8]   Laye, R.H., Larsen, F.K., Overgaard, J, Muryn, C.A, McInnes, E.J.L., Rentschler, E., Sanchez, V., Teat, S.J., Güdel, H.U., Waldmann, O., Timco, G.A., and Winpenny, R.E.P., "A family of heterometallic wheels containing potentially fourteen hundred siblings", Chem. Commun., 2005 (2005).

[9]   Noto, V.D., Boeer, A. B., Lavina, S., Muryn, C.A., Bauer, M., Timco, G.A., Negro, E., Rancan, M., Winpenny, R.E.P., Gross, S., "Functional chromium wheel-based hybrid organic-inorganic materials for dielectric applications', Adv. Funct. Mater., Vol. 19 (2009)

[10]   Moreau, W.M., "State of the Art of Acrylate Resists: An Overview of Polymer Structure and Lithographic Performance", Proc. SPIE 0333 (1982)

[11]   Hasan, S., Murphy, M., Weires, M., Grzeskowiak, S., Denbeaux, G., Brainard, R.L., "Oligomers of MORE: Molecular Organometallic Resists for EUV," Proc. SPIE 10960 (2019)

[12]   Charlesby, A., "Atomic Radiation and Polymers," Pergamon, Oxford (1960)

[13]   Bowden, M. J., Thompson, L.F., "Poly(Styrene Sulfone) – A Sensitive Ion-Millable Positive Electron Beam Resist", J. Electrochem. Soc., Vol. 121 (1974)

[14]   Carolina Sañudo, E., Muryn, C.A., Helliwell, M.A., Timco, G.A., Wernsdorfer, W., Winpenny, R.E.P., "Al, Ga and In heterometallic wheels and their by-products", Chem. Commun., 2007 (2007)

[15]   National Centre for Biotechnology Information, "PubChem Compound Summary for CID 15413, Methyl tert-butyl ether", PubChem, https://pubchem.ncbi.nlm.nih.gov/compound/Methyl-tert-butyl-ether (2021)

[16]   National Centre for Biotechnology Information, "PubChem Compound Summary for CID 7519, Anisole", PubChem, https://pubchem.ncbi.nlm.nih.gov/compound/Anisole (2021)

4

EXCALIBUR: DEVELOPING AN ION BEAM LITHOGRAPHY MONTE CARLO SIMULATION

Contents

Ions can be used as an exposure source in lithography much like electrons are in lithography. As ion source stabilities have improved the viability of ion beams as a lithography tool have increased and the benefits that ions can offer are being explored. Theoretically ions will have much larger stopping powers when compared to electrons of the same energy due to their much larger mass. Chapter 2 and 3 have shown how essential SEs are in the exposure of resist materials and the larger stopping power of ions should mean that SE generation will increase when compared to electrons.

Unlike electron beam lithography (EBL), there is a lack of simulation software for ion lithography. Popular ion simulation packages like SRIM/TRIM [1] provide

accurate data regarding ion penetration and propagation into a material. However, for the application to lithography it is essential for SE generation to be fully simulated as these are vital for resist exposure and for investigating lithographic properties such as sensitivity and the proximity effect. Developing a model that can simulate SE generation and fully track subsequent generations of low energy electrons is important to understanding resist exposure and developing new resists for ion lithography.

4.1 Ion Scattering Theory and Models

As with the EBL simulation developed in chapter 2 the focus of this chapter is not to develop new models for ions in materials but to apply already developed models in a framework that is conducive to analysing the exposure of resist materials. To this end the ion model was developed to be an analogue of the electron beam model to allow the seamless change between ions and electrons when tracking primary ions and the SEs that they generate.

4.1.1 Total Scattering Cross Section

Firstly, as with the electron model, the scattering cross section must be considered. The following are from Meuller's method of deriving the total scattering cross sections of ions in a material [2][3]. This total scattering cross sections is derived from the differential "Lindhard, Nielsen and Scharff" (LNS) cross section [4] for ions which for an ion with energy E, charge Z_1 and mass A_1 interacting with a target material with charge Z_2 and mass A_2, is given by the following equation,

$$d\sigma(E,T) = \frac{1}{2}\pi a^2 \frac{E}{\gamma E_L^2} t^{-\frac{3}{2}} f\left(t^{\frac{1}{2}}\right) dT \qquad 4.1$$

where,

$$t = \frac{E^2}{E_L^2} \frac{T}{\gamma E} \qquad 4.2$$

T is the energy that is transferred from the incident ion to the target atom. E_L is the Lindhard unit of energy,

$$E_L = Z_1 Z_2 \frac{e^2}{a} \frac{A_1 + A_2}{A_2} \qquad 4.3$$

where a is the screening length given by,

$$a = 0.885 a_0 Z^{-\frac{1}{3}} \qquad 4.4$$

Here a_0 is the Bohr radius, which is the radius of a hydrogen atom ($a_0 = 5.29 \times 10^{-11}$ m) and Z can be found by,

$$Z = \left(Z_1^{\frac{2}{3}} + Z_2^{\frac{2}{3}} \right)^{\frac{3}{2}} \qquad 4.5$$

γE is the maximum energy that can be transferred from the ion to the target, as allowed by kinematics and γ is given by,

$$\gamma = \frac{4 A_1 A_2}{(A_1 + A_2)^2} \qquad 4.6$$

The total scattering cross section can be found by integrating the differential cross section in Equation 4.1 to give,

$$\sigma(E) = \frac{1}{2} \pi a^2 \frac{E}{\gamma E_L^2} \int_{T_1}^{\gamma E} dT \, t^{-\frac{3}{2}} f\left(t^{\frac{1}{2}} \right) \qquad 4.7$$

The lower limit for this integral T_1 is the minimum energy transfer allowed which corresponds to the minimum energy needed to displace an atom in the target material. This value is material specific but is typically of the order of ~25 eV. Winterbon et al [5] fit $f(t^{1/2})$ to the following function,

$$f\left(t^{\frac{1}{2}} \right) = \lambda t^{\frac{1}{6}} \left[1 + \left(2\lambda t^{\frac{2}{3}} \right)^{\frac{2}{3}} \right]^{-\frac{3}{2}} \qquad 4.8$$

where $\lambda = 1.309$. Using a substitution of,

$$q^4 = (2\lambda)^{\frac{2}{3}} \left(t^{\frac{1}{2}} \right)^{\frac{8}{9}} \qquad 4.9$$

The differential cross section from Equation 4.7 can be written as,

$$\sigma(E) = \frac{9}{2}\pi a^2 (2\lambda)^{\frac{1}{2}} \lambda \int_{q_1}^{q_2} dq \; q^{-4}(1+q^4)^{-\frac{3}{2}} \qquad \text{4.10}$$

where the limits q_1 and q_2 are given by,

$$q_2 = (2\lambda)^{\frac{1}{6}} \left(\frac{E}{E_L}\right)^{\frac{2}{9}} \qquad \text{4.11}$$

$$q_1 = (2\lambda)^{\frac{1}{6}} \left(\frac{E T_1}{\gamma E_L^2}\right)^{\frac{1}{9}} \qquad \text{4.12}$$

Meuller derived a solution to the integral in a series form to give the final total scattering

cross section as,

$$\sigma(E) = \frac{9}{2}\pi a^2 (2\lambda)^{\frac{1}{2}} \lambda W(q_1, q_2) \qquad \text{4.13}$$

Where $W(q_1, q_2)$ is the solution to the integral in Equation 4.10 such that,

$$W(q_1, q_2) = P(q_1) - P(q_2) \qquad \text{4.14}$$

where

$$P(q) = \begin{cases} P_<(q), & q \leq 0.9 \\ P_>(q), & q \geq 0.9 \end{cases} \qquad \text{4.15}$$

with

$$P_<(q) = -1.6487831 - \sum_{n=0}^{\infty} \frac{(-)^n (2n+1)!!}{2^n n! \, (4n-3)} q^{4n-3} \qquad \text{4.16}$$

$$P_>(q) = -0.10372089 + \sum_{n=0}^{\infty} \left[\frac{(4+3)\dots(4n+3)}{4^n n!}\right] \frac{(1+q^4)^{-n-\frac{9}{4}}}{4n+9} \qquad \text{4.17}$$

This series form of the integral lends itself more easily to calculating the scattering cross

section in a simulation environment.

Once a value for the scattering cross section, $\sigma(E)$, has been found the mean free path of

an ion, that is, the average distance an ion travels between collisions with atoms in the

target material is calculated by the equation for mean free path,

$$\Lambda = \frac{A_2}{\rho\sigma(E)N_A}$$
$$\text{4.18}$$

This is the same general equation as the one used to calculate the mean free path for electrons in Chapter **2** (Equation 2.3). Here, ρ and N_A are the density of the target material and Avogadro's number and when combined with the atomic weight give the number density of the atoms in the target (atoms/cm^3). Figure **4.1**. shows the calculated values for the mean free path of ions with atomic numbers from hydrogen (Z = 1) to uranium (Z = 92) in silicon. Silicon was chosen as it is a well understood material with distinct material properties compared to the resist materials which will be studied with this model. This allows a more concise comparison to SRIM/TRIM later in this chapter. The mean free path for each ion was also calculated for the ion energies 0.1, 1, 10 and 35 KeV. 35 KeV was chosen as the highest energy as this is the highest beam energy available in experimentation using the Zeiss Orion NanoFab (Chapter **5**).
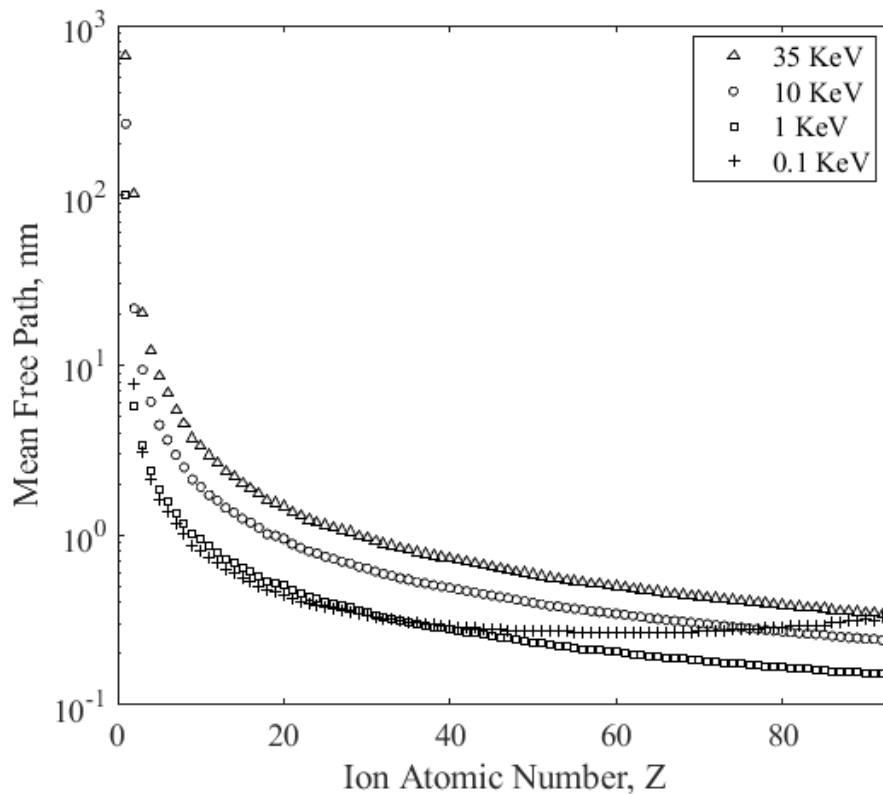
Figure 4.1 *A plot of mean free paths for ions from hydrogen (Z = 1) to uranium (Z = 92) in silicon. The mean free paths were calculated for ion energies of 0.1, 1, 10 and 35 KeV.*

As expected, the mean free path for each ion decreases with energy and then increases again as the ion energy approaches zero. This is due to the probability of interactions between an incident atom and a target atom reducing becoming less energetically viable. Also shown is the general trend of the decrease in the mean free path as the atomic number increases. This is caused by the larger stopping powers of the heavier ions limiting how far they can travel before they deplete their energy.

4.1.2 Ion Stopping Power

The stopping power for an ion travelling through a material is comprised of two main components, the electronic and the nuclear stopping power. The nuclear stopping power is the energy lost when the ion collides and scatters off the nucleus of atoms in the target material. From Zeigler et al [1] the nuclear stopping power is given by,

$$-\frac{dE}{ds} = S_n \frac{8.462 Z_1 Z_2 A_1}{\left(Z_1^{\frac{2}{3}} + Z_2^{\frac{2}{3}}\right)^{\frac{1}{2}} (A_1 + A_2)} 10^{-15} \ eVcm^{-1} \qquad 4.19$$

where,

$$S_n(\varepsilon) = \frac{\ln(1 + 1.1383\varepsilon)}{2[\varepsilon + 0.01321\varepsilon^{0.21226} + 0.19593\varepsilon^{0.5}]} \qquad \varepsilon < 30 \qquad 4.20$$

$$S_n(\varepsilon) = \frac{\ln(\varepsilon)}{2\varepsilon} \qquad \varepsilon > 30 \qquad 4.21$$

Here ε is the reduced energy given by,

$$\varepsilon = \frac{32.53 A_2 E}{\left(Z_1^{\frac{2}{3}} + Z_2^{\frac{2}{3}}\right)^{\frac{1}{2}} (A_1 + A_2)} \qquad 4.22$$

As before, this is for an inbound ion with a charge Z_1 and a mass A_1 interacts with a target material with a charge of Z_2 and a mass of A_2. For a molecular material Z_2 can be considered to be the effective Z of a material is the weighted atomic number of a molecule

given by Equation 2.33 in Chapter **2**. For the ion model the atomic weight of the molecule is treated in this way.

The electronic stopping power is the energy lost by an electron as it cascades through the material between collisions with atoms. This energy is lost through interaction with orbital electrons of atoms in the material. Theses interactions are much less energy expensive that the ion-target collisions due to the large mass and energy compared to orbital electrons. The electronic stopping power is given by,

$$-\frac{dE}{ds} = 3.83 \times 10^{-15} \frac{Z_1^{\frac{7}{6}} Z_2}{\left(Z_1^{\frac{2}{3}} + Z_2^{\frac{2}{3}}\right)^{\frac{3}{2}}} N \left(\frac{E}{A}\right)^{\frac{1}{2}} \quad eVcm^{-1} \qquad 4.23$$

where the values have their previous definitions and N is the number denstiy of the atoms in the target material [6].

The nuclear and electronic stopping powers and their combined total stopping power were calculated for He, Ne and Au in Si and are shown in Figures **4.2-4** respectively. These ions were simulated with an energies ranging from 0 to 35 KeV. The choice of these atoms is again based on those available for experimentation (Chapter **5**).

The combined stopping powers for all three atoms increase with energy however the behaviour of the nuclear and the electronic stopping power vary. For the He ions (Figure **4.2**) the electronic stopping power dominates at most energies only being overtaken by the nuclear stopping power below 3 KeV. This is significant as it means that for He ions most of their energy will be lost through the generation of secondary electrons in the target as opposed to the collision with atoms. This gives He ions good penetration in most materials.
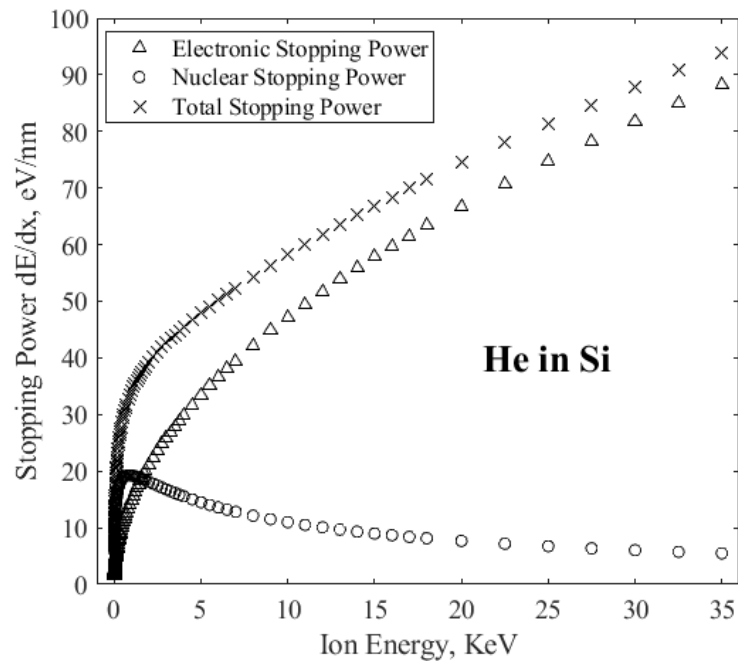
Figure 4.2 *A plot of the electronic, nuclear and total stopping power versus ion energy*

for He ions in Si.

For Ne (Figure **4.3**) at higher energies the two stopping powers appear to converge and are of a similar magnitude however as the energy decreases the nuclear stopping increases and the electronic stopping decreases. This is due to the similar atomic properties (Z, A) of Si and Ne.
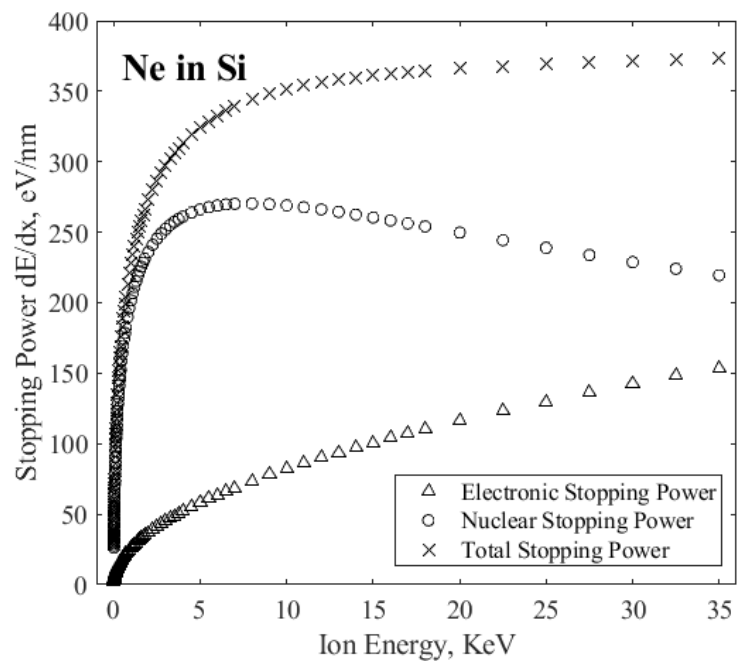
Figure 4.3 *A plot of the electronic, nuclear and total stopping power versus ion energy*

for Ne ions in Si.

Figure **4.4** shows that the nuclear stopping power of Au dominates at all energies with the electronic stopping power having only a small contribution to the overall stopping power of the ion. This corresponds with the small mean free path (Figure **4.1**) meaning the range of Au ions will be significantly smaller than that of He and Ne.
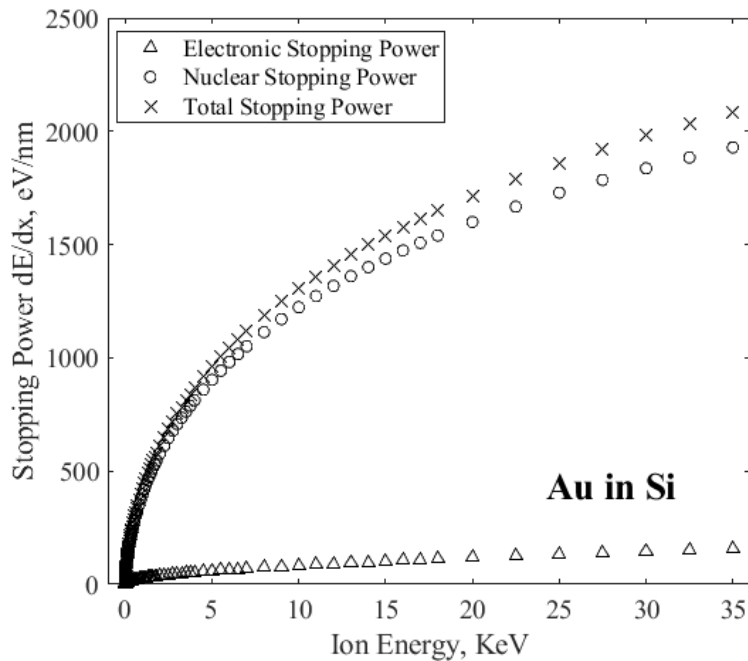
Figure 4.4 *A plot of the electronic, nuclear and total stopping power versus ion energy for Au ions in Si.*

To qualify the model, it was compared to data for the stopping powers of ions from hydrogen (Z = 1) to uranium (Z = 92) in Si at an energy of 35 KeV calculated using SRIM. This comparison is shown in Figure **4.5** and demonstrates a good agreement between the stopping powers calculated in EXCALIBUR and SRIM. The nuclear stopping power is a very good match but diverges for heavier ions. This divergence has a maximum of 10% for uranium but the average is only 3.5% which is acceptable. SRIM calculates the electronic stopping power for ions on an ion-by-ion basis considering the electronic potentials specific to each ion. The stopping power that EXCALIBUR uses is a much simpler method and matches the general trend of the data from SRIM.
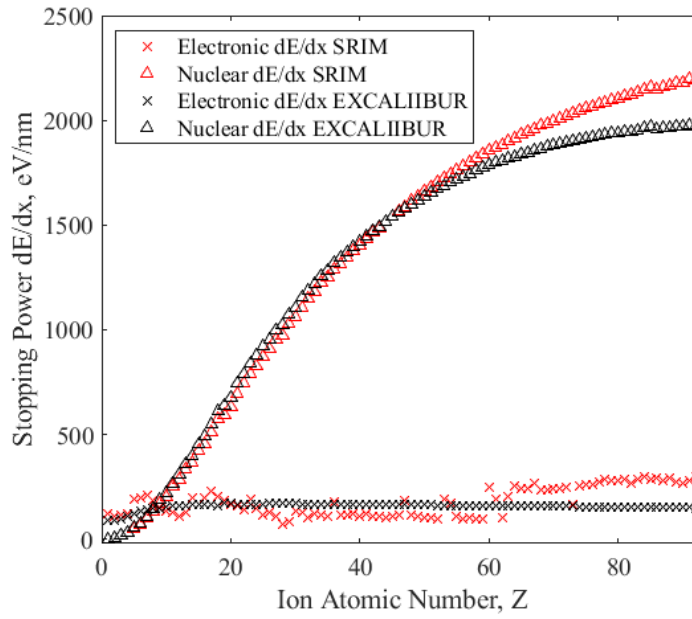
Figure 4.5 *A comparison of the electronic and nuclear stopping power for ions from hydrogen (Z = 1) to uranium (Z = 92) calculated using SRIM and EXCALIBUR.*

4.1.3 Ion Scattering Angles

Once an ion travelling through the resist has been determined to have collided with a nucleus of an atom in the target material the angle of deflection after the collision must be attained. The scattering angle for the incident ion is found using the '*Magic Formula*' derived by Biersack [7] the geometries of which are shown in the scattering triangle in Figure **4.6**. A scattering interaction between an ion M_1 and target atom M_2 in the centre of mass frame. ρ_1 and ρ_2 are the radius of curvature of the scattered particles, r_0 is the length of closest approach, P is the impact parameter and, δ_1 and δ_2 are a correction factor. This leads to the following equation,

$$\cos\frac{\theta}{2} = \frac{\rho + P + \delta}{\rho + r_0} \qquad\qquad 4.24$$

with $\rho = \rho_1 + \rho_2$ and $\delta = \delta_1 + \delta_2$. The minimum approach distance, r_0, is found using the following equation and can be found analytically using Newton's method.

$$1 - \frac{V(r_0)}{E_C} - \left(\frac{P}{r_0}\right)^2 = 0 \qquad\qquad 4.25$$

130

Here the energy is expressed as, E_C, which is the energy in the centre of mass system given by,

$$E_C = \frac{E}{1 + \frac{A_1}{A_2}}$$ 4.26

where A_1 and A_2 are the mass of the ion and target atom respectively. The radius of curvature, ρ, can be found using the following equation.

$$\rho = \frac{2(E_C - V(r_0))}{-V'(r_0)}$$ 4.27

As before, it is convenient to express the energy in units of $\frac{Z_1 Z_2 e^2}{a}$. This leads to the dimensionless reduced energy, ε, given by,

$$\varepsilon = \frac{a E_C}{Z_1 Z_2 e^2}$$ 4.28
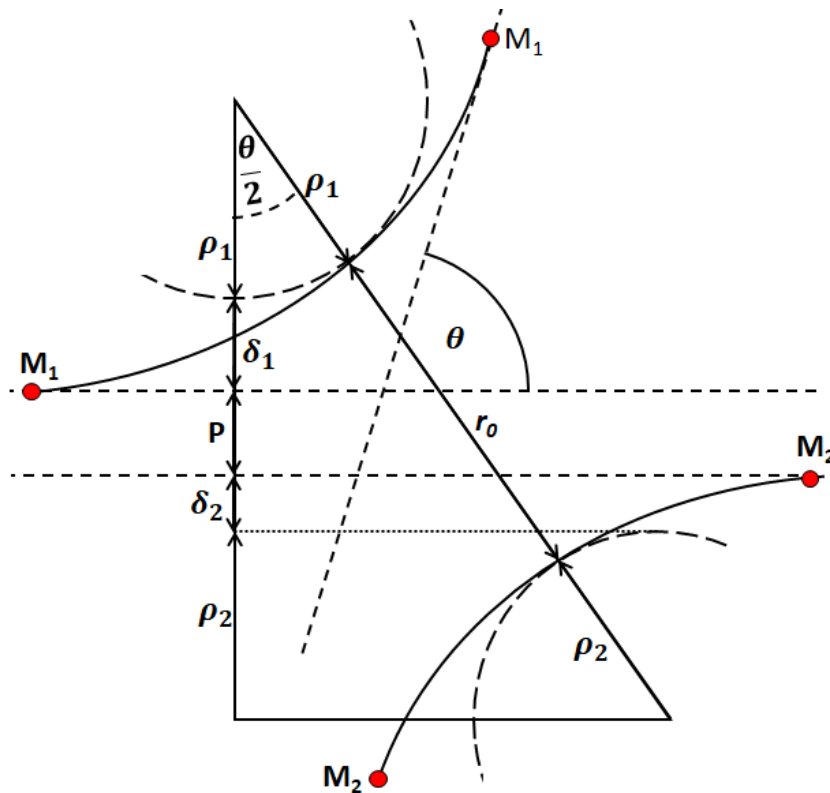
Figure 4.6 *A diagram of the geometries used to determine the scattering angle θ of an ion M₁ colliding with a target atom M₂ in the centre of mass frame. P is the impact parameter, r₀ is the minimum approach distance, ρ are the radii of curvature for the scattered particles.*

131

The universal screening length, a, is given by,

$$a = \frac{0.8853 a_0}{\left(Z_1^{\frac{2}{3}} + Z_2^{\frac{2}{3}}\right)}$$

4.29

where $a_0 = 0.529\text{Å}$ is the Bohr radius. Expressing the lengths in Figure **4.6** in units of the screening length means Equation 4.24 can be written as,

$$\cos\frac{\theta}{2} = \frac{B + R_C + \Delta}{R_0 + R_C}$$

4.30

where,

$$B = \frac{P}{a}, \qquad R_0 = \frac{r_0}{a}, \qquad R_C = \frac{\rho}{a}, \qquad \Delta = \frac{\delta}{a}$$

4.31

To calculate P, the impact parameter between the target and the incident ion two cases based on the energy of the system must be considered. For high energy interactions where $\varepsilon > 10$, the travel length of the ion, L, can be calculated from an equation based on the nuclear stopping power to given by,

$$L = \frac{0.02 \left(1 + \frac{A_1}{A_2}\right)^2}{4\pi N a^2} \frac{\varepsilon^2 + 0.052\varepsilon^{1.32}}{\ln 1 + \varepsilon}$$

4.32

where N is the number density of the target. Using this value of L, the impact parameter P can be found using the expression,

$$P = \left[-\ln\left(\frac{R_N}{\pi N L}\right)\right]^{\frac{1}{2}}$$

4.33

where R_N is a random number between 0 and 1. For the low energy case, where $\varepsilon < 10$, it is assumed that the minimum travel distance is on the order of the interatomic spacing between target atoms, $L \sim N^{1/3}$, in this case the impact parameter is found using,

$$P = \left[\frac{R_N}{\pi N^{\frac{2}{3}}}\right]^{\frac{1}{2}}$$

4.34

The fitting parameter Δ, from Equation 4.30 is a factor that is a correction for the low energy case where scattering is no longer adequately described by the coulomb interatomic potential and is given by the following equation,

$$\Delta = X \frac{R_0 - B}{1 + Y}$$

4.35

Where X and Y are given by,

$$X = 2\alpha\epsilon B^\beta, \qquad Y = \gamma\left[(1 + X^2)^{\frac{1}{2}} - X\right]^{-1}$$

4.36

$$\alpha = 1 + C_1\epsilon^{-\frac{1}{2}}, \qquad \beta = \frac{C_2 + \epsilon^{\frac{1}{2}}}{C_3 + \epsilon^{\frac{1}{2}}}, \qquad \gamma = \frac{C_4 + \epsilon}{C_5 + \epsilon}$$

4.37

And C_{1-5} are fitting parameters based on the universal interatomic potential derived by Zeigler et al [1] and are shown in the Table **4.1.** For the high energy case where $\epsilon > 10$ the scattering angle is instead found by the following equation,

$$\sin^2\left(\frac{\theta}{2}\right) = \frac{1}{1 + 2\varepsilon B^2}$$

4.38

Table 4.1. *A table for the fitting parameters calculated for the universal interatomic potential*

C_1	0.99229
C_2	0.011615
C_3	0.007122
C_4	9.3066
C_5	14.813

Scattering angles for hydrogen (Z = 1) to uranium (Z = 92) with energies of 0.1, 1, 10 and 35 KeV are plotted in Figure **4.7**. The scattering angles follow the expected behaviour that heavier ions lead to an increase in scattering angle.
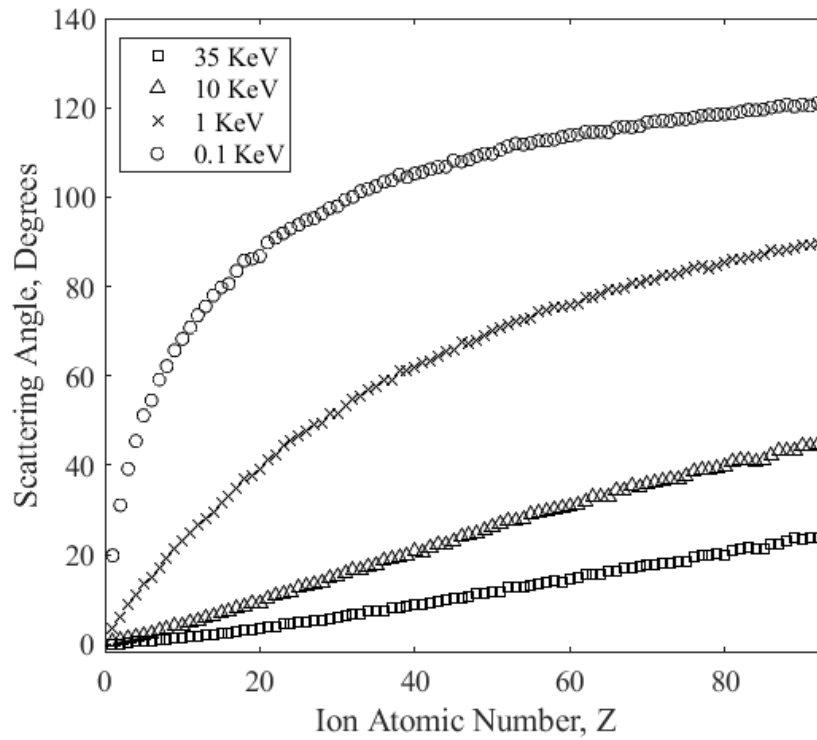
Figure 4.7 *A plot of the scattering angles for ions from H(1) to U(92) in silicon. The*

angles were calculated for incident energies of 0.1, 1, 10 & 35 KeV.

This correlates to the increase in nuclear stopping power at with heavier ions which means

that collisions with the target are more energetic and therefore to conserve momentum

there scattering angle must be larger. A decrease in energy also leads to an increase in

scattering angle. This behaviour is again consistent with the conservation of momentum.

4.1.4 <u>Secondary Electron Yield</u>

As an ion passes through a material, secondary electrons (SEs) will be generated. Once

generated, these can be handled using the electron model (Chapter **2**). The yield of SEs,

δ_{SE} is given by,

$$\delta_{SE} = -\frac{1}{\epsilon}\frac{dE}{dx} \qquad\qquad 4.39$$

Where dE/dx is the electronic stopping power and ϵ is the average energy expended in

creating an SE, ϵ is a fitting parameter determined from experimental SE yields and it is

material and ion dependent. The data sets required for every ion from hydrogen to

uranium in every target material would be extensive and whilst there is a wealth of data

much of the necessary values to make a broad simulation is missing. To this end, a value

of $\epsilon = 30$ eV was chosen as it has been shown to provide consistent results for a range of ions and targets [8]. This equation is used to calculate the number of electrons generated in each step it takes in the material. It is assumed that the electrons are distributed randomly along the ions path.

An assumption was made that due to the high momentum of the incident ions they undergo negligible deviations in angle and hence no deviations between the main nuclei collisions. Thus, as the SEs are generated in between collisions, as per the electronic stopping power, it can be assumed that they are generated perpendicularly to the direction of propagation of the ion with a scattering angle, $\theta = 90°$ and an azimuthal angle randomly distributed and given by $\varphi = 2\pi$RND.

4.2 <u>Simulation Structure</u>

To allow seamless inclusion of the ion model into the EXCALIBUR simulation environment, a switch was added to allow the incident particles to be changed from electrons to ions. This simplifies the handling of primary ions and the SEs generated by these ions using the same simulation. The inputs required for primary ions are the mass (A) and the atomic number (Z), with the energy being defined in the beam parameters usually used for primary electrons. Materials, resist layer matrix and patterns are defined in the same way as the electron model (Chapter 2). A flow diagram of how ions are tracked is shown in Figure **4.8**.

Once all the ions have been tracked and the positions, energy and direction of the SEs have been stored then the simulation is switched from ion to electron mode and then all the SEs and their cascades are tracked.

START → Define material, beam and pattern parameters

Generate co-ordinates of exposure pattern

Ion switch: **ON**
Define ion mass and Z

Insert ion

Calculate the total scattering cross section

Calculate the mean free path

Generate random step length

Calculate the electronic and nuclear stopping power → Calculate the number of SEs generated from the electronic energy loss

Calculate scattering angle

Store coordinates of ion and any SEs if applicable

Is $E_{ion} > E_{Min}$?
Yes
No

Terminate current Ion

Are there Ions remaining?
Yes
No

Ion switch: **OFF**

END

Figure 4.8 *Flow diagram of the ion beam lithography simulation for a primary ion from insertion into the material matrix until termination.*

4.3 <u>Results</u>

To produce examples of the full ion tracks generated by EXCALIBUR a series of simulations were run. The simulations were run with different incident ions which were (a) helium, (b) neon and (c) gold. To allow comparison between the results all the simulations were run with 100 input ions and an energy of 35 KeV. Due to the randomness of Monte Carlo simulations an amount of statistical error is introduced into the data, to mitigate this each simulation was run 1000 times to reduce the error to $< 1\%$. The choice of the ions is based on those available with current systems capable of ion beam lithography. Helium and neon beams can be used with the Zeiss Orion NanoFab and gold can be used with the Raith VELION. The maximum acceleration voltage of the Orion microscope is 35 KV which gives the smallest spot size of the beam (which is 400 pm) and will give the highest penetration possible (Figure **4.1**). For these reasons this is the beam energy used for the simulation.

The ion trajectories and the SEs generated by these ions are shown in Figure **4.9**. The scale between the trajectory plots were kept the same to show how the extent of the ion penetration changes between the different ions. Helium has the largest penetration depth travelling an average of ~500 nm into the silicon (Figure **4.9a**). Conversely the gold ions travel to a depth of only ~10 nm (Figure **4.9c**) this reduction in range is a combination of both the reduced mean free path and the increased stopping power. Also seen in the plots in Figure **4.9** are the SEs. These are shown in range of colours dependent on the generation that the SEs belong to with generation I being shown in red, generation II are blue, generation III are green and generation IV are magenta. Due to the low energy of these electrons (30 eV) they have do not travel very far in the silicon. Also seen is the effect of the scattering angle on the ions with the helium ions exhibiting a much lower beam spread compared to the neon and the gold which begin to spread laterally almost as soon as they enter the silicon.
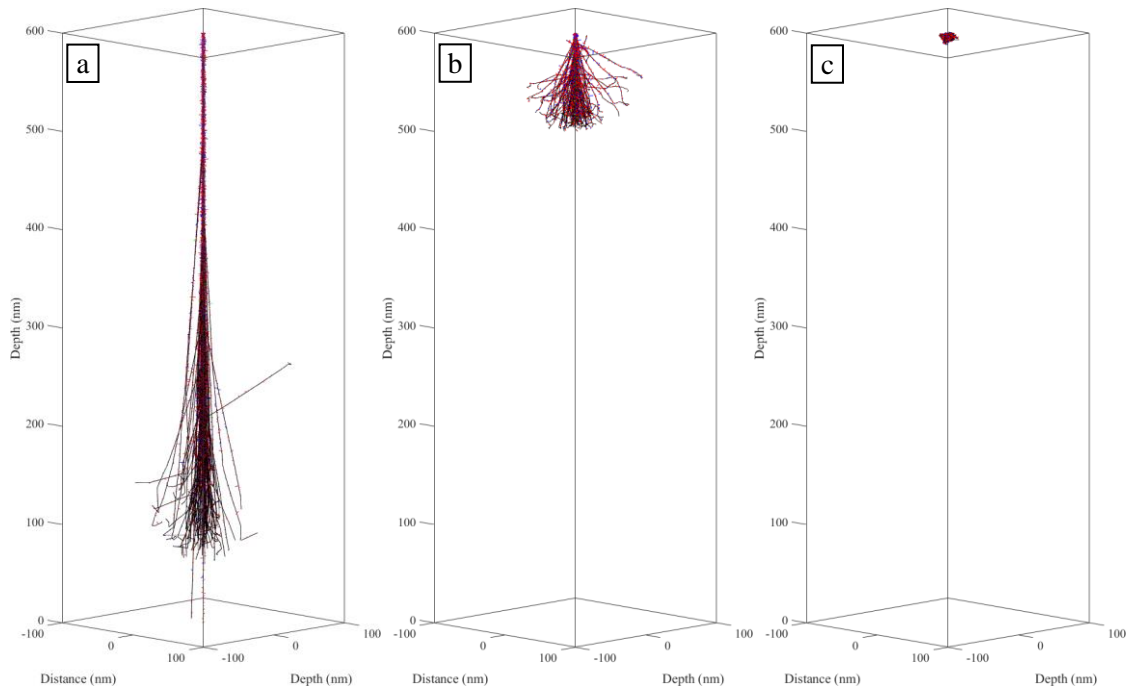
Figure 4.9 *3D trajectory plots for (a) He, (b) Ne and (c) Au in Si. Primary Ions are shown in black and SEs are shown in red (gen I), blue (gen II), green (gen III) and magenta (gen IV). These plots were generated from EXCALIBUR for 100 incident ions with energies of 35 KeV.*

The number of SEs generated for each ion exposure in Figure **4.9** are shown in Figure **4.10**. The data suggests that the general trend is that SE yield decreases for heavier ions. This is supported by the calculated values of the stopping powers of ions shown in Figure **4.5** as the electronic stopping power is of the same magnitude for, He, Ne and Au. This means that the number of SEs generated is therefore dependent of the distance of travel of an ion in the target material. As the mean free path also decreases for heavier ions (Figure **4.1**) and therefore the step length also decreases, then the amount of energy lost through electronic stopping is also reduced. Hence the SE yield decreases. This is also paired with the effect of an increased nuclear stopping power for heavier ions which mean that the energy of the ion will be exhausted quicker and the overall range of the ion in a material is greatly reduced. Again, reducing the SE yield.

It is also worth noting that the unlike the SE cascade caused by an electron beam (Chapter 2) most of the SEs are generated in the first generation of the cascade. This is

138

because the low energy of the SEs that are being generated by the ions means that they are considered by the electron model to be "slow" SEs and therefore interact through inelastic collisions. This also means that these electrons will quickly lose what little energy they had hence a reduced (rather that increased) number of electrons in the second generation. Comparing He ions to electrons the total number of SEs generated is 12.6 times larger for He ions. Which again shows the sensitivity improvements that can be gained using ions instead of electrons for lithography.
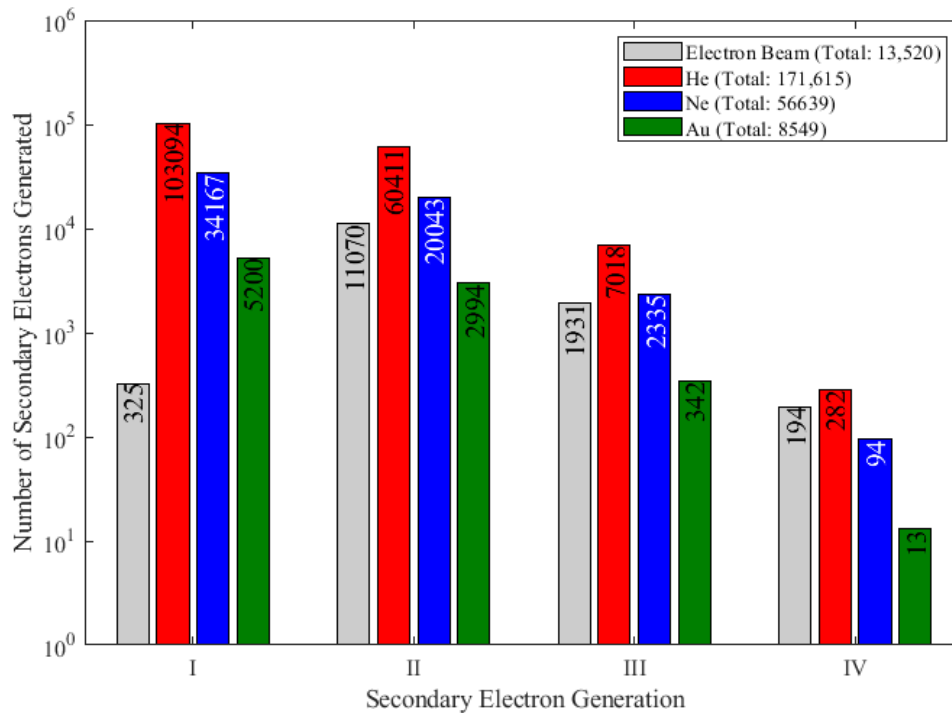
Figure 4.10 *Number of SEs generated for each generation of the SE cascade for 100 incident ions of He, Ne and Au in Silicon with energies of 35 KeV compared to 35 keV electrons. These values are the average of 1000 runs of the same simulation to ensure that the error in the data is <1%.*

The energy that is deposited by the ions in the silicon are also tracked so that a heat map of this energy can be generated. The heat maps for the simulations are shown in x-z profile in Figure **4.11** and the x-y profiles are shown in Figure **4.12**. The plots show that for helium ions the energy is deposited mainly within the profile of the main beam and most of the energy. Longitudinally, the majority of the energy is deposited before the beam starts to diverge (Figure **4.11a**). This is also seen laterally in the x-y plot (Figure **4.12a**).

The energy loss of neon is significantly different as stray ion deposits significant energy along its trajectory. This results in a much broader lateral energy spread as seen in Figures **4.11b** and **4.12b**.
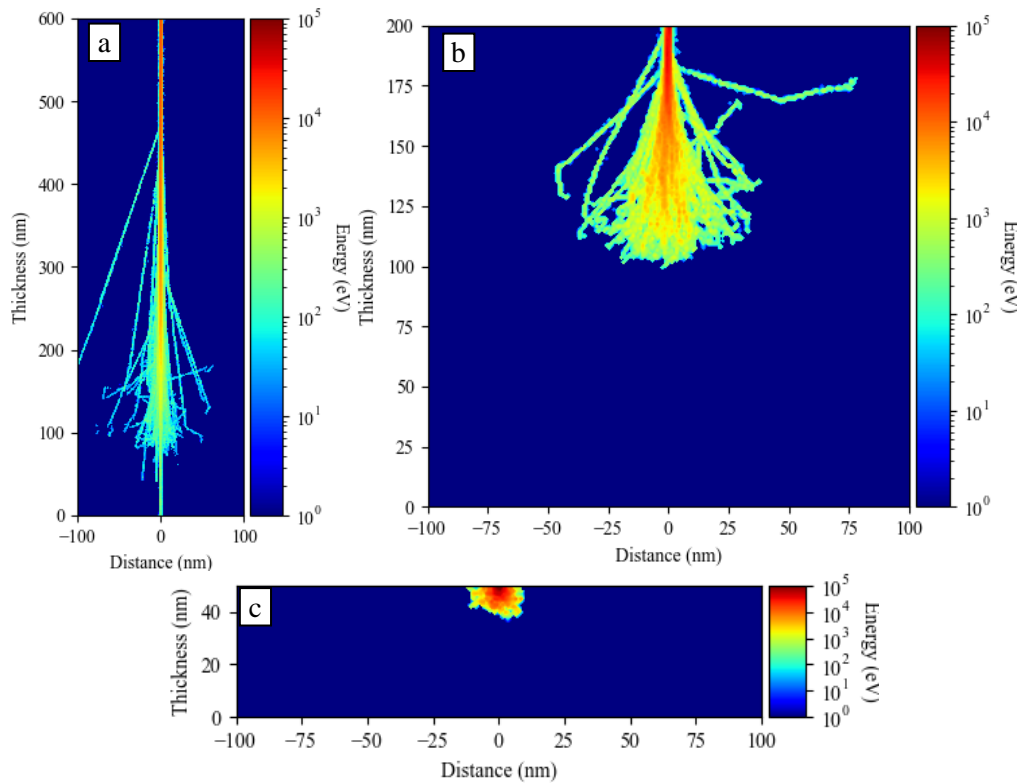
Figure 4.11 *X-Z heat maps of energy deposits for (a) He, (b) Ne and (c) Au ions in Si.*

These plots were generated from EXCALIBUR for 100 ions with energies of 35 KeV
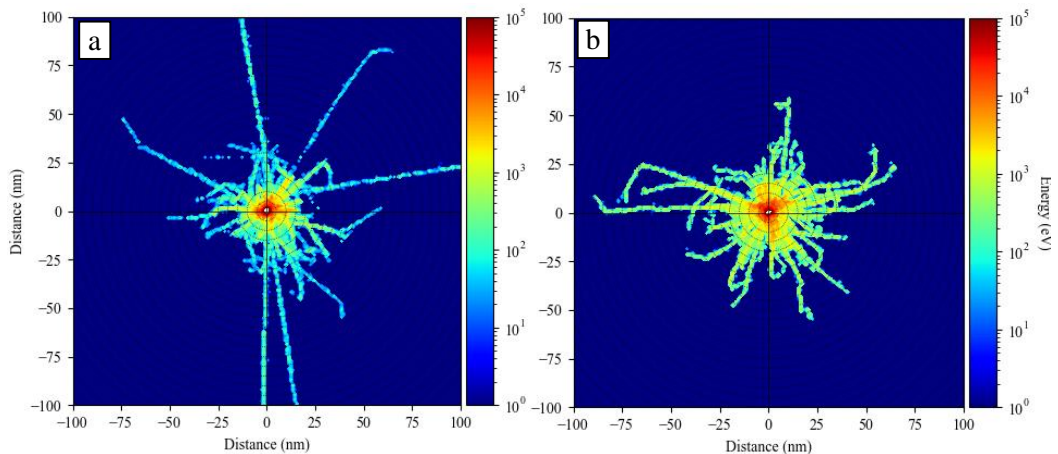
Figure 4.12 *X-Y heat maps of energy deposits for (a) He, (b) Ne and (c) Au ions in Si.*

These plots were generated from EXCALIBUR for 100 ions with energies of 35 KeV.
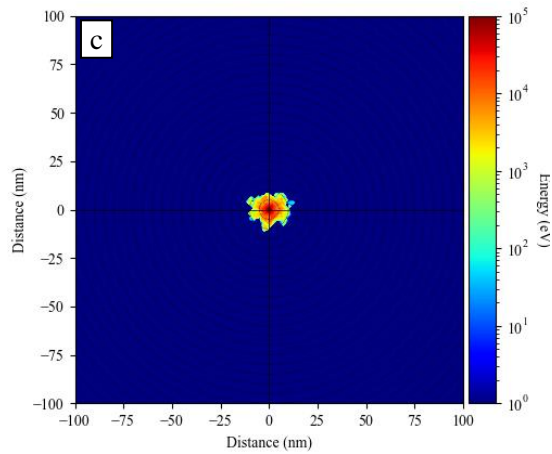
Figure 4.12 *Continued*

To predict the possible shape of an exposure in a resist material 3D energy histogram were produced. The plots are shown in Figure **4.13** and are effectively the x-y plots from Figure **4.12** which have been projected in z plane dependent on their energy. These plots help give an insight as to the potential shape of a structure if a resist material were to be exposed with each ion. The results are slightly skewed due to the full extent of the ions being included as if the plots were limited to a thickness similar to the penetration depth of the gold ions then both helium and neon would have much tighter energy spreads.
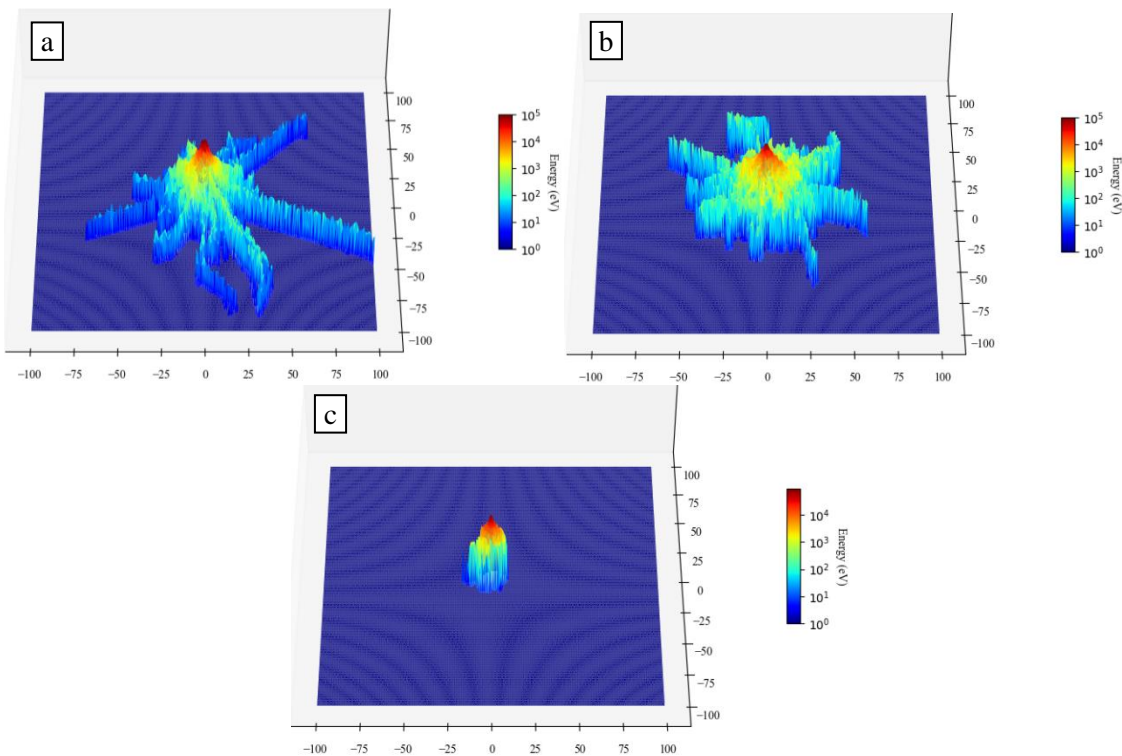
Figure 4.13 *3D heat maps of energy deposits for 35 keV (a) He, (b) Ne & (c) Au ions in Si. These plots were generated in EXCALIBUR for 100 incident ions.*

As with the electron scattering model a qualitative comparison can be made between EXACLIBUR and SRIM by comparing ion trajectory plots to see the spatial distribution of the ions. A simulation was run in both models using 500 ions with energies of 35 KeV in 100 nm of silicon. The plots show good agreement between the two models which show only the primary ion trajectories (no SEs or recoils) for clarity.
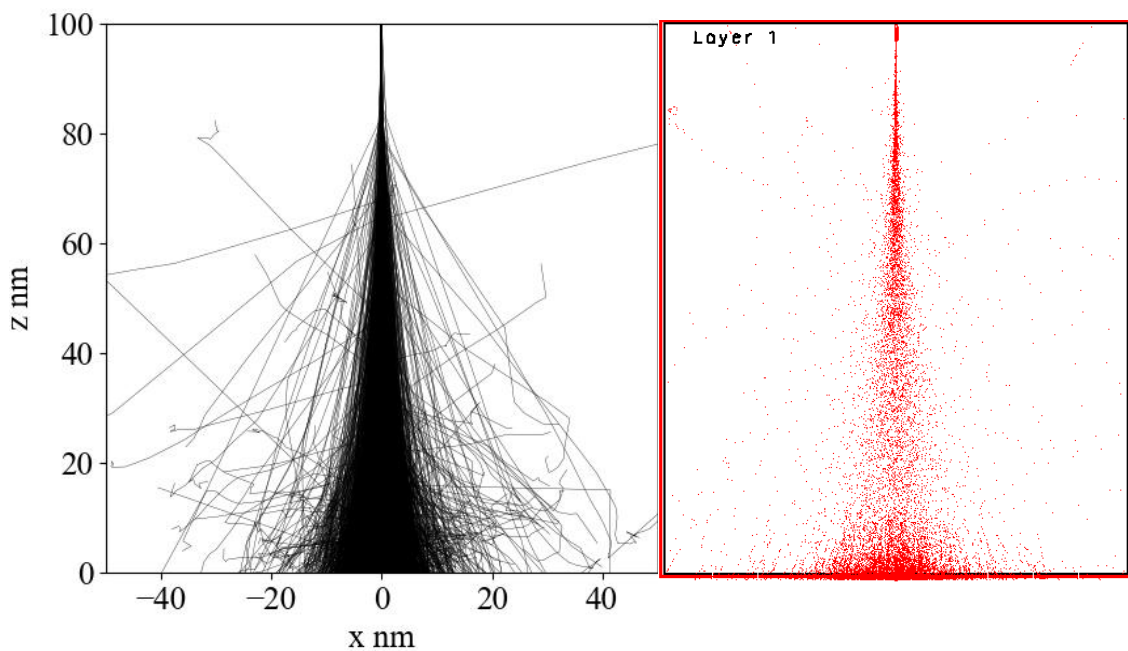
Figure 4.14 *Ion trajectory plots generated using EXCALIBUR (left) and SRIM (right). Both plots were generated using 500 35 keV ions in 100 nm of Silicon.*

4.4 <u>Summary</u>

In Chapter **2** a Monte Carlo simulation for EBL was developed to better understand and help develop and prototype resist materials and identify potentially viable candidates for nano manufacturing without the need for experimentation. The efficacy of this technique was proven in Chapter **3**. As ions offer sensitivity and hence exposure time advantages over electrons there is a growing interest from industry for IBL technologies. Therefore, the ability to use simulation to develop resists for ion exposures is needed. To this end the ion simulation model presented in this model was developed. Whilst there are already well-established ion simulation simulations such as SRIM/TRIM which have been used for many applications they had one feature missing that is essential for the exposure of

resist materials. This feature is the generation and tracking of SEs which are known to be the main mechanic of resist exposure. The ion model developed here has been successful adapted from the previous EBL simulation to be able to expose resists using ions and results have shown that the output of the model is consistent with theoretical expectations.

References

[1] Ziegler, J.F., Biersack, J.P., Littmark, U., "The Stopping and Range of Ions in Solids", Vol 1, Pergamon Press, New York, (1985)

[2] Mueller, G.P., "Total cross-section corresponding to the differential cross-section of Linhard Nielsen and Scharff", Radiat. Eff. Vol 21, pages 253–258 (1974).

[3] Ramachandra, R., Griffin, B., Joy, D., A "Model of Secondary Electron Imaging in the Helium Ion Scanning Microscope" Ultramicroscopy, Vol 109, pages 748–757 (2009)

[4] Lindhard, J., Nielsen, V., Scharff, M., "Cross Sections for Ion-Atom Collisions in Solids" Mat. Fys. Medd. Dan. Vid. Selsk, Vol 36 (1968)

[5] Winterbon, K.B., Sigmund, P., Sanders, J.B., "Spatial Distribution of Energy Deposited by Atomic Particles in Elastic Collisions", Mat. Fys. Medd. Dan. Vid. Selsk, Vol 37 (1970)

[6] Nastasi, M., Mayer, J.W., "Ion Implantation and Synthesis of Materials", Springer-Verlag Berlin Heidelberg, pages 58-60 (2006)

[7] Biersack, J.P., Haggmark, L.G., "A Monte Carlo computer program for the transport of energetic ions in amorphous layers", Nucl. Instrum. Methods, Vol 174, pages 257–269 (1980)

[8] Mahady, K., Tan, S., Greenzweig, Y., Livengood, R., Raveh, A., Fowlkes, J. D., Rack, P., "Monte Carlo simulations of secondary electron emission due to ion beam milling", J. Vac. Sci. Technol. B, Vol 35, 041805 (2017)

5

SUPRAMOLECULAR RESISTS FOR ION BEAM LITHOGRAPHY

Contents

Ion Beam Lithography (IBL) is an area of growing interest as improvements in sources and optics have allowed beams to be produced with geometries and currents that are, in the general sense, comparable with those used in Electron Beam Lithography (EBL). One of the main uses of EBL is the manufacture of photomasks for high volume manufacture (HVM) of semiconductor devices. EBL is used to pattern a resist layer on the mask which is then replaced through metallisation and lift off. Currently EBL is the only technique that can reliably produce the features sizes needed for the masks with the lowest number of defects. As the critical dimensions for the next generation technology node decreases, the complexity of the next generation photomask increases, this leads to longer photomask production times. This is because the proximity effect plays a larger role than

was present with the previous generation of photomask, hence, longer exposure times are required to produce the photomask. This creates a potential bottleneck in the use of photolithography for high volume manufacturing (HVM), where the masks become degraded as they are used to the point where they require cleaning, repairing or complete replacement. To keep up with the demand for photomasks, electron beam systems with variable shaped beam (VSB)[1-3] or multiple beams[1,4], and high beam currents are being developed. As industrial photolithography makes the switch from 193 nm lithography to EUV lithography, smaller on-mask features are required to best utilise the 13.5 nm EUV light. This means, again, an increase in the write times needed to pattern the masks and raises a question about the ability of EBL to continue to meet the demand for photomasks for HVM. IBL could be the replacement for EBL, as it can achieve better resolutions with much shorter write times with comparable beam currents [5]. The reduction in writes times is due to the nature of ions in resist materials and the increased SE yield compared to electrons. This was shown to be a factor of 12.6 for helium ions compared to electrons in silicon (Chapter **4**). Whilst conventional electron beam resists [5-8] can be used with helium ion beam lithography (HIBL) new resist materials which are optimised to exposure with ions will be needed to fully harness the capabilities of these systems.

5.1 <u>Supramolecular Ion Beam Resists</u>

In Chapter 3 a series of modular supramolecular resists were explored for EBL. These resists gave high resolution and have been shown to have ultra-high dry etch selectivity with respect to silicon dry etching, however this came at price. The resist materials required high exposure doses with even the most sensitive resists needing doses that would make write times too long for high throughput device fabrication. This is combined with the inherent increased exposure times from direct write methods compared to mask projection methods used in commercial photolithography. However, due to the nature of

the interactions of an ion beam in resist materials (Chapter **4**) compared to electron beams, the dose for these resists is expected to be reduced.

The nature of these materials and their high etch resistance is also a desirable property for IBL, where resistance to sputtering is necessary to avoid damage to the structures during the fabrication process where many organic resists would be damaged and eroded during exposure.

5.2 <u>Experimental Methodology</u>

Experimentally, the sample preparation for IBL is the same as that EBL therefore sample preparation and spin coating will not be covered here but can be read in Chapter **3.1**. For the ion beam exposures in this chapter a Zeiss Orion NanoFab was used [9]. This system is primarily a helium ion microscope (HIM) with a secondary column for gallium FIB. The helium ion beam is generated using a gas field ion source (GFIS, Chapter **1.2.3**) and a Raith ELPHY MultiBeam pattern generator is used to raster the beam for exposing the resist.

5.3 <u>Results</u>

The suitability of the modular supramolecular resists for IBL was investigated. To best test the resists, ideally, a range of ions should be used on a range of materials but due to limitations around access to this equipment only one material has been tested. This material was resist **A** (Chapter **3.3.1**) which was chosen due to it being the most tested supramolecular resist and it had well defined process parameters. This helps to interpret the results and remove any ambiguity that could come from the processing of the resist material.

5.3.1 <u>Simulation</u>

To understand how resist **A** would respond to exposure by helium ions it can be simulated and compared to results of an EBL simulation for which the exposure parameters are also known (Chapter **3**). Figure **5.1** shows electron trajectory plots for 50 nm of resist **A** on 50

nm of silicon substrate, exposed with 30 kV electrons and 35 kV helium ions. It is clear that the SE yield and energy deposited by the He ions is far greater than the electrons.
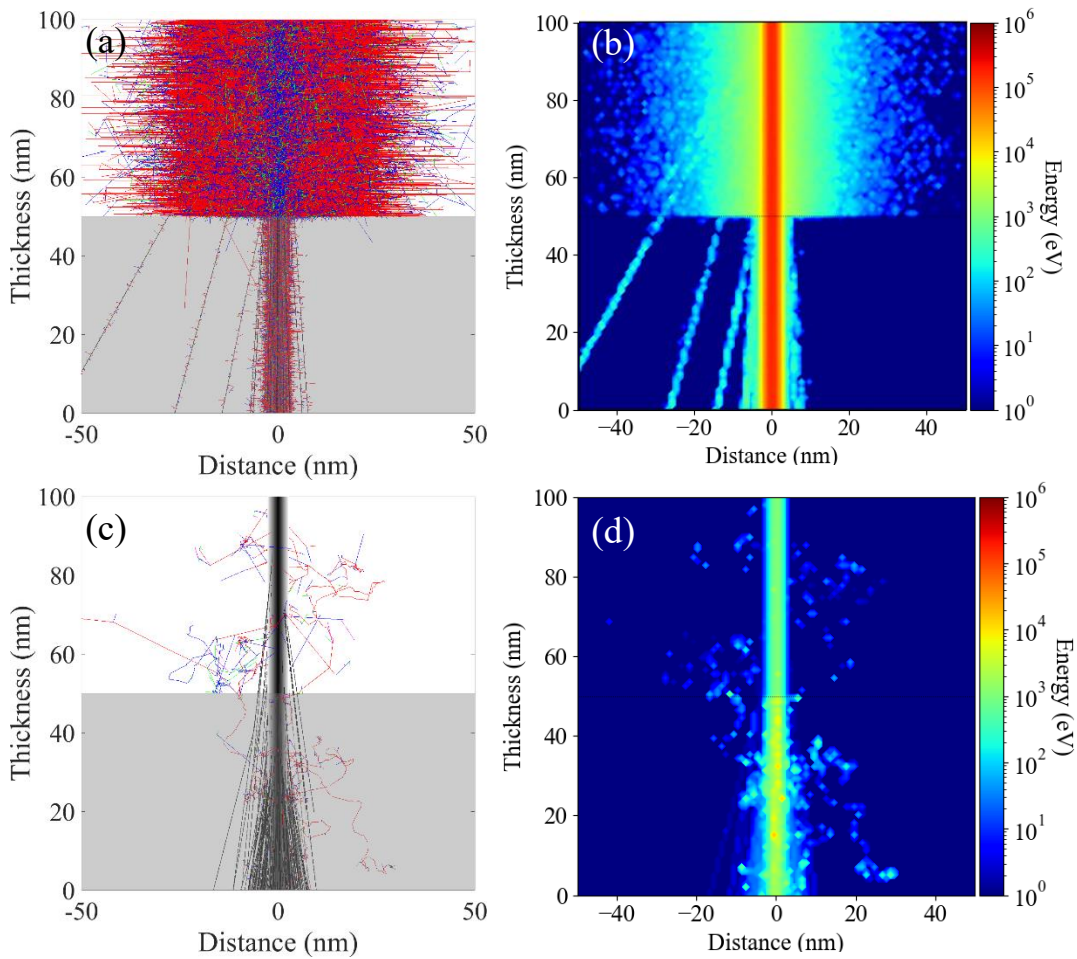
Figure 5.1 *(a&c) profile 35 kV He ion (a) and 30 kV electron (c) trajectory plots for 50 nm of resist A on 50 nm of silicon exposed with a dose of 1000 pC/cm. This equates to 2,500 primary ions/electrons. The primary trajectories a grey scale and the colours of SEs are as follows gen I: red, gen II: blue, gen III: green & gen IV: magenta. Plotted using MATLAB. (b&d) Energy deposit plots of the ion and electrons trajectory plots. All simulations run using EXCALIBUR.*

Due to the low density and high molecular weight of resist **A**, the mean free path for the low energy SEs generated is much larger than for the silicon, this effect is very apparent in Figure **5.1.a&c**. The number of SEs generated in resist **A** in the trajectory plots is shown in Figure **5.2**. The number of SEs generated for the electron plot is 858 and for the He ion plot this value is 827 times larger at 710,091. This is a dramatic increase which

suggests that the dose for exposures of resist **A** could be as low as 27 pC/cm compared to the electron beam dose of 22,000 pC/cm at 100 nm pitch. The SE cascades have been depleted by the 4th generation either by the electrons being backscattered out of the top of the resist or passing into the substrate or by the electrons terminating, having dropped below the energy threshold of the model which is defined as the C-C bond energy of 3.6eV.
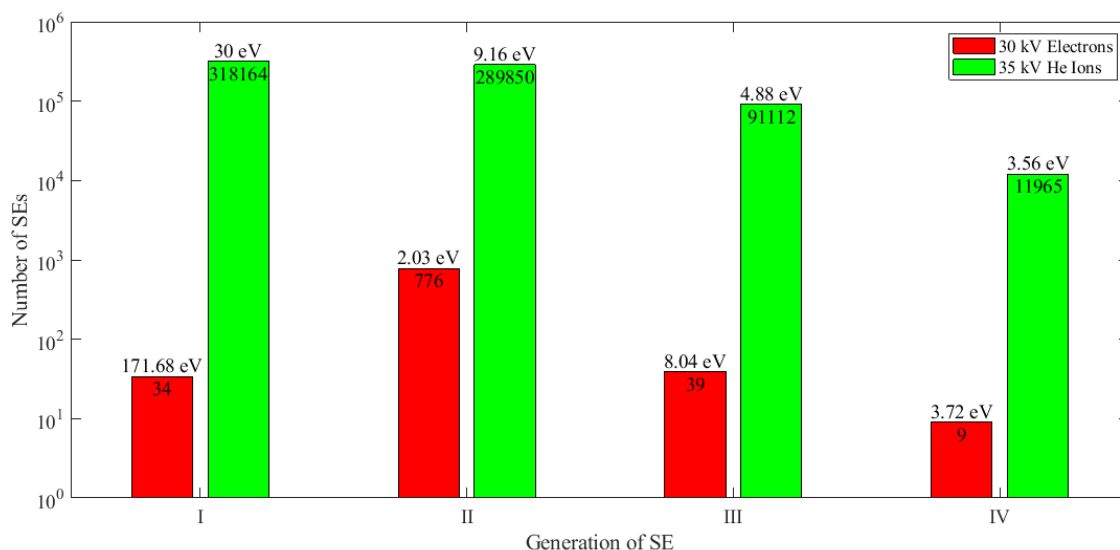
Figure 5.2 *A plot of the number of SEs generated per generation for 35 kV He ions and 30 kV electrons in 50 nm of resist **A** on a 50 nm Si substrate. Also shown are the average energies of each generation. All values are extracted from EXCALIBUR simulations where a single spot was exposed with a dose of 1000 pC/cm which corresponds to 2500 initial primaries. These values are the average for 1000 repeats.*

5.3.2 Helium Ion Beam Lithography

A solution of resist **A** was prepared in hexane (30 mg **A** in 3 g hexane) and then spun onto silicon wafers at a spin speed of 6000 rpm, this rendered films with a thickness of 4 nm as measured after exposure. The samples were then exposed with a series of lines of varying doses and pitches to explore the relationship between pitch and dose. These exposures were carried out using the Zeiss Orion Nano Fab HIM with a beam acceleration voltage of 35 kV and a beam current of 0.5 pA and a spot size of 400 pm. This acceleration

voltage, which is the maximum voltage of the system ensured the ions could fully penetrate the resist material. Once the resist was exposed it was developed using hexane and then loaded back into the HIM to be imaged. Figure **5.3** shows the resolved structures after development with pitches of 22 nm down to 16 nm. This result shows an excellent lithographic performance far outperforming the comparative results from EBL exposures.
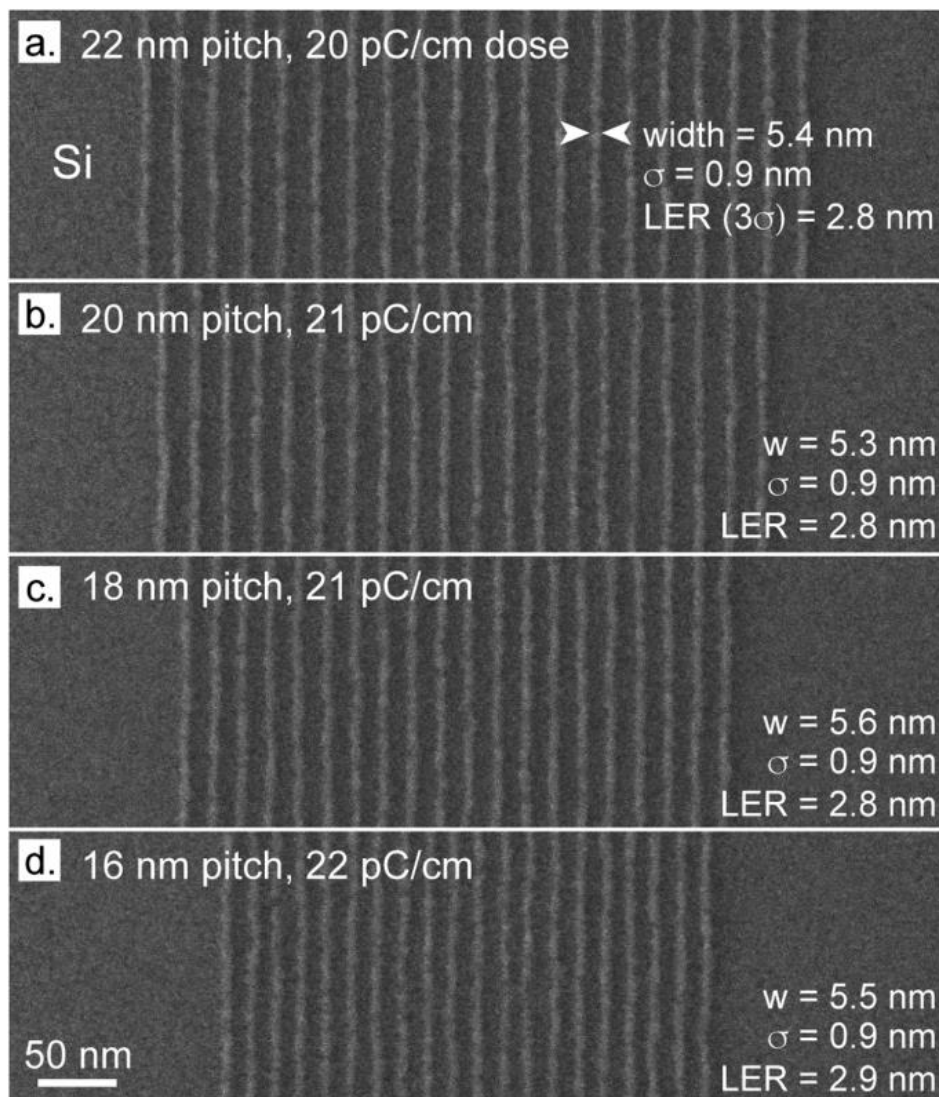
Figure 5.3 *An HIM micrograph of patterned line spaces structures in Resist A on a silicon substrate, with resolved pitches of 22-16 nm (a-d). Also shown inlaid in each subplot is the line width (w), the standard deviation of the line width (σ) and the line edge roughness (LER) [5]. These values were measured and calculated using GenISys ProSEM software [10].*

The highest resolution achieved was 16 nm lines with a line width of 5.5 nm using a dose of 22pC/cm. When compared to the EBL results for resist **A** it is apparent that the use of ions has greatly reduced the required exposure dose by 3 orders of magnitude, from 20,000-30,000 pC/cm down to 22 pC/cm all the while decreasing the pitch and maintaining a sub 10 nm feature size. The structures show good resilience to damage from helium ions which were used, for both imaging and patterning. Also, the short exposure times are below those required for helium ions to begin implanting, which can cause dislocations in the silicon substrate which would be undesirable for semiconductor device manufacturing [11]. The dose needed to expose these structures is very similar to that predicted by the model where a value of 27 pC/cm was predicted showing that He ions showing good agreement with the model. However, the SEs themselves might not be the main mechanism of exposure as even though the first wave of SEs is generated with the primary ion beam the second generation is generated over a radius of 40 nm from the centre of the ion beam which is not reflected in the resolution of the structures.

The experiment parameters used to pattern the structures seen in figure **5.3** were used to run a helium ion simulation in EXCALIBUR. In the simulation a dose of 22 pC/cm and a step size of 1 nm corresponds to a dose of 14 He ions per spot. The exposure pattern consisted of 16 nm pitch lines with every point being exposed in sequence to generate a 3D plot of the primary ion and secondary electron trajectories. Figure **5.4** show comparisons of the 3D trajectory plot generated by EXCALIBUR and tilted HIM images of the HIBL structures in Resist **A**.

In Figure **5.4.a** the primary ion tracks can be seen in grayscale and show the exposure pattern. The SEs generated from these interactions, as well as any subsequent generations of SEs from the resulting cascade, are shown with each generation bearing a different colour. First generation secondary electrons are shown in red, 2nd generation in blue, 3rd in green and 4th in magenta.
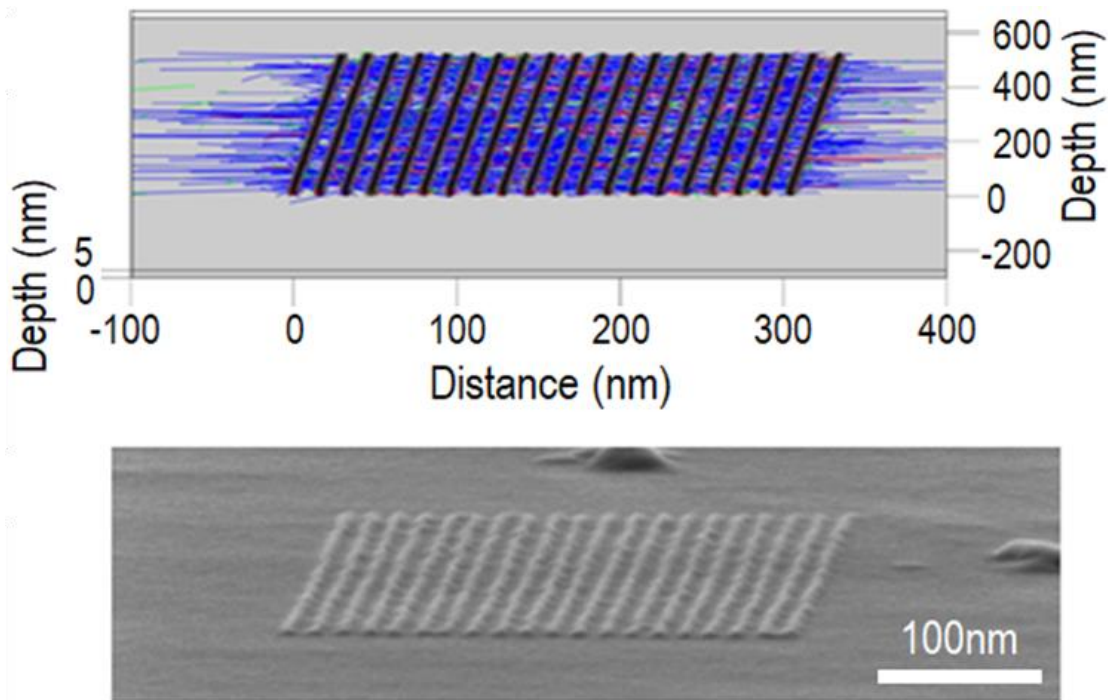
Figure 5.4 *(a) 3D simulated tracks of Incident Ions (Black) and subsequent generations of secondary electrons (I:Red, II:Blue, III:Green and IV: Magenta) generated using EXCALIBUR. (b) Helium ion micrograph of 16 nm pitch helium ion beam lithography (HIBL) structures in resist **A** on a silicon substrate.*

To allow for better visualisation of the exposure of the resists the primary ions can be removed from the render and then the remaining SE tracks are superimposed over the images of the HIM micrographs seen in Figure **5.5**.
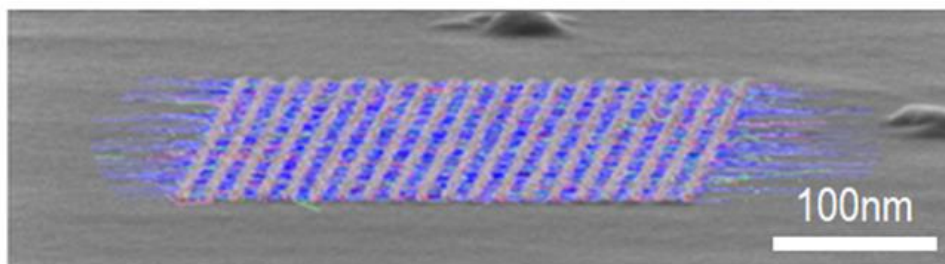
Figure 5.5 *A composite image showing the simulated ion trajectory plot shown in Figure **5.4.a** superimposed over the HIM micrograph Figure **5.4b**. Both the simulation and the micrograph show the exposure of Resist **A** (Chapter **3**) on an Si substrate by 35 kV helium ions.*

This puts the proximity exposure of the SEs into context and shows how these cascades can lead to LER and bridging between structures. However, these structures do not show high LER (2.8 nm) and very low pitches have been achieved that would not be possible according to the spread of the SEs

To investigate how the energy is deposited across the whole pattern a plot of the spatial distribution of the energy in the XY plane was made and is shown in Figure **5.6**, the Z axis has a value defined by the energy of the XY box (1 x 1 nm) to give a volumetric representation of the energy deposit. It is evident that nearly all the energy transferred to the resist is deposited within the footprint of the primary exposure beam which is in agreement with the hypothesis that the primary ions and the creation of the first generation of SEs are responsible for the exposure of the resist.
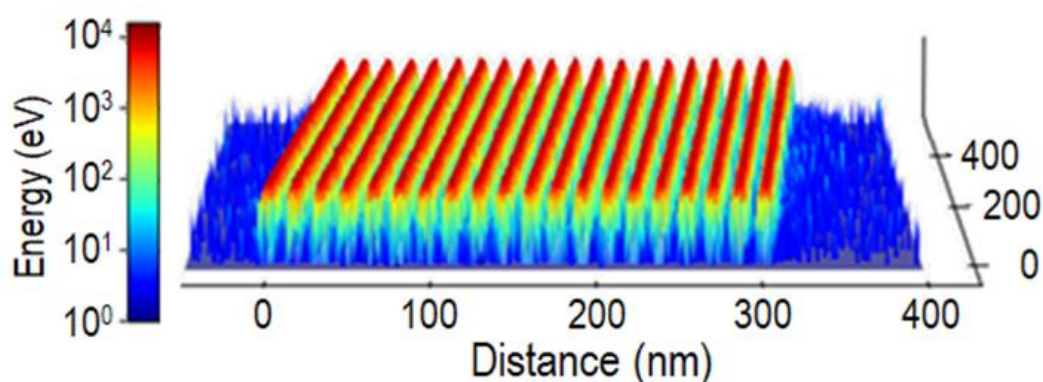
Figure 5.6 *Energy deposit plot for He ions in 4 nm of resist A on a Si substrate showing where energy is deposited in the x-y plane during HIBL exposure. The 16 nm pitch pattern was exposed with a dose of 22 pC/cm and has the same geometries as those used in Figure 5.4*

5.3.3 Beyond Helium Ions

To fully understand the extent of applications for which the supramolecular resists could be used, it will be necessary to expose the chromium ring resist with a range of ion sources. The types of ion sources that could be utilised for lithography vary but some examples of those with the necessary beam parameters for high resolution lithography are

the helium and neon ion beams generated by the Zeiss Orion NanoFab and the Au ions from the Raith VELION.

It is understood that heavier ions have increased stopping power and therefore higher secondary electron yields. This could mean that by moving up the periodic table away from He could mean even lower doses than those observed for HIBL, there is however a trade-off with penetration depth.
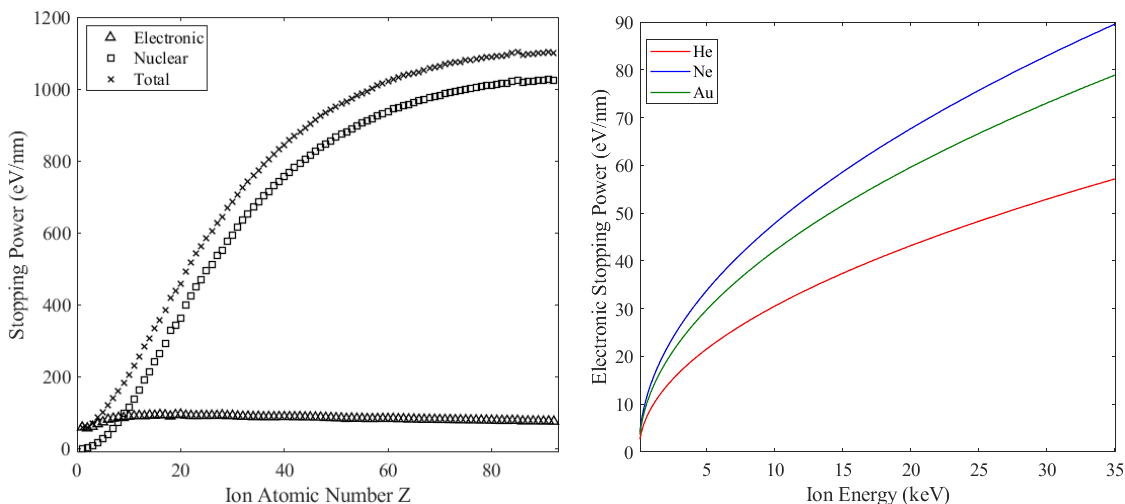
Figure 5.7 *(a) Electronic, nuclear and total stopping powers for ions form hydrogen to uranium with an energy of 35 keV in Resist **A** and (b) a comparison of the electronic stopping powers for He, Ne and Au for a range of energies from 1 eV to 35 KeV in Resist **A**. All data calculated using EXCALIBUR.*

Figure **5.7.a** shows how both the nuclear and electronic stopping powers change as the atomic number increases. As discussed in Chapter 4 for He the electronic stopping power dominates and so the nuclear stopping power can be somewhat neglected for lithography simulations. As the secondary electron yield is directly proportional to the electronic stopping power then Figure **5.7.b** would suggest that Ne would be a better candidate than Au for higher sensitivity lithography. However, for Au the nuclear stopping power is no longer insignificant, and this means that it can no longer be ignored.

The nuclear stopping power encompasses interatomic effects between the incident ion and the atoms of the molecules in the resist, the most important of which, for this

study, is the generation of secondary ions. These secondary ions will themselves generate secondary electrons as they travel through the resist and if they have sufficient energy, they could generate further secondary ions. The overall effect of this is that Au will have a much greater SE yield than at first suggested.

5.4 <u>Outlook</u>

As seen in EBL the sensitivity of resist to exposure can be increased to give faster write speeds and hence increased manufacturing throughput. However, this comes at a cost, as the proximity effect from the increase in secondary electrons could lower the maximum resolution of the lithography and hence the minimum feature size that could be fabricated on a photomask. This is not a concern for IBL as the increase in secondary electron yield means that resist sensitivity does not have to pushed to it limits. Also, the exposure dose can theoretically be reduced by using a heavier ion that than helium, but this will lead to potentially decreased resolution due to the reduction of range in the ions and their lateral in the resist. However, current results for EUV which display the smallest features sizes show 14 nm structures with a pitch of 24 nm for a single patterning process [12]. This means that any feature on the mask will be larger than this. Therefore, the loss of maximum resolution may not outweigh the increase in mask throughput especially as industry looks to toward double patterning to reach smaller feature sizes.

Looking forward, IBL is an important area for nanotechnology and may one day even replace EBL for the manufacture of photomasks if the results shown here and by others continue to be replicated and improved upon. As this technology is proven to be a reliable technique and systems such as the Zeiss Orion and Raith VELION FIB-SEM become more widely available to research applications then the demand for suitable materials will also increase. However, source stability is still an issue for GFIS's with stable currents only being achievable for a few hours before the tip must be reconditioned. This would be undesirable for mask manufacture. Nevertheless, the use of heavier ions

generated using LMAIS's such as that of the Raith VELION may provide this stability, with Raith reporting 1% current fluctuation per 4 hours [13].

5.5 <u>Summary</u>

The experimental results presented here show that the modular resist platform of supramolecular resists developed earlier in this thesis have yielded promising results for HIBL, having fabricated structures 5.5 nm lines with a 16 nm pitch the current best result for EBL of 60 nm pitch (at 30 kV) using the same material. This improvement was attained whilst also giving a reduction in dose by 3 orders of magnitude from 22,000 - 28,000 pC/cm (100 – 50 nm pitch) down to 22 pC/cm (16 nm pitch). The same resist design philosophy used to vastly improve the EBL resists (Chapter **3**) could be applied to HIBL which may realise ion beam resists with high write speeds and etch selectivity, whilst maintaining the pitch and feature size shown here. This provides evidence that IBL could be a successor to EBL as the main process of the manufacture of photomasks.

References

[1] Shamoun, B., et al, "Multi-Beam Mask Writer in EUV era - Challenges and Opportunities", Proc. SPIE 11610, Novel Patterning Technologies 2021 (2021)

[2] Hahmann, P., et al, "High Resolution Variable-Shaped Beam Direct Write", Microelectronic Engineering 84 (2007)

[3] Fujimura, A., Willis, J., "2020 Mask Maker Survey Conducted by the eBeam Initiative," Proc. SPIE 11518, Photomask Technology 2020, 115180E (2020)

[4] Klein, C., Platzgummer, E., "MBMW-101: World's 1st High-throughput Multi-beam Mask Writer" Proc. SPIE 9985, Photomask Technology 2016 (2016)

[5] Lewis, S.M., Hunt, M.S., DeRose, G.A., **_Alty, H.R._**, Li, J., Wertheim, A., De Rose, L., Timco, G.A., Scherer, A., Yeates, S.G., Winpenny, R.E.P, "Plasma-Etched Pattern Transfer of Sub-10 nm Structures Using a Metal–Organic Resist and Helium Ion Beam Lithography", Nano Lett., Vol. 19 (2019)

[6] Bruchhausa, L., et al, "High Resolution and High Density Ion Beam Lithography Employing HSQ Resist", Microelectronic Engineering, Vol. 97 (2012)

[7]   Shi, X., Prewett, P., Huq, E., Bagnall, D. M., Robinson, A.P.G., Boden, S.A., "Helium Ion Beam Lithography on Fullerene Molecular Resists for Sub-10 nm Patterning", Microelectronic Engineering, Vol. 155 (2016)

[8]   Sidorkin, V., van Veldhoven, E., van der Drift, E., Alkemade, P., Salemink, H., Maas, D., "Sub-10-nm Nanolithography with a Scanning Helium Beam" J. Vac. Sci. Technol. B Microelectron. Nanometer Struct., Vol. 27 (2009)

[9]   Elswick, D., Ananth, M., Stern, L., Marshman, J., Ferranti, D., Huynh, C., "Advanced Nanofabrication using Helium, Neon and Gallium Ion Beams in the Carl Zeiss Orion NanoFab Microscope.", Microscopy and Microanalysis, Vol. 19 (2013)

[10]   ProSEM, GenISys GmbH, Munich, Germany

[11]   Livengood, R., Tan, S., Greenzweig, Y., Notte, J., McVey, S., "Subsurface Damage from Helium Ions as a Function of Dose, Beam Energy, and Dose Rate.", J. Vac. Sci. Technol. B Microelectron. Nanometer Struct., Vol. 27 (2009)

[12]   De Simone, D., et al, "28nm Pitch Single Exposure Patterning Readiness by Metal Oxide Resist on 0.33NA EUV Lithography," Proc. SPIE 11609, Extreme Ultraviolet (EUV) Lithography XII (2021)

[13]   Bauerdick, S., Sanabia, J., Mazarov, P., Fridmann, J., Bruchhaus, L., Jede, R., "Advanced Ion Source Technology for High Resolution and Stable FIB Nanofabrication employing Gallium and new Ion Species." Microscopy and Microanalysis, Vol. 20, 312-313 (2014)

6

3D NANOLITHOGRAPHY

Contents

6.1 <u>Introduction</u>

As the semiconductor has progressed to keep the pace set by Moore's law for silicon-based ICs there has always been research across the wider field of nanotechnology to find the next step for IC fabrication and architecture. Whilst there are endeavours to extend the development road map for Silicon based technologies this progress is becoming slower and more expensive with every step. Consequently, the key areas of research have been shifting to developing new materials to succeed silicon as the favoured substrate or new device architectures which can make use of emerging fabrication technologies to achieve new concepts that were previously unattainable. This chapter will focus on one of these emerging fabrication technologies that could potentially allow the manufacture of 3D ICs. Whilst some may currently consider current microprocessors to employ 3D

architectures [1], these are just interconnected layers of 2D devices stacked to make a 3D structure, here is presented a novel process that can make truly 3D structures using conventional EBL processes.

6.2 State of the Art

Whilst manufacturing devices using 3D lithographic methods is not a new idea, the advent and growing popularity of conventional 3D printing [2] has again drawn the focus of research toward development of 3D nanofabrication techniques.

A method of nanofabrication that is used for producing 3D structures is two photon polymerization (TPP). TPP uses the two photon absorption phenomena to expose and hence polymerize resist materials to fabricate structures. Two photon absorption occurs when an atom is energised by simultaneously absorbing two photons as seen in Figure **6.1**. The energising of these atoms breaks bonds in the resist creating free radicals which lead to cross linking of the polymer chains of the resist rendering the exposed voxel insoluble. [3]
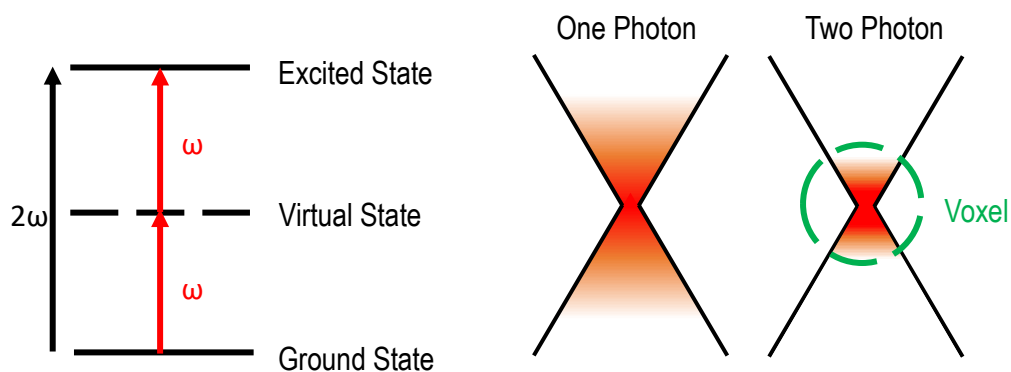
Figure 6.1 *The left diagram is a simple schematic of Two Photon Absorption (TPA) showing the energy levels involved in a two-photon interaction. The right diagram is a comparison of the cone exposure for two photon compared to a single photon exposure. Marked in green is the exposure area or voxel that will remain after development.*

To initiate the two-photon effect a mono chromatic laser is fired into the resist material, the focal point of the beam is the point at which the probability of TPP occurring is highest, generating a point of exposed resist or voxel suspended in the resist. This effect

is shown in Figure **6.1** in contrast to conventional direct write laser lithography. A series of points are then connected to form a structure. As with any other method of the lithography the remaining unexposed resist is removed in development realising the structures. Two photon lithography is a diffraction limited process limiting the smallest feature sizes to approximately 100 nm [4][5]. Whilst this is suitable for many lithographic applications it limits its use as a true nano fabrication technique and as a candidate for next generation manufacturing. Some progress has been made in reducing the minimum feature size down to features as small as 15 nm but these features were not discrete and were instead polymerized bridges between adjacent structures effectively harnessing the proximity effect [6]. Once a structure has been produced using TPP it can be metalized to make the structure conductive or to give it mechanical rigidity. The metallisation of these structures is similar to the lift off process where a metal is thermally evaporated so that it coats the structure and then the underlying resist is removed either through dissolving or etching. [7]

Despite the demonstrated success of TPP there has been a shift towards Focused Electron Beam Induced Processing (FEBIP) to produce 3D nanostructures and devices. FEBIP is an encompassing term used to describe a range of nano fabrication techniques that, like lithography, rely on the use of electron or ion beams to dissociate precursor chemicals to generate structures on a substrate. The most relevant technique as a comparison to the work presented here is Focused Electron Beam Induced Deposition (FEBID). This technique is an additive process where a gas of a precursor material is flowed over a substrate, so the molecules adsorb onto the surface. An electron beam is then used to expose the substrate, dissociating the molecules in the gas, so they are deposited on the material and will not desorb from the surface. By repeatedly exposing a pattern, layers are built up to fabricate a structure. This process is highly dependent on the material properties of the precursor, such as its propensity for adsorption and its

159

volatility which will affect both the growth rate of the layers and the time before desorption. As this is an additive process FEBID can be thought of as an analogue of conventional 3D printing for nanofabrication. By using metal carbonyl precursor materials, it is possible to use FEBIP to produce metal nanostructures. This eliminates the need for lithography, metallisation and lift off.

The 3D nano structures that can be created using this technique can take on a high complexity [8] and as the resolution of the process is dependent on the diameter of the electron beam used [9] then the minimum feature size is theoretically comparable to EBL [10]. Practically, this is often not the case. This is due to the volatility of the precursor and the proximity exposure from the secondary electrons generated in the dissociation process and backscattered from the substrate.

The nature of FEBID precursor materials means that attaining metal structures with a high purity needs a series of steps to remove the undesired carbon, oxygen and other organic molecules remaining as by products after exposure. Regardless, high purity metal structures (Pt=100% Au>90%) have been achieved by heating the substrate to promote desorption and using a parallel reactive gas injection. Purity can also be improved by irradiating the structures post fabrication with electrons or high-powered lasers. The combination of these techniques into one process has led to the development of the so named "Cleanroom in an SEM" which as a concept aims to complete full device fabrication and analysis in one chamber [11].

FEBID is a direct write process, so it has the same downsides as EBL as a potential mass manufacturing process due to the long write times vastly reducing throughput compared to conventional methods. However, similarly to EBL, Ions are starting to be explored as exposure sources for focused ion beam induced deposition (FIBID) [12]. The use of Ions greatly increases the efficiency of dissociation of precursors hence reducing the exposure time whilst increasing the resolution. [13]

FEBID and TPP are both capable of producing 3D metal structures which are an essential feature of semiconductor devices however, to truly harness this technology it must be possible to manufacture structures using semiconductor materials. This would allow geometries of semiconductor devices that are not currently possible and reduce the number of manufacturing steps needed to produce current devices.

6.3 <u>Depositing Resists via Thermal Deposition</u>

The first step toward directly patterning a semiconductor material is being able to directly pattern a resist material that either has inherent semiconductor properties or a material that can be processed to become semiconducting after fabrication. In a similar way to FEBID these resist materials need to be used under vacuum conditions, hence they require a unique characteristic. This characteristic is that when heated sufficiently the resist materials can be sublimed. The thermal sublimation of these resists means they can be deposited on a substrate without the need for spin coating and can be "developed" after exposure through resublimation of the unexposed material, removing the need for solvents. Therefore, this process can be done completely within a vacuum allowing the layers that need to be built up for the 3D patterning to be deposited in the patterning environment.

One such suitable resist material for deposition via sublimation is zinc acetate dihydrate. The viability of this material to be used as an electron beam resist is published in a 2021 paper in ACS Applied Nano Materials [14]. This material can be sublimed when heated in a vacuum to allow it to be deposited on a resist. Figure **6.2** shows the chemical reactions as the material changes into its form that is deposited during evaporation. Firstly, the water that held interstitially in the molecule is evaporated out of the bulk material through gentle heating in a vacuum, then the remaining zinc acetate will then react to form the basic zinc acetate molecule $Zn_4O(O_2CCH_3)_6$ as well as acetone and carbon dioxide both of which will diffuse out of the resist. It is this molecule that is then

evaporated and deposited onto the substrate. It was hypothesised that the basic zinc acetate could then be converted into ZnO which is an n-type wide a band gap II-VI semiconductor. This conversion was hypothesised to be carried out through annealing of the resist by the electron beam during exposure.

$$Zn(CH_3COO)_2 \cdot 2H_2O(s) \Rightarrow Zn(CH_3COO)_2(s) + 2H_2O(g)$$

$$4Zn(CH_3COO)_2(s) \Rightarrow Zn_4O(CH_3COO)_6(s) + CH_3COCH_3(g) + CO_2(g)$$
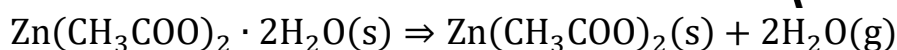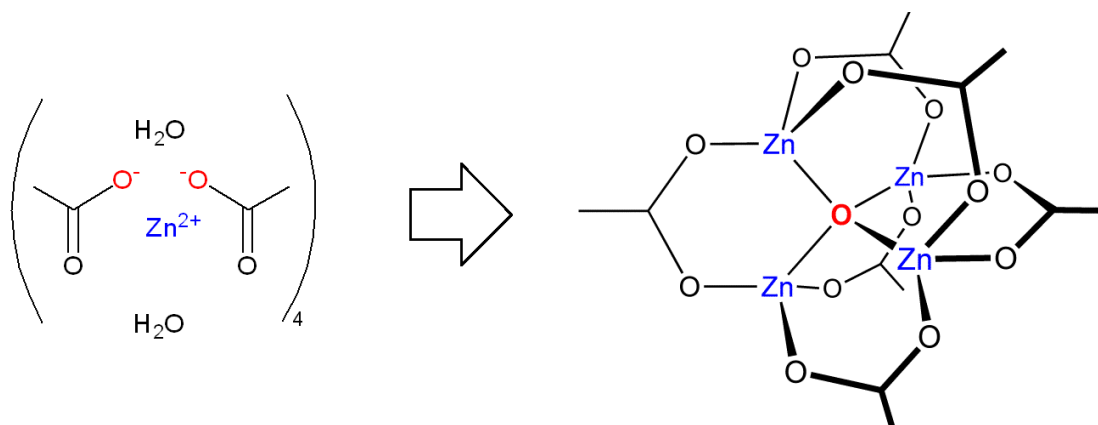
Figure 6.2 *Molecular diagrams of the conversion that zinc acetate dihydrate undergoes when heated in a vacuum and converted into basic zinc acetate which can then be evaporated. The two chemical reactions responsible for the conversion of zinc acetate dihydrate to basic zinc acetate are shown beneath the diagrams.*

6.4 Experimental Methodology

The process for the thermal evaporations of the zinc oxide is as follows. The evaporation of the samples was initially carried out using an Edwards thermal evaporator. To evaporate the samples, the micro-crystalline powders were loaded into a molybdenum foil boat, placed in the evaporator, and then pumped to a vacuum pressure of 8×10^{-6} mbar. The zinc acetate dihydrate starting material will dehydrate as the pressure decreases, hindering the pumping of the chamber. Therefore, the sample can be gently heated to promote dehydration with care being taken not to strain the vacuum system. Once the starting pressure is reached the boat can be heated slowly until evaporation is detected by the Thin Film Thickness Monitor (TFTM) which is a FTM6. The film is then deposited, controlling the temperature to maintain a deposition rate of 1 nm/s. This rate was found

to give the most even films, whereas if the evaporation rate goes beyond this some larger particles will be caught in the evaporation stream and deposited on the substrate thus decreasing the film quality. Once the required thickness is achieved the heating of the material can be stopped, the boat allowed to cool, and the chamber evacuated.

The process by which the 3D structures are fabricated is that a layer will be deposited and patterned, then the next layer is deposited and patterned. This process is repeated until the required structure pattern is exposed. The full matrix of layers can then be developed all at once leaving the 3D structure. To maintain alignment of the subsequent patterns in each layer, aluminium alignment marks were used. These marks were fabricated on the substrate using a standard lithography metallisation and lift-off process with PMMA [15].
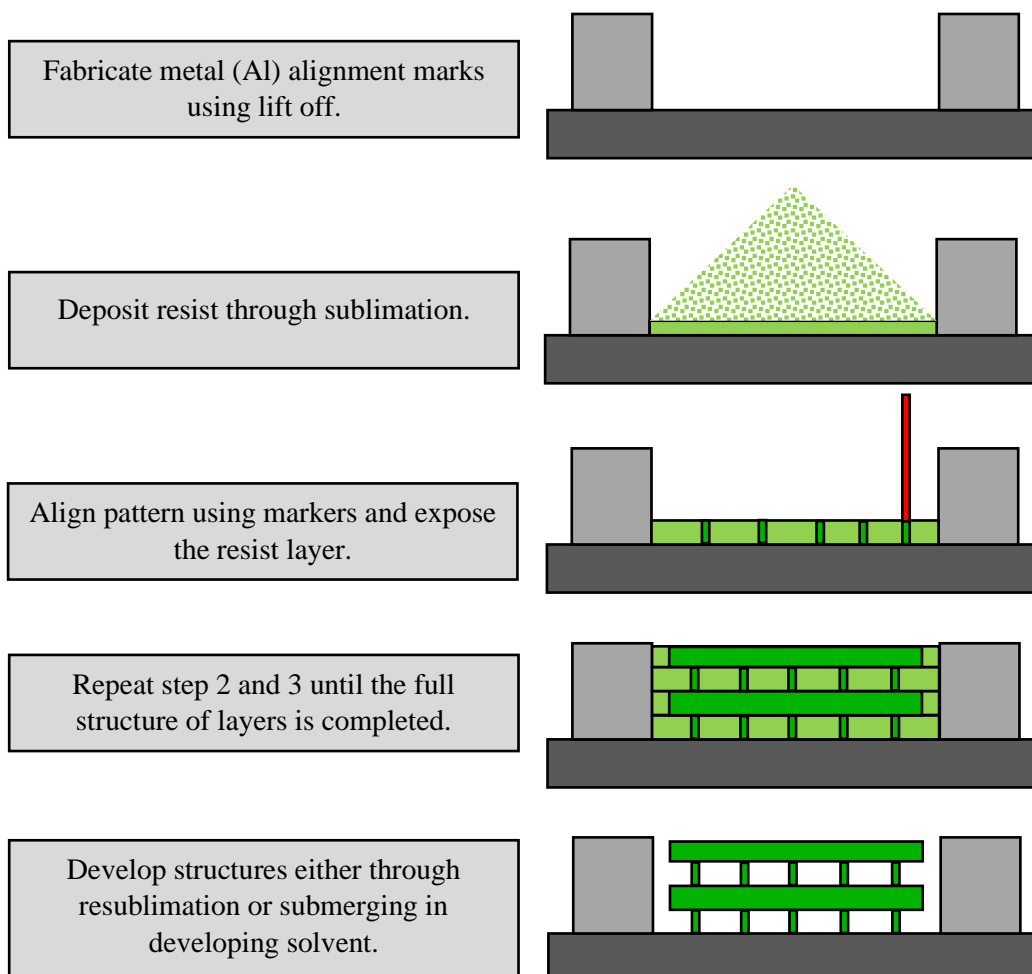
Figure 6.3 *Process flow and schematics of the resist sublimation and exposure for a 3D nanostructure.*

6.5 <u>Results</u>

6.5.1 <u>Depositing and Nano-patterning Semiconductor Materials</u>

Using thermal sublimation, a 74 nm layer of zinc acetate was deposited on a silicon wafer and then exposed using EBL. The pattern was exposed with an acceleration voltage of 30 kV and a beam current of 37 pA and a step size of 2 nm. The structures were then developed by being submerged in methanol for 10 s. Figure **6.4** shows the resolved structures after development. These structures were realised using an exposure dose of 25,000 pC/cm. As can be seen from Figure **6.4** 12 nm lines with a pitch of 40 nm were achieved showing the resists ability to produce high resolution nanostructures.
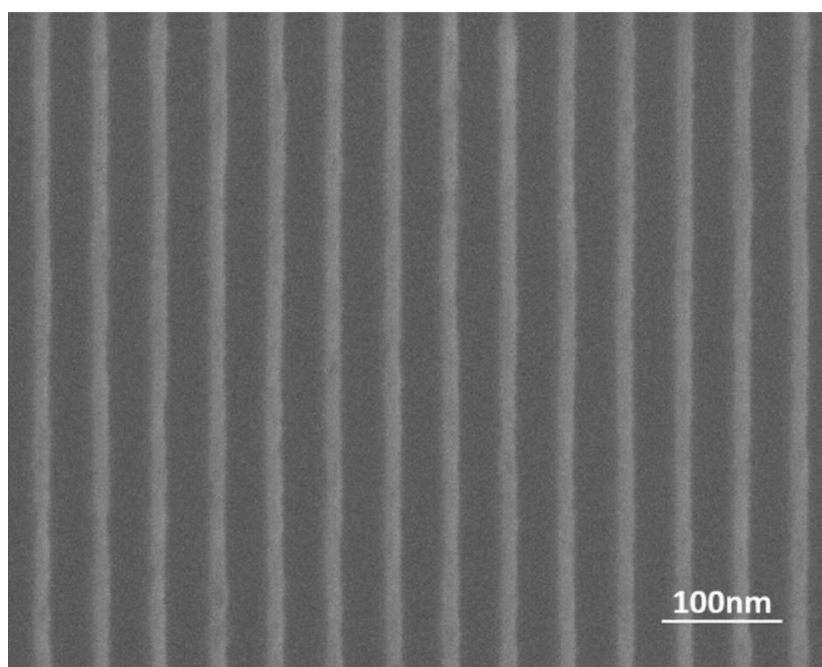
Figure 6.4 *12 nm lines with a 40 nm pitch in basic zinc acetate resist deposited through sublimation. The structures were patterned with a dose of 25,000 pC/cm at 30 kV [14].*

The aforementioned hypothesis was that the basic zinc acetate of the resist would be converted to ZnO through exposure from electron beam. To confirm this change XPS analysis was carried out on a sublimed sample of basic zinc acetate that was then exposed in situ and the XPS spectra was recorded both before and after exposure. Figure **6.5a** show the spectral data for the Zn 2p peaks before and after exposure. These peaks have shifted to lower binding energies after exposure, suggesting a shift to more metallic zinc

compounds. The Zn 2p$_{3/2}$ peak shifted from 1022.1 eV to 1021.7 eV. This is consistent with Zinc Acetate's higher binding energy compared to ZnO [16]. The O 1s spectra (Figure **6.5b**) is also shown before and after exposure. Before exposure the peak is dominated by the carboxylate group (acetate) at 532 eV with the ZnO component of the peak appearing as a small shoulder at 530.4 eV. After exposure, the peak from the carboxylate group was reduced by a factor of 2.7. Conversely, the ZnO peak increased by a factor of 1.7. These changes, of the O 1s peaks and the metallic shift of the Zn 2p, lend plausibility to the hypothesis that when exposed with the electron beam the Zinc Acetate is decomposing and being converted to ZnO as when it is thermally annealed [16, 17].
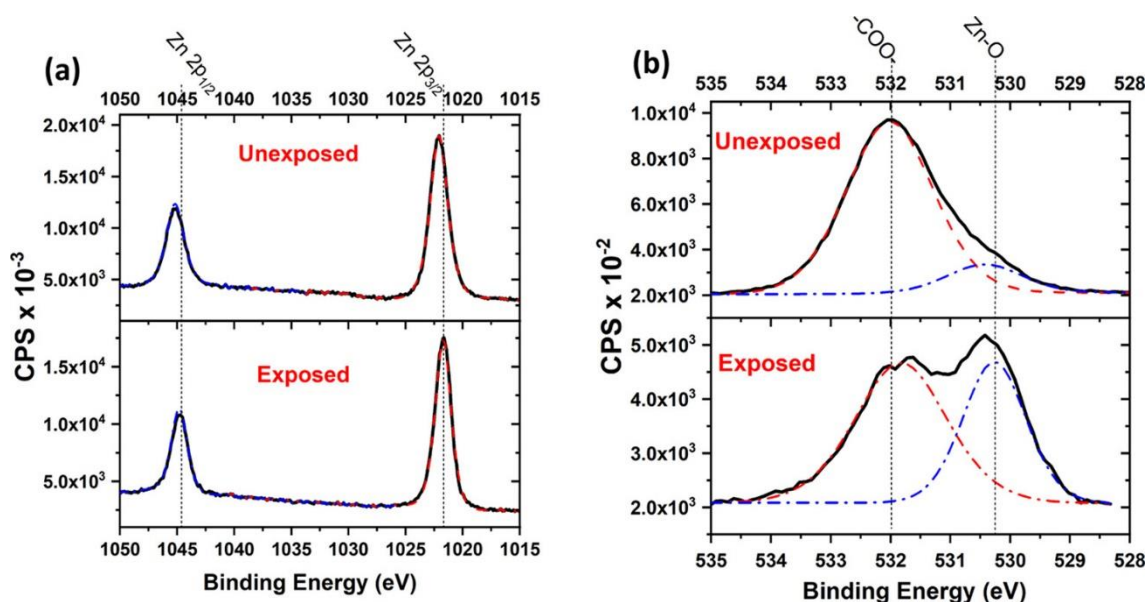
Figure 6.5 *(a)* *XPS spectra of Zn 2p peaks for basic zinc acetate before and after exposure by electron beam. (b) Spectra of the O 1s peak for basic zinc acetate before and after exposure.*

6.5.2 Building 3D Nanostructures Using Supramolecular Resists

As explained in **3.2** the composition of the chromium ring family of resist is, in its most basic form, a ring of 8 chromium atoms connected with fluorine and surrounded by pivalate ligands (Resist **A**). The pivalate ligands that surround these rings allows them to be sublimed when heated. The stability of these rings when heated has been explored using thermogravimetric analysis (TGA) [18] and they were found to be stable when

heated and hence they sublime before they thermally decompose. The pivalate ligands and molecular size means the intermolecular interaction between molecules are relatively weak hence the increased volatility necessary for sublimation [19].

Before experimentally testing the viability of 3D structures produced using resist **A**, a multilayer simulation of a 1 um x 1 um alternating mesh structure was completed using EXCALIBUR. An electron trajectory plot of the full structure can be seen in Figure **6.6**. This simulation was carried out using a beam energy of 30 keV and a dose of 30,000 pC/cm which equates to 75,000 electrons per spot with a 4 nm step size. The plot shown was produced with a reduced number of electrons to reduce the computational demand and time.
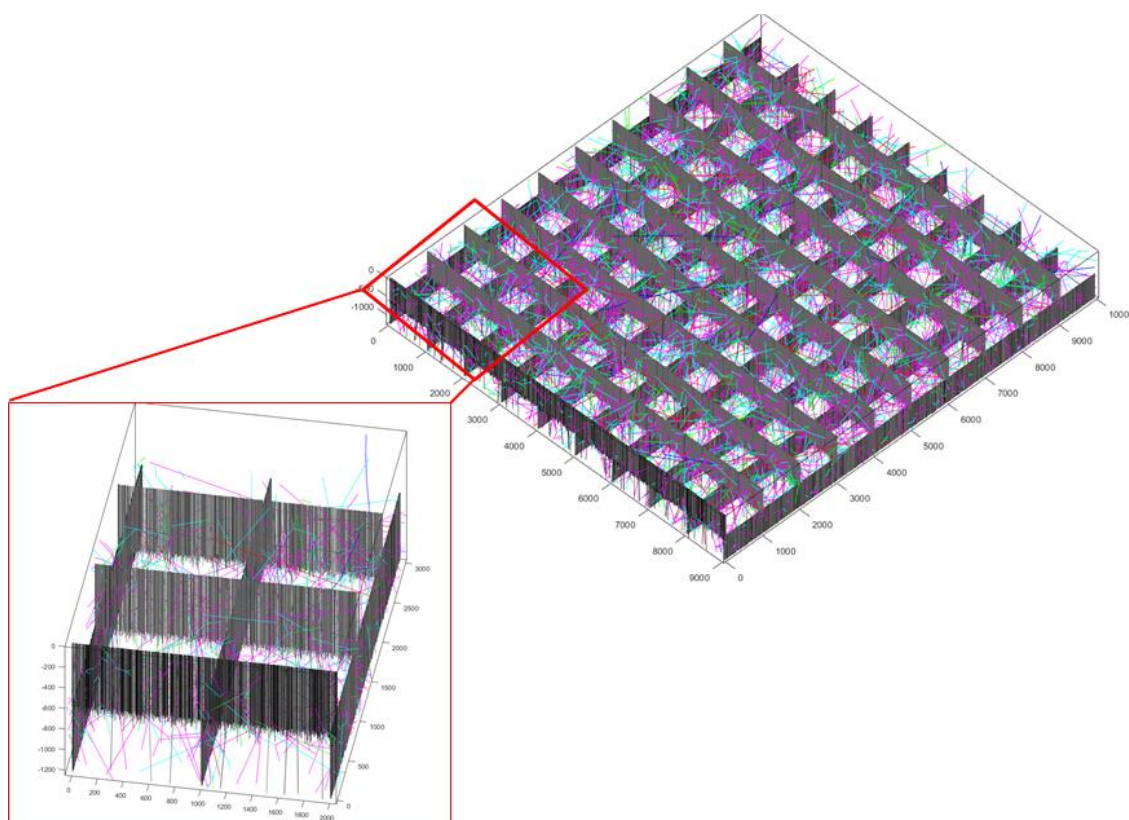
Figure 6.6 *3D electron trajectory plot to show the expected structure of an alternating mesh pattern in Resist* **A**. *Exposed with a beam energy of 30 keV and a dose of 75,000 electrons per spot (30,000 pC/cm).*

The electron tracks for the simulation show that as expected many of the primary electrons will pass through multiple layers of the resist and hence there is the concern that

when a pattern higher up in the stack is exposed then all layers below will also be exposed. To investigate this issue the profile view energy heat maps shown in Figure **6.7** were produced. The heat maps show that in the energy deposited by the primary beam in the first 600 nm (first layer) is an order of magnitude larger than the energy deposited in the second layer. This suggested that it would be possible to pattern suspended structures without effecting the layers below. This effect is clearer to see in Figure **6.7b** where the energy range has been narrowed to remove the background and show the energy gradient of the primary beam more clearly. Obviously, there will still be some amount of exposure caused in the underlying layers so to avoid overexposure the lower layers must be underexposed.
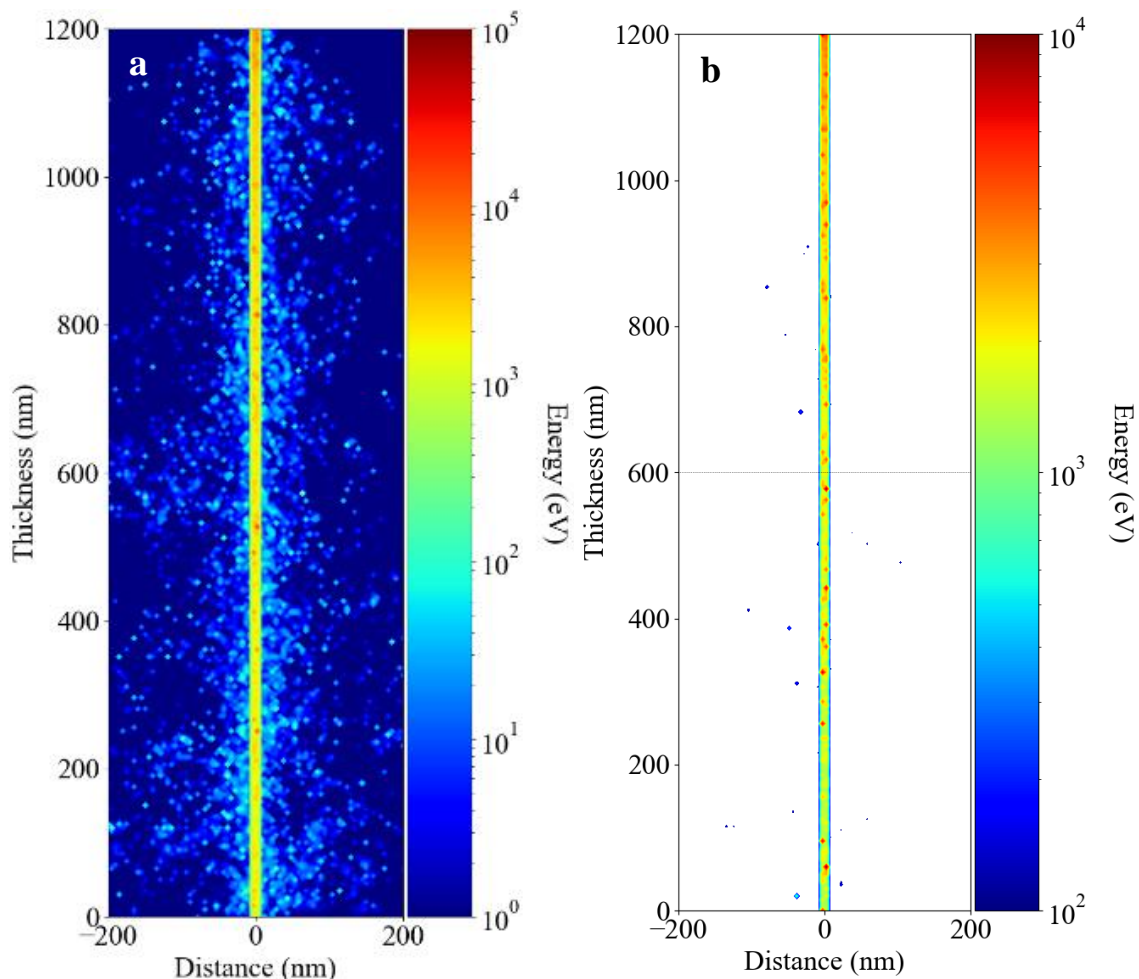
Figure 6.7 *(a) a profile view, energy heat map of 75,000 30 keV primary electrons in 2 600 nm layers of Resist **A** (b) the same energy heatmap with a restricted energy range to highlight the energy change of the primary beam.*

Once satisfied that the simulation had confirmed that the production of the 3D mesh structure was possible then resist **A** was deposited using sublimation onto a polished silicon wafer chip prepared in the same way as those used for spin coating in section Chapter **3.1**. The film was deposited at a rate of 1 nm/s until a thickness of 600 nm was recorded on the TFTM. The sample was then written in using a FEI Sirion SEM with an acceleration voltage of 30 kV, a current of 50pA and a single pixel line dose of 36,000 pC/cm. This deposition and writing process was repeated twice, with each set of lines being perpendicular to the previous set. The whole sample was then developed using hexane for 30 seconds. To better observe the 3D structures a set of small two-layer structures were fabricated in the same manner as the previous experiment but with a larger pitch between the lines in the second layer to allow them to be imaged clearly on a tilted angle. The resolved structures are shown in Figure **6.8** revealing the "air gap" below the lines of the second layer showing the structures are completely suspended by the first layer. This shows the resist material is mechanically strong enough after exposure to hold the structure over the 1 µm gap between the lines of the bottom layer. However, the arched shape of the structures suggests that the exposure between layers cannot be ignored. The proximity exposure in the first layer means that the top layer exposure is greater closer to these structures and hence the lines from the top layer reach deeper into the first layer. The lines themselves were measured to have a width of 40 nm with a layer thickness of 550 nm after exposure delivering an aspect ratio of 13.8:1. It is also clear to see that by underdosing the first layer meant that the lines were not overexposed at the crossing points but the lines that were not crossed by the 2nd layer lines collapsed due to underexposure. This further suggests that the 2nd layer lines are bracing and supporting those in the bottom layer.
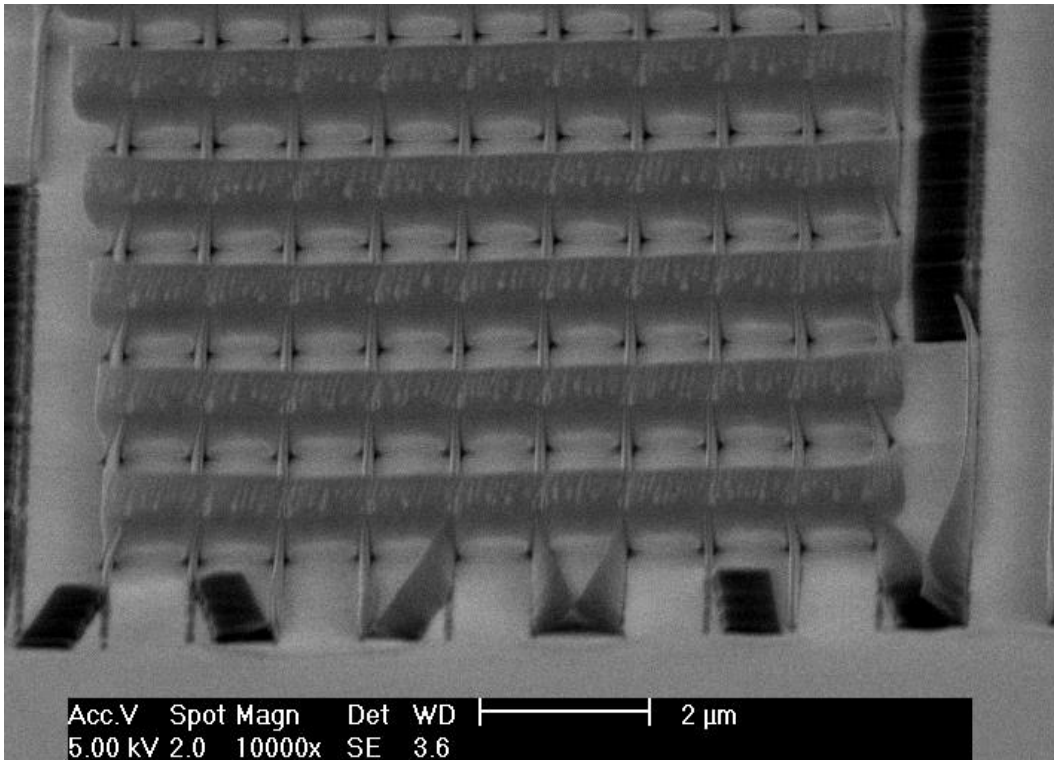
Figure 6.8 *A titled SEM micrograph of two layers of crossing lines. The tilt allows the air gap under the top layer structures to be observed. The collapsed lines were underdosed to prevent overexposure through cumulative exposure.*

To further show the similarity between the simulation and the lithographic results the electron trajectory plots like those shown in Figure **6.6** can be superimposed over the SEM micrographs of the structures the result of which is shown in Figure **6.9**. By doing this it confirms the spatial exposure of the resists by the primary and the secondary electrons matches the experimental results and also acts a useful visual aid in understanding how the structures are formed.
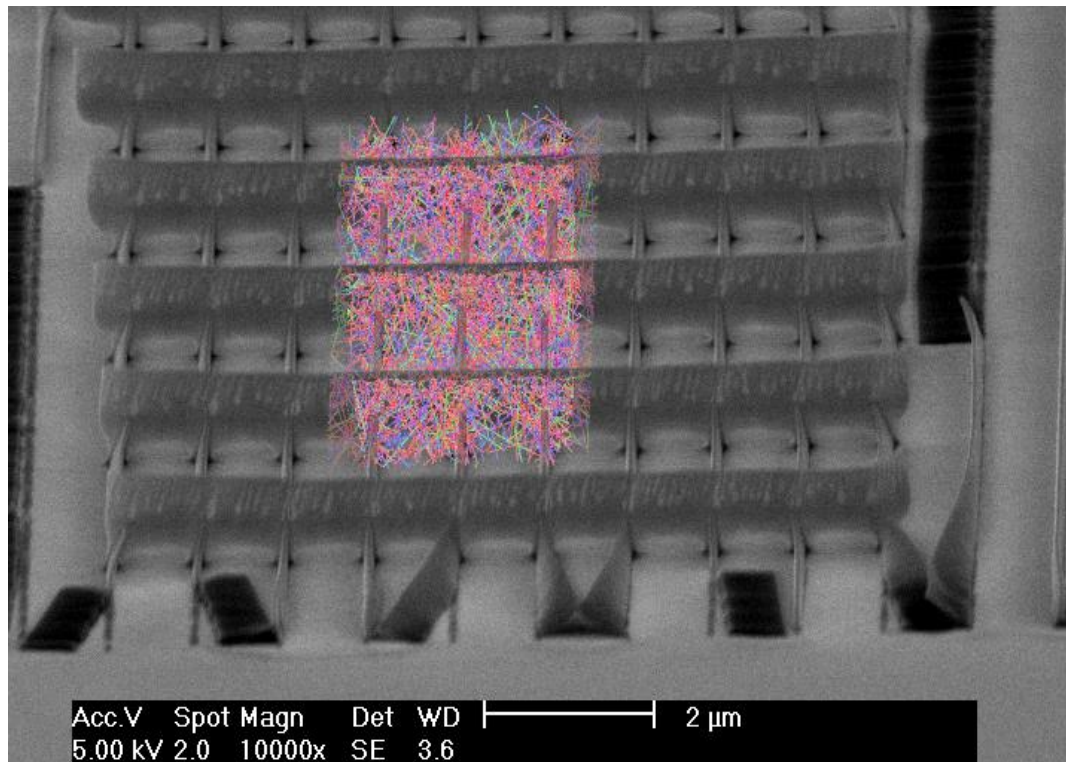
Figure 6.9 *A tilted SEM micrograph of 3D structures with an overlaid image of the*

electron trajectories from the simulation of the exposure of the 3D pattern in resist A.

The simulation plot was generated using EXCALIBUR.

6.6 <u>Summary</u>

The viability of a novel approach to 3D lithography was investigated. For this process two resist materials were explored to understand their viability for sublimation and subsequent exposure by electron beam. Whilst this technique is similar to FEBID, there are some important distinctions. Firstly, the resist films are applied with thicknesses comparable to conventional EBL processes rather than atomic layers like in FEBID. This means that the intended pattern only needs to be applied once per layer rather than repeatedly scanned thus reducing exposure times. Secondly, one of the major advantages of FEBID is that it provides the direct application of metal structures removing the many processing steps required for metallisation. However, the materials here provide exploration of the combination of 3D lithography with traditional pattern transfer techniques such as dry etching. Also, ZnO is a semiconductor material known for its optical transparency with many emerging applications from transparent contacts for

electronics such as liquid crystal displays and photovoltaic windows. The method of applying the films through thermal deposition also allows these resist materials to be applied to unconventional surfaces that would not be suitable for spin coating.

The next step for investigating this technology is to streamline the process to allow films to be deposited either directly in the SEM vacuum chamber or a dedicated chamber connected to the SEM. This would reduce the time taken in transferring the sample from the evaporator to the SEM and the respective pumping times. Also, whilst preliminary experiments were promising, further investigation of the ability to "develop" these resists through heating or annealing of the structures would again be valuable for streamlining the overall process. The characteristics of the modular resist **A** that allow it to be sublimed are also shared by many of resists in the family providing a wealth of materials for this technique. These developments would facilitate the fabrication of more complex 3D structures with a wider variety of materials.

References

[1] Black, B., et al., "Die Stacking (3D) Microarchitecture," 2006 39th Annual IEEE/ACM International Symposium on Microarchitecture, pages 469-479 (2006)

[2] Shahrubudina, N., Lee, T.C., Ramlana, R., "An Overview on 3D Printing Technology: Technological, Materials, and Applications", Procedia Manufacturing, Vol. 35 (2019)

[3] Zhou, X., Hou, Y., Lin, J., "A review on the processing accuracy of two-photon polymerization", AIP Advances, Vol. 5 (2015)

[4] Varapnickas, S., Malinauskas, M., "Processes of Laser Direct Writing 3D Nanolithography", In: Sugioka K. "Handbook of Laser Micro- and Nano-Engineering", Springer, Cham (2020)

[5] Rekstyte, S., et al, "Direct laser fabrication of composite material 3D microstructured scaffolds", 2013 Conference on Lasers & Electro-Optics Europe & International Quantum Electronics Conference CLEO EUROPE/IQEC (2013)

[6] Tan, D., Li, Y., Qi, F., Yang, H., Gong, Q., "Reduction in feature size of two-photon polymerization using SCR500", Appl. Phys. Lett., Vol. 90 (2007)

[7]   Meza1, L.R., Das, S., Greer, J.R., "Strong, lightweight, and recoverable three-dimensional ceramic nanolattices", Science, Vol. 345 (2014)

[8]   Winkler, R., Fowlkes, J.D., Rack, P.D., Plank, H., "3D nanoprinting via focused electron beams", J. Appl. Phys. Vol. 125 (2019)

[9]   Plank, H., et al, "Focused Electron Beam-Based 3D Nanoprinting for Scanning Probe Microscopy: A Review.", Micromachines, Vol 11 (2020)

[10]   Huth, M., Porrati, F., Dobrovolskiy, O.V., "Focused electron beam induced deposition meets materials science", Microelectronic Engineering, Vol. 185-186 (2018)

[11]   Jeevanandam, G., van der Meijden, V., Birnie, L.D., Kruit, P., Hagen, C.W., "'Cleanroom' in SEM", Microelectronic Engineering, Vol. 224 (2020)

[l2]   Fedorov, A.G., Kim, S., Henry, M., Kulkarni, D., Tsukruk, V.V., "Focused-electron-beam-induced processing (FEBIP) for emerging applications in carbon nanoelectronics", Appl. Phys. A, Vol. 117, (2014)

[13]   Córdoba, R., Orus, P., Strohauer, S. et al, "Ultra-fast direct growth of metallic micro- and nano-structures by focused ion beam irradiation.", Sci. Rep., Vol. 9 (2019)

[14]   Chaker, A., ***Alty, H.R.***, Tian, P., Kotsovinos, A., Timco, G.A., Muryn, C.A., Lewis, S.M., Winpenny, R.E.P., "Nanoscale Patterning of Zinc Oxide from Zinc Acetate Using Electron Beam Lithography for the Preparation of Hard Lithographic Masks", ACS Appl. Nano Mater., Vol 4. (2021)

[15]   Blanchard-Dionne, A.P., Meuniera, M., "Electron beam lithography using a PMMA/P(MMA 8.5 MAA) bilayer for negative tone lift-off process", Journal of Vacuum Science & Technology B, Vol. 33 (2015)

[16]   Ma, J., Ji, F., Ma, H.L., Li, S.Y., "Preparation and characterization of ZnO films by an evaporating method", J. Vac. Sci. Technol., A, Vol. 13 (1995)

[17]   Mar, L.G., Timbrell, P.Y., Lamb, R.N., "An XPS study of zinc oxide thin film growth on copper using zinc acetate as a precursor", Thin Solid Films, Vol. 223 (1993)

[18]   Lljina, E., "The volatile pivalates of Y, Ba and Cu as prospective precursors for metal-organic chemical vapour deposition", Materials Science and Engineering: B, Vol 18 (1993)

[19]   Ghirri, A., "Self-Assembled Monolayer of Cr7Ni Molecular Nanomagnets by Sublimation", ACS Nano, Vol. 5 (2011)

7

CONCLUSIONS AND OUTLOOK

The first aim of this thesis was to create a simulation which could aid the development of these new resist materials. The reasoning behind the use of a simulation in resist development was that it allowed potential new materials to be identified without the need to synthesise and characterise them. Thereby streamlining the process, potentially, by several months. Unfortunately, the simulations currently available do not offer sufficiently in-depth modelling of SE or AE cascades to fully predict the effects of the chemical changes of the resist on the sensitivity and lithographic performance. EXCALIBUR was developed as a simulation that combines both electron and ion models into one environment to allow both to be used as the primary exposure source. The inclusion of a low energy electron model allowed full modelling of SE cascades generated by primary ions and electrons and tracking of all SEs down to energies below the lower limit of the simulation, this being the carbon-carbon bond (3.6 eV). The upper limit of 100 keV for electrons means that the complete range of energies that could be used in a lithographic experiment are covered by the simulation.

The ion model can calculate trajectories for wide range of primary ions including the trajectories of any SEs generated when they interact with a resist. As it is based on the same models as those used for SRIM it has a solid foundation for predicting ion trajectories in materials.

However, the ion simulation currently suffers from the lack of a secondary ion model. This is particularly evident for more heavy ions (Z>10) as most of their energy is

lost through ion-atom interactions governed by the nuclear stopping power which describes the energy that is passed on to displaced atoms in the resist. It is these displaced ions that are considered to be secondary ions and they have the potential to go on to generate more scattering events which could generate both SEs and a SIs. This lack of a secondary ion model creates some difficulty in fully understanding the costs/benefits of secondary ions using different ion sources for lithography beyond helium ions.

EXCALIBUR was shown to predict the sensitivity of a resist material to exposure by both ions and electrons and hence predict the exposure dose of a resist. The accuracy of this approach varies with the best results coming from small changes in the resist chemistry being compared to another a baseline resist. This is because these changes do not greatly affect the lithographic processing of the resist and hence a comparison can be made, such as the comparison of resists **B**, **C** and **D**. When resist chemistry is changed more dramatically as in the case of resists **F** and **G**, this comparison weakens as they cannot be normalised as effectively against a baseline resist.

As a proxy to lithographic performance, the plotting of trajectories allows the proximity effect as well as the stochastic noise that leads to LER of resist materials to be understood. This mean that the resolution and LER could be estimated before experimentation. This method was much less accurate than the sensitivity predication as there isn't currently a way to quantify these parameters from the simulation results and so a qualitative approach had to be taken. To quantify these values the results could be calibrated to understand exactly what level of exposure or what amount of energy would need to be deposited into the resist to cause an area to become fully exposed. If this calibration was also carried out with a variety of solvents the development of resists after exposure could also be simulated. This is a vital area of lithography that is currently completely missed by EXCALIBUR and causes a huge change in lithographic performance as shown for resist **F** where the dose increased by a factor of 5.9 when the

developing solvent was changed. However, the viability of this level of calibration is questionable as it would require such a vast amount of experimentation which would reduce the efficacy of developing such a model.

The second aim was to use the model to develop new supramolecular resist materials for next generation lithography. Whilst these resists are not suitable for the processes used for the direct manufacture of semiconductor devices which is EUVL, their high resolution and high etch selectivity made them suitable for the manufacture of photomasks. However, the dose required by resist **A**, the original resist in the family was too high for any manufacturing and therefore a series of resists were developed with the aim of increasing sensitivity without degrading the lithographic performance. This was achieved by exploring chemical changes to the starting chromium ring resist (**B**) based on the evaluation of the model parameters. Firstly, adding ligands to increase the atomic number and density proved to decrease the dose by a factor of 3.2. whilst pitch remained comparable and line width and LER increasing slightly but not beyond the gains from the sensitivity. The second idea was to reduce the overall size of the molecule to decrease molecular weight which led to the development of resist **F**. This successfully reduced the dose by a factor of 4.5, but the reduction in quality of the lithography prevented the viability of this resist. The final idea was to change the ring molecule from chromium to a heavier more reactive molecule which in this case was indium. This resist **G** gave exciting initial results with the greatest overall reduction in sensitivity by a factor of 7 producing 60 nm pitch lines with a dose of 1400 pC/cm. However, the inclusion of these more sensitive atoms led to lithography problems potentially caused by the sensitivity of the resist to light and moisture which affects the processability of the resist. The supramolecular resist platform also proved to be suitable for HIBL, which is a growing field of lithography which is yet to prove its viability as a manufacturing technique. However, improvements in the dose of resist **A** by 3 orders of magnitude without any

further augmentation shows the promise of this technique. Additionally, the resolution and line width of the structures were also improved compared to the results from EBL producing structures with a pitch of 16 nm at a dose of 22 pC/cm.

The final aim was to build on a unique characteristic of certain resist materials to develop a new method of 3D nanolithography. This characteristic is that some resist materials can be sublimed when heated, which means that they can be thermally deposited onto a substrate without the need for spin coating. Whist similar to FEBID, this method uses more conventional thick layers of resist as opposed to monolayers. This means that patterns only need to be exposed once per layer, rather than for every monolayer, therefore reducing write times. Also shown was the ability to use this technique to fabricate structures using a semiconductor material which opens the door to new areas of fabrication which could remove the need for conventional silicon pattern transfer.

Overall substantial progress has been made toward developing the supramolecular resists for both advanced, ion and electron beam lithography. This has been shown through not increasing the viability of supramolecular resist by developing it through a modular resist platform but by also developing a process for investigating new resists using simulation.

Looking forward there are developments to EXCALIBUR that can be made to improve the accuracy of the predictions for which it is being employed. Similar to the developer processing problem described earlier there is also the potential to further develop the discrete model of resist materials which is currently used for tacking how the energy is deposited in the resist during exposure. By combining this with an energy threshold for exposure it would therefore be possible to visualise post developed structures and calculate the required energy deposits needed to render the resist insoluble in varying solvents. To improve the accuracy of this concept it could be possible to

include a model of energy propagation. For example, if 1 keV is deposited in a 1 nm^3 box it will not only be stored in the box but will be transferred to the surrounding atoms in adjacent boxes via a diffusive process. If this is combined with the thermal properties of the resist materials, one could begin to understand the impact of resist heating during exposure and link this to thermal decomposition of materials. This is especially relevant to the high sensitivity indium-based resist **G,** which is thermally unstable to the point that it cannot be baked after spin coating.

Another option is to begin investigation into how these resists for EBL could be used as negative tone resists for EUV. As with electron and ion beam lithography, secondary electrons are known to be the main mechanic for the exposure of resists in EUV exposures. This would make the simulation of EUV exposures significantly easier than lower energy exposures which depend on photochemical reactions and diffusion of radicals in the exposure area, which is much more specific for each resist. This would require a new model to be built for EXCALIBUR that would allow the primary ions and electrons to be replaced by photons. Then by using the absorption cross sections of the atoms in the resist materials, the number of photo electrons emitted could be calculated. As their energy would be below 92 eV they could be tracked using the already established low energy electron model. This addition would allow the same simulation and prototyping development process used for designing the electron beam resists to be applied to EUV resists.

The path of development for the modular supramolecular resists could be to investigate if the benefits of resists **C** and **D** over resist **B** could be repeated for resist **G**. Thus, leading to an even further reduction in dose and a whole family of indium-based resists. This speculation is purely dependent on whether the chemistry is possible. However, if they could be synthesised then resists with possible doses of 320 - 400 pC/cm could be developed, which would be a substantial development for this project and the

wider field. If this resist could also be used for ion beam lithography, then doses in the hundreds of fC/cm could theoretically be possible. However, the practicalities of patterning at such low doses would prove to be difficult because in order to get such a dose would either require a very low current or a very low exposure time. A low current would increase the effect of stochastic noise on the exposure and a low exposure time would require a pattern generator with a very high frequency.

The next step for the 3D lithography would be to increase the number of layers in the patterns and investigate a variety of patterns and shapes to discover the limits of the geometries that could be possible. Also, the theory of development by resublimation could be investigated further to try and fully contain the 3D lithographic process in one chamber. Further to this a plasma coil could be included in the chamber so that lithography and pattern transfer could be combined into one step. Additionally, it would be beneficial to discover more materials that can be used in this process and to investigate the effect of layering different materials to potentially build semiconductor and oxide structures.

PUBLICATIONS

1 Lewis, S. M., Fernandez, A., DeRose, G. A., Hunt, M. S., Whitehead, G. F. S., Lagzda, A., **_Alty, H. R_**., Ferrando-Soria, J., Varey, S., Kostopoulos, A. K., Schedin, F., Muryn, C. A., Timco, G. A., Scherer, A., Yeates, S. G., and Winpenny, R. E. P., "Use of Supramolecular Assemblies as Lithographic Resists", Supplementary Information, Angew. Chem. Int. Ed., Vol. 56 (2017).   178

DOI: https://doi.org/10.1002/anie.201700224

2 **_Alty, H. R.,_** Lewis, S. M., Yeates, S. G., Winpenny, R. E. P., "Using 3D Monte Carlo simulation to develop resists for next-generation lithography", Proc. SPIE 10810 (2018).   182

DOI: https://doi.org/10.1117/12.2501813

3 Lewis, S. M., DeRose, G. A., **_Alty, H. R.,_** Hunt, M. S., Li, J., Werthiem, A., Fowler, T., Lee, S. K., Muryn, C. A., Timco, G. A., Scherer, A., Yeates, S. G., Winpenny, R. E. P., "Design and implementation of the next generation electron beam resists for the production of EUVL photomasks", Proc. SPIE 10810 (2018)   192

DOI: https://doi.org/10.1117/12.2501808

4 Lewis, S.M., Hunt, M.S., DeRose, G.A., **_Alty, H.R._**, Li, J., Wertheim, A., De Rose, L., Timco, G.A., Scherer, A., Yeates, S.G., Winpenny, R.E.P, "Plasma-Etched Pattern Transfer of Sub-10 nm Structures Using a Metal–Organic Resist and Helium Ion Beam Lithography", Nano Lett., Vol. 19 (2019)   204

DOI: https://doi.org/10.1021/acs.nanolett.9b01911

5 Chaker, A., **_Alty, H.R._**, Tian, P., Kotsovinos, A., Timco, G.A., Muryn, C.A., Lewis, S.M., Winpenny, R.E.P., "Nanoscale Patterning of Zinc Oxide from Zinc Acetate Using Electron Beam Lithography for the Preparation of Hard Lithographic Masks", ACS Appl. Nano Mater., Vol 4. (2021)   210

DOI: https://doi.org/10.1021/acsanm.0c02756

Use of Supramolecular Assemblies as Lithographic Resists

Scott M. Lewis,* Antonio Fernandez, Guy A. DeRose, Matthew S. Hunt, George F. S. Whitehead, Agnese Lagzda, Hayden R. Alty, Jesus Ferrando-Soria, Sarah Varey, Andreas K. Kostopoulos, Fredrik Schedin, Christopher A. Muryn, Grigore A. Timco, Axel Scherer, Stephen G. Yeates, and Richard E. P. Winpenny*

Abstract: *A new resist material for electron beam lithography has been created that is based on a supramolecular assembly. Initial studies revealed that with this supramolecular approach, high-resolution structures can be written that show unprecedented selectivity when exposed to etching conditions involving plasmas.*

Supramolecular chemistry has reached a major landmark with the award of the 2016 Nobel Prize for work on molecular machines.[1] There are remarkably imaginative and potentially transformative proposals to use supramolecular assemblies, for example, as components of memory devices,[2] as molecular robots to assemble small peptides,[3] as rotary motors powered with light,[4] or as supramolecular spin valves.[5] Real-world applications of this branch of nanoscience will only appear in the future.

The major technological advances in nanoscience to this point have arisen from fabrication by lithography of integrated circuits (ICs). The main component of an IC is a field effect transistor (FET), and the reduction in the size of FETs has led to a revolution in electronics over the last five decades. The size-limiting fabrication step is lithography, which involves writing a pattern into a resist material prior to etching.[6] Conventional resist materials are organic polymers such as poly(methyl methacrylate) (PMMA).[7] The technological roadmap in electronics[8] requires still further reduction in the size of FETs and drives massive investment in lithographic equipment. New resists are therefore needed, and the materials studied include copolymers and block copolymers, hydrogen silsesquioxane (HSQ),[9] fullerenes,[10] composites,[11] and metal–oxide films.[12] There remains a huge scope for further advances based on design, and we wondered whether supramolecular chemistry could make a contribution in designing resist materials. There has been very significant work on creating patterns on surfaces by self-assembly, for example, of hydrogen-bonded networks[13] or through coordination chemistry,[14] but these structures have not been studied for lithography.

Herein, we report studies of a complex supramolecular assembly as a resist. To demonstrate the potential of the new resist for use with silicon, nanostructures that are 9 nm wide and 330 nm high have been fabricated in one writing–etching cycle using industrially relevant processes. Such structures resemble the Fin-FETs presently being introduced by Intel.

To design a new resist, we have developed Monte Carlo simulations that are based on the Joy model,[15] expanding this approach to incorporate quantum effects using the hard-sphere model to consider the low-energy electrons (<500 eV).[16] Patterns can be calculated for a putative resist material without any assumptions concerning the underlying chemistry of the resist. The only parameters considered are the molecular weight of the material, the weighted average atomic number of the elements present, and the density of the material. Simulations show that to achieve a high resolution, the ideal resist would have a high molecular weight and a very low density; together, these generate a very large molecular volume. The inclusion of elements with high atomic numbers improves the speed with which the resist can be written. Based on these predictions, an excellent candidate is $[Ni_{12}(chp)_{12}(O_2CMe)_6(H_2O)_6\{[NH_2{}^nPr_2][Cr_7NiF_8(O_2C^tBu)_{15}(O_2C\text{-pyridine})]\}_6$ **1** (Hchp = 6-chloro-2-hydroxypyridine, HO_2C-pyridine = isonicotinic acid; Figure 1).[17]

This compound involves the binding of six octametallic {Cr$_7$Ni} rings around a central {Ni$_{12}$} ring. The internal structures of the various rings are described in detail elsewhere.[17] Here, we are only concerned with the overall topology. The six octametallic rings pack inefficiently around the central ring, rather like six small plates attached at their edges to one larger central plate. The density of **1** in crystalline form is low (0.81 g cm^{-3}) despite the molecular weight of the supramolecule being high (16887 Da). The exterior of **1** consists entirely of *tert*-butyl groups, which gives the compound high solubility in solvents suitable for preparing films on silicon substrates.

Compound **1** was deposited on silicon by spin-coating from *tert*-butyl methyl ether. X-ray photoelectron spectros-

[*] Dr. S. M. Lewis, Dr. A. Fernandez, Dr. G. F. S. Whitehead, A. Lagzda,
H. R. Alty, Dr. J. Ferrando-Soria, Dr. S. Varey, A. K. Kostopoulos,
Dr. C. A. Muryn, Dr. G. A. Timco, Prof. S. G. Yeates,
Prof. R. E. P. Winpenny
The School of Chemistry
The University of Manchester
Oxford Road, Manchester, M13 9PL (UK)
E-mail: scott.lewis@manchester.ac.uk
        richard.winpenny@manchester.ac.uk

Dr. G. A. DeRose, Dr. M. S. Hunt, Prof. A. Scherer
The Kavli Nanoscience Institute
California Institute of Technology
1200 East California Boulevard, 107-81, Pasadena, CA 91125 (USA)

Dr. F. Schedin
The National Graphene Institute
The University of Manchester
Oxford Road, Manchester M13 9PL (UK)

Supporting information and the ORCID identification number(s) for
the author(s) of this article can be found under:
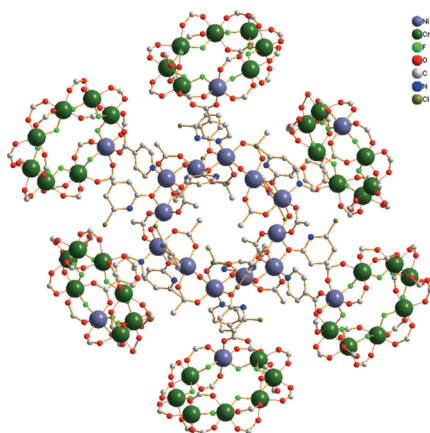https://doi.org/10.1002/anie.201700224.

Figure 1. The structure of **1** in the crystal in ball-and-stick representation. Ni light blue, Cr green, F yellow, O red, N dark blue, Cl brown, C gray. H atoms and C atoms of ^tBu groups omitted for clarity.

copy (XPS) studies show that the films, as deposited, contain intact molecules of **1** (Supporting Information, Table S1), and AFM studies show that these films are smooth, with a surface roughness < 4 nm, as deposited and after the writing step (see the Supporting Information). The film was written using a 30 KeV e-beam within a scanning electron microscope. After developing the pattern using hexane for 30 s, we can write 7 nm lines that are separated by 20 nm into a 30 nm film (Figure 2a); these match the Monte Carlo simulations precisely (Figure 2b).

The pattern written into compound **1** has a high selectivity for etching when compared with the silicon substrate (Figure 3). Post-writing the material appears to be mainly Cr_2O_3, as shown by XPS studies (see Table S2), but doped with fluoride and the second metal. In Figure 3A, we show 14 nm lines written into a 60 nm thick film of **1**. The underlying silicon was then etched in a pseudo-Bosch process that uses an inductively coupled plasma (ICP) of SF_6 and C_4F_8 gases. This generates silicon nanostructures that are 14 nm wide and 155 nm high; the resist could still be seen at the tip of the silicon structures (Figure 3B). The resist layer can be removed by wet-etching the silicon dioxide (SiO_2) layer immediately beneath the resist using buffered HF for 60 s; this yielded silicon fins that are 155 nm high and 12 nm wide (Figure 3C).

These etching results were so unusual[18] that they were pursued further. First, the resist was patterned with a larger line width of 25 nm and a pitch of 200 nm in a 60 nm thick film (Figure 3D). The etching time was extended to 210 s, which led to the etching undercutting the resist (Figure 3E); undercutting is normally an undesirable result, but here the final structures are straight with little line edge roughness. The remaining resist was 58 nm high and can be seen at the tip of
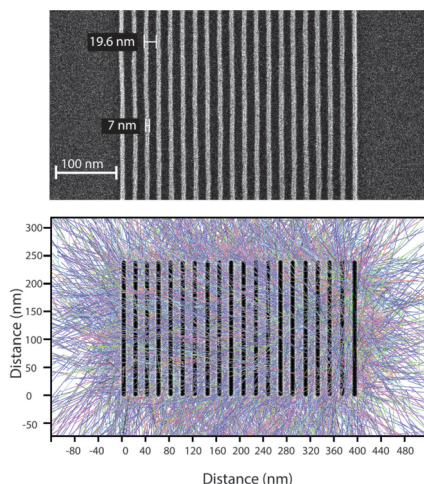

Figure 2. a) The 7 nm lines written in **1** using a 30 KeV source at a pitch of 20 nm into a 30 nm deep film. b) Monte Carlo simulation of the performance of **1** under the same conditions. The black lines represent the electrons for the e-beam writer, and the red lines are secondary electrons generated from collisions with **1** during the writing with energies > 500 eV. Purple, cyan, and green lines are further secondary electrons with associated energies below 500 eV generated by first-, second-, and third-order collisions, respectively. The blue lines are back-scattered electrons.

the silicon fins (Figure 3E). This gives a resist etching rate of 0.12 nm s^{-1} while the silicon etching rate was 1.55 nm s^{-1}. The silicon was etched 130 times faster than the resist, which is a selectivity twice as good as the best observed previously (with aluminum oxide masks).[12b] Removal of the resist gives silicon nanostructures with a height of 330 nm and a width of 9 nm, that is, a 36:1 aspect ratio in one writing–etching cycle (Figure 3F).

The process generates silicon structures that are almost three times narrower than the resist pattern written by the e-beam (compare Figures 3D and F). To the best of our knowledge, such behavior is unprecedented and is caused by the huge resistance of structures written in **1** to the plasma etching process. Most of the resist remains after etching for 210 s (Figure 3E). The resist is therefore capable of surviving for longer etching times; in the future, we will examine the maximum depth of etching that can be achieved. The targets are large-area patterns etched to contain structures that are taller than the 330 nm fins shown here.

The use of a large supramolecular assembly such as **1** for such processes demonstrates a potentially new area to be explored using supramolecular chemistry. Our studies of **1** are the most complete; however, we have studied many related compounds in this context. These include individual hetero-metallic rings such as $[NH_2Pr_2][Cr_7NiF_8(O_2CR)_{16}]$ (R = ^tBu
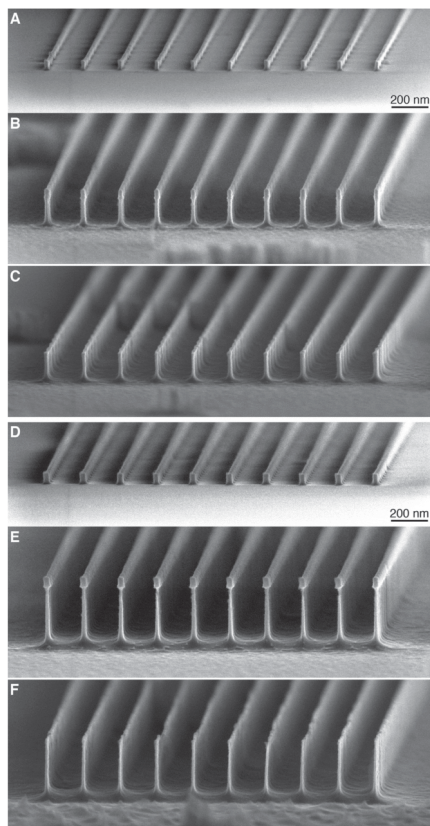
181

Figure 3. A) The 14 nm lines on a 200 nm pitch that were written in
1 at 30 KeV and then developed before the plasma etching process.
B) The resist after a 90 s pseudo-Bosch plasma etching process.
C) Fins with a 12 nm width after removal of the resist using buffered
hydrofluoric acid. D) The 25 nm lines written in **1** at a 200 nm pitch
before the plasma etching process. E) The resist after a 210 s pseudo-
Bosch plasma etching process, which resulted in 10 nm wide struc-
tures. F) Removal of the resist, resulting in 330 nm tall pillars that are
9 nm wide.

(**2**) or -CH(Me)CH$_2$CH=CH$_2$ (**3**)),[19] a [7]rotaxane containing
six heterometallic rings around a central oxo-centered metal
triangle (**4**),[20] and an 8 nm molecular nanoparticle with
24 heterometallic rings, each containing eight metal centers
around a {Pd$_{12}$} cuboctahedron (**5**).[21] We found that all of
them are suitable as electron beam resists, but that the larger
compounds **1**, **4**, and **5** are better for high-resolution
structures (Figure S3). For example, 8 nm lines are easily

written into **5**. We believe that this is because the electron
beam is writing into a molecular material, and most scattering
events occur when the beam hits an individual molecule. This
event occurs far more rarely for a very large molecule than
a small molecule, and hence the scattering is lower for larger
molecules, and the resolution is concomitantly higher. We
compared **2** with **3** to examine whether simpler chemical
engineering of performance was possible. We found that the
unsaturated side chain on the carboxylate in **3** leads to a resist
that writes more quickly, but where we lose resolution.

In all cases, XPS studies show that the material is based on
Cr$_2$O$_3$ post-writing, which gives the extreme etch selectivity.
Therefore, we can conclude that the etching performance is
due to the presence of an early d block metal in the initial
resist.

These initial studies show that we can design a material
with a combination of unique and potentially transformative
properties in an area of immediate technological relevance.
The processes applied are typical of those used in industry
with polymeric resists, and silicon structures can be produced
with an aspect ratio greater than 30:1. The key chemical
features are a low-density but high-molecular-weight material
to allow high-resolution features to be written, decomposition
in the e-beam to a hard material, in this case Cr$_2$O$_3$, which is
strongly resistant to the etching plasma, and solubility in the
solvents, mainly nonpolar organic solvents, used in the
semiconductor industry. Considering examples where these
key features are combined it is apparent that many metal-
losupramolecular compounds could be useful; for example,
the metal capsules made by Fujita and co-workers are hollow
and hence have a low density.[22] Possibly the most unusual
feature of compounds **1**–**5** is actually the high solubility in
suitable solvents, and hence their processability.

Other new routes to nanometer-sized lithographed struc-
tures are being explored. An interesting comparison is with
direct laser writing of nanostructures.[23, 24] This alternative
approach has huge flexibility and greater speed than we can
achieve at present owing to the advantages of laser writing
compared with e-beam writing. However, the resulting
materials are organic polymers and, as with other polymeric
resist materials,[18] are unlikely to demonstrate the very high
etching selectivity of **1**. The array of new techniques[13,14,23]
being developed to pattern surfaces and nanostructures
should be regarded as complementary, and constitute possible
routes forward to make still smaller nanodevices in the
future.[8]

Acknowledgements

Conflict of interest

There are two patents held by three authors (S.M.L., S.G.Y., R.E.P.W.) based on the work described in the paper.

[1] "The Nobel Prize in Chemistry 2016", www.nobelprize.org, Nobel Media AB, **2016**.

[2] J. E. Green, J. W. Choi, A. Boukai, Y. Bunimovich, E. Johnston-Halpern, E. Delonno, Y. Luo, B. A. Sheriff, K. Xu, Y. S. Shin, H.-R. Tsong, J. F. Stoddart, J. R. Heath, *Nature* **2007**, *445*, 414.

[3] B. Lewandowski, G. De Bo, J. W. Ward, M. Papmeyer, S. Kuschel, M. J. Aldegunde, P. M. E. Gramlich, D. Heckmann, S. M. Goldup, D. M. D'Souza, A. E. Fernandes, D. A. Leigh, *Science* **2013**, *339*, 189–193.

[4] D. Zhao, T. van Leeuwen, J. Cheng, B. L. Feringa, *Nat. Chem.* **2017**, *9*, 250.

[5] M. Urdampilleta, S. Klyatskay, J.-P. Cleuziou, M. Ruben, W. Wernsdorfer, *Nat. Mater.* **2011**, *10*, 502.

[6] a) U. Okoroanyanwu, *Chemistry and Lithography*, SPIE Press, Washington, **2011**; b) C. A. Mack, *Fundamental Principles of Optical Lithography: The Science of Microfabrication*, Wiley, London, **2007**.

[7] M. J. Rooks, E. Kratschmer, R. Viswanathan, J. Katine, R. E. Fontana, Jr., S. A. MacDonald, *J. Vac. Sci. Technol. B* **2002**, *20*, 2937.

[8] International Roadmap for Semiconductors 2.0, ITRS, **2015**.

[9] A. E. Grigorescu, C. W. Hagen, *Nanotechnology* **2009**, *20*, 292001.

[10] A. Frommhold, J. Manyam, R. E. Palmer, A. P. G. Robinson, *Microelectron. Eng.* **2012**, *98*, 552.

[11] L. Merhari, K. E. Gonsalves, Y. Hu, W. He, W.-S. Huang, M. Angelopoulos, W. H. Bruenger, C. Dzionk, M. Torkler, *Microelectron. Eng.* **2002**, *63*, 391.

[12] a) Z. Huang, N. Geyer, P. Werner, J. de Boor, U. Gösele, *Adv. Mater.* **2011**, *23*, 285; b) D. Henry, S. Walavalkar, A. Homyk, A. Scherer, *Nanotechnology* **2009**, *20*, 255305.

[13] J. A. Theobald, N. S. Oxtoby, M. A. Phillips, N. R. Champness, P. H. Beton, *Nature* **2003**, *424*, 1029.

[14] U. Schlickum, R. Decker, F. Klappenberg, G. Zoppellaro, S. Klyatskaya, M. Ruben, I. Silanes, A. Arnau, K. Kern, H. Brune, J. V. Barth, *Nano Lett.* **2007**, *7*, 3813.

[15] D. C. Joy, *Monte Carlo Modeling for Electron Microscopy and Microanalysis*, Oxford University Press, New York, **1995**.

[16] "SML electron beam resist: ultra-high aspect ratio nanolithography": S. M. Lewis, G. A. DeRose in *Frontiers of Nanoscience, Materials and Processes for Next Generation Lithography*, **2016**, *11*, 421.

[17] G. F. S. Whitehead, F. Moro, G. A. Timco, W. Wernsdorfer, S. J. Teat, R. E. P. Winpenny, *Angew. Chem. Int. Ed.* **2013**, *52*, 9932; *Angew. Chem.* **2013**, *125*, 10116.

[18] A. Goodyear, M. Boettcher, I. Stolberg, M. Cooke, *Proc. SPIE-Int. Soc. Opt. Eng.* **2015**, *9428*, 94280V.

[19] E. J. L. McInnes, G. A. Timco, G. F. S. Whitehead, R. E. P. Winpenny, *Angew. Chem. Int. Ed.* **2015**, *54*, 14244; *Angew. Chem.* **2015**, *127*, 14450, and references therein.

[20] A. Fernandez, J. Ferrando-Soria, E. M. Pineda, F. Tuna, I. J. Vitorica-Yrezabal, C. Knappke, J. Ujma, C. A. Muryn, G. A. Timco, P. E. Barran, A. Ardavan, R. E. P. Winpenny, *Nat. Commun.* **2016**, *7*, 10240.

[21] J. Ferrando-Soria, A. Fernandez, E. M. Pineda, S. A. Varey, R. W. Adams, I. J. Vitorica-Yrezabal, F. Tuna, G. A. Timco, C. A. Muryn, R. E. P. Winpenny, *J. Am. Chem. Soc.* **2015**, *137*, 7644.

[22] Y. Inokuma, M. Kawano, M. Fujita, *Nat. Chem.* **2011**, *3*, 349.

[23] M. Deubel, G. von Freymann, M. Wegener, S. Pereira, K. Busch, C. M. Soukoulis, *Nat. Mater.* **2004**, *3*, 444.

[24] E. Blasco, M. Wegener, C. Barner-Kowollik, *Adv. Mater.* **2017**, *29*, 1604005.

PROCEEDINGS OF SPIE

Using 3D Monte Carlo simulation to develop resists for next-generation lithography

Alty, Hayden, Lewis, Scott, Yeates, Stephen, Winpenny, Richard E.

SPIE.

Using 3D Monte Carlo Simulation to Develop Resists for Next-Generation Lithography

Hayden R. Alty[*], Scott M. Lewis, Stephen G. Yeates, Richard E. P. Winpenny
School of Chemistry, The University of Manchester, Oxford Road, Manchester M13 9PL, United Kingdom

ABSTRACT

This paper investigates the ability of a novel and bespoke Monte Carlo simulation to model the experimental outcome of exposure of resist materials by electron beam. The resists are a family of organo-metallic Chromium rings $(Cr_8F_8(O_2CtBu)_{16})$, which have high resolution and low LER making them ideal candidates for the fabrication of the next generation of photomasks for EUV lithography. The model shows how the electron scattering in the resist material and the subsequent production of secondary electrons lead to the resists high resolution. The resist family can be modified to increase speed by up 17.3 times, by replacing the pivalate ligand with a methacrylate ligand, whilst still maintaining their desirable properties.

Keywords: Monte Carlo, Simulation, Electron Beam Lithography, 3D visualisation, Organometallic Resist

1. INTRODUCTION

All modern consumer electrical good contain microprocessors and most simple tasks are becoming dependent on this technology. The success of the microprocessor and the semiconductor industry is due to the constant progress of increasing processing power and miniaturization. This progress is driven by 'Moore's law' which is an observation made by Gordon Moore in 1965, that the number of integrated circuits per unit area would double every year [1]. Since Moore's observation the progress has slowed but has remained the benchmark and driving force for the semiconductor industry. The miniaturization of this technology is enabled by the ability to fabricate structures on the order of nanometres. These devices are fabricated using photolithography which uses a photomask to project a pattern onto a resist. In order to reach smaller feature sizes these photomasks require ever increasing resolution.

Electron Beam Lithography (EBL) is used in the production of around 30% of photomasks [2] and is increasingly being used for mask repair. This increase in demand for masks with ever smaller feature sizes drives the need for improved EBL resists. These resists must meet the demand for smaller resolution (7nm node) and also reduce the write times for mask production. Developing such resists is a long, experimentally expensive, process of rapid prototyping to find suitable candidates followed by detailed characterisations to determine the resolution limits and development properties post exposure.

Currently, the majority of masks written using EBL are produced using Variable Shaped Beam (VSB) systems which use an acceleration voltage of 50kV, whereas other commercial lithography systems such as the Vistec EBPG5200, uses 100kV and the Raith E-line uses 30kV. This mean that a resist that can be used at all commercial acceleration voltages and produce consistent results would be extremely beneficial.

1.1 Monte Carlo Simulation

Monte Carlo Modelling is a technique which uses pseudo random numbers as input into a probability distribution to find the average probability of an event. Monte Carlo techniques have long been used to simulate physical models and EBL is no exception with many already established methods of modelling electron scattering and interaction in a variety of materials. There are also several programs that provide useful data and interpretation for example CASINO, PENELOPE and Tracer. However, to fully understand exposure of resists by electron beam, not only do the initial (primary) electrons, from the incident beam, need to be considered but also secondary electrons which are generated in the resist. In many resist matrices these secondary electrons are the main mechanic for exposure. Compared to the incoming

[*] Tel: +44 (0)161 2757855; E-mail: hayden.alty@postgrad.manchester.ac.uk

primary electrons they have much lower energy so scattering events, as well as inelastic collisions, are much more likely and it is these events that break bonds creating free radicals, cross linking or chain scissioning. Therefore, secondary electrons are tracked up to 4th generation by this simulation. Electrons are tracked to their full extent within the bounds of the resist and the substrate, down to the energy of the weakest bond in the material. Below this any interactions will have too low an energy to cause any further exposure. Another important source of secondary electrons is Auger transitions as these generate electrons of desirable energies for exposure and will generate more secondary electrons as they travel through the resist.

1.2 Materials

The resists explored in this paper are all from the same family of modular resists being developed by the University of Manchester. They are negative tone organometallic resists that are comprised of a Chromium ring [3] with an organic ligand attached around the ring. These organic ligands can be changed whilst the base chromium ring remains the same hence the modular nature. Here, the effect of changing these ligands in simulation will be explored in order to identify possible candidates for further investigation thus showing the potential of the model to reduce experimentation time.

Table 1. A table of components of all the molecules simulated, including molecular formulas and diagrams.
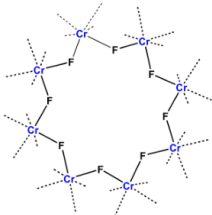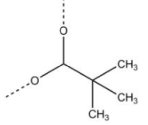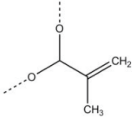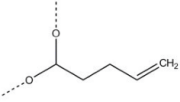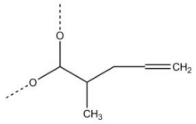
Name	Formula	Diagram
Chromium Ring	Cr_8F_8	
Pivalate	$O_2C_5H_9$	
Methacrylate	$O_2C_4H_5$	
4-Pentenoate	$O_2C_5H_7$	
4-Methyl-4-Pentenoate	$O_2C_6H_9$	

Table 1 shows the components which make up the 4 molecules simulated in this paper. Each molecule consists of the Chromium ring with 16 ligands attached to the outside for example $Cr_8F_8(Pivalate)_{16}$. These ligands change the solubility of the molecule which determines which casting solvents can be used.

2. SIMULATION

The Monte Carlo model consists of 4 major parts these being: 1. The "fast" scattering model is the foundation of the model and is used to track primary electrons and any electrons above 500eV; 2. A "slow" (low energy) quantum model which deals with low energy secondary electrons or any primary electrons if the resist and substrate are thick enough to prevent them escaping; 3. An Auger model which checks for generation of auger electrons; 4. A visualisation code used to generate different 3D plots of the electron tracks. For each section the main equations have been shown from each model, these being the collision probability and energy loss of an electron in the material. There are further equations used to model the scattering angles and steps of the electron in order to build the full tracks and these are shown in a previous publication [4].

2.1 Fast Scattering Model

The following model uses the model described by David C. Joy in *Monte Carlo Modelling for Electron Microscopy and Microanalysis* [5] which is a classical model based on Rutherford scattering and as previously stated is only accurate for electrons with energy above 500eV.

As an electron travels through a material it will undergo both elastic and inelastic collisions. The cross section for inelastic collisions, $\sigma_{elastic}$ (cm^2/atom), is given by,

$$\sigma_{elastic} = 5.21 \times 10^{-21} \frac{Z^2}{E^2} \frac{4\pi}{\alpha(1+\alpha)} \left(\frac{E+511}{E+1024}\right)^2 \tag{1}$$

where Z is the effective atomic number of the whole molecule and E is the energy of the incident electron (keV). The screening factor, α, is calculated using,

$$\alpha = 3.4 \times 10^{-3} \frac{Z^{0.67}}{E}. \tag{2}$$

The distance travelled by an electron between elastic collisions is the elastic mean free path, $\lambda_{elastic}$ (cm), and is given by,

$$\lambda_{elastic} = \frac{A}{N_a \rho \sigma_{elastic}} \tag{3}$$

where A is the molecular weight (g/mol), ρ is the density of the molecule (g/cm^3) and N_a is Avogadro's constant. The inelastic scattering cross section is given by the following differential cross section,

$$\frac{d\sigma_{inelastic}}{d\Omega} = \frac{\pi e^4}{E^2} \left(\frac{1}{\Omega^2} + \frac{1}{(1+\Omega)^2}\right) \tag{4}$$

where E again is the energy of the incident electron and ΩE is the energy of the generated secondary electron. The mean free path for an inelastic scattering event is given by,

$$\lambda_{inelastic} = \frac{A}{N_a Z \rho \sigma_{inelastic}} \tag{5}$$

This simulation uses a constant energy loss model described by a modified Bethe-Bloch equation. The stopping power of a material, $\frac{dE}{dS}$, is given by,

$$\frac{dE}{dS} = 78500 \frac{Z}{AE} \ln\left(1.166 \frac{E+0.86J}{J}\right) \tag{6}$$

where J is the min ionization potential (keV), calculated using,

$$J = \left[9.76Z + \frac{58.5}{Z^{0.19}}\right] \times 10^{-3} \tag{7}$$

2.2 Slow Scattering Model

In order to extend the model to account for lower energy (slow) electrons D Joy suggested a partial wave expansion method (PWEM). The PWEM used was described by J. J. Sakurai in *Modern Quantum Mechanics* [6].

The slow scattering cross section is given by,

$$\sigma_{slow} = \frac{4\pi}{k^2} \sum_{l=0}^{\infty} (2l+1) \sin^2(ka)^{2l+1} \tag{8}$$

which when expanded for the dominant terms (l=0,1,2,3) gives,

$$\sigma_{slow} = \frac{4\pi}{k^2} \left(\sin^2(ka) + 3\sin^2(ka)^3 + 5\sin^2(ka)^5 + 7\sin^2(ka)^7 \right) \tag{9}$$

where k is the wavenumber, $k = \frac{\sqrt{2ME}}{\hbar}$ and a was estimated to be ~0.025nm (atomic radius of Carbon) using the Thomas-Fermi atomic radius approximation, $a = 0.468Z^{-\frac{1}{3}}$ Å. The mean free path can be found using σ_{slow} in equation 3. Similarly, as with the fast scattering model the equations for generating scattering angels and steps between collisions has been omitted.

2.3 Auger Electrons

The inclusion of the production of secondary electrons through Auger transitions and cascades is important as the secondary electrons generated by these events are low energy. Therefore, they will create more secondary electrons as they travel through the material causing high amounts of local exposure. Auger electron emissions are more likely from transition to inner shells. This method was laid out by You et al [7]. The cross section for inner shell ionizations is given by the Casnati cross section,

$$\sigma_c = \frac{a_0^2 F R^2 AB \ln U}{U E_U^2} \tag{10}[8]$$

where a_0 is the first Bohr radius (a_0= 5.292x10^{-11} m), R is the Rydberg energy (R=13.605 eV) and U=E/E_U. E is the energy of the incident electron and E_U is the binding energy of the shell. The other factors can be calculated by,

$$F = \left(\frac{2+J}{2+T}\right)\left(\frac{1+T}{1+J}\right)^2 \times \left[\frac{(J+T)(2+T)(1+J)^2}{T(2+T)(1+J)^2 + J(2+J)}\right]^{\frac{3}{2}}$$

$$A = \left(\frac{E_U}{R}\right)^d ; B = 10.57\exp\left(-\frac{1.736}{U} + \frac{0.317}{U^2}\right);$$

$$d = -0.0318 + \frac{0.3160}{U} - \frac{0.1135}{U^2};$$

$$J = \frac{E_U}{m_e c^2} ; T = UJ \tag{11}$$

When Auger transitions occur, there can either be an electron or an X-ray emitted. The probability of an electron being emitted for the different transition channels is given by,

$$\gamma_{AX} = 1 - \frac{Z^4}{Z^4 + Z_0^4} \begin{cases} Z_0 = 32.4, & X = K \\ Z_0 = 89.4, & X = L \\ Z_0 = 155.9, & X = M \\ Z_0 = 300, & X = N \end{cases} \tag{12}[9]$$

2.4 3D Visualisation

A separate code is used to plot the data in MATLAB. This is because matplotlib in Python, the language the simulation is written in, does not have a true 3D engine so the electron tracks do not plot correctly. Below is an example plot of a

single beam entry point. In combination with the Monte Carlo simulation whole patterns of exposure can be plotted, depending on computational resources.

Figure 1. below, shows an example plot of a single spot of electron scattering. The resist (grey) thickness is 100nm on a silicon substrate with a thickness of 50 nm. The primary electrons are plotted in greyscale to show their distance from the centre point of the beam
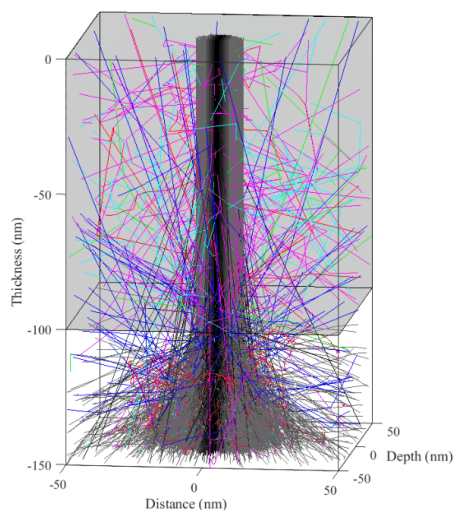
Figure 1. An Example plot of a 3D simulated image of electron tracks. Primary electrons are plotted in greyscale, backscattered electrons are blue, fast secondary electrons are red, slow secondary electrons are magenta, 2nd generation slow electrons are cyan and 3rd Generation slow electrons are green.

3. RESULTS

Simulations were completed for the four materials: **1**. $Cr_8F_8(Pivalate)_{16}$, **2**. $Cr_8F_8(Methacrylate)_{16}$, **3**. $Cr_8F_8(4$-Pentenoate$)_{16}$, **4**. $Cr_8F_8(2$-Methyl-4-Pentenoate$)_{16}$. All materials were simulated as a 100nm thick layer on a 50nm thick substrate of Silicon. Material **1** is a known and tested material with a dose of 43,000$\mu C/cm^2$ at 100kV with a pitch of 60nm and is used as a comparison for the simulated values of the other materials. The properties for the materials used in the simulation are displayed in Table 2.

Table 2. A table of values of all the molecules simulated including effective atomic number, Z; Molecular weight, A and Density, ρ. *Density values for Materials **2**, **3** and **4** are estimated from the measured value for **1** and the change in ligand density.

Name	Formula	Effective Atomic Number, Z	Molecular Weight, A, (g/mol)	Density*, ρ, (g/cm³)
1. $Cr_8F_8(Pivalate)_{16}$	$Cr_8F_8O_{32}C_{80}H_{144}$	8.93	2192	1.21
2. $Cr_8F_8(Methacrylate)_{16}$	$Cr_8F_8O_{32}C_{64}H_{80}$	9.85	1929	1.32
3. $Cr_8F_8(4$-Pentenoate$)_{16}$	$Cr_8F_8O_{32}C_{80}H_{112}$	9.26	2154	1.28
4. $Cr_8F_8(4$-Methyl-4-Pentenoate$)_{16}$	$Cr_8F_8O_{32}C_{96}H_{144}$	8.79	2378	1.25
Silicon	Si	14	28.09	2.3

189

The properties of the materials shown in Table 2 give a good indication of how the materials will react in the simulation. From equation 1, for the elastic scattering cross section, it is clear that a higher Z value gives a larger scattering cross section which in combination with an increased stopping power (equation 6) means that the electrons will lose energy more quickly as they pass through the material. As an electron loses energy the probability of an inelastic scattering event increases as the mean free path for inelastic scattering events is inversely proportional to Z. This increase in inelastic scattering events means that more secondary electrons will be generated in the material. The generation of these secondary electrons cause chain scissioning and crosslinking in the material which leads to changes in solubility and hence exposure of the resist. The secondary electrons generated have a low energy compared to the primary electrons which means that they are much more likely to go on to generate more secondary electrons in a cascade. Similarly, with density, a higher density means a shorter mean free path between collisions meaning more scattering events will occur as an electron passes through the material. A low molecular weight also means a lower mean free path causing similar effects as those previously explained.

(A)　　　　　　　　　　　　　　　　　　　　(B)

(C)　　　　　　　　　　　　　　　　　　　　(D)

Figure 2. (A) A 3D plot of 100nm thick film of material **1** on a 50nm thick silicon substrate each line has a step size of 5nm an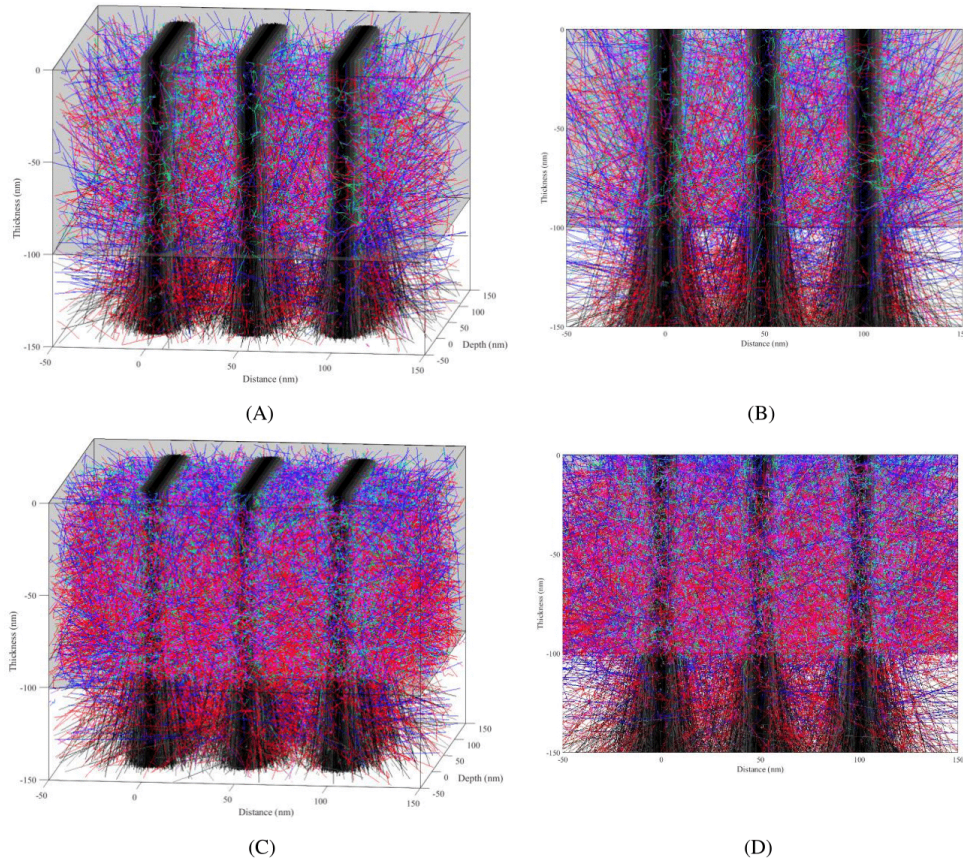d a pitch of 50nm. (B) A front on, cross section view of plot (A). (C) A 3D plot of 100nm thick film of material **2** on a 50nm thick silicon substrate each line has a step size of 5nm and a pitch of 50nm. (D) A front on, cross section view of plot (C). All images were produced with a beam energy of 50keV. Colours of different electrons are explained in figure 1.

Knowing this, when comparing the resist materials, material **2** would be a much better candidate for increased electron sensitivity compared to the starting material **1**. This can clearly be seen in figure 2 where material **2** (C and D) has a large increase in secondary electrons generated in the resist when compared to material **1**.

Also, in these images the spread of the electron beam can be seen as it passes through the material, the broadening of the beam in the resist shows how the resolution will decrease. In both resist materials the beam remains unchanged showing that the high resolution of material **1** is maintained in material **2**. Both materials have the same number of incident primary electrons so that the increase in secondary electron generation can be seen. These are not real doses as material **2** would be over-exposed with this amount of electron generation.

The extent of the spread of secondary electrons can also be seen. This lateral exposure away from the line is responsible for the proximity effect and also a broadening of the structures. Due to the energy disparity between the high energy primary electron and much lower energy secondary electron, the generation angle of most first order secondary electrons is over 80°, which is the cause of the lateral direction. The green electrons in the plots are the lowest energy electrons and the highest generation of secondary electrons and they show where the highest level of exposure is occurring. This is where the most collisions are happening, hence the most electrons being generated and therefore where the resist is being exposed. These materials have a high resolution due to the low amount of lateral exposure with these low energy secondary electrons being focused around the beam.

Even though there appears to be more electrons generated in the resist compared to the silicon substrate this is not the case. It is due to the mean free path being so much lower in the silicon. This means that the electrons cannot travel as far before their energy is lost, so they are contained within the center of the beam and so are obscured in the image by the divergence of the beam. The high scattering properties of silicon also mean that large amounts of resist exposure occur at the resist-silicon interface, due to backscattering of low energy electrons from the silicon into the resist.
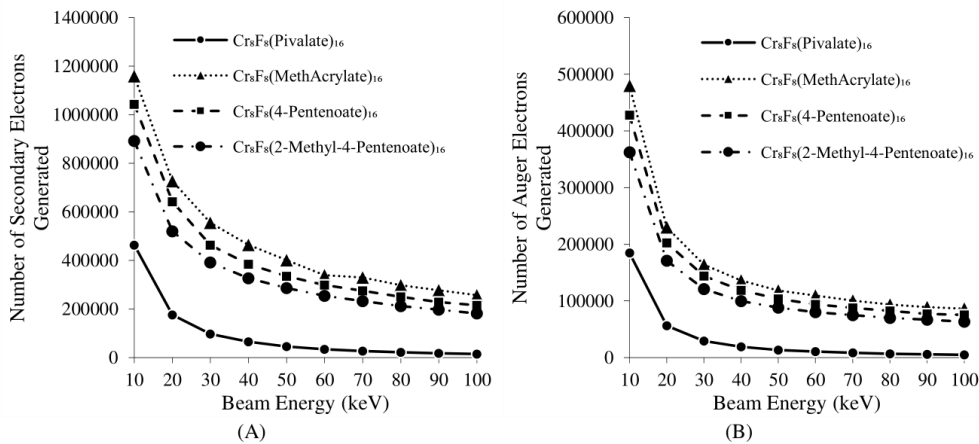
Figure 3. (A) A plot of secondary electrons generated in the 4 materials. Each material was simulated using 1 million electrons at acceleration voltages of 10-100kV. (B) A plot of auger electrons generated in the 4 materials. Each material was simulated using 1 million electrons at acceleration voltages of 10-100kV.

Figure 3 shows the number of secondary electrons and the number of auger electrons generated in all four materials for beam energies in the range of 10 to 100keV. This range was chosen as it covers most conventional lithography energies, with the resist family in this paper usually being written at 30 and 100 kV and with the common industry technique VSB being at 50kV. 1,000,000 incident electrons were used in the simulations of all the materials at all energies, as this provides a sufficiently large data size to reduce statistical error. It is clear to see that as the energy increases the number of secondary electrons generated also decreases. This is due to the scattering cross sections being inversely proportional to the energy of the incident electron. So, as the energy increases, the chance of collisions and hence generation of secondary electrons decreases. This also means that while the resist is less sensitive at higher energies it will also have better resolution. These results confirm those shown in figure 2 where material **2** is the most sensitive of the four

materials. While it may seem that the number of inner shell ionizations would decrease with lower energy this is only apparent for the K shell. The L, M and N shell transitions start to dominate at lower electron energies meaning that auger electrons become a large contributor to the exposure of the resist as long as the incident beam energy is kept above the highest electron binding energy of the molecule.
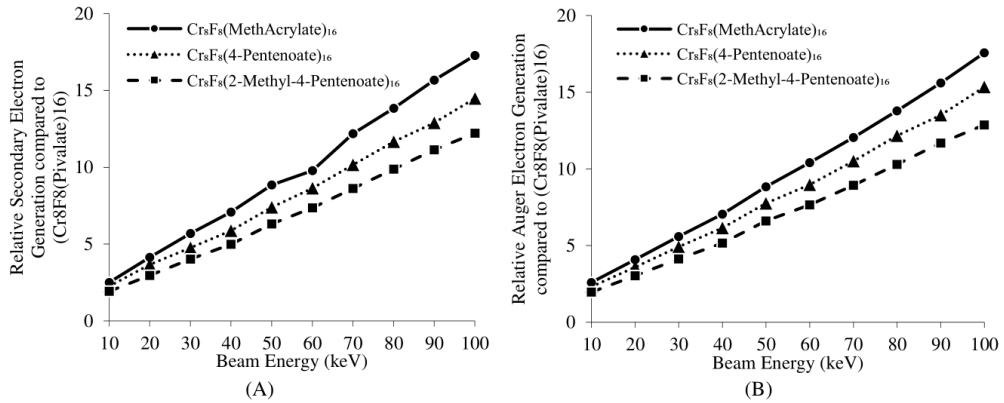

Figure 4. A plot of the ratio of Electrons generated in materials **2**, **3**, and **4** in comparison to material 1 for acceleration voltages 10-100kV.

Figure 4 shows the relative number of secondary electrons generated in each material when compared to material 1. This shows an increase in electron generation for each material (**2,3&4**) when compared to a known and tested material (i.e. material **1**). From table 2 it is clear why material **2** and **3** should be faster as they have properties which are more inducive of electron scattering. However, material **4** does not have these properties yet still has an increase by a factor of 12.8. This increase is because the ligands that replace the pivalate on the chromium ring have an exposed double carbon bond on the end of the molecule. This means that when secondary electrons are generated from the molecule there is a high chance that two electrons are emitted causing a large increase in electron generation when an electron collides with the ligand. Also, the reduction of carbon and hydrogen in the molecules increases the effective Z and the density of the molecule leading to reduced mean free path and consequently more collisions. This data shows that the molecules presented here would offer an increase in generation of secondary electrons and hence an increase of sensitivity of 17.3 times for material **2** at 100kV.

4. CONCLUSION

New generations of a family of resists were explored using Monte Carlo Modelling. New potential candidates for improvement to the resist material have been found by simulating a change in ligand on the metallic ring. A potential improvement in dose by a factor of 17.3 was found by replacing the pivalate ligand on the current material with a methacrylate ligand. This estimation of the increase in dose does not take into account many factors which affect the dose of a resist material such as solubility in the casting and developing solvents. Changing these ligands will greatly change their solubility. Also due to this change in solubility the LER and resolution of the material will be affected beyond what is suggested by the simulations. Overall this shows that costly and time-consuming experimentation can be reduced by using simulation before chemical synthesis and testing of the resist material is required.

REFERENCES

[1] G. E. Moore, "Cramming more components onto integrated circuits", Electronics, Volume 38, Number 8, April 19, (1965).
[2] Fujimura, A., Willis, A., "2017 mask maker survey conducted by the eBeam Initiative", Proc.SPIE, 10451 (2017).

[3] Lewis, S. M., Fernandez, A., DeRose, G. A., Hunt, M. S., Whitehead, G. F. S., Lagzda, A., Alty, H. R., Ferrando-Soria, J., Varey, S., Kostopoulos, A. K., Schedin, F., Muryn, C. A., Timco, G. A., Scherer, A., Yeates, S. G., and Winpenny, R. E. P., "Use of Supramolecular Assemblies as Lithographic Resists", *Supplementary Information*, Angew. Chem. Int. Ed., 56, (24), 6749-6752 (2017).

[4] Laye, R. H., Larsen, F. K., Overgaard, J, Muryn, C. A, McInnes, E. J. L., Rentschler, E., Sanchez, V., Teat, S. J., Güdel, H. U., Waldmann, O., Timco, G. A., and Winpenny, R. E. P., "A family of heterometallic wheels containing potentially fourteen hundred siblings", Chem. Commun., 9, 1125–1127 (2005).

[5] Joy, D. C., "Monte Carlo Modeling for Electron Microscopy and Microanalysis", New York: Oxford University Press, (1995).

[6] Sakurai, J. J., and Tuan, San Fu., "Modern Quantum Mechanics.", Menlo Park, California; Wokingham: Benjamin-Cummings, (1985).

[7] You, D. S., Li, H. M., and Ding, Z. J., "Monte Carlo simulation of Auger electron emission from thin film on substrate" J. Electron Spectrosc. Relat. Phenom., 222, 156–161 (2018).

[8] Casnati, E., Tartari, A., and Baraldi, C., "An empirical approach to K-shell ionisation cross section by electrons", J. Phys. B: At. Mol. Phys. 15 155 (1982).

[9] Matthew, J.A.D., "The Auger Process, Scanning Auger Electron Microscopy", John Wiley & Sons, Ltd, pp. 15-44 (2007)

PROCEEDINGS OF SPIE

Design and implementation of the next generation electron beam resists for the production of EUVL photomasks

Lewis, Scott, DeRose, Guy, Alty, Hayden, Hunt, Matthew, Li, Jarvis, et al.

SPIE.

Design and implementation of the next generation electron beam resists for the production of EUVL photomasks

Scott M. Lewis,[a,b]* Guy A. DeRose,[b] Hayden R. Alty,[a] Matthew S. Hunt,[b] Jarvis Li,[b] Alex Werthiem,[b] Trevor Fowler,[b] Sang Kook Lee[b], Christopher A. Muryn,[a] Grigore A. Timco,[a] Axel Scherer,[b] Stephen G. Yeates[a] & Richard E. P. Winpenny[a]*

[a] School of Chemistry and Photon Science Institute, The University of Manchester, Oxford Road, Manchester M13 9PL, United Kingdom; E-mail: scott.lewis@,manchester.ac.uk or Slewis2@Caltech.edu
[b] The Kavli Nanoscience Institute, California Institute of Technology, 1200 East California Boulevard, 107 – 81, Pasadena, CA USA 91125.

ABSTRACT

A new class of resist materials has been developed that is based on a family of heterometallic rings. The work is founded on a Monte Carlo simulation that utilizes a secondary and Auger electron generation model to design resist materials for high resolution electron beam lithography. The resist reduces the scattering of incident electrons to obtain line structures that have a width of 15 nm on a 40 nm pitch. This comes at the expense of lowering the sensitivity of the resist, which results in the need for large exposure doses. Low sensitivity can be dramatically improved by incorporating appropriate functional alkene groups around the metal-organic core, for example by replacing the pivalate component with a methacrylate molecule. This increases the resist sensitivity by a factor of 22.6 and demonstrates strong agreement between the Monte Carlo simulation and the experimental results. After the exposure and development processes, what remains of the resist material is a metal-oxide that is extremely resistant to silicon dry etch conditions; the etch selectivity has been measured to be 61:1.

Keywords: Metal Organic electron beam resist, electron beam lithography, 3D Secondary and Auger electron Monte Carlo Simulation

1. INTRODUCTION

The ability to write structures at the nanoscale using lithography underpins all modern, computer-based technology. The electronic devices we take for granted contain integrated circuits, the key component of which are field-effect transistors (FETs). These have reduced in size by a factor of two every two years over the past forty years, following "Moore's Law". The roadmap for the electronics industry now assumes that this constant reduction of size will continue, at least until the mid-2020s. Immersion 193 nm optical lithography (i193nm) is the current technique used to manufacture FinFETs, field-effect transistors with a shape resembling a fin. Unfortunately, this technique is reaching its physical limits in resolution. To counteract this, extreme ultra violet lithography (EUVL) has been promised to replace this technology. After two decades of outstanding research, numerous technical achievements, and multi-billion dollar investment, EUVL technology has only recently arrived into the research element of the semiconductor industry. While EUVL tools are being delivered, there is still a great need to develop new resist materials that will result in the creation of suitable EUVL photomasks. To achieve the 7 nm node that is expected to be in production by 2024, the features on the photomask, which are presently produced using electron beam lithography (EBL), are required to be 30 nm. Current e-beam resists cannot hit that specification, which means that new resists are needed in order to extract the full potential from EUVL.

Negative tone resists that are currently being used to fabricate photomasks for i193nm lithography are NEB22 (Sumitomo) and EVN30 (Shipley); they have a resolution of 40 and 50 nm, respectively [1, 2]. This resolution is required because the i193nm tools project the image onto photoresist and have lens reduction of 4x. Thus, to achieve the 14 nm node, features on the photomask need to be 56 nm. This is well outside the specification of 30 nm that is required for the production of EUVL photomasks. Another well-known issue presented by reducing feature sizes is that the

required exposure dose to make them increases. This leads to longer write times, thus decreasing the throughput of photomask creation. To alleviate this issue, new EBL tools that utilise multiple beams are being designed to fabricate these photomasks. These tools have as many as 262,144 beams and have demonstrated a half-pitch resolution capability of 11 nm [3], but exposure times required for to exposure a full photomask are still too long. Therefore, new resist materials are required with higher sensitivities and higher resolution, and are the subject of this work.

Once the high-resolution pattern has been achieved, it must be transferred into the underlying substrate. This is usually achieved using an inductively-coupled plasma (ICP) etching technique. Etching nanostructures at dimensions that are less than 50 nm pitch, however, is very difficult because the probability of landing the neutral ions between features is extremely low [4]. This leads to a decrease in etch efficiency, which inherently decreases the etch rate and selectivity. To increase the etching efficiency, the ICP forward power can be increased, but this increases the etch rate of the resist, too, which would then require thicker resist to achieve the proper etch depth, which itself would require higher dose and result in reduced resolution. To avoid these interrelated issues, the ideal resist must be able to withstand the aggressive nature of the etching plasma. One method of achieving this is to incorporate metal materials into the resist. It has been shown that resists that are comprised of metal species exhibit small etch rates (because they have very little or no chemical reactivity with the gases that are used to etch the substrate) and consequently demonstrate large selectivities [4].

To address all of the above issues, we have developed a new class of resist materials that is based on a family of heterometallic rings [5]. Our resist material uses rigidity within the metal-organic molecule to achieve a very low density (ρ=1.212) while exhibiting a large molecular weight (2192 g/mol), which produces high resolution nanostructures. Figure 1a shows the resist molecule, established by the binding of eight chromium (Cr) atoms (in green) to form a ring-like frame structure; its chemical formula is $Cr_8F_8(C_5H_9O_2)_{16}$, denoted henceforth as $Cr_8F_8(Pivalate)_{16}$. The fabrication of this structure is described elsewhere [6]. The exterior of the compound, composed entirely of *tert*-butyl groups (pivalates), gives the compound high solubility in non-polar solvents and allows it to be spun onto substrates, e.g., silicon and chromium. Upon exposure to electrons, a bond scission interaction occurs, resulting in the carbon and oxygen atoms in the pivalate molecule reacting to form CO_2 gas, which volatilizes in the vacuum. This leaves behind a chromium oxide material that is insoluble in the developer solvent [4]. These resists write with very high resolution, but at the expense of lower sensitivity. To improve the resist sensitivity, we hypothesized that replacing the pivalate molecule with a methacrylate molecule (see Figure 1b) would lead to a reduction in the exposure dose without negatively impacting the resolution. The chemical formula of the resultant resist is $Cr_8F_8(C_4H_5O_2)_{16}$, denoted henceforth as $Cr_8F_8(Methacrylate)_{16}$. This resist has dangling alkene groups outside of the molecule that are free to activate a secondary electron (SE) generation mechanism when irradiated by incident lithography electrons. This results in more electrons scattering inside the resist, thus creating a chain reaction of cascading electrons that, upon each collision, exposes the resist in the immediate write area. This has the effect of increasing the overall sensitivity of the resist. It comes at the expense, of a large contribution to the proximity effect.
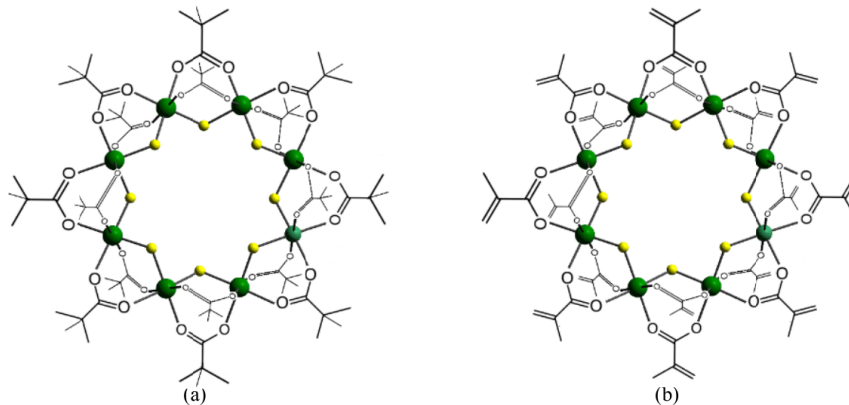

Figure 1 a) Cr8F$_8$(Pivalate)$_{16}$, b) Cr$_8$F$_8$(Methacrylate)$_{16}$. The structure of the molecules in a crystal, in ball-and-stick representation. Cr atoms are green and F atoms are yellow. H atoms are omitted for clarity.

2. SIMULATION AND EXPERIMENTAL

A Monte Carlo simulator was developed at the University of Manchester to gain a physical understanding of the internal electron scattering effects inside the $Cr8F_8(Pivalate)_{16}$ and $Cr_8F_8(methacrylate)_{16}$ resist systems [4, 7]. Unfortunately, no single model accurately describes the electron behaviour in a resist for the energy range of 5 eV – 100 KeV. The simulator therefore uses two models to describe the electron scattering behaviour. The first utilizes the Joy model, which is based on Rutherford scattering and is an accepted estimate for electrons with kinetic energies above 500 eV, where quantum effects are ignored [8]. With each scattering event, the incident electron loses a portion of its initial energy and very often ends up with an energy below the 500 eV threshold. Therefore, a model for low-energy electrons (100eV and below) was also employed. This model uses the hard-sphere potential approximation, which exploits a quantum mechanical approach to electron scattering [9]. It incorporates the use of the partial wave expansion method (PWEM), which is a method for modelling low energy electrons scattering through metals and other solids [10 – 12].

It has been hypothesized that upon a collision event, both the primary electrons (PEs) and SEs experience the statistical chance of exhibiting the correct energy to emit an Auger electron (AE). Understanding the behaviour of these electrons is essential because they will be emitted from inner shells of the scattering atoms and will have a low energy that is suitable for generating even more SEs and AEs (this happens because the AE energy is lower than the first generation of AE emission, resulting in AE generation from the outer shells). Ultimately, this causes a cascading event as AEs travel through the immediate exposure area of the resist. These electrons contribute significantly to the proximity effect and therefore must be evaluated by the simulator. The Auger generation model is based on the work by Ding, which uses the Casnati cross-section for understanding inner shell ionization [13, 14].

The simulation was performed on a 30 nm layer of each electron beam resist, $Cr_8F_8(Pivalate)_{16}$ and $Cr_8F_8(Methacrylate)_{16}$, with an underlying 50 nm substrate of silicon and chromium, respectively. Table 1 shows the physical properties of each material. The incident electron beam had a Gaussian distribution of 3σ, where the spot size had a diameter of 2 nm. The simulation was run using 1,000,000 electrons to reduce the statistical error.

Physical property	$Cr_8F_8(Pivalate)_{16}$	$Cr_8F_8(Methacrylate)_{16}$	Silicon	Chromium
Density (g/cm^3)	1.2	1.2	2.33	7.14
Effective Atomic Number	9.0	9.7	14	24
Average Atomic Weight (g/mol)	2192	3794	28.0855	51.9
Mean Ionization Potential (eV)	126.4	132.8	174	266.2

Table 1: Physical properties of the resist materials and substrates.

To fabricate a photomask, chromium is typically used as the absorbing photon layer. Therefore, the resist must be deposited on this material and patterned successfully by the EBL tool, followed by transfer of the high-resolution pattern into the Cr layer. In more detail, a 100 mm Si<100> wafer was coated with Cr using magnetron sputtering in an AJA Orion UHV series sputter system. The wafer process pressure was kept at 3 mtorr, as measured by a capacitance manometer utilizing downstream adaptive pressure control. Process gas species flow rates were kept constant at 20 sccm using a mass flow controller. The argon gas used for sputtering was of semiconductor grade purity. The thin film thickness and deposition rate data were measured by a quartz crystal thickness monitor. The system base pressure was 1E-8 torr prior to beginning deposition. The Cr layer was deposited with simultaneous RF substrate etching in order to smooth the RMS roughness. The substrate was pre-sputtered for 60 seconds at 100 W RF prior to the shutter opening. Deposition parameters included 200 W DC with a target power density of approximately 10 W/cm^2, to achieve a deposition rate of 1.22 Angstroms/s and an approximate thickness of 50 nm. The Cr layer was pre-sputtered for 60 seconds prior to shutter opening using the deposition parameters of 230 W DC with a target power density of approximately 10 W/cm^2, and a deposition rate of 0.58 Angstroms/s and an approximate thickness of 100 nm. The 100 W RF substrate etch was continued for the duration of the Chromium deposition and extended to account for back-sputtered material caused by the RF power delivered to the substrate. After the magnetron's shutter closed the RF power is ramped down over 40 seconds, resulting in some slight etching without any incoming Cr flux. The wafer was diced into 20 mm × 20 mm substrates.

The resist fabrication process is as follows. First, introduce 30 mg of $Cr_8F_8(Pivalate)_{16}$ to 3 g of Hexane and filter it using a 0.2 μm PTFE syringe filter. The $Cr_8F_8(Pivalate)_{16}$ resist was spun onto 20 mm × 20 mm silicon substrates. The resist was spun using a spin cycle of 6000 rpm for 40 seconds, which was followed by a soft bake at 100°C for 2 minutes, allowing the cast solvent to evaporate. The resulting resist film had a thickness of 30 nm. This process was

repeated for the $Cr_8F_8(Methacrylate)_{16}$ resist, except the hexane solvent was replaced with anisole. The $Cr_8F_8(Pivalate)_{16}$ resist was spun onto the Cr-coated silicon substrates using the same process that was used for coating the silicon substrates.

The exposure clearing dose of each resist material was determined from a one-dimensional matrix of a single pixel lines that were 5 μm long; the width of the line was the width of the electron beam, i.e. 2 nm. The one-dimensional matrix had each single pixel line separated by a pitch of 60, 55, 50, 45, and 40 nm. These were exposed with a dose range from 1000 to 80000 μC/cm² in incremental steps of 50 μC/cm². All resists were exposed using a Raith EPBG 5200 electron beam writer. The patterns were exposed using an acceleration voltage of 100 KeV, a probe current of 300 pA, and a step size of 5nm. The $Cr_8F_8(Pivalate)_{16}$ and $Cr_8F_8(Methacrylate)_{16}$ resists were developed in a bath of hexane and anisole, respectively, for 10 seconds. All samples were blown dry using Nitrogen (N_2).

3. RESULTS AND DISCUSSION

Figure 2 shows a 3D scattering trajectory plot that illustrates that both of the resists confine the primary electrons (PEs) to within a 15 nm diameter of the immediate write area, suggesting that high resolution nanostructures would be expected. It is evident that $Cr_8F_8(Methacrylate)_{16}$ resist generates more SEs in the resist (see Figure 2b and d) than the $Cr_8F_8(Pivalate)_{16}$ resist (see Figure 2a and c).

(a)   (b)

(c)   (d)
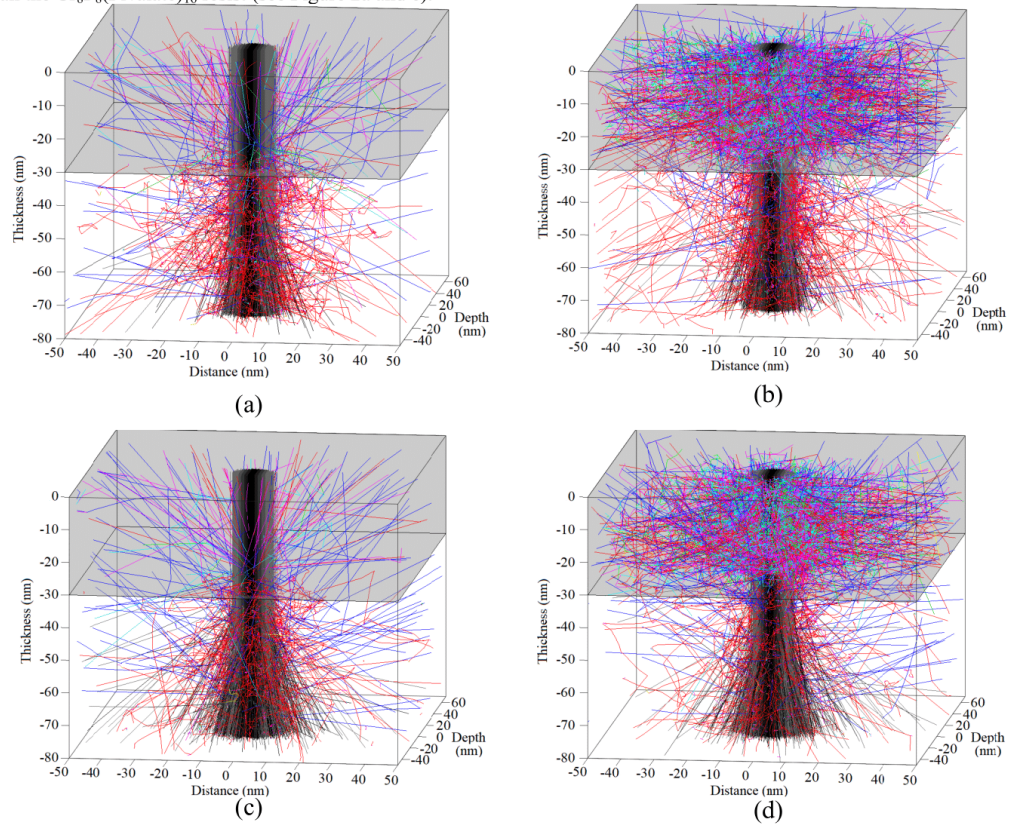
Figure 2 Point spread function of the internal electron scattering interactions inside (a) $Cr_8F_8(Pivalate)_{16}$ resist on 50 nm of Si. (b) $Cr_8F_8(Methacrylate)_{16}$ resist on 50 nm of Si, (c) $Cr_8F_8(Pivalate)_{16}$ resist on 50 nm of Cr, (d) $Cr_8F_8(Methacrylate)_{16}$ resist on 50 nm of Cr. The acceleration voltage used was 100 KeV. The black lines represent the PEs from the incident beam while the SEs above 500 eV are represented by the red lines. The SEs, which have associated energies below 500 eV, were generated by first, second and third order collisions and are indicated by purple, cyan and green, respectively. The blue lines are backscattered electrons. One million electrons are inserted into a single spot.

This is important as these electrons are responsible for exposing the resist and subsequently increase the overall sensitivity while contributing to the proximity effect. When the methacrylate molecule is appended to the outside of the molecule, the dangling alkene groups are induced by the PEs to eject further SEs, which contribute to the reduction of the overall exposure dose. The associated energy of the SEs is considerably lower than that of the PEs, leading to an increased number of scattering events, with subsequent collisions generating even more SEs, thereby producing a cascade of scattering events. This effect can be seen in Figures 2b and d, where SEs are scattered at angles larger than 80° in arbitrary trajectories away from the primary beam, exposing the resist laterally. This is how the SE plays a major role in both widening the size of the nanostructure and producing a more sensitive resist.

Figure 3a shows the number of SEs generated inside each of the resists as a function of acceleration voltage. At the lower energies of 10 to 50 KeV, the PE is slow enough to cause multiple inelastic scattering events and generate more SEs, increasing the sensitivity of the resist while sacrificing resolution. At the higher energies of 50 to 100 KeV, the PEs have a lower probability of generating SEs and therefore more collisions are required in the resist material to lose sufficient energy and therefore to increase the probability of generating an SE (see Figure 2). As a consequence, a substantial number of incident electrons will come to rest deep in the Si substrate below without having participated significantly in exposing the resist, or otherwise can be backscattered into the underside of the resist material approximately 30-40 μm away from the immediate exposure area. Thus, while 100 KeV can achieve high resolution by narrowly confining the forward scattering of electrons inside the resist, this comes at the expense of higher dose and longer writing times. Currently, 50 KeV EBL tools are employed by the semiconductor industry because it best optimizes resolution versus writing time; Figure 3 reflects this philosophy.
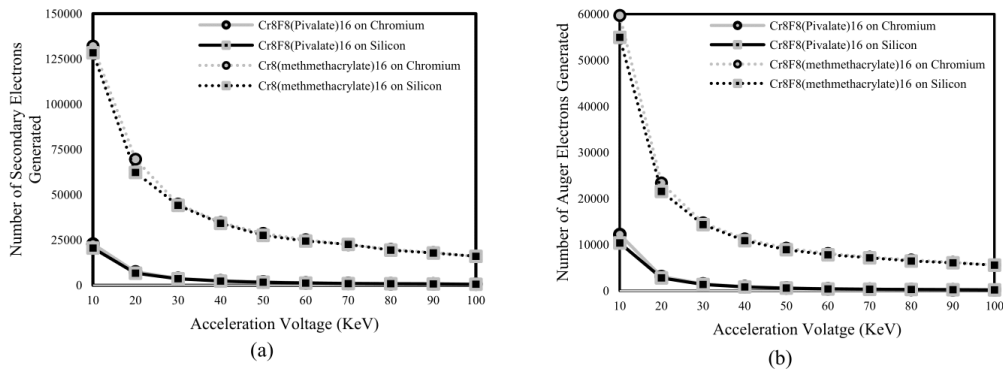
Figure 3 The number of Electrons generated in 30 nm thick resist films on 50 nm thick Si substrate. a) Total number of secondary electrons generated, b) Total number of Auger electrons generated from the resist materials.

It is clear that replacing the pivalate molecule with the methacrylate molecule significantly increases the number of SEs that are generated, thus predicting that the $Cr_8F_8(Methacrylate)_{16}$ resist will have increased sensitivity compared to $Cr_8F_8(Pivalate)_{16}$. This is due to the methacrylate's alkene groups generating SEs in close proximity of Cr atoms in the resist; Cr has a larger electron energy stopping power than that of the C, O and H atoms in the organic molecule and therefore reduces the energy of the electron. As the energy reduction of the incident electron passes the threshold of which the probability of a secondary electron being created, they are free to collide with the Alkene groups in the Methacrylate molecule and this will allow more secondary electrons to be generated (their energy will be reduced more than the first generation) and this will create an avalanche effect until their associated energy is lower than 3.6 eV (which is the energy required to scission a C − C bond). As a result of the scattering angle the secondary electron penetrates through the $Cr_8F_8(Methacrylate)_{16}$ resist it exposes it laterally. This has the effect of reducing the resolution of the pitch.

The number of AEs generated is significant because there is a high probability of emitting low energy AEs from the 1S shell, since the lowest associated energy (5989 eV) for an incident electron shown in Figure 3b was 10 KeV. The Cr atom requires the largest associated incident electron energy to emit an AE in both resist systems because the excitation energy that is essential to ionize the electron from its ground state to a higher orbit is 5989 eV. EBL tools that operate at higher incident electron energies of the Cr electronic ground state are therefore able to take advantage of this process. It must be noted that EBL tools that use large acceleration voltages (50 KeV and above) will have a lower probability of emitting an AE because the scattering interaction is lower and this can be seen in Figure 3b. It is evident that incident electrons with low energies emit more AEs because the emitted AEs have low energy with respect to the energy of the incident electron, thereby increasing the statistical chance of creating further secondary and secondary Auger electrons (if the excitation energy of the secondary AEs is correct) upon each collision. Hence causing a chain reaction of cascading electrons in the immediate exposure area, leading to a significant reduction in exposure dose. It is clear that the dangling alkene groups of the methacrylate molecule are induced by all types of electrons (PEs, SEs and AEs) and generate significantly more AEs than that of the $Cr_8F_8(Pivalate)_{16}$ resist because they have an electron from the carbon atom that is free to be ionized from the ground state (this requires an excitation energy of 284.2 eV and the probability of generated SEs and emitted AEs having this discrete energy is high).

To build on the result and the explanation of Figure 3, Figure 4 shows the number of SEs and AEs that are generated in the $Cr_8F_8(Methacrylate)_{16}$ resist compared to the number generated in the $Cr_8F_8(Pivalate)_{16}$ resist, expressed as a ratio. This ratio was calculated to communicate the overall improvement in exposure performance of the alkene groups compared to the pivalates, which are expected to be less sensitive. It was found that the presence of the methacrylate molecule increased the sensitivity of the resist material, as predicted, thereby reducing the exposure doses required to produce a pattern. This is another way of expressing the results previously given in Figure 2 and 3, which show the same overall effect.
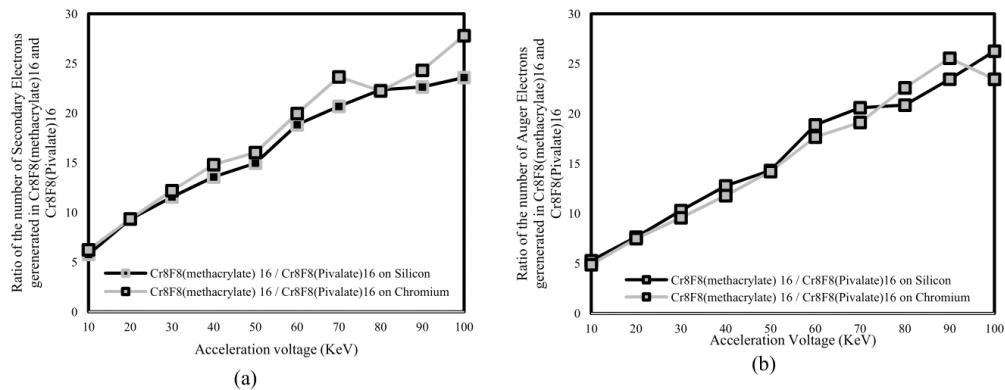
Figure 4. a) The ratio of secondary electrons generated by $Cr_8F_8(Methacrylate)_{16}$ and $Cr_8F_8(Pivalate)_{16}$ resists on 50 nm Si and Cr with varying acceleration voltage, b) The ratio of Auger electrons generated by $Cr_8F_8(Methacrylate)_{16}$ and $Cr_8F_8(Pivalate)_{16}$ resists on Siand Cr with varying acceleration voltage.

Compared to pivalate, methacrylate increases the number of generated SEs and AEs by a factor of 3.7 and 4.9, respectively, over the acceleration voltage range presented. The amplifications seen here increase the speed of the write times by increasing the solubility of the molecule upon the development process. Thus, to achieve the maximum resolution while avoiding overexposure, the exposure dose must be decreased to compensate for the extra concentration of electrons in the immediate exposure area. From this, the maximum write speed that can be theoretically achieved by $Cr_8F_8(Methacrylate)_{16}$ is approximately 23.6 times faster than $Cr_8F_8(Pivalate)_{16}$ at 100 KeV. This particular acceleration voltage is of interest as it was used to validate theoretical results with experimental results, which are presented next.

Figure 5 shows scanning electron microscope (SEM) micrographs of developed nanostructures written into $Cr_8F_8(Pivalate)_{16}$ and $Cr_8F_8(Methacrylate)_{16}$ resists. It is evident that $Cr_8F_8(Methacrylate)_{16}$ required an exposure dose lower than $Cr_8F_8(Pivalate)_{16}$ due to the introduction of the alkene groups. Even though the clearing dose of $Cr_8F_8(Methacrylate)_{16}$ is considerably reduced, Figure 5b clearly shows that the nanostructures could only be resolved at

a pitch 60 nm (and no lower) as predicted by the results of the simulations (see Figure 3), while $Cr_8F_8(Pivalate)_{16}$ produced a pattern with a pitch as small as 40 nm. Figure 5c shows 15 nm features written into $Cr_8F_8(Pivalate)_{16}$ resist on 100 nm of Cr. Interestingly, only a 45 nm pitch could be achieved on those samples; this is because Cr, compared to Si only, leads to a higher number of BSEs emitted from the substrate layer back into the underside of the resist, contributing to the proximity effect. This is expected because the atomic number of Cr is 1.71 larger than that of Si; this is predicted by the results of the simulation.
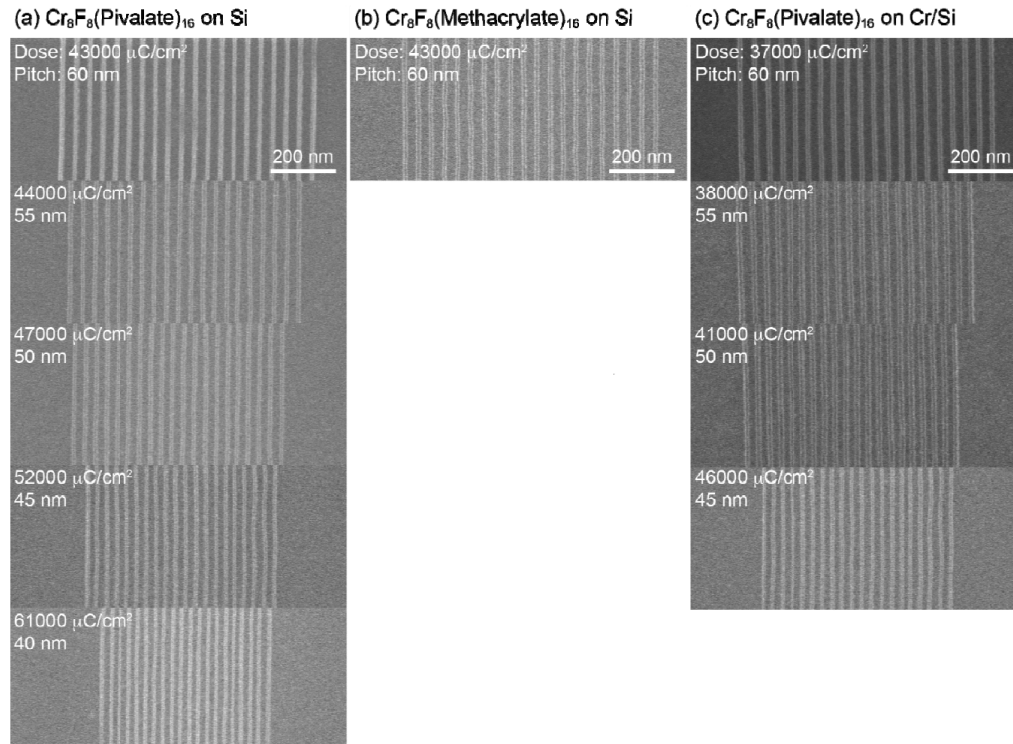
(a) $Cr_8F_8(Pivalate)_{16}$ on Si   (b) $Cr_8F_8(Methacrylate)_{16}$ on Si   (c) $Cr_8F_8(Pivalate)_{16}$ on Cr/Si

Figure 5 Effect of electron doses versus pitch on Si and Cr substrate materials. (a) Top down view of 15 nm lines on a 60, 55, 50, 45 and 40 nm pitch fabricated in $Cr_8F_8(Pivalate)_{16}$ resist on Si substrate. (b) Top down view of 15 nm lines on a 60 nm pitch fabricated in $Cr_8F_8(methacrylate)_{16}$ resist on Si substrate. (c) Top down view of 15 nm lines on a 60, 55, 50 nm pitch fabricated in $Cr_8F_8(Pivalate)_{16}$ resist on 100 nm of Cr on Si substrate.

Figure 6 shows how the exposure clearing doses vary with pitch of the pattern and confirms the role of the methacrylate molecules acting as SE and AE generators. The clearing dose in $Cr_8F_8(Methacrylate)_{16}$ is 22.6 lower than that in $Cr_8F_8(Pivalate)_{16}$, showing strong agreement with the factor of 23.6 predicted by simulation. The 4.3% simulation error is likely due to the Si substrate only having a thickness of 50 nm, whereas in the experiment, the substrate is 550 μm thick. The pattern exposure took place using incident electrons that had an acceleration voltage was 100 KeV; at this energy, the electrons can penetrate as deeply as 40 μm into the Si substrate and generate BSEs that get deposited into the underside of the resist, thus lowering both the exposure dose required and the patterning resolution.

It must be pointed out here again that the Monte Carlo simulator uses two models; the semi classical model accounts for electrons with energies of 500 eV and above and the hard sphere method models quantum effects for electron energies of 100 eV and below. Clearly, some electrons may have energy in the 400 eV gap between the models, and are therefore unaccounted for. The simulator also does not account for x-rays generated by the electrons. These x-rays can cause bond scissions in the immediately exposure area and have the effect of lowering the exposure dose.
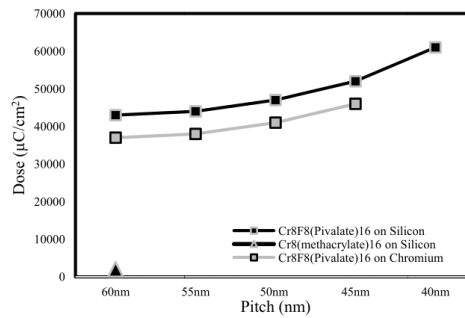
Figure 6 Electron exposure doses for the two resist materials on Si and Cr substrates.

Figure 7a shows 15 nm nanostructures with a 40 nm pitch that have been patterned in the $Cr_8F_8(Pivalate)_{16}$ resist on a Si substrate. The resist exhibited extremely high dry etch selectivity when compared with Si. Since it is difficult to distinguish between the resist and Si in the micrographs, the Si was etched with conditions that created an undercutting effect, where the resist–Si interface can clearly be seen. Although this helps with characterization, it must be noted that this kind of undercut is an undesirable result in real FinFET fabrication.
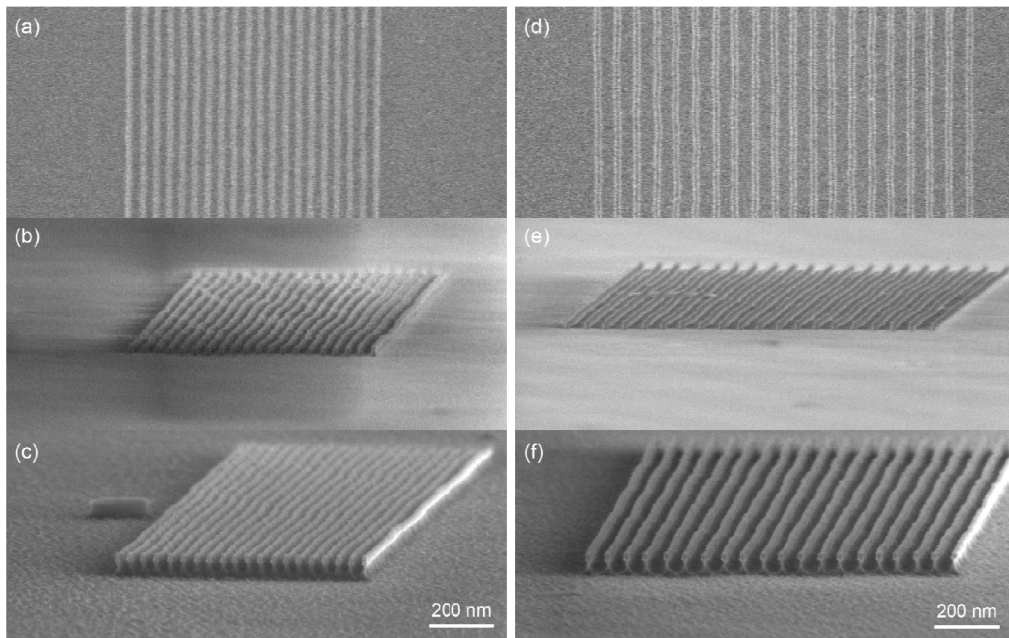
Figure 7 a) Top down view of 15 nm lines with a 40 nm pitch fabricated in $Cr_8F_8(Pivalate)_{16}$ resist on a Si. (b) Profile view of 15 nm lines on a 40 nm pitch fabricated in $Cr_8F_8(Pivalate)_{16}$ resist on Si. c) Profile view of $Cr_8F_8(Pivalate)_{16}$ resist on Si after a 20 sec pseudo Bosch dry etch process. d) Top down view of 15 nm lines on a 60 nm pitch fabricated in $Cr_8F_8(Methacrylate)_{16}$ resist on Si. (e) Profile view of 15 nm lines on a 60 nm pitch fabricated in $Cr_8F_8(Methacrylate)_{16}$ resist on Si. f) Profile view of $Cr_8F_8(Methacrylate)_{16}$ resist on Si substrate after a 20 sec pseudo Bosch dry etch process. Parameters: SF_6 and C_4F_8 gases were used with flow rates of 22 and 35 sccm, respectively; the deep reactive ion etching (DRIE) forward power was 20 W and the ICP forward power was 1200 W.

The underlying Silicon was etched with a pseudo Bosch dry etch process that uses ICP of SF_6 and C_4F_8 gases. Before the etching process, Figure 7b shows that the resist produced a resolution of 15 nm while exhibiting a height of 25.4 nm. Figure 7c shows the resolution of the Si nanostructures after the etch was 11 nm, while exhibiting a height of 36.3 nm. The remaining resist thickness is measured to be 24.6 nm, which leads to an effective resist etch rate of 0.04 nm/sec over the 20 seconds of etch time, while the Si etch rate was 1.8 nm/sec. These measurements indicate a selectivity of 45:1.That is, the silicon etches 45 times faster than the resist. Figure 7d shows 15 nm nanostructures with a 60 nm pitch that have been patterned in the $Cr_8F_8(Methacrylate)_{16}$ resist on Si substrate; this was the best resolution that was obtained. Figure 7e shows 15 nm nanostructures with a 60 nm pitch while exhibiting a height of 22.5 nm. Figure 7f shows the width of Si nanostructures after the etch to be 16 nm, while exhibiting a height of 43 nm. The remaining resist thickness is measured to be 21.8 nm, which leads to the resist etch rate of 0.035 nm/sec, while the Si etch rate was 2.15 nm/sec. This indicates a selectivity of 61.4:1. This is approximately equivalent to the selectivity that is achieved with aluminum oxide masks [15], which were to this point the best masks available (it should be noted that the use of aluminum oxide masks requires more processing steps and has increased costs compared to this process). It is evident that the additives of the methyl methacrylate do not affect the etching performance of this material; clearly the chromium oxide does not react with the SF_6 or C_4F_8 gases. As the gases come into contact with the resist, there is no chemical reactivity, thus the resist keeps its structural integrity and yields a large selectivity. This is significant because other resists such as PMMA, ZEP520A and HSQ have etch selectivities of only 2:1, 2.89:1 and 4.16:1, respectively [16]. That is, the highest dry etch resistance among these commonly used resists is only a little over 4 times that of Si. The new material reported here outperforms each of these materials by a factor of at least ~14.75.

At first glance, it appears that the Si etching process for the $Cr_8F_8(Pivalate)_{16}$ resist exhibits a poorer etch selectivity when compared to the $Cr_8F_8(Methacrylate)_{16}$ resist. This is not the case, because the pitch was 20 nm smaller and therefore the etch efficiency was decreased, which inherently decreased the etch rate of the underlying substrate and produced a smaller etch depth, leading to a decrease in the selectivity. An experiment in which the pitch is extended to 100 or 200 nm is expected to show equal or near-equal etch selectivity, once the small pitch effect is mitigated [4].

Figure 8a shows 15 nm lines on a 50 nm pitch that have been patterned in the $Cr_8F_8(Pivalate)_{16}$ resist on a 100 nm Cr layer that was deposited on Si substrate. The underlying Cr layer was etched with a dry etch process that uses an ICP of Cl_2 and O_2 gases. Before the etching process, Figure 8b shows that the resist yielded line widths of 15 nm while exhibiting a height of 26.7 nm. Figure 8c shows the width of the Cr nanostructures after the etch was 15 nm, while exhibiting a height of 20 nm. The profile of these Cr nanostructures are triangular in shape, likely due to over etching. The resist has been totally eroded away, which leads to a calculated resist etch rate of 1.33 nm/sec, while the Cr etch rate was 1.0 nm/sec. This yields a selectivity of 0.75:1, meaning that Cr etches 0.25 times slower than $Cr_8F_8(Pivalate)_{16}$ resist with this etch. This is not a surprising result because after electron beam exposure, the $Cr_8F_8(Pivalate)_{16}$ resist is converted into a chromium oxide material and the chemical reaction rate of the Cl_2 gas with the chromium oxide is expected to be high.

4. CONCLUSION

In summary, two metal organic negative tone electron beam resist have been investigated. It was shown by the Monte Carlo simulations that the $Cr_8F_8(Methacrylate)_{16}$ resist material generated a significant number of secondary and Auger electrons within the resist when compared to the $Cr_8F_8(Pivalate)_{16}$ resist, due to the presence of alkene groups. It was found that $Cr_8F_8(Pivalate)_{16}$ resist produced very high-resolution nanostructures (15 nm in width) while exhibiting a pitch of 40 nm. This high resolution came at the expense of sensitivity, however; the clearing dose of this resist material was 61000 $\mu C/cm^2$ at 40 nm pitch and 43000 $\mu C/cm^2$ at 60 nm pitch. It was shown that the low sensitivity was dramatically improved by replacing the pivalate component with a methacrylate molecule; the clearing dose of this altered resist material was 1900$\mu C/cm^2$ at 60 nm pitch (40 nm pitch was not achievable with this material). Substituting methacrylate for pivalate, therefore, resulted in a 22.6 fold increase in resist sensitivity. This experimental result was in strong agreement with simulations, which predicted an increase by a factor of 23.6. Preliminary studies showed that both resists have a remarkable pseudo Bosch dry etch resistance compared to silicon (selectivity was calculated to be 61:1 for the methacrylate resist and 45:1 for the pivalate resist). The high etch resistance is due to the presence of the d-block metal (Cr) in the initial resist, which ultimately yields a chromium oxide hard mask following exposure to an electron beam and subsequent development in solvent.
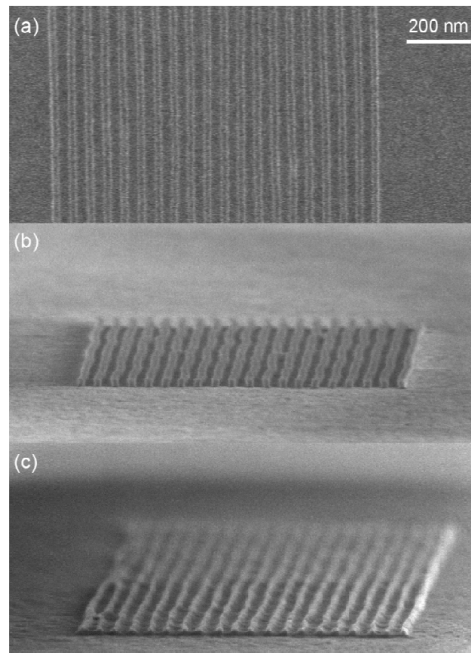
Figure 8 a) Top down view of 15 nm lines with a 50 nm pitch fabricated in $Cr_8F_8(Pivalate)_{16}$ resist on a 100 nm layer of Cr on Si substrate. (b) Profile view of the nanostructures shown in (a). (c) Profile view of the nanostructures following a 20 sec pseudo Bosch dry etch process, showing fins with a 8 nm width. Parameters: Cl_2 and O_2 gases were used with flow rates of 100 and 3 sccm, respectively; the DRIE forward power was 100 W and the ICP forward power was 1000 W.

5. ACKNOWLEDGEMENTS

REFERENCES

[1] van Dodewaard, A. J., Roes, R. F. M., Kwinten, J. A. J., van Delft, F. C. M J. M., van Run, A. J., van Langen-Suurling, A. K., Romijn, J., 'Comparison of Negative tone resists NEB22 and UVN30 in E-beam lithography', Microelectronic engineering 53 (1 – 4) 461 – 464 (2000).

[2] Masnyj, Z., Mangat, P., Ainley, E., Nordquist, K., Resnick, D., 'Evalution of negative DUV UVN30 for electron beam exposure of NGL masks', Proc. SPIE 3997, Emerging technologies IV, 0277-786x, (2000).

[3] Klein, C., Loeschner, H., Platzgummer, E., '50KeV electron multibeam mask writer for the 11nm HP node: first results of the proof of concept tool (eMET POC)', Proc SPIE 8323, Alternative Lithographic Technologies IV, 83230G (2012).

[4] Lewis, S. M., Fernandez, A., DeRose, G. A., Hunt, M. S., Whitehead, G. F. S., Lagzda, A., Alty, H. R., Ferrando-Soria, J., Varey, S., Kostopoulos, A. K., Schedin, F., Muryn, C. A., Timco, G. A., Scherer, A., Yeates, S. G., and Winpenny, R. E. P., "Use of Supramolecular Assemblies as Lithographic Resists", *Angew. Chem. Int. Ed.*, *56*, (24), 6749-6752 (2017).

[5] Noto, V. D., Boeer, A. B., Lavina, S., Muryn, C. A., Bauer, M., Timco, G. A., Negro, E., Rancan, M., Winpenny, R. E. P., and Gross, S., "Functional chromium wheel-based hybrid organic-inorganic materials for dielectric applications', Adv. Funct. Mater. 2009, 19, 3226–3236, (2009).

[6] Laye, R. H., Larsen, F. K., Overgaard, J, Muryn, C. A, McInnes, E. J. L., Rentschler, E., Sanchez, V., Teat, S. J., Güdel, H. U., Waldmann, O., Timco, G. A., and Winpenny, R. E. P., "A family of heterometallic wheels containing potentially fourteen hundred siblings", Chem. Commun., , 1125–1127 (2005).

[7] Lewis, S. M, and DeRose, G. A., Frontiers of Nanoscience, Materials and Processes for Next Generation Lithography, Elsevier, 421, 12, (2016).

[8] Joy, D. C. Monte Carlo Modeling for Electron Microscopy and Microanalysis. New York: Oxford University Press, 1995.

[9] Sakurai, J. J, and Tuan, San Fu. *Modern Quantum Mechanics.* Menlo Park, California; Wokingham: Benjamin-Cummings, 1985.

[10] Wolff, P.A., "Theory of Secondary Electron Cascade in Metals", Physical Review, 95 (1) (1954)

[11] Shimizu, R., and Ze-Jun, D., "Monte Carlo modelling of electron-solid interactions", Rep. Prog. Phys. 487-531(1992).

[12] Zianni, X., Velessiotis, D., Glezos, N., Trohidou, K. N., "Application of the partial wave expansion method in 3-D low energy electron beam lithography simulation", Microelectronic Engineering, 57-58: 297-302 (2001).

[13] You, D. S., Li, H. M., and Ding, Z. J., "Monte Carlo simulation of Auger electron emission from thin film on substrate" J. Electron Spectrosc. Relat. Phenom., , 222, 156–161 (2018).

[14] Casnati, E., Tartari, A., and Baraldi, C., "An empirical approach to K-shell ionisation cross section by electrons", J. Phys. B: At. Mol. Phys. 15 155 (1982).

[15] Henry, D., S. Walavalkar, S., Homyk, A., Scherer, A., "Alumina etch masks for fabrication of of high-aspect-ratio silicon micropillars and nanopillars", Nanotechnology, 20, (25), 255305 (2009).

[16] A. Goodyear, M. Boettcher, I. Stolberg, M. Cooke, 'Direct comparisoin of the performance of commonly used e-beam resists during nanoscale plasma etching of Si, SiO_2 and Cr' , Proc. SPIE 9428, 94280V, (2015).

Plasma-Etched Pattern Transfer of Sub-10 nm Structures Using a Metal−Organic Resist and Helium Ion Beam Lithography

Scott M. Lewis,[*,†,‡] Matthew S. Hunt,[‡] Guy A. DeRose,[‡] Hayden R. Alty,[†] Jarvis Li,[‡] Alex Wertheim,[‡] Lucia De Rose,[‡] Grigore A. Timco,[†] Axel Scherer,[‡] Stephen G. Yeates,[†] and Richard E. P. Winpenny[*,†]

[†]School of Chemistry and Photon Science Institute, The University of Manchester, Oxford Road, Manchester M13 9PL, United Kingdom

[‡]Department of Applied Physics and Materials Science and the Kavli Nanoscience Institute, California Institute of Technology, 1200 East California Boulevard, MC 107-81, Pasadena, California 91125, United States

ABSTRACT: Field-emission devices are promising candidates to replace silicon fin field-effect transistors as next-generation nanoelectronic components. For these devices to be adopted, nanoscale field emitters with nanoscale gaps between them need to be fabricated, requiring the transfer of, for example, sub-10 nm patterns with a sub-20 nm pitch to substrates like silicon and tungsten. New resist materials must therefore be developed that exhibit the properties of sub-10 nm resolution and high dry etch resistance. A negative tone, metal−organic resist is presented here. It can be patterned to produce sub-10 nm features when exposed to helium ion beam lithography at line doses on the order of tens of picocoulombs per centimeter. The resist was used to create 5 nm wide, continuous, discrete lines spaced on a 16 nm pitch in silicon and 6 nm wide lines on an 18 nm pitch in tungsten, with line edge roughness of 3 nm. After the lithographic exposure, the resist demonstrates high resistance to silicon and tungsten dry etch conditions (SF_6 and C_4F_8 plasma), allowing the pattern to be transferred to the underlying substrates. The resist's etch selectivity for silicon and tungsten was measured to be 6.2:1 and 5.6:1, respectively; this allowed 3 to 4 nm thick resist films to yield structures that were 21 and 19 nm tall, respectively, while both maintained a sub-10 nm width on a sub-20 nm pitch.

KEYWORDS: *Metal−organic resist, ion beam resist, helium ion beam lithography, high-resolution pattern, high dry etch resistance*
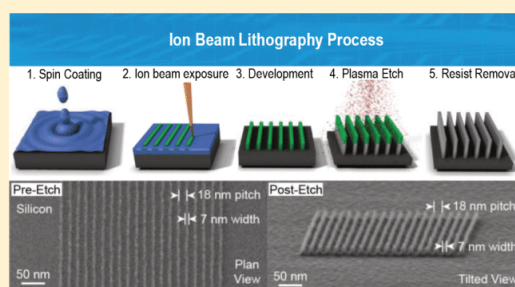
The ability of integrated circuit technology to follow Moore's law has depended on the continuous reduction in the size of field-effect transistors (FETs), first in the planar metal−oxide−semiconductor field-effect transistor (MOSFET) architecture and now more recently in the 3D fin field-effect transistor (FinFET) architecture. This has been accomplished by reducing the FET's channel length, width, and gate oxide thickness and by changing the gate dielectric material according to Dennard's scaling rules.[1] Unfortunately, these scaling rules have begun to break down because as the gate length is reduced to dimensions of 32 nm or smaller, the supply voltages need to be scaled down as well, but doing so does not provide enough voltage to turn on the p−n junction. Furthermore, the power density in the newest microprocessors has become so large that powering all transistors simultaneously would rapidly exceed the thermal power budget for the chip, resulting in diminished performance, decreased lifetime and, eventually, permanent device failure. Overheating can be addressed by powering 50% of transistors on a single chip on a single clock cycle,[2] but this presents a significant technical design challenge. Considering these problems together, it has been predicted by the International Technology Roadmap for Semiconductors (ITRS) that it will no longer be economically feasible to decrease FET device dimensions past the "7 nm node",[3] thus imbuing a sense of uncertainty on the future direction of the semiconductor industry.

Field-emission devices are promising candidates to succeed silicon FinFETs because they can operate in high-power-density regimes where chip temperatures can reach ≥300 °C. Solid-state transistors fail in this regime because the p−n junction's functionality is lost when electrons in the p-doped regions are thermally excited to the same conduction electron concentration as that in the n-doped regions.[4] Conversely, field-emission devices remain operational because as the temperature is elevated, the current remains exponentially dependent on the field until the temperature is sufficient to initiate thermionic emission, which usually occurs hundreds of degrees above 300 °C.[5] These devices are also attractive because they are capable of operating at frequencies of hundreds of gigahertz; this has been achieved by fabricating 150 nm vacuum gaps using optical lithography and resist trimming.[6] Other researchers recently demonstrated that when

6043

sub-50 nm emitter−collector gaps were fabricated, electric fields high enough for field emission could be achieved at <10 V; the devices were complementary metal−oxide−semiconductor (CMOS)-compatible, functional at atmospheric pressure, and able to be independently gated on a single integrated chip.[4] Turn-on voltages can be further reduced by fabricating sharper emitters with smaller emitter−collector gaps, incentivizing the creation of new fabrication techniques that yield tightly spaced, sub-10 nm structures.

Whereas electron beam lithography (EBL) offers high-resolution patterning to create sub-10 nm structures in the resist,[7] it is difficult to pattern these with high density, for example, with sub-10 nm wide lines spaced <20 nm apart. This is because secondary, Auger, and backscattered electrons (SEs, AEs, and BSEs) scatter in between the nanostructures during patterning, which exposes the resist in that space, resulting in bridges between lines following the development process.[8] This "proximity effect" limits the resolution of the pattern that can be produced. To alleviate this issue, a technique that uses a focused helium ion beam instead of an electron beam has been explored over the past decade. Previous helium ion beam lithography (HIBL) studies have demonstrated a reduced proximity effect[9] owing to less backscattering, the smaller interaction volume with the substrate, and the subnanometer beam diameter,[10] resulting in sub-10 nm resolution.[11] This is accompanied by orders of magnitude higher resist sensitivity than can be achieved with EBL[12] due to a higher SE yield per incident helium ion compared with each incident electron.[13]

Once the pattern has been defined in the resist by lithography, it must be transferred to the underlying material, which is often done using inductively coupled plasma reactive-ion etching (ICP−RIE). The most common metal used to produce field-emission devices is tungsten, which exhibits a low work function and has a high thermal conductivity, preventing the device from being destroyed via Joule heating.[4] Transferring the desired nanoscale pattern (e.g., sub-10 nm structures with sub-10 nm gaps in between) to tungsten is a challenge because the probability of landing ions in ever smaller gaps becomes ever lower. This leads to a decrease in etch efficiency, which inherently decreases the etch rate and selectivity. To increase the etching efficiency, the ICP forward power must be increased, but this also increases the etch rate of the resist. The thickness of the resist would then need to be increased to achieve the desired etch depth, which would require a higher dose, which, in turn, would reduce the resolution of the pattern. To avoid this problem, one may use a hard mask to withstand the aggressive nature of the plasma etch,[4] but doing this introduces more processing steps and leads to higher production costs. Another route is to enhance the etch selectivity of the resist by introducing into the molecular chemistry a metal species that effectively oxidizes upon lithographic exposure to become the hard mask. This has previously been demonstrated by our group using supramolecular Ni- and Cr-containing assemblies while maintaining a sub-10 nm patterning capability,[14] albeit at a relatively low pattern density compared with what is needed for modern nanoelectronics.

In this Letter, a metal−organic, negative tone resist candidate, $Cr_8F_8(O_2C^tBu)_{16}$ (Figure 1), first introduced by our group in ref 15 and henceforth denoted as $Cr_8F_8(pivalate)_{16}$, is presented. It is formed by the binding of eight chromium atoms (in green in Figure 1) in a ring-like structure, with an exterior composed entirely of *tert*-butyl
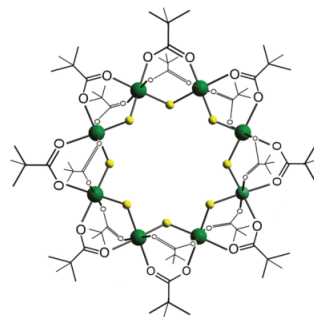

Figure 1. Structure of the $Cr_8F_8(pivalate)_{16}$ molecule in a ball-and-stick representation. Chromium atoms are green and fluorine atoms are yellow. Hydrogen atoms are omitted for clarity.

groups (pivalates).[15] The pivalates provide a high solubility in nonpolar solvents, which allows the resist molecule to be dissolved in hexane and spun onto substrates (e.g., Si and W). The molecule achieves high-resolution patterning because it is simultaneously low density ($\rho = 1.212$ g cm^{-3}), meaning that it does not have many lateral scattering centers for the lithography beam to interact with as it travels through, and has a high molecular weight (2192 g mol^{-1}), meaning that the number of resist molecules that are required to produce a thin film is significantly reduced, leading to a high-resolution pattern. Upon exposure, SEs and AEs break carbon bonds in the resist, liberating some C and O atoms while permitting other O and Cr atoms to react to form a chromium−oxide hard mask that is particularly resistant to the ICP−RIE chemistry used to etch both silicon and tungsten.[14]

Prior to the spin-on application of the $Cr_8F_8(pivalate)_{16}$ resist, atomic force microscopy (AFM) was used to evaluate the surface morphology of silicon and tungsten substrates (Figure 2a,b). The root-mean-square (RMS) roughness was measured to be 0.29 nm for silicon. For tungsten, which was sputter-deposited onto silicon as a 100 nm thick film on top of a 5 nm sputter-deposited titanium adhesion layer, the RMS roughness was 0.42 nm. The tungsten was 45% rougher than silicon; topographical contrast revealed that the film was composed of nanograins that individually were ∼5 nm wide and as long as 50 nm. For all sputter processes, wafers were first cleaned inside the chamber with argon plasma, and targets were presputtered for 60 s to remove surface oxides.

The exact nature of the resist film in this stage is uncertain. Previous studies of similar compounds sublimed onto gold show that an ordered monolayer forms,[17] but subsequent layers are not ordered because there are only weak van der Waals interactions between the molecules of metal rings. The films formed here, shown here by AFM (Figure 2c,d) to be ∼3.5 nm thick (approximately two layers), are therefore amorphous. The resist is monodispersed and in some ways resembles the molecules studied by Ober and coworkers[18] that form molecular glasses rather than conventional polymeric resists. We have not observed a glass-transition temperature because $Cr_8F_8(pivalate)_{16}$ sublimes before such a transition is observed. This low sublimation temperature is again due to the very weak intermolecular forces within the resist films.

Samples were created by dicing wafers into 20 mm × 20 mm pieces. Both substrate types, bare silicon and tungsten-coated silicon, provided a smooth enough surface upon which sub-10
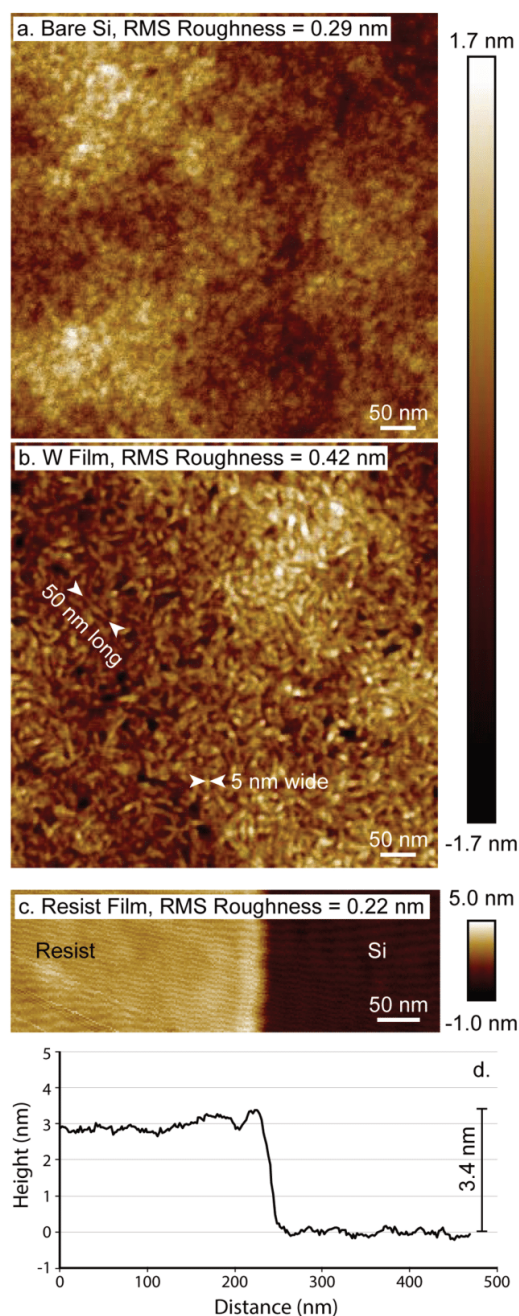
Figure 2. AFM images of substrates prior to spin-on application of the resist: (a) silicon and (b) 100 nm tungsten film (on silicon). (c) Roughness and (d) thickness of the patterned resist are also demonstrated by AFM.

nm features could be clearly resolved. This is evident in Figure 3, which shows plan-view helium ion microscope (HIM) images of $Cr_8F_8(pivalate)_{16}$ resist nanostructures following HIBL and the subsequent development in hexane. The

$Cr_8F_8(pivalate)_{16}$ resist (30 mg) was dissolved in hexane (3 g); then, the solution was filtered using a 0.2 μm polytetrafluoroethylene syringe filter before being spun onto substrates with a spin rate of 6000 rpm for 40 s, followed by a 100 °C soft bake for 2 min to evaporate the solvent. The spacing of adjacent lines (i.e., the pitch) was set to be 16−22 nm using a Raith ELPHY MultiBeam pattern generator, which controlled the helium focused ion beam (35 keV, 0.50 pA) on a Zeiss ORION NanoFab apparatus. The exposure clearing dose of the resist on each substrate was determined using a 1D matrix of single-pixel-wide lines that were 5 μm long. The width of the line was therefore the width of the ion beam, which is estimated at 0.5 nm;[10] the beam step size was 1 nm. At any pitch, patterns were exposed in sets of 20 lines with one pass of the beam per line, and the line dose of each set ranged from 10 to 100 pC/cm with incremental steps of 1 pC/cm. Following lithography, the resist was developed in hexane for 10 s to dissolve away the unexposed resist, then blown dry with nitrogen.

It can be seen in Figure 3 that discrete, continuous lines were successfully patterned at all pitches on silicon, with no bridging between any adjacent lines. On tungsten, patterning was likewise successful at 18, 20, and 22 nm pitches; at a 16 nm pitch (Figure 3h), the line uniformity was poor and bridging had occurred, a hallmark of being just beyond the lithographic resolving limit. The line width, on average, was measured to be 5.5 nm (standard deviation, $\sigma = 0.9$ nm) on silicon at a 16 nm pitch and 5.6 nm ($\sigma = 0.9$ nm) on tungsten at an 18 nm pitch. The line edge roughness (LER), defined as 3σ, was ~3 nm for both sets of Si and W lines. Tungsten performed slightly worse than silicon in both the minimum achievable pitch and the minimum line width because tungsten has a significantly larger atomic number ($Z = 74$ for W, $Z = 14$ for Si) and therefore leads to a larger number of SEs and AEs generated by the primary ion beam; this effect is triggered by both incident electrons in EBL[16] and incident He ions in HIBL.[13] The ejected SEs can be calculated using the Joy model[19] to have a scattering angle of 80° relative to the incident beam vector,[20] which leads to the exposure of the resist material adjacent to the beam's entry point. A similar mechanism is at play with low -energy ion recoil events initiated by incident ions, which scatter SEs at the same high angle in addition to physically displacing atoms.[21] The more SEs and AEs that are generated, the wider the exposure radius is that surrounds the beam entry point, leading to wider lines and, when the pitch is too small, bridging between them. Whereas this proximity effect diminishes the smallest achievable line width and pitch, the generation of more SEs and AEs also has the benefit of decreasing the necessary exposure dose, which was as much as 1.9 times lower at an 18 nm pitch for tungsten (11 pC/cm) compared with silicon (21 pC/cm). The necessary exposure dose also decreased on tungsten as a function of decreasing pitch, whereas it did not for silicon due to the intensity of the proximity effect when lines are written ever closer to each other on a high-Z material. On the basis of these results, the outlook for patterning sub-10 nm wide lines on tungsten is that the achievable pitch may be slightly higher compared with silicon (18 versus 17 nm), in exchange for nearly half of the exposure dose. It must also be noted that these HIBL doses are an order of magnitude below the threshold dose at which He implantation has been shown to induce dislocation damage in Si.[22]
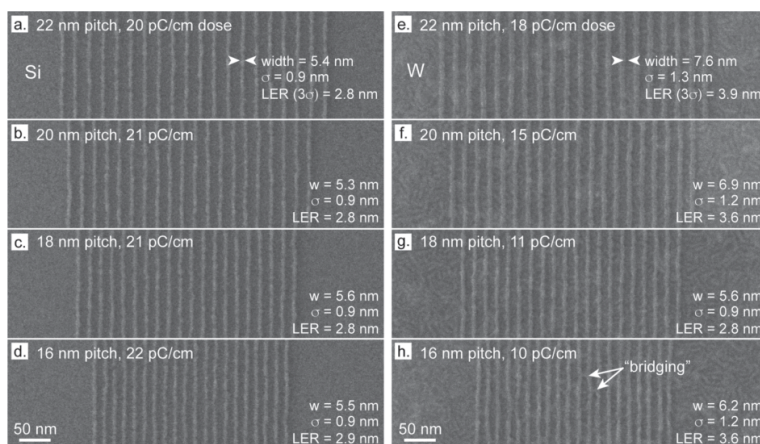
Figure 3. Plan-view HIM images of lines spaced with pitches of 22, 20, 18, and 16 nm on silicon substrate (a−d, respectively) and on a 100 nm thick tungsten film that was sputter-deposited onto a silicon substrate (e−h, respectively). Average width (w), standard deviation (σ) and line edge roughness (LER) (3σ) to the nearest 0.1 nm were determined using GenISys ProSEM software.
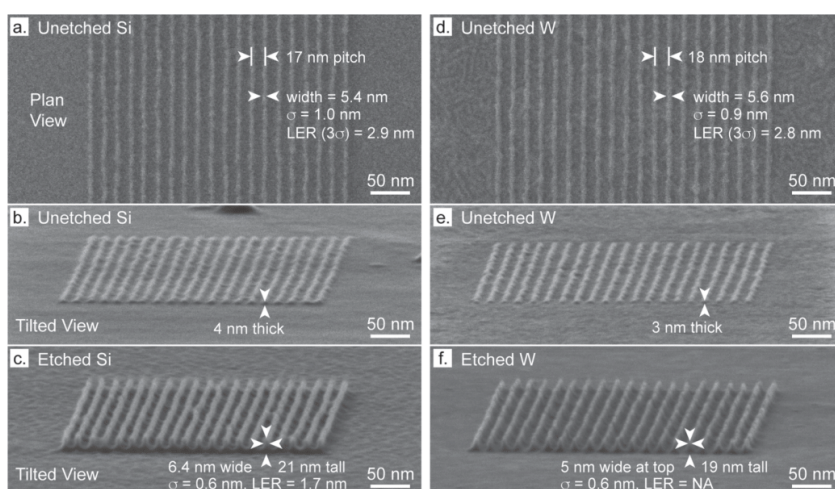

Figure 4. HIM images of lines spaced with pitches of 17 and 18 nm on silicon substrate (a−c) and on a 100 nm thick tungsten film that was sputter-deposited onto a silicon substrate (d−f), respectively. In the top row of images (a,d), developed resist structures are shown in plan view prior to an ICP−RIE etch. In the middle row (b,e), developed resist structures are shown when tilted to 87° prior to the etch. In the bottom row (c,f), fin-like structures are shown following the etch. Measurements to the nearest 0.1 nm were made using GenISys ProSEM software. The LER of etched Si lines was determined via the plan-view image (not shown); the LER of etched W lines was not determined because the triangular shape of the cross-section does not lend itself to the LER calculation.

In Figure 4, the resist is shown at its smallest successfully etched pitch for silicon (17 nm) and tungsten (18 nm), both in plan view (Figure 4a,d), and when tilted to 87° to better show its thickness (Figure 4b,e). The same spin settings were used to apply the resist to both silicon and tungsten. The resist thickness was measured at the front edge of the tilted lines (the higher tungsten roughness perhaps accounts for the thinner measurement) and confirmed by AFM (Figure 2c,d). It should be noted that the resist had been changed to a chromium−oxide material by the time the lines were imaged as a result of the lithographic exposure. It has been observed that this resist can shrink under the exposure of an electron or helium ion beam; as bonds are broken and carbon and oxygen are volatilized, the resist film volume consolidates slightly into the

oxide material. The initial resist thickness, which was not measured, is therefore necessarily larger than depicted here. Regardless, the tilted view images in Figure 4 show more clearly than the plan-view images that the resist structures are resolvable against the roughness of the substrates beneath them. The ability to spin the resist into a sub-5 nm thick film also helps to reduce the smallest feature size and dose; a thinner resist yields fewer lateral scattering sites for the traversing beam and also means that fewer ions are needed to generate enough SEs and AEs to change the small volume of resist material into the chromium−oxide material.

It is important to note that when characterizing these nanostructures, each HIM image was captured via a single scan of a 600 nm × 600 nm area, meaning that sputtering of the

nanostructure material by the low-current He ion beam (1.0 pA, 30 keV) was negligible; tests were done to show that even multiple scans of the same area at these settings did not alter the size of structures. This ensured that HIM imaging could be used as a nondestructive technique while offering higher resolution (and higher depth of field, important for imaging tilted structures) than, for example, a scanning electron microscope operated with an immersion lens. Furthermore, measurements made on AFM and HIM micrographs were calibrated against images taken of a NIST traceable standard (50 nm wide gold lines spaced on a 100 nm pitch); the same microscope settings were used on both the experimental samples and the standard to ensure measurement accuracy.

After characterizing the resist on substrate, samples for both silicon and tungsten were subjected to the same 30 s ICP−RIE process (forward power: 20 W RIE, 1200 W ICP) using SF_6 and C_4F_8 gases flowing at 22 and 35 sccm, respectively. Figure 4c shows that the average width of the resultant silicon fins was 6.4 nm, with an average height of 21 nm; the resist has been completely etched away. The effective etch rates, based on a 3.4 nm resist thickness (Figure 2d), were therefore determined to be 0.11 and 0.70 nm/s for the resist and silicon, respectively. This indicates that silicon etches ~6.2 times faster than the resist when subjected to these etch conditions (i.e., the selectivity is 6.2:1). For tungsten (Figure 4f), the structures etched with less of a straight-sidewall fin shape and more of an angled-sidewall triangular shape, suitable for a sharp-tipped field emitter. The average width at the top and bottom of the triangle was 5 and 16 nm, respectively, with an average height of 19 nm. The resist was completely etched away from the top of these W structures in 30 s, resulting in etch rates of 0.11 and 0.63 nm/s for the resist and tungsten, respectively (i.e., the selectivity is 5.6:1). It is impossible to compare these results directly with other common resists because the etch selectivities of those resists have not been reported for sub-20 nm pitches. At a 100 nm pitch, the etch selectivities of common resists on silicon are 2.0:1 for poly(methyl methacrylate) (PMMA), 2.9:1 for ZEP520A, and 4.2:1 for hydrogen silsesquioxane (HSQ).[23] Etch selectivity is expected to decrease at a smaller pitch due to the decreasing probability of landing ions between the features, so the 6.2:1 selectivity for Si reported here at a 17 nm pitch is especially notable, by comparison. The improvement in etch performance demonstrated here by $Cr_8F_8(pivalate)_{16}$ on silicon has also been previously demonstrated for related metal−organic resists, where selectivities greater than 100:1 could be achieved at larger pitches.[14] It is also notable that whereas lines narrower than those shown in Figures 3 and 4 have been patterned by other groups in the resist (e.g., 4 nm lines on a 8 nm pitch by a combination of HIBL and nanoimprint lithography[24]), the etched structures reported here are both the narrowest and the tallest to be transferred to substrate on a sub-20 nm pitch. The next smallest transferred patterns found in the literature are on a 22 nm pitch via thermal scanning probe lithography.[25]

In comparison with a previous study of $Cr_8F_8(pivalate)_{16}$ with EBL (100 keV, 300 pA),[15] HIBL required a dose three orders of magnitude smaller to achieve its smallest pitched lines. (EBL achieved 40 nm pitch lines at a 30 500 pC/cm line dose compared with a 16 nm pitch at 22 pC/cm here.) It must be mentioned that an orders-of-magnitude smaller dose with HIBL is accompanied by an orders-of-magnitude smaller current as well (e.g., 0.5 pA He ions versus 300 pA electrons). Whereas at first glance that might indicate that HIBL writing

speeds are approximately equivalent to EBL writing speeds, it is important to also consider how the resist thickness impacts doses. In the EBL study, the resist was 10 times thicker (30 nm) than in this HIBL study. If the resist thickness were to increase here, then we might expect the HIBL dose to actually decrease because we would be taking advantage of a cascade of scattering events that cannot similarly take place when the thickness is confined to something as small as 3 nm. (That decrease in dose with increasing thickness, it must be noted, would come at the expense of resolution.) Additionally, it is well known that the clearing dose increases as a function of the decreasing pitch, as was the case in the comparative EBL study, where the smallest pitch was 40 nm. If we were able to compare the 17 nm pitch EBL lines with the 17 nm pitch HIBL lines shown here, then we would expect the HIBL dose to be even more favorable than the three orders of magnitude difference noted above.

For mass manufacturing, the high exposure doses inherent to EBL, which translate into long writing times, have always outweighed the allure of EBL's small-probe, high-resolution capability. Much work has been put into developing EBL tools that split one primary beam into many beamlets to decrease writing times by exposing many patterns in parallel.[26] Here we see a demonstration of HIBL yielding both better resolution and an orders-of-magnitude smaller dose than EBL. Whereas single-beam HIBL, with the same pixel-by-pixel exposure mechanism as EBL, may still not offer the lithographic speed desired by the industry, perhaps this study indicates that if any beam is to be split and operated in parallel, then it is a beam of helium ions and not electrons.

In conclusion, it has been demonstrated that the molecule $Cr_8F_8(pivalate)_{16}$, when used as a resist, is capable of producing sub-10 nm structures in silicon and tungsten, spaced on a sub-20 nm pitch, following pattern transfer with an ICP−RIE. This result is due to several interrelated factors associated with the resist material and the method of lithography, HIBL. First, the ability to spin the resist into sub-5 nm thick films reduces the lateral scattering as the beam travels through the resist, resulting in high resolution. Second, the material's high molecular weight and low density limit the number of scattering sites that the beam encounters, which also improves resolution. Third, the nature of helium ion beam interactions yields more SEs and AEs per incident beam species than is achievable by the more traditional EBL; the HIBL dose can therefore be orders of magnitude lower, which allows for a low current to be selected, which results in a subnanometer probe diameter that further improves the patterning resolution. Finally, because exposing the resist changes it from a metal−organic compound to a chromium−oxide material, the material exhibits extremely high etch selectivity to both silicon and tungsten in the presence of an SF_6/C_4F_8 etch, allowing for the transfer of 6 nm wide lines into the substrates, even when the etch efficiency is reduced by tightly spacing the lines on a sub-20 nm pitch. It is therefore possible to fabricate sub-10 nm wide, 19 nm tall silicon and tungsten structures in a single lithography-and-etch step, opening new possibilities for future nanoelectronics. The role of HIBL in the future should also not be discounted.

■ **AUTHOR INFORMATION**

Corresponding Authors
*E-mail: scott.lewis@manchester.ac.uk; slewis2@caltech.edu.
*E-mail: richard.winpenny@manchester.ac.uk.

ORCID

Scott M. Lewis: 0000-0002-4183-1906

Richard E. P. Winpenny: 0000-0002-7101-3963

Notes

The authors declare no competing financial interest.

■ REFERENCES

(1) Dennard, R. H.; Gaensslen, F. H.; Rideout, V. L.; Bassous, E.; LeBlanc, A. R. Design of Ion-Implanted MOSFET's with Very Small Physical Dimensions. *IEEE J. Solid-State Circuits* **1974**, *9* (5), 256−268.

(2) Shafique, M.; Garg, S.; Henkel, J.; Marculescu, D. The EDA Challenges in the Dark Silicon Era: Temperature, Reliability, and Variability Perspectives. *Proceedings of the The 51st Annual Design Automation Conference on Design Automation Conference - DAC '14* **2014**, 1−6.

(3) *International Technology Roadmap for Semiconductors 2.0*; ITRS, 2015. https://www.semiconductors.org/wp-content/uploads/2018/06/0_2015-ITRS-2.0-Executive-Report-1.pdf (accessed on Aug 19, 2019).

(4) Jones, W. M.; Lukin, D.; Scherer, A. Practical Nanoscale Field Emission Devices for Integrated Circuits. *Appl. Phys. Lett.* **2017**, *110* (26), 263101.

(5) Neudeck, P. G.; Okojie, R. S.; Chen, L.-Y. High-Temperature Electronics - a Role for Wide Bandgap Semiconductors? *Proc. IEEE* **2002**, *90* (6), 1065−1076.

(6) Han, J.-W.; Sub Oh, J.; Meyyappan, M. Vacuum Nano-electronics: Back to the Future?—Gate Insulated Nanoscale Vacuum Channel Transistor. *Appl. Phys. Lett.* **2012**, *100* (21), 213505.

(7) Maile, B. E.; Henschel, W.; Kurz, H.; Rienks, B.; Polman, R.; Kaars, P. Sub-10 nm Linewidth and Overlay Performance Achieved with a Fine-Tuned EBPG-5000 TFE Electron Beam Lithography System. *Jpn. J. Appl. Phys.* **2000**, *39* (12), 6836.

(8) Yang, J. K. W.; Cord, B.; Duan, H.; Berggren, K. K.; Klingfus, J.; Nam, S.-W.; Kim, K.-B.; Rooks, M. J. Understanding of Hydrogen Silsesquioxane Electron Resist for Sub-5-Nm-Half-Pitch Lithography. *J. Vac. Sci. Technol. B Microelectron. Nanometer Struct.* **2009**, *27* (6), 2622.

(9) Winston, D.; Cord, B. M.; Ming, B.; Bell, D. C.; DiNatale, W. F.; Stern, L. A.; Vladar, A. E.; Postek, M. T.; Mondol, M. K.; Yang, J. K. W.; et al. Scanning-Helium-Ion-Beam Lithography with Hydrogen Silsesquioxane Resist. *J. Vac. Sci. Technol. B Microelectron. Nanometer Struct.* **2009**, *27* (6), 2702.

(10) Hill, R.; Faridur Rahman, F. H. M. Advances in Helium Ion Microscopy. *Nucl. Instrum. Methods Phys. Res., Sect. A* **2011**, *645* (1), 96−101.

(11) Sidorkin, V.; van Veldhoven, E.; van der Drift, E.; Alkemade, P.; Salemink, H.; Maas, D. Sub-10-nm Nanolithography with a Scanning Helium Beam. *J. Vac. Sci. Technol. B Microelectron. Nanometer Struct.* **2009**, *27* (4), L18.

(12) Shi, X.; Prewett, P.; Huq, E.; Bagnall, D. M.; Robinson, A. P. G.; Boden, S. A. Helium Ion Beam Lithography on Fullerene Molecular Resists for Sub-10 nm Patterning. *Microelectron. Eng.* **2016**, *155*, 74−78.

(13) Notte, J.; Hill, R.; McVey, S.; Farkas, L.; Percival, R.; Ward, B. An Introduction to Helium Ion Microscopy. *Microsc. Microanal.* **2006**, *12* (S02), 126−127.

(14) Lewis, S. M.; Fernandez, A.; DeRose, G. A.; Hunt, M. S.; Whitehead, G. F. S.; Lagzda, A.; Alty, H. R.; Ferrando-Soria, J.; Varey, S.; Kostopoulos, A. K.; et al. Use of Supramolecular Assemblies as Lithographic Resists. *Angew. Chem., Int. Ed.* **2017**, *56* (24), 6749−6752.

(15) Lewis, S.; DeRose, G.; Hunt, M.; Scherer, A.; Yeates, S.; Winpenny, R. E. P.; Alty, H. R.; Werthiem, A.; Li, J.; Fowler, T.; et al. Design and Implementation of the next Generation Electron Beam Resists for the Production of EUVL Photomasks. *Photomask Technology* **2018**, 24.

(16) Lin, Y.; Joy, D. C. A New Examination of Secondary Electron Yield Data. *Surf. Interface Anal.* **2005**, *37* (11), 895−900.

(17) Ghirri, A.; Corradini, V.; Bellini, V.; Biagi, R.; del Pennino, U.; De Renzi, V.; Cezar, J.; Muryn, C. A.; Timco, G. A.; Winpenny, R. E. P.; Affronte, M. *ACS Nano* **2011**, *5*, 7090−7099.

(18) Dai, J.; Chang, S. W.; Hamad, A.; Yang, D.; Felix, N.; Ober, C. K. *Chem. Mater.* **2006**, *18*, 3404−3411.

(19) Joy, D. C. *Monte Carlo Modeling for Electron Microscopy and Microanalysis*; Oxford University Press, 1995.

(20) Lewis, S. M.; DeRose, G. A. SML Electron Beam Resist. *Front. Nanosci.* **2016**, *11*, 421−446.

(21) Ziegler, J. F. *Handbook of Stopping Cross-Sections for Energetic Ions in All Elements*; Pergamon Press: New York, 1980.

(22) Livengood, R.; Tan, S.; Greenzweig, Y.; Notte, J.; McVey, S. Subsurface Damage from Helium Ions as a Function of Dose, Beam Energy, and Dose Rate. *J. Vac. Sci. Technol. B Microelectron. Nanometer Struct.* **2009**, *27* (6), 3244.

(23) Goodyear, A.; Boettcher, M.; Stolberg, I.; Cooke, M. Direct Comparison of the Performance of Commonly Used E-Beam Resists during Nano-Scale Plasma Etching of Si, SiO$_2$, and Cr. *SPIE Advanced Lithography* **2015**, 94280V.

(24) Li, W.-D.; Wu, W.; Stanley Williams, R. Combined Helium Ion Beam and Nanoimprint Lithography Attains 4 nm Half-Pitch Dense Patterns. *J. Vac. Sci. Technol., B: Nanotechnol. Microelectron.: Mater., Process., Meas., Phenom.* **2012**, *30* (6), No. 06F304.

(25) Ryu Cho, Y. K.; Rawlings, C. D.; Wolf, H.; Spieser, M.; Bisig, S.; Reidt, S.; Sousa, M.; Khanal, S. R.; Jacobs, T. D. B.; Knoll, A. W. Sub-10 Nanometer Feature Size in Silicon Using Thermal Scanning Probe Lithography. *ACS Nano* **2017**, *11* (12), 11890−11897.

(26) Chang, T. H. P.; Mankos, M.; Lee, K. Y.; Muray, L. P. Multiple Electron-Beam Lithography. *Microelectron. Eng.* **2001**, *57−58*, 117−135.

Nanoscale Patterning of Zinc Oxide from Zinc Acetate Using Electron Beam Lithography for the Preparation of Hard Lithographic Masks

Ahmad Chaker, Hayden R. Alty, Peng Tian, Anastasios Kotsovinos, Grigore A. Timco, Christopher A. Muryn, Scott M. Lewis,* and Richard E. P. Winpenny*

ACCESS | ☐ Metrics & More | ☐ Article Recommendations

ABSTRACT: An approach is presented for nanoscale patterning of zinc oxide (ZnO) using electron beam (e-beam) lithography for future nanoelectronic devices and for hard lithographic masks. Zinc acetate $(Zn_4O(CH_3COO)_6)$ films were exposed using a scanning electron microscope (SEM), causing decomposition of $Zn_4O(CH_3COO)_6$ into ZnO. The exposure of $Zn_4O(CH_3COO)_6$ using an electron beam was successfully utilized to fabricate 12 nm zinc oxide lines with a 40 nm pitch on silicon. The chemical composition of zinc acetate (film before e-beam exposure) and ZnO (film after e-beam exposure) was investigated using X-ray spectroscopy (XPS). The Zn 2p shift peaks and the O 1s contribution confirmed the decomposition of zinc acetate into zinc oxide after exposure. To confirm this transformation into ZnO, the optical band gap of the film was determined and the electrical resistivity of the film was measured. The electrical resistivity and the optical band gap results revealed the transformation into a ZnO film with a band gap of 3.31 eV at room temperature and an electrical resistivity of 91.5 Ω cm. The ZnO patterns were used as a hard mask to etch silicon, and it showed a good selectivity of 27:1 for dry etching silicon using SF_6 and C_4F_8.

KEYWORDS: zinc acetate, zinc oxide, electron beam lithography, exposure, decomposition
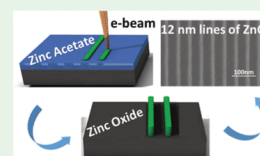
■ INTRODUCTION

The unique and fascinating, physical, and chemical properties of zinc oxide make it one of the most studied materials in the nanotechnology field. This II–VI semiconductor has high chemical stability, a wide direct band gap of 3.3 eV, very good piezo- and pyroelectric properties, and optical transparency in the visible region. These properties make it attractive for different applications in electronics and optoelectronics.[1−3]

Different techniques are used to deposit ZnO films such as atomic layer deposition (ALD), physical vapor deposition (PVD), chemical vapor deposition (CVD), and sol–gel and screen-printing techniques.[4−8] Several precursors have been considered for the formation of ZnO films such as zinc chloride, zinc nitrate hexahydrate, zinc 2-ethylhexanoate, zinc nitrate, and zinc acetate. The precursor choice has a major influence on the structural morphology and properties of the film.[9−11] Zinc acetate is the most commonly used precursor for ZnO thin-film deposition. This precursor is inexpensive and soluble and has a low decomposition temperature, making it an ideal candidate for use in many deposition techniques such as metal–organic chemical vapor deposition (MOCVD), spray pyrolysis, sol–gel technique, and thermal evaporation.[12−16] Many papers report the structural, morphological, optical, and electrical properties of zinc oxide films prepared from zinc acetate. This film is controlled by adjusting the deposition parameters such as the heating conditions, the thickness of the layer, or the solvent concentration.[12−18]

Nagase et al. presented a different method to prepare ZnO films using KrF excimer laser irradiation of sol–gel zinc acetate films.[19] They showed that the structural characteristics and optical and electrical properties of the ZnO film depend on the energy of the laser, where the crystallization process is controlled by laser irradiation and is discussed in terms of its thermal and direct photoinduced effects.[19] Asakuma et al. reported photoinduced structural changes in ZnO thin films derived from zinc acetate using UV radiation at wavelengths of 185 and 254 nm. The exposure of the films to an ultraviolet lamp induced formation of ZnO crystals. The photoinduced crystallization and reduction are ascribed to the electronic excitation by energetic photons.[20] It has been demonstrated that UV photodecomposition of zinc acetate to form suitable seed layers for the growth of ZnO nanowires (NWs). It was noted from the X-ray photoelectron spectroscopy (XPS)

406
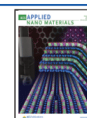
analysis that the seed layers confirmed the conversion of the zinc acetate to ZnO with exposure to UV.[21] A similar report demonstrated micropatterns of ZnO nanoarrays fabricated by ultraviolet irradiation in a zinc acetate layer.[22] Moreover, Hong et al. showed a novel method of digital patterning ZnO NWs by decomposing a zinc acetate precursor selectively using a focused scanning laser as a heat source.[23]

The fabrication of sub-15 nm structures requires new types of technologies to be developed with a reduction in technology steps (deposition, lithography, and etching). A potential technique for such nanometer fabrication can be obtained using an electron beam.[24−29] The desired materials can be created in a scanning electron microscope (SEM) from the specific precursor by exposure to the electron beam. This exposure process is based on a local decomposition of a precursor gas adsorbed at the surface or after spinning of a thin film. It is used for creating different materials using a scanning electron microscope (SEM) such as aluminum, gold, titanium, platinum, and silicon oxide.[24−26] The benefits of this technology are the creation of nanostructures at predefined locations within a scanning electron microscope. ZnO has been investigated to be obtained using an electron beam using SEM. Saifullah et al. showed that zinc naphthenate was capable of forming 7 nm lines.[28] Moreover, Jones et al. showed the possibility of fabricating ZnO nanowires down to 10 nm width after exposure of a zinc neodecanoate precursor using an electron beam tool at 100 kV.[29]

When fabricating a device, patterning of ZnO films plays a key role and is performed by an etching process. Most ZnO etching processes are dominated by wet etching due to the simple operation and the possibility of etching ZnO in different acids and alkalis such as H_2O_2, HCl, H_3PO_4, or NH_4Cl.[30−32] Etching at the microdimension using wet chemistry is sufficient; unfortunately, it is not suitable at the nanoscale because the wet chemistry technology etches isotropically, meaning that manufacturing deep nanostructures is not possible. To counteract this, different plasma chemistries have been investigated for dry etching ZnO films such as CF_4/Ar, $BCl_3/CH_4/H_2$, IBr, and BI_3 plasma chemistries.[33−35] Unfortunately, to produce zinc oxide nanostructures for devices requires multiple processing steps and adds to the associated production costs.

In this work, a new approach for manufacturing ZnO nanostructures without the need for etching is confirmed for future nanoelectronic devices and for hard lithographic masks. The work presented here proposes the preparation of ZnO films using an electron beam. It has been found that ZnO nanostructures can be produced from a zinc acetate material that was sublimed inside a vacuum chamber *ex situ* to the electron beam. Using the electron beam as an exposure tool, it is possible to lithographically fabricate ZnO nanoscale patterns in one processing step. Upon exposure to the electron beam, the zinc acetate leads to the decomposition of Zn_4O-$(CH_3COO)_6$ to produce ZnO nanostructures. The optical and electrical properties of ZnO patterns obtained using e-beam exposure are investigated to confirm the decomposition of zinc acetate into zinc oxide (Scheme 1). It has recently been reported that ZnO can be utilized as a hard mask material for fabrication of silicon devices. This is because it has a high selectivity of 27:1 for dry etching silicon using a SF_6/O_2 gas mixture.[36] Unfortunately, there are several processing steps are required to produce a hard mask. It has been recently discovered by our group that by employing metal−organic

Scheme 1. Decomposition of Zinc Acetate into Zinc Oxide
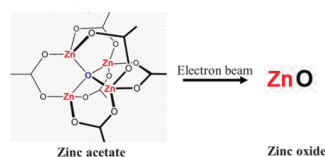
chemistry as the electron beam resists can be patterned with an ultrahigh resolution of 20 nm half-pitch while producing ultrahigh dry etch selectivities of >100:1.[37,38] The work described here investigates the possibility of using ZnO nanopatterns as a hard mask. The results imply that devices based on ZnO can be produced by a simple technique, which may be applicable to integrated electronic systems or for hard lithographic masks

■ EXPERIMENTAL SECTION

The zinc oxide nanostructures were produced by subliming zinc acetate dihydrate $(Zn(CH_3COO)_2 \cdot 2H_2O)$ (99.9%), which was obtained from Sigma-Aldrich, onto a silicon substrate. The sublimation process was performed in a vacuum (using an Edwards thermal evaporator) at a base pressure of 2×10^{-5} mbar. The growth rate of zinc acetate dihydrate $(Zn(CH_3COO)_2 \cdot 2H_2O$ was measured to be 0.5 Å/s. This resulted in a film of 74 nm thickness of zinc acetate as measured via AFM. To produce the zinc oxide nanostructures, the zinc acetate layer was exposed using a Sigma Zeiss scanning electron microscope (SEM). The electron beam was driven using a Raith Elphy plus pattern generator. The pattern consisted of a one-dimensional matrix of single-pixel lines that were 5 μm long and separated by pitches of 100 down to 40 nm with a step size of 2 nm. These were exposed with a dose scale from 1000 to 50 000 μC/cm^2. The pattern was exposed using an acceleration voltage of 30 kV, a beam current of 37 pA, and a step size of 2 nm, and it was found that a dose of 24 763 pC/cm was necessary to fully transform the material from zinc acetate to zinc oxide. The nanostructures were revealed by a development process, which consisted of submerging the sample in a methanol bath for 10 s, followed by dry nitrogen blow drying. The topography and the thickness of the obtained films before and after e-beam exposure were measured with a Multimode 8 atomic force microscope (AFM) from Bruker. The *ex situ* heat treatment of the zinc acetate samples was carried out on a hot plate at 400 °C for 10 min in air. Analysis of the electron beam exposure mechanism was achieved by employing the X-ray photoelectron spectroscopy (XPS) technique, and the high-resolution spectra were taken using a near ambient pressure NAP-XPS instrument. This instrument had a high-resolution monochromatic Al Kα X-ray source (1486.6 eV) with a pass energy of 70 eV and a step resolution of 0.1 eV. The instrument setup had a supplementary low-energy electron diffraction (LEED) gun within the chamber, which means that the zinc acetate could be exposed *in situ* while collecting the XPS spectra, hence ascertaining the exposure mechanism. To further understand the transformation of the zinc acetate into zinc oxide, the electrical properties were investigated via its optical band gap and current−voltage characteristics. The optical band gap measurement was carried out at room temperature using ultra-violet−visible (UV−vis) spectroscopy, and the optical band gap was determined from the transmission spectra. Current−voltage measurements were achieved using a Keithley 4200-SCS electrical character-ization system.

■ RESULTS AND DISCUSSION

The zinc oxide nanostructures were produced by subliming zinc acetate dihydrate. This process of deposition is done in two steps: the first step is the dehydration process to make
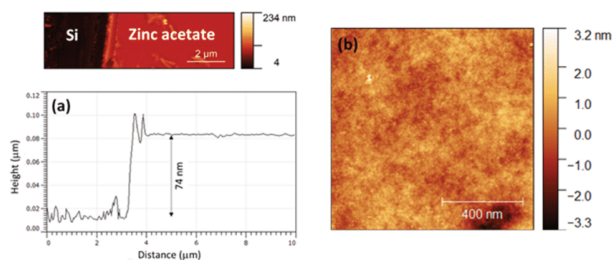
213

Figure 1. (a) AFM image showing zinc acetate thickness after the sublimation process. The area where the height was measured is shown above. (b) AFM image of the zinc acetate surface after the sublimation process.

anhydrous zinc acetate $(Zn(CH_3COO)_2)$ as shown by reaction 1, followed by the next step to form $(Zn_4O(CH_3COO)_6)$ as described by reaction 2. Both steps are performed in a vacuum to avoid any reaction or degradation of the compound. The heating rate should be below 10 °C/min to avoid the possible coexistence of ZnO and $Zn_4O(CH_3COO)_6$.

$$Zn(CH_3COO)_2 \cdot 2H_2O(s)$$
$$\Rightarrow Zn(CH_3COO)_2(s) + 2H_2O(g) \qquad (1)$$

$$4Zn(CH_3COO)_2(s)$$
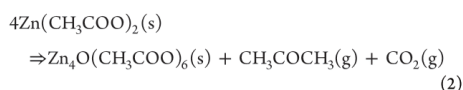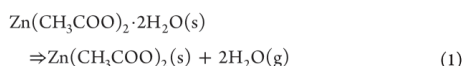$$\Rightarrow Zn_4O(CH_3COO)_6(s) + CH_3COCH_3(g) + CO_2(g) \qquad (2)$$

Figure 1a shows that the thickness of the zinc acetate film measured using AFM is 74 nm. Prior to exposing the zinc acetate film to the electron beam, atomic force microscopy (AFM) was used to evaluate the thickness and surface morphology of the zinc acetate film. The root-mean-square (RMS) surface roughness was measured to be 0.56 nm (Figure 1b).

To produce the zinc oxide nanostructures, the zinc acetate film was exposed using a Sigma Zeiss scanning electron microscope (SEM). The electron beam was driven using a Raith Elphy plus pattern generator. The pattern was exposed using an acceleration voltage of 30 kV, a beam current of 37 pA, a step size of 2 nm, and a dose of 24 763 pC/cm. The nanostructures were revealed by a development process in a methanol bath for 10 s. It can be seen in Figure 2 that discrete,
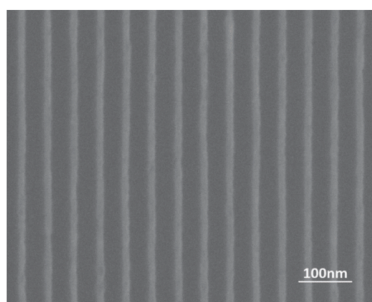

Figure 2. Top-down view of 12 nm lines on a 40 nm pitch fabricated on a Si substrate.

continuous lines were successfully patterned on silicon, with no bridging between any adjacent lines. The line width, on average, was measured to be 12 nm on silicon at 40 nm pitch, which was the ultimate resolution with an aspect ratio of around 2. Unexposed zinc acetate areas remain soluble in the developer and can be washed away by immersion in a MeOH bath for 10 s.

X-ray photoelectron spectroscopy (XPS) was employed to gain vital insight into how the zinc acetate transforms into zinc oxide upon electron beam exposure. This was achieved by utilizing a near ambient pressure NAP-XPS instrument. The experiment performed consisted of zinc acetate being sublimed into the vacuum chamber (pressure 3×10^{-5} mbar) onto a silicon substrate; this avoided adventitious carbon being deposited on the sample surface. The XPS spectra were collected *in situ*, so that the condition of the zinc acetate could be understood before exposing it to an electron beam. Once the unexposed spectra were collected, the second sample of zinc acetate was sublimed onto a silicon substrate and was exposed to the electron beam (LEED) (acceleration voltage was 1 kV, current was 10 μA) that was set up within the XPS chamber. Once the zinc acetate was fully exposed to the electron beam, an XPS spectrum was collected *in situ* and the results were compared.

Figure 3a shows the XPS spectra in the range of Zn $2p_{1/2}$ and Zn $2p_{3/2}$ signals before and after e-beam exposure. The single binding energy peak obtained by deconvolution of Zn $2p_{3/2}$ before the exposure is observed at 1022.1 eV; this peak is shifted to the lower binding energies at 1021.7 eV after exposure.[39,40] This shift was attributed to the fact that the zinc component became more metallic. A higher binding energy has been reported for $[Zn_4O(CH_3COO)_6]$ compared with ZnO.[39,41] Figure 3b displays XPS spectra of the O 1s region of the same film before and after electron beam exposure. For the unexposed film, two peaks are observed; the peak at 532 eV is attributed to the oxygen in the carboxylate group, and the other peak at 530.4 eV is assigned to ZnO contribution. For the exposed film, both peaks are detected with a shift for −0.2 eV. The area ratio of the carboxylate group before and after exposure is reduced by a factor of 2.7, and the ZnO area is increased after exposure by a factor of 1.7.

The reduction of the carboxyl area and the shift of Zn 2p after e-beam exposure can be explained by a decomposition mechanism of zinc acetate into zinc oxide. E-beam exposure is expected to produce instantaneously a local thermal influence on the precursor film and then decompose zinc acetate into zinc oxide by the same thermal decomposition mechanism of zinc acetate to produce ZnO crystals with volatile acetone and
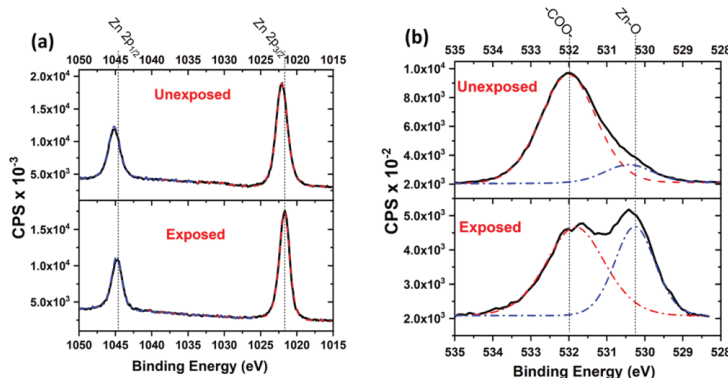
214

Figure 3. (a) High-resolution XPS Zn-2p spectra of a zinc acetate film before and after electron beam exposure. (b) High-resolution XPS O 1s spectra of the zinc acetate film before and after electron beam exposure. The dotted line spectra result from the XPS spectrum deconvolution.

CO_2 as shown by reaction 3.[42] This mechanism also explains the reduction by 61% of film thickness after e-beam exposure (see the AFM image of Figure 7b).

$$Zn_4O(CH_3COO)_6(s)$$
$$\Rightarrow 4ZnO(s) + 3CH_3COCH_3(g) + 3CO_2(g) \qquad (3)$$
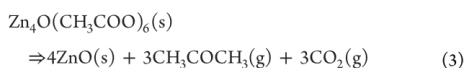
The presence of carboxyl organic residue after e-beam exposure can be explained by the low exposure dose or insufficient exposure time to obtain complete zinc acetate decomposition. It is also possible that the volatile components in the reaction have not completely diffused from the film.

In addition, X-ray photoelectron spectroscopy was used to evaluate the work function of the material before and after e-beam exposure. The work function was determined by the following equation

$$\Phi = h\gamma - \Delta E \qquad (4)$$

where ΔE is the energy difference between the cutoff and Fermi-level energy. During the XPS measurement, the samples were biased at −9.69 eV to avoid charging effects of the instrument work function. The Fermi edge location of each sample was estimated using platinum. The XPS excitation light source is monochromatic aluminum ($h\gamma$ = 1486.71 eV). Figure 4 presents the cutoff energy of the XPS spectra before and after e-beam exposure. An important shift of binding energy due to charging is detected for zinc acetate before exposure. This shift is attributed to the insulator property of the zinc acetate film. After correction according to C−C peaks, a work function equal to Φ = 6.98 eV has been obtained. After e-beam exposure, no charging shift is detected; this is due to the semiconductor properties of the ZnO as the film loses the insulator property as expected. The cutoff energy leads to a work function of Φ = 4.78 eV for zinc acetate after e-beam exposure. This compares well with literature values for ZnO, which range from 4.2 to 4.9 eV.[43,44] The work function energy of the film after exposure is reduced by 2.2 eV; this evolution is also consistent with decomposition of $[Zn_4O(CH_3COO)_6]$ into ZnO.

Figure 5a reveals the variation of transmittance with the incident wavelength in the region between 200 and 800 nm for zinc acetate films before and after electron beam exposure
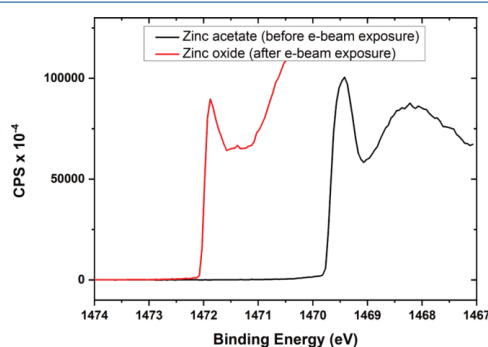

Figure 4. Cutoff energy of the XPS spectrum recorded for zinc acetate before and after e-beam exposure.

obtained using ultraviolet-visible (UV−vis) spectroscopy. The zinc acetate was sublimed onto two quartz substrates, where one was exposed to the electron beam (acceleration voltage was 5 kV, current was 2.5 nA, step size was 50 nm) and the exposure area was 1 cm^2 to detect enough transmission light by a UV−vis detector. The zinc acetate film shows high transmittance between 300 and 800 nm; this transmission decreases after e-beam exposure due to the creation of the ZnO film. Using the transmission data, the optical band gap can be calculated by the following relation.[45]

$$(\alpha h\nu) = A(h\nu - E_g)^{1/2} \qquad (5)$$

where α is the absorption coefficient, $h\nu$ is the photon energy, A is a constant, and E_g is the optical band gap. Figure 5b shows the plot of the $(\alpha h\nu)^2$ function of the photon energy measured from the transmission spectra. The value of the band gap for the zinc acetate thin film deposited on the quartz substrate before exposure (Figure 5b) was found to be 5.68 eV. The estimated values of the optical E_g were found to reduce after exposure of the films with E_g equal to 3.31 eV (Figure 5a), the same value of the band gap energy of ZnO crystals (3.3 eV), which is the reported value of the band gap for standard ZnO.[1]
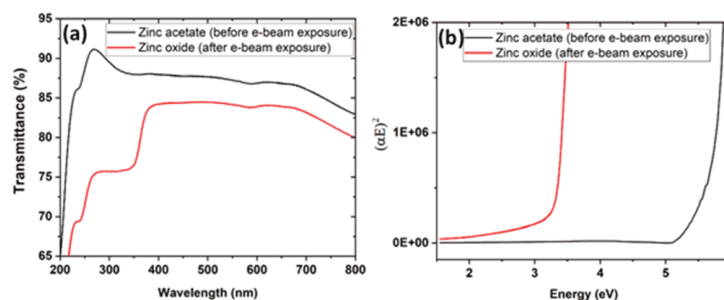
215

Figure 5. (a) Transmission spectra for zinc acetate films before and after electron beam exposure. (b) Plot of $(\alpha h\nu)^2$ versus photon energy for zinc acetate thin films before and after electron beam exposure.

The electrical properties were measured before and after e-beam exposure. To carry out this measurement, ohmic contacts were required. To produce the contact pad, a layer of 50 nm of gold was deposited by thermal evaporation through a "shadow" mask. The shadow mask had four contact pads; two contact pads were separated by 400 μm, while the other two contact pads were rotated by 90° with respect to the first contact pads and they were also separated by 400 μm. The thickness of the shadow mask was 1 mm. Thin gold electrodes were evaporated on zinc acetate before exposure and on 1 mm^2 of ZnO after exposure. The exposed film was annealed at 400 and 300 °C for 10 min to evacuate the carboxyl organic residue detected by XPS. As expected, an insulator was observed before exposure as shown in Figure 6, and the conductivity
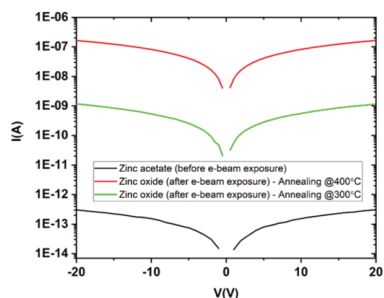

Figure 6. $I-V$ characteristic of zinc acetate thin films before and after electron beam exposure with annealing at 300 and 400 °C.

does not improve immediately on writing using the electron beam. Annealing the ZnO nanopatterns improves the conductivity (Figure 6), and the improvement is greater at 400 °C than at 300 °C. The improvement in conductivity properties can be attributed to the reduction of carbon content, which has diffused out of the ZnO nanopatterns as carbon monoxide during the annealing process. The film annealed at 400 °C possesses an electrical resistivity of 91.5 Ω cm, and the same order of magnitude of electrical resistivity is obtained for the ZnO deposited by sol–gel spin-coating using zinc acetate.[46,47] The $I-V$ curves for the zinc acetate after exposure shows a linear dependence, indicating an Ohmic behavior of the Au-ZnO-Au structure. Ohmic Au/ZnO contacts are frequently observed for air-exposed ZnO surfaces

and have been attributed to an accumulation layer induced by OH adsorbates.[48,49]

Zinc oxide is expected to have hard mask properties with respect to silicon dry etching conditions.[36] Figure 7a shows a larger line with a width of 30 nm and a pitch of 100 nm. The surface thickness of the films was investigated by an *ex situ* atomic force microscope (AFM). The film thickness after e-beam exposure is 23 nm, which means the zinc acetate film thickness is decreased by 68.9% after exposure and is confirmed by the AFM measurement shown in Figure 7b. Therefore, the aspect ratio of postexposure and pre-etch is 1.3. The film thickness reduction before and after e-beam exposure (68.9%) is equal to the density difference between zinc acetate (1.74 g cm^{-3}) and zinc oxide (5.61 g cm^{-3}).

After lithography, the ZnO nanostructures were subjected to the ICP−RIE process, and Figure 7c shows that the average width of the resultant silicon fins was 27 nm, with an average height of 179.1 nm (Figure 7d). It can be seen in Figure 7c that the ZnO mask still remains on the top of the silicon structures and the initial thickness does not change significantly when compared to its initial thickness. The residual ZnO mask is easily removed using a 3 M NH$_4$Cl aqueous solution, following literature precedent.[31,32] This removal process produces silicon fins that are 162.1 nm tall as presented in SEM and AFM images (Figure 7e,f). It was determined that the ZnO thickness after the dry etch process was 17 nm. The effective etch rates were therefore determined to be 0.2 and 5.42 nm/s for the ZnO material and silicon, respectively, and the silicon was etched approximately 27 times faster than the resist when subjected to these etching conditions, which is in agreement with the literature.[36] These results can be directly compared with other common resists, and the etch selectivities of common resists on silicon are 2.0:1 for PMMA, 2.9:1 for ZEP520A, and 4.2:1 for HSQ.[50] We have not yet explored other combinations of plasma and wet etching for this hard mask.

■ CONCLUSIONS

In summary, we have shown the possibility of making ZnO nanoscale patterns by exposing zinc acetate films to an electron beam. It has been demonstrated that by exposing zinc acetate to an electron beam, the zinc acetate is transformed into a zinc oxide nanomaterial and is capable of producing sub-15 nm structures, spaced on a 40 nm pitch. The transformation is confirmed by the XPS, optical band gap (3.3 eV), and electrical measurements, which show the decomposition of zinc acetate
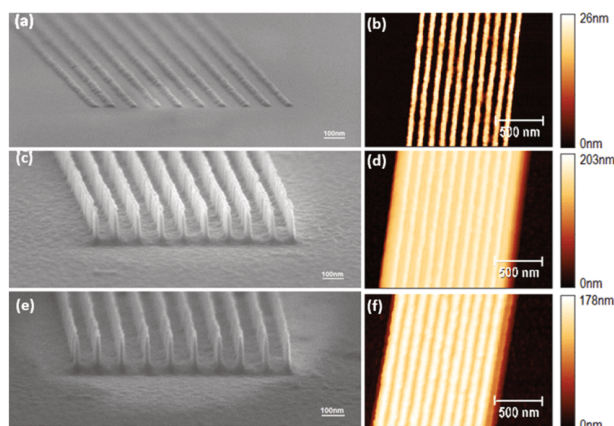
216

Figure 7. (a) SEM and (b) AFM images of the 30 nm lines on a 100 nm pitch that was written at 30 keV. (c) SEM and (d) AFM images of the resist after a 20 s plasma etching. (e) SEM and (f) AFM silicon patterns after removal of the resist using an NH_4Cl aqueous solution (3 mol/L). The dry etch experiments were carried out in an Oxford Instrument Plasma Pro 100 Cobra ICP etching system. The plasma is based on SF_6/C_4F_8 (22 sccm:35 sccm) gases at a pressure of 10 mTorr with a deep reactive ion etching (DRIE) power of 20 W and a forward inductively coupled plasma (ICP) power of 1200 W; the etching time was 20 s.

into zinc oxide using an electron beam. Moreover, we have shown that these zinc oxide nanopatterns can be used as a hard mask for high-selectivity ICP−RIE etching of silicon using standard silicon plasma etching conditions. It was determined that the zinc oxide nanomaterial exhibits extremely high etch selectivity to silicon in the presence of an SF_6/C_4F_8 etch, allowing for the transfer of 27 nm wide lines into the silicon substrate. It is therefore possible to fabricate sub-50 nm wide, 160 nm tall silicon structures in a single lithography-and-etch step. Thanks to its relative simplicity, this opens up exciting new possibilities for future nanoelectronics because we have shown not only that this material exhibits excellent dry etch properties when compared to the industry standard resists but also that this material is a wide band gap semiconductor, which can be used to explore new nanoelectronic devices with ease.

■ AUTHOR INFORMATION

Corresponding Authors

Scott M. Lewis − *Department of Chemistry, The University of Manchester, Manchester M13 9PL, United Kingdom; Sci-Tron Limited, Walsall WS9 8LZ, United Kingdom; Department of Applied Physics and Materials Science, Kavli Nanoscience Institute, California Institute of Technology, Pasadena, California 91125, United States;* ⊙ orcid.org/0000-0002-4183-1906; Email: scott.lewis@manchester.ac.uk

Richard E. P. Winpenny − *Department of Chemistry, The University of Manchester, Manchester M13 9PL, United Kingdom; Sci-Tron Limited, Walsall WS9 8LZ, United Kingdom;* ⊙ orcid.org/0000-0002-7101-3963; Email: richard.winpenny@manchester.ac.uk

Authors

Ahmad Chaker − *Department of Chemistry, The University of Manchester, Manchester M13 9PL, United Kingdom;* ⊙ orcid.org/0000-0001-6881-1270

Hayden R. Alty − *Department of Chemistry, The University of Manchester, Manchester M13 9PL, United Kingdom*

Peng Tian − *Department of Chemistry, The University of Manchester, Manchester M13 9PL, United Kingdom*

Anastasios Kotsovinos − *Department of Chemistry, The University of Manchester, Manchester M13 9PL, United Kingdom*

Grigore A. Timco − *Department of Chemistry, The University of Manchester, Manchester M13 9PL, United Kingdom*

Christopher A. Muryn − *Department of Chemistry, The University of Manchester, Manchester M13 9PL, United Kingdom*

Complete contact information is available at:
https://pubs.acs.org/10.1021/acsanm.0c02756

Notes
The authors declare no competing financial interest.

■ REFERENCES

(1) Djurišić, A. B.; Chen, X.; Leung, Y. H.; Ng, A. M. C. ZnO nanostructures: growth, properties and applications. *J. Mater. Chem.* **2012**, *22*, 6526−6535.

(2) Wang, Z. L. Splendid one-dimensional nanostructures of zinc oxide: a new nanomaterial family for nanotechnology. *ACS Nano* **2008**, *2*, 1987−1992.

(3) Kołodziejczak-Radzimska, A.; Jesionowski, T. Zinc oxide from synthesis to application: a review. *Materials* **2014**, *7*, 2833−2881.

(4) Han, S. H.; Agbenyeke, R. E.; Lee, G. Y.; Park, B. K.; Kim, C. G.; Lee, Y. K.; Son, S. U.; Chung, T. M. Synthesis and characterization of novel zinc precursors for ZnO thin film deposition by atomic layer deposition. *Dalton Trans.* **2020**, *49*, 4306−4314.

(5) Hamelmann, F. U. Thin film zinc oxide deposited by CVD and PVD. In Journal of Physics. *J. Phys.: Conf. Ser.* **2016**, *764*, No. 012001.

(6) Chen, Z.; Shum, K.; Salagaj, T.; Zhang, W.; Strobl, K. In ZnO Thin Films Synthesized By Chemical Vapor Deposition, *2010 IEEE Long Island Systems, Applications and Technology Conference*, 2010; pp 1−6.

(7) Lan, W.; Peng, X.; Liu, X.; He, Z.; Wang, Y. Preparation and properties of ZnO thin films deposited by sol-gel technique. *Front. Mater. Sci. China* **2007**, *1*, 88−91.

(8) Zargar, R. A.; Arora, M.; Bhat, R. A. Study of nanosized copper-doped ZnO dilute magnetic semiconductor thick films for spintronic device applications. *Appl. Phys. A* **2018**, *124*, 36.

(9) Bacaksiz, E.; Parlak, M.; Tomakin, M.; Özçelik, A.; Karakız, M.; Altunbaş, M. The effects of zinc nitrate, zinc acetate and zinc chloride precursors on investigation of structural and optical properties of ZnO thin films. *J. Alloys Compd.* **2008**, *466*, 447−450.

(10) Gusatti, M.; Barroso, G. S.; Campos, C. E. M. D.; Souza, D. A. R. D.; Rosário, J. D. A. D.; Lima, R. B.; Milioli, C. C.; Silva, L. A.; Riella, H. G.; Kuhnen, N. C. Effect of different precursors in the chemical synthesis of ZnO nanocrystals. *Mater. Res.* **2011**, *14*, 264−267.

(11) Jayatissa, A. H.; Guo, K.; Gupta, T.; Jayasuriya, A. C. Spin coating of transparent zinc oxide films using novel precursor. *J. Mater. Sci.: Mater. Electron.* **2009**, *20*, 577−581.

(12) Duan, Y.; Li, J.; Yang, X.; Hu, L.; Wang, Z.; Liu, Y.; Wang, C. Kinetic analysis on the non-isothermal dehydration by integral master-plots method and TG−FTIR study of zinc acetate dihydrate. *J. Anal. Appl. Pyrolysis* **2008**, *83*, 1−6.

(13) Krunks, M.; Mellikov, E. Zinc oxide thin films by the spray pyrolysis method. *Thin Solid Films* **1995**, *270*, 33−36.

(14) Saleem, M.; Fang, L.; Ruan, H. B.; Wu, F.; Huang, Q. L.; Xu, C. L.; Kong, C. Y. Effect of zinc acetate concentration on the structural and optical properties of ZnO thin films deposited by Sol-Gel method. *Int. J. Phys. Sci.* **2012**, *7*, 2971−2979.

(15) Lin, C. C.; Li, Y. Y. Synthesis of ZnO nanowires by thermal decomposition of zinc acetate dihydrate. *Mater. Chem. Phys.* **2009**, *113*, 334−337.

(16) Bahadur, H.; Srivastava, A. K.; Sharma, R. K.; Chandra, S. Morphologies of solgel derived thin films of ZnO using different precursor materials and their nanostructures. *Nanoscale Res. Lett.* **2007**, *2*, 469−475.

(17) Velázquez-Nevárez, G. A.; Vargas-García, J. R.; Aguilar-Hernández, J.; Vega-Becerra, O. E.; Chen, F.; Shen, Q.; Zhang, L. Optical and electrical properties of (002)-oriented ZnO films prepared on amorphous substrates by sol-gel spin-coating. *Mater. Res.* **2016**, *19*, 113−117.

(18) Kumar, V.; Singh, N.; Mehra, R. M.; Kapoor, A.; Purohit, L. P.; Swart, H. C. Role of film thickness on the properties of ZnO thin films grown by sol-gel method. *Thin Solid Films* **2013**, *539*, 161−165.

(19) Nagase, T.; Ooie, T.; Sakakibara, J. A novel approach to prepare zinc oxide films: excimer laser irradiation of sol−gel derived precursor films. *Thin Solid Films* **1999**, *357*, 151−158.

(20) Asakuma, N.; Hirashima, H.; Imai, H.; Fukui, T.; Toki, M. Crystallization and reduction of sol-gel-derived zinc oxide films by irradiation with ultraviolet lamp. *J. Sol-Gel Sci. Technol.* **2003**, *26*, 181−184.

(21) Lloyd, J. S.; Fung, C. M.; Alvim, E. J.; Deganello, D.; Teng, K. S. UV photodecomposition of zinc acetate for the growth of ZnO nanowires. *Nanotechnology* **2015**, *26*, No. 265303.

(22) Hu, X.; Masuda, Y.; Ohji, T.; Kato, K. Micropatterning of ZnO nanoarrays by forced hydrolysis of anhydrous zinc acetate. *Langmuir* **2008**, *24*, 7614−7617.

(23) Hong, S.; Yeo, J.; Manorotkul, W.; Kang, H. W.; Lee, J.; Han, S.; Rho, Y.; Suh, Y. D.; Sung, H. J.; Ko, S. H. Digital selective growth of a ZnO nanowire array by large scale laser decomposition of zinc acetate. *Nanoscale* **2013**, *5*, 3698−3703.

(24) Utke, I.; Hoffmann, P.; Melngailis, J. Gas-assisted focused electron beam and ion beam processing and fabrication. *J. Vac. Sci. Technol., B: Microelectron. Nanometer Struct.* **2008**, *26*, 1197−1276.

(25) Riazanova, A. V.; Rikers, Y. G.; Mulders, J. J.; Belova, L. M. Pattern shape control for heat treatment purification of electron-beam-induced deposition of gold from the Me2Au (acac) precursor. *Langmuir* **2012**, *28*, 6185−6191.

(26) Hirt, L.; Reiser, A.; Spolenak, R.; Zambelli, T. Additive manufacturing of metal structures at the micrometer scale. *Adv. Mater.* **2017**, *29*, No. 1604211.

(27) Botman, A.; Mulders, J. J. L.; Hagen, C. W. Creating pure nanostructures from electron-beam-induced deposition using purification techniques: a technology perspective. *Nanotechnology* **2009**, *20*, No. 372001.

(28) Saifullah, M. S. M. SUB-10 NM DIRECT PATTERNING OF OXIDES USING AN ELECTRON BEAM—A REVIEW. *Cosmos* **2009**, *5*, 1−21.

(29) Jones, G. A. C.; Xiong, G.; Anderson, D. Fabrication of nanoscale ZnO field effect transistors using the functional precursor zinc neodecanoate directly as a negative electron beam lithography resist. *J. Vac. Sci. Technol., B: Microelectron. Nanometer Struct.* **2009**, *27*, 3164−3168.

(30) Wang, Y.; Wu, T.; Chen, M.; Su, L.; Zhang, Q.; Yuan, L.; Zhu, Y.; Tang, Z. Well-controlled wet etching of ZnO films using hydrogen peroxide solution. *Appl. Surf. Sci.* **2014**, *292*, 34−38.

(31) Zhang, T.; Sun, L.; Han, D.; Wang, Y.; Han, R. In Surface Uniform Wet Etching of ZnO Films and Influence of Oxygen Annealing on Etching Properties. 6th IEEE International Conference on Nano/Micro Engineered and Molecular Systems, 2011; pp 626−629.

(32) Sun, J.; Bian, J.; Liang, H.; Zhao, J.; Hu, L.; Zhao, Z.; Liu, W.; Du, G. Realization of controllable etching for ZnO film by NH4Cl aqueous solution and its influence on optical and electrical properties. *Appl. Surf. Sci.* **2007**, *253*, 5161−5165.

(33) Kim, D.; Hwang, I.; Son, J.; Kim, H. Inductively coupled-plasma dry etching of a ZnO thin film by Ar-diluted CF4 gas. *J. Korean Phys. Soc.* **2011**, *58*, 1536−1540.

(34) Bae, J. W.; Jeong, C. H.; Kim, H. K.; Kim, K. K.; Cho, N. G.; Seong, T. Y.; Park, S. J.; Adesida, I.; Yeom, G. Y. High-rate dry etching of ZnO in BCl3/CH4/H2 plasmas. *Jpn. J. Appl. Phys.* **2003**, *42*, No. L535.

(35) Lim, W. T.; Stafford, L.; Song, J. I.; Park, J. S.; Heo, Y. W.; Lee, J. H.; Kim, J. J.; Pearton, S. J. High-density plasma etching of indium−zinc oxide films in Ar/Cl2 and Ar/CH4/H2 chemistries. *Appl. Surf. Sci.* **2006**, *253*, 2752−2757.

(36) Gwiazda, A.; Rumyantseva, A.; Gokarna, A.; Nomenyo, K.; Chevalier-César, C.; Lérondel, G. Simple and versatile high aspect ratio nanostructuring via zinc oxide masking. *Adv. Mater. Technol.* **2017**, *2*, No. 1700107.

(37) Lewis, S. M.; Hunt, M. S.; DeRose, G. A.; Alty, H. R.; Li, J.; Wertheim, A.; De Rose, L.; Timco, G. A.; Scherer, A.; Yeates, S. G.; Winpenny, R. E. P. Plasma-etched pattern transfer of sub-10 nm structures using a metal−organic resist and helium ion beam lithography. *Nano Lett.* **2019**, *19*, 6043−6048.

(38) Lewis, S. M.; Fernandez, A.; DeRose, G. A.; Hunt, M. S.; Whitehead, G. F.; Lagzda, A.; Alty, H. R.; Ferrando-Soria, J.; Varey, S.; Kostopoulos, A. K.; Schedin, F.; Winpenny, R. E. P.; et al. Use of supramolecular assemblies as lithographic resists. *Angew. Chem.* **2017**, *129*, 6853−6856.

(39) Kim, Y. R. Room Temperature Vacuum Processing of Zinc Acetate and Oxide Films. Ph.D Thesis, Imperial College London Department of Materials, 2016; p 77.

(40) Al-Gaashani, R.; Radiman, S.; Daud, A. R.; Tabet, N.; Al-Douri, Y. J. C. I. XPS and optical studies of different morphologies of ZnO nanostructures prepared by microwave methods. *Ceram. Int.* **2013**, *39*, 2283−2292.

218

(41) Mar, L. G.; Timbrell, P. Y.; Lamb, R. N. An XPS study of zinc oxide thin film growth on copper using zinc acetate as a precursor. *Thin Solid Films* **1993**, *223*, 341−347.

(42) Ma, J.; Ji, F.; Ma, H. L.; Li, S. Y. Preparation and characterization of ZnO films by an evaporating method. *J. Vac. Sci. Technol., A* **1995**, *13*, 92−94.

(43) Moormann, H.; Kohl, D.; Heiland, G. Work function and band bending on clean cleaved zinc oxide surfaces. *Surf. Sci.* **1979**, *80*, 261−264.

(44) Wei, M.; Li, C. F.; Deng, X. R.; Deng, H. Surface work function of transparent conductive ZnO films. *Energy Procedia* **2012**, *16*, 76−80.

(45) Blatt, F. J. *Physics of Electronic Conduction in Solids*; McGraw-Hill: New York, 1968; pp 182−243.

(46) Natsume, Y.; Sakata, H. Zinc oxide films prepared by sol-gel spin-coating. *Thin Solid Films* **2000**, *372*, 30−36.

(47) Adl, A. H.; Kar, P.; Farsinezhad, S.; Sharma, H.; Shankar, K. Effect of sol stabilizer on the structure and electronic properties of solution-processed ZnO thin films. *RSC Adv.* **2015**, *5*, 87007−87018.

(48) Gu, Q. L.; Ling, C. C.; Chen, X. D.; Cheng, C. K.; Ng, A. M. C.; Beling, C. D.; Fung, S.; Djurišić, A. B.; Lu, L. W.; Brauer, G.; Ong, H. C. Hydrogen peroxide treatment induced rectifying behavior of Au/ n-ZnO contact. *Appl. Phys. Lett.* **2007**, *90*, No. 122101.

(49) Brillson, L. J.; Lu, Y. ZnO Schottky barriers and Ohmic contacts. *J. Appl. Phys.* **2011**, *109*, 8.

(50) Goodyear, A.; Boettcher, M.; Stolberg, I.; Cooke, M. March. Direct comparison of the performance of commonly used e-beam resists during nano-scale plasma etching of Si, SiO2, and Cr. *Advanced Etch Technology for Nanopatterning IV* **2015**, *9428*, No. 94280V.

219